WET AND DRY PERIODS IN REGIONS SURROUNDING THE ATLANTIC OCEAN BASIN

EDITED BY: Anita Drumond, Belen Rodriguez-fonseca, Chris Reason
and Silvina A. Solman

PUBLISHED IN: Frontiers in Environmental Science, Frontiers in Earth Science
and Frontiers in Physics

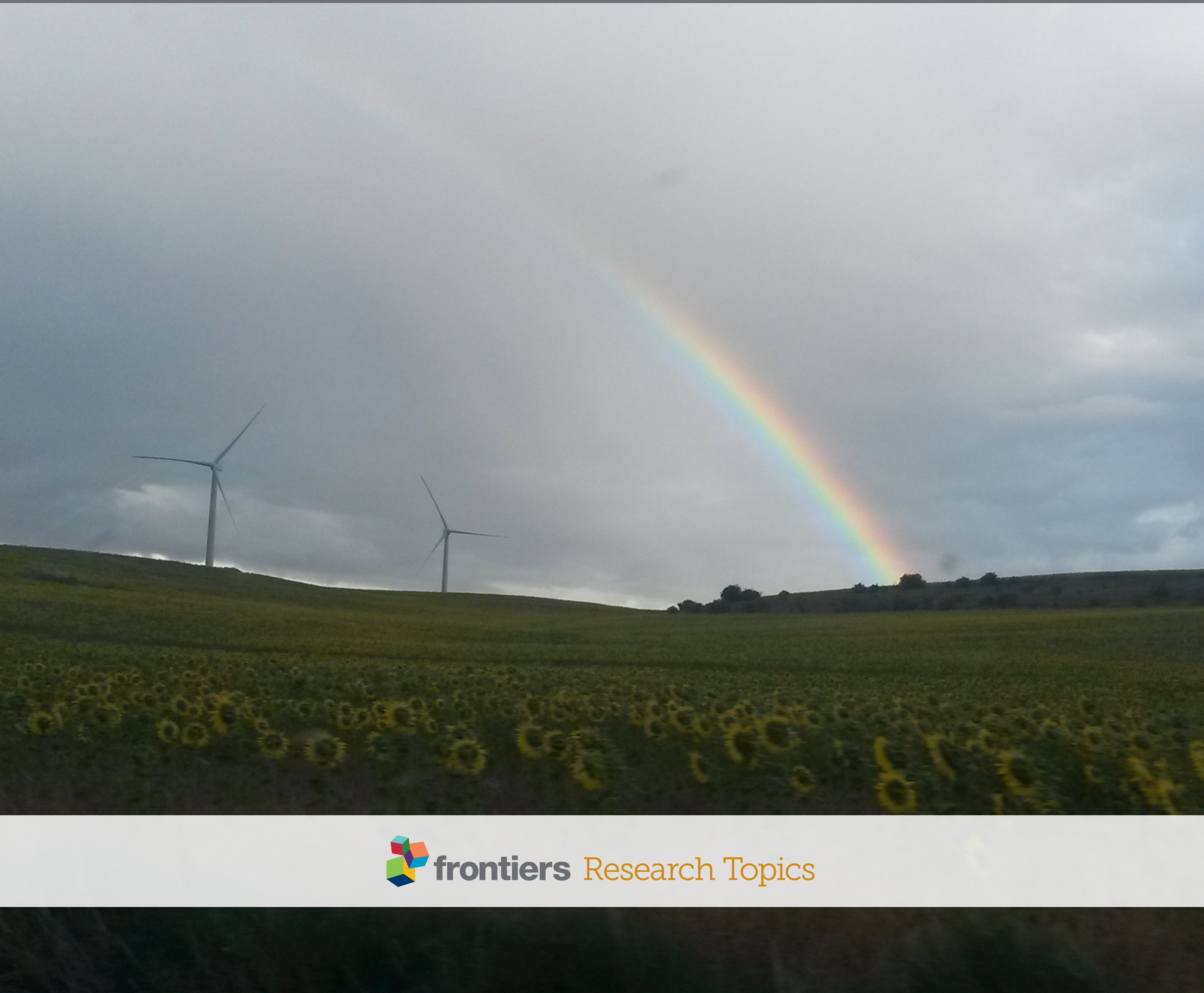

frontiers Research Topics

About Frontiers

Frontiers is more than just an open-access publisher of scholarly articles: it is a pioneering approach to the world of academia, radically improving the way scholarly research is managed. The grand vision of Frontiers is a world where all people have an equal opportunity to seek, share and generate knowledge. Frontiers provides immediate and permanent online open access to all its publications, but this alone is not enough to realize our grand goals.

Frontiers Journal Series

The Frontiers Journal Series is a multi-tier and interdisciplinary set of open-access, online journals, promising a paradigm shift from the current review, selection and dissemination processes in academic publishing. All Frontiers journals are driven by researchers for researchers; therefore, they constitute a service to the scholarly community. At the same time, the Frontiers Journal Series operates on a revolutionary invention, the tiered publishing system, initially addressing specific communities of scholars, and gradually climbing up to broader public understanding, thus serving the interests of the lay society, too.

Dedication to Quality

Each Frontiers article is a landmark of the highest quality, thanks to genuinely collaborative interactions between authors and review editors, who include some of the world's best academicians. Research must be certified by peers before entering a stream of knowledge that may eventually reach the public - and shape society; therefore, Frontiers only applies the most rigorous and unbiased reviews.

Frontiers revolutionizes research publishing by freely delivering the most outstanding research, evaluated with no bias from both the academic and social point of view.

By applying the most advanced information technologies, Frontiers is catapulting scholarly publishing into a new generation.

What are Frontiers Research Topics?

Frontiers Research Topics are very popular trademarks of the Frontiers Journals Series: they are collections of at least ten articles, all centered on a particular subject. With their unique mix of varied contributions from Original Research to Review Articles, Frontiers Research Topics unify the most influential researchers, the latest key findings and historical advances in a hot research area! Find out more on how to host your own Frontiers Research Topic or contribute to one as an author by contacting the Frontiers Editorial Office: **researchtopics@frontiersin.org**

ISSN 1664-8714
ISBN 978-2-88919-824-5
DOI 10.3389/978-2-88919-824-5

WET AND DRY PERIODS IN REGIONS SURROUNDING THE ATLANTIC OCEAN BASIN

Topic Editors:
Anita Drumond, Universidad de Vigo, Spain
Belen Rodriguez-fonseca, Universidad Complutense de Madrid, Spain
Chris Reason, University of Cape Town, South Africa
Silvina A. Solman, Centro de Investigaciones del Mar y la Atmósfera (CIMA/CONICET-UBA)-DCAO(FCEN-UBA), Argentina

Surrounding area of Medina de Rioseco (Castile and Leon, Spain).
Image by Iñigo Gómara

The Atlantic Ocean is the second largest of the world's oceanic divisions. It is bounded by the continents of America, Europe and Africa and at its polewards margins by the Arctic and the Southern Oceans. Different climatic patterns can be observed along its large latitudinal domain, which extends from the equator to sub-polar regions. Thus, different tropical and extra-tropical meteorological systems may have some influence on the characterization of precipitation regimes observed surrounding the basin, such as the Intertropical Convergence Zone (ITCZ), tropical monsoon systems, westerly storm tracks and atmospheric rivers. The subtropical regions of the Azores and South Atlantic high pressure systems are large evaporative areas which act as important moisture sources for the adjacent continents. Variations in the oceanic characteristics may influence the moisture transport towards the neighboring landmasses and alter the precipitation. The influence of climatic variability modes manifest not only over the Atlantic Ocean, but also over other oceanic regions, may also interact with the regional hydrological budget, thereby generating long periods of drought or excessive precipitation over the Atlantic rim landmasses.

This Research Topic intends to highlight the advances of the scientific community in investigating the continental precipitation surrounding the Atlantic Ocean and its variability on various temporal and spatial scales.

Citation: Drumond, A., Rodriguez-fonseca, B., Reason, C., Solman, S. A., eds. (2016). Wet and Dry Periods in Regions Surrounding the Atlantic Ocean Basin. Lausanne: Frontiers Media.
doi: 10.3389/978-2-88919-824-5

Table of Contents

frontiers in Environmental Science

EDITORIAL
published: 01 February 2016
doi: 10.3389/fenvs.2016.00001

Editorial: Wet and Dry Periods in Regions Surrounding the Atlantic Ocean Basin

Anita Drumond[1]*, *Belen Rodriguez-Fonseca*[2, 3], *Chris Reason*[4] and *Silvina A. Solman*[5]

[1] EPhysLab, Departamento de Física Aplicada, Facultad de Ciencias, Universidade de Vigo, Ourense, Spain, [2] Departamento de Geofísica y Meteorología, Universidad Complutense de Madrid, Madrid, Spain, [3] Instituto de Geociencias, Consejo Superior de Investigaciones Científicas, Universidad Complutense de Madrid, Madrid, Spain, [4] Department of Oceanography, University of Cape Town, Cape Town, South Africa, [5] Centro de Investigaciones del Mar y la Atmósfera (CIMA/CONICET-UBA), Departamento de Ciencias de la Atmosfera y los Oceanos, Facultad de Ciencias Exactas y Naturales, Universidad de Buenos Aires, Buenos Aires, Argentina

Keywords: Atlantic Ocean basin, climate variability, moisture transport, precipitation, droughts

The Editorial on the Research Topic

Wet and Dry Periods in Regions Surrounding the Atlantic Ocean Basin

The Atlantic Ocean is the second-largest of the world's oceanic divisions. It is bounded by the continents of America, Europe, and Africa and at its polewards margins by the Arctic and the Southern Oceans. Different climatic patterns can be observed along its large latitudinal domain, which extends from the equator to sub-polar regions. Thus, different tropical and extra-tropical meteorological systems may have some influence on the characterization of precipitation regimes observed surrounding the basin, such as the Intertropical Convergence Zone (ITCZ), tropical monsoon systems, westerly storm tracks, and atmospheric rivers. The subtropical regions of the Azores and South Atlantic high pressure systems are large evaporative areas which act as important moisture sources for the adjacent continents. Variations in the oceanic characteristics may influence the moisture transport toward the neighboring landmasses and alter the precipitation. The influence of climatic variability modes manifest not only over the Atlantic Ocean, but also over other oceanic regions, may also interact with the regional hydrological budget, thereby generating long periods of drought, or excessive precipitation over the Atlantic rim landmasses.

This Research Topic intends to highlight the advances of the scientific community in investigating the continental precipitation surrounding the Atlantic Ocean and its variability on various temporal and spatial scales. Out of the 10 works published, three of them are focused on the Northeastern Brazil (NE), a region prone to social-economical problems associated with arid climatic conditions and one of the tropical areas with the largest interannual variability in rainfall (de Albuquerque Cavalcanti). Although the linear component of the inter-annual variability may be modulated by the Equatorial Eastern Pacific and tropical South Atlantic sea surface temperature (SST) variability and the associated modifications in the Hadley and Walker cells, the non-linear signal may be influenced by others oceanic regions (da Silva and Mendes). For example, the composite analysis of de Albuquerque Cavalcanti revealed extratropical atmospheric influences of the North and South Atlantic in the pre-rainy season of NE. The non-stationary influence of the Atlantic and Pacific Niños on North Eastern South American rainfall in the twentieth century was investigated by the numerical study of Torralba et al. The authors found that while the Atlantic El Niño was of influence at the beginning of the last century, the Pacific El Niño plays a major role from 1970 onwards. However, the combined effect of both basins after the 1970s amplifies the anomalous rainfall response in the NE. The importance of considering the non-linear processes

Edited by:
Víctor Orlando Magaña,
Universidad Nacional Autónoma de México, Mexico

Reviewed by:
Sergio M. Vicente-Serrano,
Spanish National Research Council, Spain

***Correspondence:**
Anita Drumond
anitadru@uvigo.es

Specialty section:
This article was submitted to Atmospheric Science, a section of the journal Frontiers in Environmental Science

Received: *12 November 2015*
Accepted: *11 January 2016*
Published: *01 February 2016*

Citation:
Drumond A, Rodriguez-Fonseca B, Reason C and Solman SA (2016) Editorial: Wet and Dry Periods in Regions Surrounding the Atlantic Ocean Basin. Front. Environ. Sci. 4:1. doi: 10.3389/fenvs.2016.00001

for a more accurate local precipitation forecast was verified by da Silva and Mendes, who suggested the use of an Artificial Neural Network as a complementary forecast tool for improving the simulation of the daily precipitation over NE during the rainy season by general circulation models.

Still focusing on South America, the South Atlantic Convergence Zone (SACZ) is the dominant summertime cloudiness feature of the subtropics and the western South Atlantic Ocean. In order to facilitate the investigation on SACZ and climate change through the use of numerical simulations, Ambrizzi and Ferraz proposed an alternative objective criterion of the SACZ identification based mainly on precipitation, a variable easily obtained from general circulation models, instead of the intensely used outgoing long wave radiation.

Given the influence of the Tropical Atlantic over the annual migration of the ITCZ and, consequently, over the West African and Brazilian rainfall, oceanic processes in this region was the theme of two model studies. Faye et al. investigated the seasonality of SST and circulation in the North-eastern Atlantic Tropical Upwelling System, a component of the Guinea Gyre characterized by one of the largest annual SST cycles in the tropics. Polo et al. investigated the growth and decay of the equatorial Atlantic SST mode by means of closed heat budget in a coupled general circulation model.

Other studies show the importance of different sub-regions other than the tropical Atlantic in modulating the precipitation. For example, Sori et al. investigated how the moisture transport from the Atlantic Warm Pool may affect North/Central America and Western Europe through a Lagrangian analysis, exploring the interannual variability of moisture contribution from the pool in terms of its areal extent, and of the El Niño Southern Oscillation. Reason and Smart investigated warm events in the tropical south east Atlantic and associated episodes of large positive rainfall anomalies over Southern Africa during its late rainy season (February–April).

Finally, two articles illustrate the efforts in investigating the precipitation in the Atlantic basin during the past. Wade et al. analyzed the spatial representativeness of rainfall over the Saloum delta (Senegal), from seasonal to decadal timescales, useful for evaluating the significance of local long-term reconstructions of precipitation over northern Africa from paleoclimate proxies. They found that the summer rainfall shows extended spatial coherence associated with the West African Monsoon. An example of historical recompilation using several data sources, such as newspapers, meteorological data digitized from stations in Portugal and Spain and the twentieth century Reanalysis, is the case study of the record precipitation and flood event in south-western Iberia in December 1876 presented by Trigo et al. The authors reported an intense negative North Atlantic Oscillation Index event and the floods resulted from the continuous precipitation recorded between 28 November and 7 December, due to the consecutive passage of Atlantic low-pressure systems fuelled by the presence of an atmospheric-river tropical moisture flow over the central Atlantic Ocean.

The Atlantic Ocean still presents strong challenges in analysis and modeling. Most numerical models have important rainfall, wind and SST biases in the Atlantic, which compromise the representation of the climate. To enhance the reliability of models, the observational record must be better understood, and the origin of ocean variability and the role of the atmospheric components associated with rainfall need to be clarified. For this reason, this issue tackles the different hot topics at the cutting edge of the current state of the art, making a step forward in current understanding of the climate variability in the Atlantic Ocean.

AUTHOR CONTRIBUTIONS

All authors listed, have made substantial, direct, and intellectual contribution to the work, and approved it for publication.

ACKNOWLEDGMENTS

AD acknowledges the Spanish Government and FEDER through the support of the SETH project (CGL2014-60849-JIN). BR received funding from the EU FP7/2007-2013 under grant agreement no. 603521.

Conflict of Interest Statement: The authors declare that the research was conducted in the absence of any commercial or financial relationships that could be construed as a potential conflict of interest.

frontiers
in Environmental Science

ORIGINAL RESEARCH
published: 30 April 2015
doi: 10.3389/fenvs.2015.00034

The influence of extratropical Atlantic Ocean region on wet and dry years in North-Northeastern Brazil

Iracema F. de Albuquerque Cavalcanti *

Center of Weather Forecasting and Climate Studies, National Institute of Space Research, São Paulo, Brazil

The rainy season of north-Northeastern Brazil (NE), one of the tropical regions with the largest rainfall interannual variability, is associated with the Intertropical Convergence Zone (ITCZ) influence, which is located in the southermost position during this season (March-April-May). However, there is a large interannual variability in the ITCZ position, associated with atmospheric and oceanic anomalies, responsible for dry or wet years in the region. Besides the tropical Pacific Sea Surface Temperature (SST) anomalies and the Tropical Atlantic SST gradient influences on this variability, extratropical atmospheric influences are identified over the North and South Atlantic. Composites of cases with anomalous precipitation during the middle of the rainy season (April) indicate the El Niño-Southern Oscillation (ENSO) features and northern and southern Atlantic atmospheric anomalies in December-January-February (DJF). When El Niño and La Niña years are removed from the composites of dry and wet cases, respectively, the centers of action over the extratropical North Atlantic in DJF remain, and features of extratropical South Hemisphere become more evident. The tropical SST dipole is still present with inverted signs in each case, consistent with the NE precipitation anomalies. The main mode of variability in the Southern Hemisphere (South Annular Mode) and in the Northern Hemisphere (North Annular Mode) is present in DJF during the dry cases. These annular patterns occur in the composites of Northeast Brazil precipitation anomalies including or excluding ENSO years. Therefore, besides ENSO relations with SAM discussed in previous studies, another connection exists over the South Atlantic, linking anomalies between high and tropical latitudes. The precipitation anomalies over NE have contributions of the two extratropical Atlantic hemispheres regions. The atmospheric anomalies observed in the pre-rainy season can be a helpful tool in monitoring the North Northeastern Brazil rainfall variability.

Keywords: Northeast Brazil, Atlantic Ocean, ITCZ, precipitation anomalies, North Atlantic centers of action

Edited by:
Anita Drumond,
University of Vigo, Spain

Reviewed by:
Everaldo Barreiros De Souza,
Universidade Federal do Para, Brazil
Leila Vespoli Carvalho,
University of California, Santa Barbara, USA

***Correspondence:**
Iracema F. de Albuquerque Cavalcanti,
Center of Weather Forecasting and Climate Studies, National Institute of Space Research, Rodovia Presidente Dutra, km 40, CEP 12630-000, São Paulo, Brazil
iracema.cavalcanti@cptec.inpe.br

Specialty section:
This article was submitted to Atmospheric Science, a section of the journal Frontiers in Environmental Science

Received: *11 November 2014*
Accepted: *16 April 2015*
Published: *30 April 2015*

Citation:
de Albuquerque Cavalcanti IF (2015) The influence of extratropical Atlantic Ocean region on wet and dry years in North-Northeastern Brazil. Front. Environ. Sci. 3:34. doi: 10.3389/fenvs.2015.00034

Introduction

The rainy season in the northern sector of Northeastern Brazil (NE) occurs in March-April-May (MAM), associated with the displacement of the Intertropical Convergence Zone (ITCZ) along the year, following the seasonal warm Sea Surface Temperature (SST) displacement north-south (Hastenrath, 1984). The ITCZ variability depends on the tropical inter-hemispheric Atlantic SST and atmospheric circulation mechanisms (Hastenrath and Heller, 1977; Moura and Shukla, 1981;

Hastenrath and Greischar, 1993) and affects the NE rainfall. A review of impacts of the rainfall variability in this region was presented in Hastenrath (2012). Besides the tropical Atlantic, the Pacific Ocean has a strong influence on NE precipitation, in El Niño years (Covey and Hastenrath, 1978; Kousky et al., 1984). The changes in the Walker circulation with ascent motion in the eastern or central Pacific and subsidence over Northeast Brazil and Atlantic Ocean during El Niño, were discussed by Kousky et al. (1984), Pezzi and Cavalcanti (2001), Souza and Ambrizzi (2002), and Tedeschi et al. (2013). Enfield and Mayer (1997) showed a relation between the Pacific SST and Atlantic SST in ENSO years. On the other hand, the influence of Atlantic anomalies on the Pacific ENSO, through changes in the Walker circulation was shown by Rodríguez-Fonseca et al. (2009). Besides interannual climate variability, intraseasonal variability indicated by Madden and Julian Oscillation (MJO) affects NE precipitation, as shown in Kayano and Kousky (1999).

Influences of synoptic systems on a daily basis that cause heavy precipitation over Northeast Brazil have been discussed by Kouadio et al. (2012), who analyzed the influence of easterly waves, (Kousky, 1980), who identified squall lines, and Cavalcanti (2012), who reported specific events associated with easterly disturbances. Other synoptic system that can affect rainfall variability over north Northeast Brazil is the upper tropospheric cyclonic vortice (Kousky and Gan, 1981). These synoptic systems are affected by larger spatial and temporal scales of atmospheric and oceanic conditions.

Extratropical teleconnection influences, such as the Pacific North America (PNA) pattern on NE rainfall was discussed in Rao and Brito (1985) and Nobre and Shukla (1996). Extreme precipitation events over NE were also associated with middle latitude wavetrains from the North and South Hemispheres (Liebmann et al., 2011). Extratropical features in December-January-February (DJF) associated with the shifting of the North Atlantic Oscillation (NAO) centers are connected to the ITCZ position in April (Souza and Cavalcanti, 2009). When the ITCZ is displaced southward, there are two anomalous centers of Sea Level Pressure (SLP) or geopotential at middle levels over extratropical North Atlantic, which are related to the shifting of the positive phase of NAO centers of action. In this way, the subtropical North Atlantic High is enhanced, intensifying the northerlies trade winds and pushing the convergence zone southwards. At the same time, the SST in the tropical North Atlantic is colder than normal, consistent with the stronger than normal trade winds and the atmospheric circulation at low levels. When the ITCZ is displaced northwards of the climatological position, the tropical SST and extratropical atmospheric anomalies display opposite conditions.

In the present study, wet and dry cases over northern NE, in April, are selected to analyze the atmospheric extratropical features in the Atlantic region more extensively, extending the area to the Pacific Ocean and removing the ENSO effects in order to identify other features associated with the NE precipitation.

Data and Method

The period of analysis is 1980–2009, accomplishing 30 years of climatology. Monthly precipitation data was obtained from the Global Precipitation Climatology Project (GPCP), (Adler et al., 2003) with horizontal resolution of $2.5^0 \times 2.5^0$. Monthly SST with horizontal resolution of $2^0 \times 2^0$, from Extended Reconstructed Sea Surface Temperature (ERSST), (Smith et al., 2008), and monthly atmospheric data from ERA–Interim reanalyses with horizontal resolution of $1.5^0 \times 1.5^0$ (Dee et al., 2011) were used to analyze the large scale features.

The area of analysis is the northern of Northeast Brazil (NE). Wet and dry cases over NE in April are selected using the Standardized Precipitation Index (SPI) proposed by McKee et al. (1993), applied to the spatial average of precipitation anomalies in the area (46^0W– 35^0W; 6^0S– 2^0S). The index identifies extreme wet/dry ($SPI \geq 2.0/SPI \leq -2.0$), severe wet/dry ($1.5 \leq SPI \leq 2.0)/-2 < SPI \leq -1.5$), and moderate wet/dry ($1.0 \leq SPI < 1.5)/(-1.5 < SPI \leq -1.0$) conditions. Another category was introduced to identify weak wet and dry cases ($0.5 < SPI < 1.0/-1.0 < SPI < -0.5$) that affect also the region. The index is obtained dividing the precipitation anomaly by the standard deviation. The anomalies were calculated considering the climatological period of 1980–2009. Composites of wet and dry selected cases and new sets without ENSO years are analyzed to identify other features. ENSO years were obtained from CPC/NOAA MAM conditions. The students test was applied to precipitation composites to show the significance of each wet and dry cases. Precipitation and SST anomalies of April, and atmospheric fields of DJF are analyzed for the composites. An Empirical Orthogonal Function (EOF) analysis is applied to SLP anomalies over the Atlantic Ocean to discuss the relations between the main modes of interannual variability and the precipitation anomalies over NE.

The evolution of the tropical Atlantic SST dipole defined as the difference between the tropical North Atlantic (20^0N–10^0N; 50^0W–20^0W) and tropical South Atlantic (0^0–10^0S; 30^0W–10^0W) anomalous SST is compared to the evolution of NE SPI during the analyzed period. The precipitation variability in NE is also compared to the timeseries of the Principal Component coefficients associated with the second mode of Atlantic SLP variability. Correlations of NAI index defined in Souza and Cavalcanti (2009) as the normalized SLP anomaly difference at two points, P1: 35^0N; 40^0W and P2: 50^0N; 10^0W, with SLP anomalies in all grid points, reinforce some aspects of extratropical influences. Correlations of SLP in the anomalous center close to South Africa (50^0S; 5^0E), identified in Souza and Cavalcanti (2009), with other gridpoints are analyzed to investigate extratropical connections. Timeseries of anomalous pressure over extratropical South Atlantic are compared to NE SPI.

Composites of Wet and Dry NE. Precipitation and Atmospheric/Oceanic Anomalies

In **Table 1** and timeseries of SPI for April (**Figure 1**, blue line) it is seen that there are not cases in the extreme category. There are two wet and dry severe cases, four moderate wet cases, five moderate dry cases, four wet weak cases, and three dry weak cases. Although there is one severe wet case in the 80's and one in the first decade of the twenty-first century, there are more

TABLE 1 | Selected years in each category of Wet and Dry April cases.

	Extreme	Severe	Moderate	Weak
Wet	–	1985, 2009	1984, 1986, 1989, 1995	1988, 1996, 2001, 2006
Dry	–	1981, 1983	1980, 1987, 1992, 1993, 1998	1990, 1991, 2005

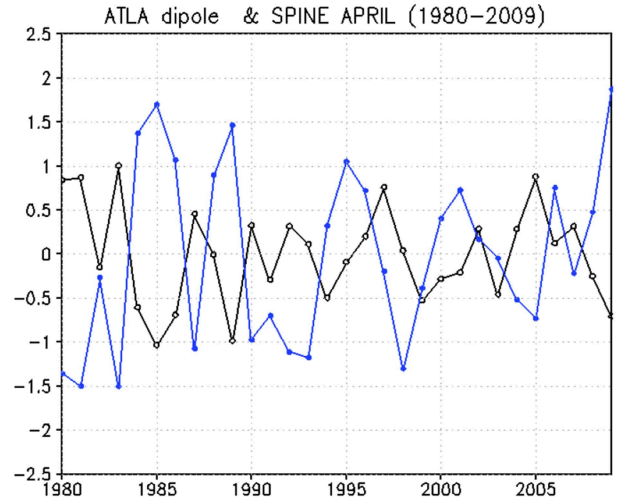

FIGURE 1 | SPI time series in north-Northeastern Brazil (46^{0}W–35^{0}W; 6^{0}S–2^{0}S) (blue line) and timeseries of SST dipole, defined as the difference between the tropical North Atlantic (20^{0}N–10^{0}N; 50^{0}W–20^{0}W) and tropical South Atlantic (0^{0}–10^{0}S; 30^{0}W–10^{0}W) anomalous SST (^{0}C) in April.

dry cases in the first decade than in the last decade. This finding could suggest a relation to trends in the tropical Atlantic SST. However, the timeseries of SST dipole, in **Figure 1** (black line), does not show such trend. A longer timeseries should be analyzed to explore the trends in the Atlantic and Pacific that could be related to trends in NE precipitation, which is out of the present study objective. An inspection in the precipitation anomalies of all individual cases shows that they present similar influences of the ITCZ displacement. Therefore, a composite analysis was performed with 10 cases in each category (**Figure 2**). The influence of ITCZ is very clear in the composites. Although the ITCZ develops over the ocean, the strongest precipitation anomalies occur over the extreme northern sector of NE and anomalies extend to eastern Amazonia, in both wet and dry cases. At the same time, opposite anomalies occur over northern South America and in part of southeastern South America. The opposite conditions in the north are associated with the displacement of the ITCZ southwards in the wet NE and northwards in the dry NE. The opposite sign in the southern region is likely to be associated with wavetrains from the Pacific Ocean and moisture flux anomalies from the Amazon region. Anomalies in the Indonesia and Pacific region can trigger Rossby wavetrains identified in several studies of precipitation and convection anomalies over South America, such as Mo and Higgins (1998), Mo and Paegle (2001), Cunningham and Cavalcanti (2006) among others. Precipitation anomalies over La Plata basin have been also related to moisture flux from tropical regions of South America (Drumond et al., 2008). While this latter mechanism can be related directly to precipitation anomalies in the tropical South America, the former connection with the ITCZ behavior needs further investigation, which is out of the present study scope.

The SLP anomalies composites in DJF for wet and dry cases display the North Atlantic extratropical high-low dipole, with opposite signs in each category (**Figure 3**, contour), similar to that found in Souza and Cavalcanti (2009) in cases of the ITCZ displacement. In the wet composite, the anomalous high pressure over the North Atlantic indicates its influence on the southward shifting of the ITCZ, and also on the establishment of cold waters in the tropical North Atlantic. At the same time there is low pressure over the South Atlantic Ocean, which favors the positive SST anomalies in the tropical South Atlantic region. In the dry composite, the anomalous low pressure center over the North Atlantic is consistent with the northward ITCZ displacement and warm waters in the tropical North Atlantic. SST anomalies in April (**Figure 3**, shaded), display the Tropical Atlantic dipole or SST north-south gradient, which is typical of the ITCZ displacement (Hastenrath and Greischar, 1993; Nobre and Shukla, 1996). The presence of the Atlantic extratropical atmospheric anomalies is consistent with the SST anomalies.

The extratropical high-low pressure dipole in the dry and wet composites is related to the second mode of variability over the Atlantic Ocean, resulting from an EOF analysis of SLP, as seen in **Figure 4B**. The SLP main mode of variability in DJF over the Atlantic Ocean is the NAO, seen in **Figure 4A**. It was suggested, in Souza and Cavalcanti (2009) that the two extratropical centers of action associated with the displacement of the ITCZ represented the shifting of the NAO centers. This shifting can produce climate anomalies also over western Europe, with anomalous high or low pressure, as seen in **Figure 3**. Among others, the role of NAO on precipitation over Europe has been discussed by Trigo et al. (2002), focusing on the Iberian Peninsula, and by Uvo (2003), on Norway, Sweden and Finland. Shifting of NAO centers was analyzed by Vicente-Serrano and López-Moreno (2008) in interdecadal scale, showing influences over Europe. **Figure 3** shows that low (high) pressure anomaly would favor wet (dry) conditions in western Europe, during DJF. The relation between anomalous precipitation in NE and the second mode of SLP is shown in **Table 2** and **Figure 5**. For example, the severe dry year of 1980 (negative SPI) has positive PC, which indicates negative SLP anomaly at the southern center of extratropical high-low dipole over North Atlantic. On the other hand, the severe wet year of 2009 has negative PC, which point to positive anomaly in that center. All dry years, selected by SPI, except 1998, have

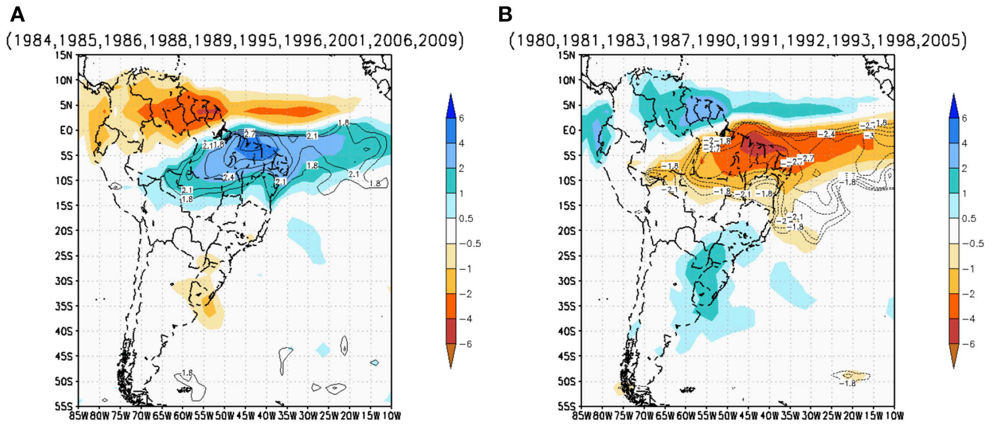

FIGURE 2 | Precipitation anomaly composites (mm/day) [shading] of (A) wet and (B) dry April years in north-Northeastern Brazil. Contour lines above 1.8 (wet) and below −1.8 (dry) indicate regions in NE with significance of 95%.

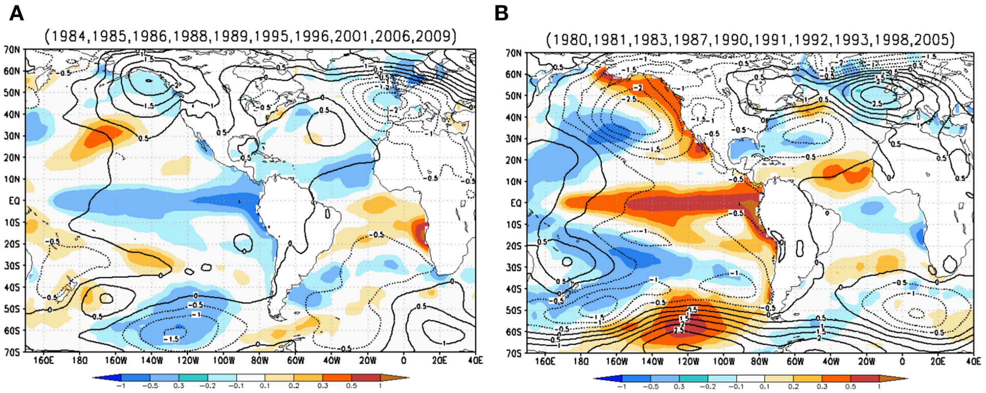

FIGURE 3 | SST anomaly in April (^{0}C) [shading] and SLP anomaly in DJF (hPa) [contour] (A) wet cases; (B) dry cases.

positive principal component coefficients of second mode (PC2) that indicate the desintensification of the North Atlantic Subtropical High, which is consistent with the ITCZ displaced northwards. The SST dipole is also positive, except in 1991, which indicates warmer tropical North Atlantic that favors the northward ITCZ displacement (**Table 2**). The relation between the PC2 and SPI for wet cases does not occur every year, and the SST dipole favorable to southward ITCZ displacement occurs in 7 out of 10 years. In the next section, the influence of the extratropical South Atlantic region on NE precipitation is discussed to show its complementary contribution for NE precipitation variability.

Besides the two centers of action over the extratropical North Atlantic Ocean, an anomalous SLP center near the west coast of North America changes sign from wet to dry cases, being located at the same region of the northern center of the Pacific Decadal Oscillation (PDO). Influences of PDO on South America precipitation, including NE region were discussed in Kayano and Andreoli (2007). The combined effect of ENSO and PDO has impacts on South America. Andreoli and Kayano (2005) showed the circulation changes in cases of ENSO and PDO and their influences over South America. They mention the existence of divergence at high levels in the tropical region, Rossby wavetrains in both hemispheres, changes in the subtropical jet stream and in the Walker and Hadley cells. In the extratropical South Hemisphere, the alternating SLP anomalies over South Pacific also change signs, as well as the center to the south of South Africa, in the wet and dry composites (**Figures 3A,B**).

Composites without ENSO Years

As the composites include ENSO years, its signature is seen in the anomalous SST composites (**Figure 3**, shading). There are La Niña conditions (cold anomalies in Eastern equatorial Pacific) in wet cases, and El Niño conditions (warm anomalies) in dry cases. These characteristics are expected, since the NE precipitation is affected by ENSO, as seen in several studies (e.g., Covey and Hastenrath, 1978; Kousky et al., 1984; Kayano et al., 1988; Kayano and Andreoli, 2006; Tedeschi et al., 2013). Therefore, to remove the ENSO influence, the wet composites were divided in groups of La Niña years and without La Niña years and the dry

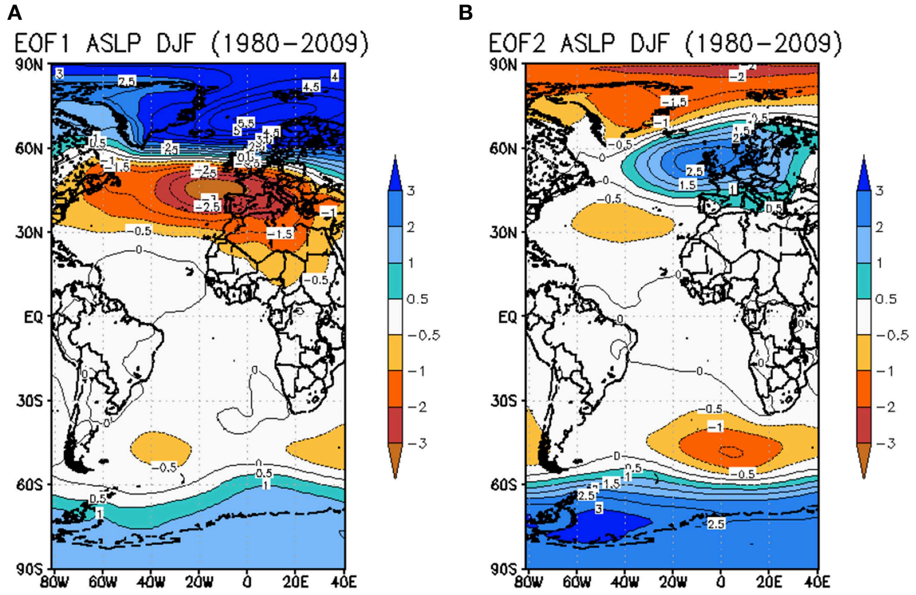

FIGURE 4 | EOF of SLP in DJF, 1980–2009 (A) First mode, (B) Second mode.

TABLE 2 | Signs of: Principal component coefficients of mode 2 (PC2), SST dipole, defined as the difference between the tropical North Atlantic (20^0N–10^0N; 50^0W–20^0W) and tropical South Atlantic (0^0S–10^0S; 30^0W–10^0W) anomalous SST, anomalous SLP at 40^0W; 60^0S (ASLP ATLSUL).

DRY	PC2	SST dipole	ASLP ATLSUL	WET	PC2	SST dipole	ASLP ATLSUL
1980	+	+	+	**1984**	+	–	–
1981	+	+	–	1985	+	–	+
1983	+	+	+	**1986**	–	–	–
1987	+	+	–	1988	–	0	–
1990	+	+	+	1989	+	–	+
1991	+	–	+	**1995**	–	–	+
1992	+	+	+	1996	0	+	+
1993	+	+	+	**2001**	+	–	–
1998	–	0	–	**2006**	+	+	+
2005	+	+	–	**2009**	–	–	–

Yellow and blue shade indicate the conditions of neutral years (bold) for dry and wet cases respectively.

composites were divided in groups of El Niño years and without El Niño years. **Table 3** indicates El Niño and La Niña years.

Figure 6 shows the precipitation anomaly composites of six neutral ENSO years in each category (indicated in bold in **Table 2**). The same features observed in the total composites are identified, indicating that other mechanisms responsible for the precipitation anomalies are still present. The SST Tropical Atlantic dipole is still present in both wet and dry composites without ENSO years and also consistent with the ITCZ influence on NE precipitation. The wet composite without La Niña still shows colder than normal waters in the eastern equatorial Pacific (**Figure 7A**), but in the dry cases there are also cold anomalies in this region (**Figure 7B**). Analyzing year-by-year, negative SST anomalies close to western South America occurred, although weaker, in April of some years of wet or dry composites. Even excluding ENSO years, western and extratropical Pacific SST anomaly configuration display opposite signs in wet and dry NE, but extratropical atmospheric patterns over the North Pacific are very different. The SST composites of wet and dry cases, in the Pacific Ocean, display opposite SST anomalies at equatorial data line and a boomerang-shape pattern, also with opposite anomalies. Tedeschi et al. (2013) identified boomerang patterns in ENSO composites and discussed their extratropical influences on atmospheric circulation with impacts on South America precipitation. It is seen in the present study that these patterns happen also in neutral ENSO years. Opposite SST anomalies in each composite are seen also close to western North America and southern South Pacific. A connection of these opposite SST anomalies in the Pacific with atmospheric circulation and effects on NE precipitation in non-ENSO years is still a subject of investigation.

The two North Atlantic extratropical anomalous centers of opposite signs remain in the wet and dry composites, consistent with the tropical North Atlantic SST anomalies, after removing the effect of ENSO (**Figure 7**). In April 2009, heavy precipitation and flooding occurred in several areas of Northeast, and these anomalous North Atlantic extratropical centers were identified, as shown in Cavalcanti (2012). In the SLP anomalous composites, the pattern changes over the Pacific close to the western coast of North America compared to the total composites. In both wet and dry composites there is a north-south dipole of high-low pressure, indicating that it does not have relation with NE precipitation anomalies (**Figure 7**). Over the extratropical South Pacific and South Atlantic, opposite anomalies are identified in the wet and dry composites, which may act as forcing of changes in the tropical South Atlantic atmospheric circulation.

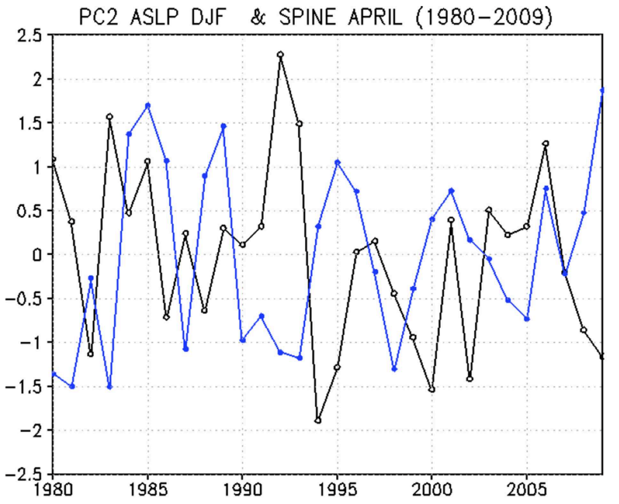

FIGURE 5 | Timeseries of Principal Component Coefficient of the second mode of SLP variability represented in Figure 4 (black line) and timeseries of NE SPI (blue line).

TABLE 3 | El Niño and La Niña (April years).

La Niña	1985, 1988, 1989, 1996,
El Niño	1983, 1987, 1992, 1998

The centers of action over the North Atlantic are identified also in the geopotential at 500 hPa level (**Figure 8**). In the wet composite they are part of a wave number three configuration in the Northern Hemisphere, identified by the troughs and ridges. In the dry composite, the positive phase of the North Annular Mode (NAM) can be recognized, with negative geopotencial anomalies over the polar region and opposite anomalies at middle latitudes. In the Southern Hemisphere (**Figure 9**), the dry composite of geopotencial anomalies at 500 hPa displays the negative phase of the Southern Annular Mode (SAM), with positive anomalies over the polar region and negative anomalies at middle latitudes. In the wet composite a wavenumber one is evident at middle and high latitudes. Therefore, in the dry case, the NAM and SAM in opposite phases seems to be extratropical forcings influencing tropical features. It is suggested that the intensification of the North Polar Vortex (positive NAM phase and associated lower pressure) and desintensification of the South Polar Vortex (negative SAM phase and associated higher pressure) could affect the tropical atmospheric circulation by changes in the Atlantic Subtropical Highs and in the trade winds.

Centers of Action over the Extratropical North and South Atlantic Oceans

Correlations of the NAI index with SLP anomalies in all grid points, show the two centers of action over the North Atlantic and opposite anomalies at high latitudes of the North and South Hemispheres, besides features of the Southern Oscillation (**Figure 10A**). The correlation of anomalous center close to South Africa (50^0S; 5^0E), identified in Souza and Cavalcanti (2009) and also shown in the second mode of SLP variability (**Figure 4B**), with the other grid points, indicate relations of SAM, ENSO features and tropical Atlantic (**Figure 10B**). The relation between

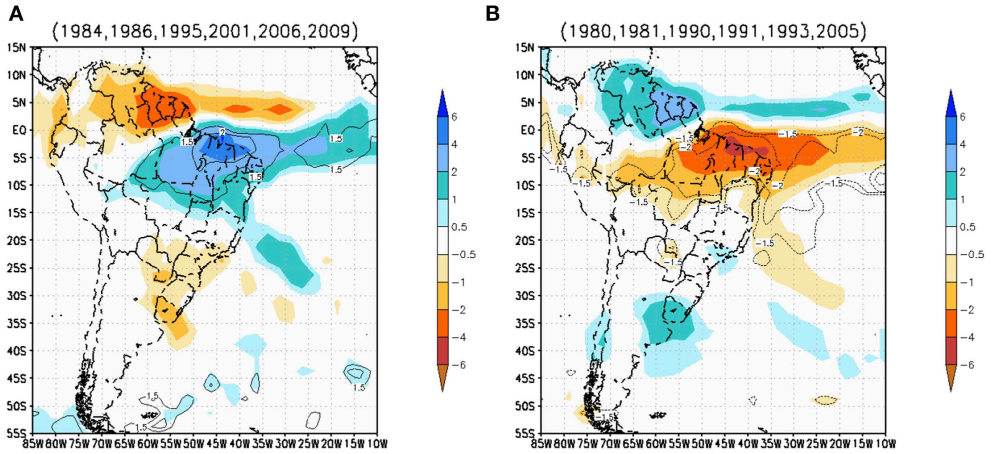

FIGURE 6 | Precipitation anomaly composites (mm/day) [shading] of (A) wet and (B) dry years in north-Northeastern Brazil, excluding ENSO years. Contour lines above 1.5 (wet) and below −1.5 (dry) indicate regions in NE with significance of 95%.

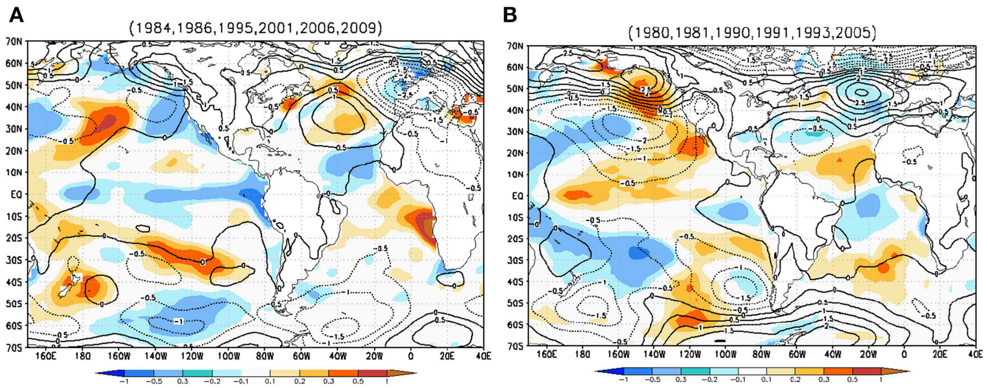

FIGURE 7 | SST anomaly in April (°C) [shading] and SLP anomaly in DJF (hPa) [contour] excluding ENSO years (A) wet cases; (B) dry cases.

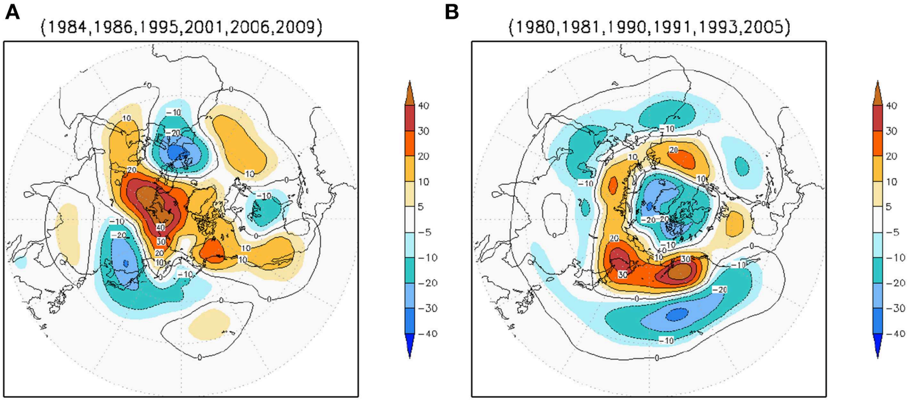

FIGURE 8 | Geopotential anomaly in DJF, N.H., at 500 hPa (mgp) excluding ENSO years (A) wet cases, (B) dry cases.

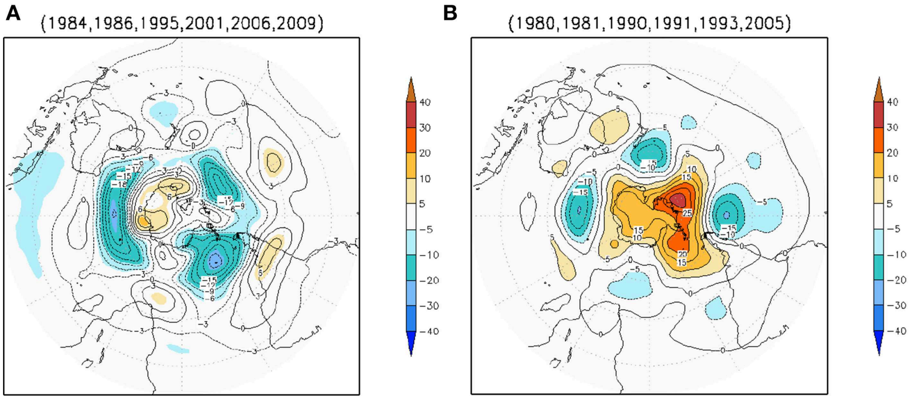

FIGURE 9 | Geopotential anomaly in DJF, S.H., at 500 hPa (mgp) excluding ENSO years (A) wet cases, (B) dry cases.

ENSO and the Antarctic Oscillation or SAM has been identified and discussed in several studies, such as Carvalho et al. (2005), L'Heureux and Thompson (2006), Fogt et al. (2012). Opposite correlations between eastern equatorial Pacific and equatorial Atlantic regions, seen in **Figure 10B**, are related to the ENSO influences, as discussed in Covey and Hastenrath (1978). The connection of the SAM with tropical South Atlantic is also seen in **Figure 11**, which shows correlations of the South Atlantic SLP average (35^0W–0^0) between 50^0 S and latitudes from the Southern Pole to the equator. The same sign at high and tropical

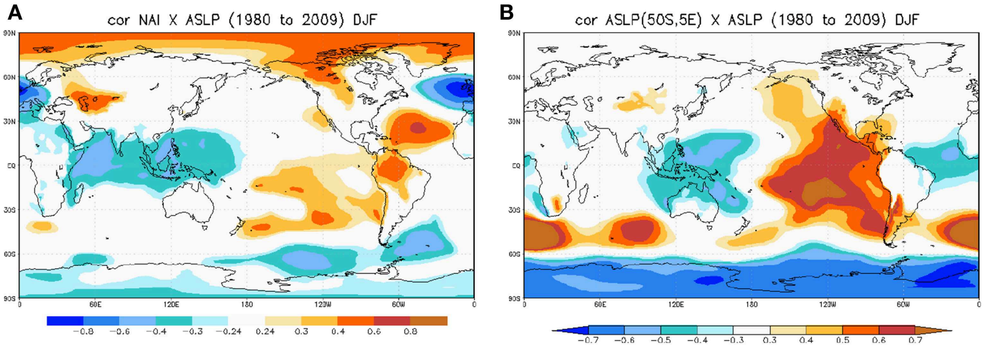

FIGURE 10 | (A) Correlations of NAI with SLP with significance levels of 90% (above 0.24) and 95% (above 0.3), **(B)** correlations of SLP at 50^0S; 5^0E with other gridpoints, with significance of 95% above 0.3.

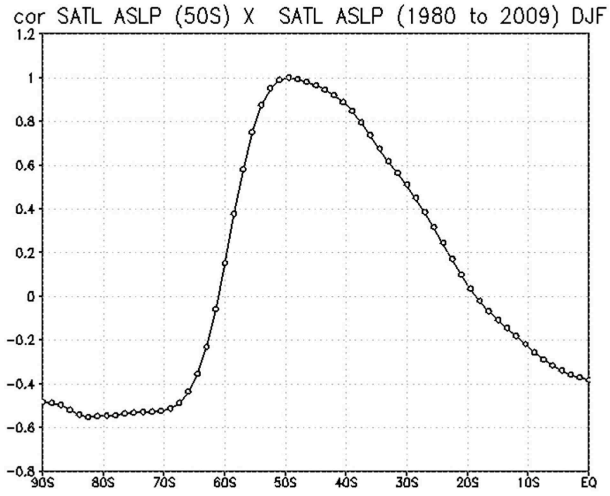

FIGURE 11 | Correlation of South Atlantic SLP average (35^0W–0^0) between 50^0 S and latitudes from the Southern Pole to the equator.

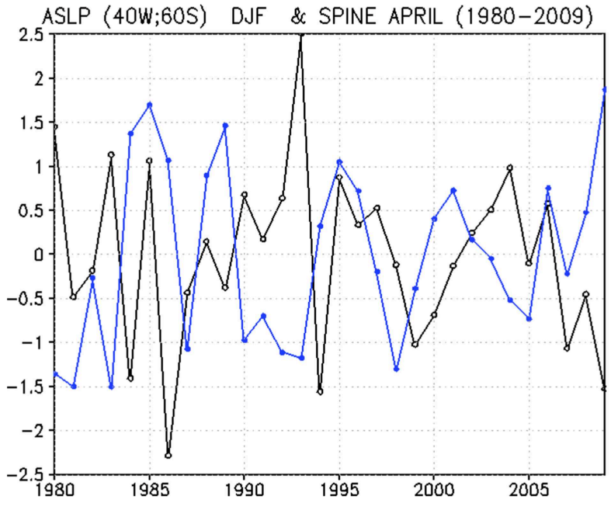

FIGURE 12 | Timeseries of anomalous SLP at 40^0W; 60^0S (black line) and timeseries of NE SPI (blue line).

latitudes and opposite signs at middle latitudes seen in **Figure 11**, were discussed by Mo and White (1985), who showed correlations of zonally averaged anomalies of SLP at 50^0S with other latitudes, in the austral wintertime. Here, the same connections occur in the austral summer time, however only for the Atlantic sector.

To investigate the role of the extratropical South Atlantic region on the NE precipitation, the variability of anomalous pressure at (40^0W; 60^0S), identified as a center with opposite signs in **Figure 7**, is analyzed in **Table 2** and **Figure 12**. The composites show anomalous low pressure for wet cases and anomalous high pressure for dry cases over extratropical Pacific and Atlantic close to South America. Four out of the six cases without El Niño (without La Niña) presented positive (negative) anomaly in this center. In the other two dry cases, the North Atlantic centers of action were favorable (PC2 +). In the other two wet cases that presented positive anomalous SLP in the extratropical South Atlantic, one had influence of the North Atlantic PC2 (1995) and in 2006 the two indices and also the SST dipole were unfavorable to anomalous NE rainfall. This year was selected as weak wet in the SPI category, and other features could be responsible for the anomalous precipitation, like the easterly disturbances or the high level cyclonic vortex position, discussed in the introduction.

Conclusion

Composites of wet and dry cases over northern Northeast Brazil (NE) indicated that besides ENSO influences, there are extratropical Atlantic anomalies, which affect the precipitation variability of this region. Removing the ENSO influence, both Atlantic hemispheres contribute to the precipitation anomalies over NE. The extratropical centers of action, displayed by the second mode of North Atlantic atmospheric variability, have strong influences on the ITCZ and NE precipitation. The high (low) pressure anomalies of the southern center affect the tropical SST and trade winds, which result in ITCZ shiftings and wet (dry) cases over

NE. High latitude anomalies over the South Atlantic affect also the tropical features of atmosphere and ocean. Low (high) pressure anomalies occur over extratropical South Atlantic in wet (dry) cases. The combined influence of both extratropical hemispheres contributes to the strong precipitation anomalies over northern NE region.

The SAM centers, which represent the dominant Southern Hemisphere mode of variability, have connections with the tropical Atlantic and seem to affect also the conditions for ITCZ displacement. When NAM and SAM are well-characterized and in opposite phases, an anomalous high pressure dominates high latitudes of the Southern Hemisphere at the same time that anomalous low pressure dominates high latitudes of the Northern Hemisphere in the Atlantic. These anomalous atmospheric conditions seem to influence NE precipitation variability particularly during non-ENSO years. Additional analyses are necessary to further understand the inter-hemispheric extratropical influence on convection in the ITCZ and precipitation over NE. However, observed anomalies over extratropical North and South Atlantic in DJF could be used in monitoring rainfall during the peak of the rainy season over Northeastern Brazil.

Acknowledgments

To CNPq (Brazil) for the research funding. The GPCP combined precipitation data were provided by the NASA/Goddard Space Flight Center's Laboratory for Atmospheres, which develops and computes the dataset as a contribution to the GEWEX Global Precipitation Climatology Project. Era Interim is provided by the European Centre for Medium-Range Weather Forecasts (ECMWF).

References

Adler, R. F., Huffman, G. J., Chang, A., Ferraro, R., Xie, P., Janowiak, J., et al. (2003). The version 2 Global Precipitation Climatology Project (GPCP) monthly precipitation analysis (1979-Present). *J. Hydrometeorol.* 4, 1147–1167. doi: 10.1175/1525-7541(2003)004<1147:TVGPCP>2.0.CO;2

Andreoli, R. V., and Kayano, M. T. (2005). ENSO-related rainfall anomalies in South America and associated circulation features during warm and cold Pacific decadal oscillation regimes. *Int. J. Climatol.* 25, 2017–2030. doi: 10.1002/joc.1222

Carvalho, L. M. V., Jones, C., and Ambrizzi, T. (2005). Opposite phases of the Antarctic Oscillation and relationships with intraseasonal to interannual activity in the tropics during the austral summer. *J. Clim.* 18, 702–718. doi: 10.1175/JCLI-3284.1

Cavalcanti, I. F. A. (2012). Large scale and synoptic features associated with extreme precipitation over South America: a review and case studies for the first decade of the 21st century. *Atmos. Res.* 118, 27–40. doi: 10.1016/j.atmosres.2012.06.012

Covey, D. L., and Hastenrath, S. (1978). The Pacific El Niño phenomenon and the Atlantic circulation. *Mon. Weather Rev.* 108, 1280–1287.

Cunningham, C. A. C., and Cavalcanti, I. F. A. (2006). Intraseasonal modes of variability affecting the South Atlantic Convergence Zone. *Int. J. Climatol.* 26, 1165–1180. doi: 10.1002/joc.1309

Dee, D. P., Uppala, S. M., Simmons, A. J., Berrisford, P., Poli, P., Kobayashi, S., et al. (2011). The ERA-Interim reanalysis: configuration and performance of the data assimilation system. *Q. J. R. Meteorol. Soc.* 137, 553–597. doi: 10.1002/qj.828

Drumond, A., Nieto, R., Gimeno, L., and Ambrizzi, T. (2008). A lagrangian identification of major sources of moisture over Central Brazil and La Plata Basin. *J. Geophys. Res.* 113, D14128. doi: 10.1029/2007JD009547

Enfield, D. B., and Mayer, D. A. (1997). Tropical Atlantic sea surface temperature variability and its relation to El Niño-Southern Oscillation. *J. Geophys. Res.* 102, 929–945. doi: 10.1029/96JC03296

Fogt, R. L., Jones, J. M., and Renwick, J. (2012). Seasonal zonal asymmetries in the Southern Annular Mode and their impact on regional temperature anomalies. *J. Clim.* 25, 6253–6270. doi: 10.1175/JCLI-D-11-00474.1

Hastenrath, S. (1984). Interannual variability and annual cycle: mechanisms of circulation and climate in the Tropical Atlantic sector. *Mon. Weather Rev.* 112, 1097–1107.

Hastenrath, S. (2012). Exploring the climate problems of Brazil's Nordeste: a review. *Clim. Change* 112, 243–251. doi: 10.1007/s10584-011-0227-1

Hastenrath, S., and Greischar, L. (1993). Further work on the prediction of Northeast Brazil rainfall anomalies. *J. Clim.* 6, 743–758.

Hastenrath, S., and Heller, L. (1977). Dynamics of climatic hazards in northeast Brazil. *Q. J. R. Meteorol. Soc.* 103, 77–92. doi: 10.1002/qj.49710343505

Kayano, M. T., and Kousky, V. E. (1999). Intraseasonal (30–60 day) variability in the global tropics: principal modes and their evolution. *Tellus A* 51, 373–386. doi: 10.1034/j.1600-0870.1999.t01-3-00003.x

Kayano, M. T., Rao, V. B., and Moura, A. D. (1988). Tropical circulations and the associated rainfall anomalies during two contrasting years. *J. Climatol.* 8, 477–488. doi: 10.1002/joc.3370080504

Kayano, M. T., and Andreoli, R. V. (2006). Relationships between rainfall anomalies over northeastern Brazil and the El Niño–Southern Oscillation. *J. Geophys. Res.* 111. D13101. doi: 10.1029/2005JD006142

Kayano, M. T., and Andreoli, R. V. (2007). Relations of South American summer rainfall interannual variations with the Pacific Decadal Oscillation. *Int. J. Climatol.* 27, 531–540. doi: 10.1002/joc.1417

Kouadio, Y. K., Servain, J., Machado, L. A. T., and Lentini, C. A. D. (2012). Heavy rainfall episodes in the eastern Northeast Brazil linked to large-scale ocean-atmosphere conditions in the Tropical Atlantic. *Adv. Meteorol.* 2012:369567. doi: 10.1155/2012/369567

Kousky, V. E. (1980). Diurnal rainfall variation in Northeast Brazil. *Mon. Weather Rev.* 108, 488–498.

Kousky, V. E., Kayano, M. T., and Cavalcanti, I. F. A. (1984). A review of the Southern Oscillation: oceanic-atmospheric circulation changes and related rainfall anomalies. *Tellus* 36A, 490–504. doi: 10.1111/j.1600-0870.1984.tb00264.x

Kousky, V. E., and Gan, M. A. (1981). Upper tropospheric cyclonic vortices in the tropical South Atlantic. *Tellus* 33, 538–551. doi: 10.1111/j.2153-3490.1981.tb01780.x

L'Heureux, M. L., and Thompson, D. W. J. (2006). Observed relationships between the El Niño-Southern Oscillation and the extratropical zonal-mean circulation. *J. Clim.* 19, 276–287. doi: 10.1175/JCLI3617.1

Liebmann, B., Kiladis, G. N., Allured, D., Vera, C. S., Jones, C., Carvalho, L. M. V., et al. (2011). Mechanisms associated with large daily rainfall events in Northeast Brazil. *J. Clim.* 24, 376–396. doi: 10.1175/2010JCLI3457.1

McKee, B., Doesken, N. J., and Kleist, J. (1993). "The Relationship of drought frequency and duration to time scales," in *Proceedings of the 8th Conference on Applied Climatology* (Anaheim, CA), 179–184.

Mo, K. C., and Higgins, R. W. (1998). The Pacific-South American modes and tropical convection during the Southern Hemisphere winter. *Mon. Weather Rev.* 126, 1581–1596.

Mo, K. C., and Paegle, J. N. (2001). The Pacific-South American modes and their downstream effects. *Int. J. Climatol.* 21, 1211–1229. doi: 10.1002/joc.685

Mo, K. C., and White, G. H. (1985). Teleconnections in the Southern Hemisphere. *Mon. Weather Rev.* 113, 22–37.

Moura, A. D., and Shukla, J. (1981). On the dynamics of droughts in Northeast Brazil: observations, theory, and numerical experiments with a general circulation model. *J. Atmos. Sci.* 38, 2653–2675.

Nobre, P., and Shukla, J. (1996). Variations of sea surface temperature, wind stress and rainfall over the Tropical Atlantic and South America. *J. Clim.* 9, 2464–2479.

Pezzi, L. P., and Cavalcanti, I. F. A. (2001). The relative importance of ENSO and Tropical Atlantic sea surface temperature anomalies for seasonal precipitation over South America. *Clim. Dyn.* 17, 205–212. doi: 10.1007/s003820000104

Rao, V. B., and Brito, J. I. B. (1985). Teleconnections between the rainfall over Northeast Brazil and the winter circulation of Northern Hemisphere. *Pure Appl. Geophys.* 123, 951–959. doi: 10.1007/BF00876982

Rodríguez-Fonseca, B., Polo, I., García-Serrano, J., Losada,T., Mohino, E., Mechoso, C. R., et al. (2009). Are Atlantic Niños enhancing Pacific ENSO events in recent decades? *Geophys. Res. Lett.* 36, L20705. doi: 10.1029/2009GL040048

Smith, T. M., Reynolds, R. W., Peterson, T. C., and Lawrimore, J. (2008). Improvements to NOAAs historical merged land–ocean temperature analysis (1880–2006). *J. Clim.* 21, 2283–2296. doi: 10.1175/2007JCLI2100.1

Souza, E. B., and Ambrizzi, T. (2002). ENSO impacts on the South American rainfall during 1980s: Hadley and Walker circulation. *Atmósfera* 15, 105–120.

Souza, P., and Cavalcanti, I. F. A. (2009). Atmospheric centres of action associated with the Atlantic ITCZ position. *Int. J. Climatol.* 29, 2091–2105. doi: 10.1002/joc.1823

Tedeschi, R. G., Cavalcanti, I. F. A., and Grimm, A. M. (2013). Influences of two types of ENSO on South American precipitation. *Int. J. Climatol.* 33, 1382–1400. doi: 10.1002/joc.3519

Trigo, R. M., Osborn, T. J., and Corte-Real, J. (2002). The North Atlantic oscillation influence on Europe: climate impacts and associated physical mechanisms. *Clim. Res.* 20, 9–17. doi: 10.3354/cr020009

Uvo, C. B. (2003). Analysis and regionalization of northern European winter precipitation based on its relationship with the North Atlantic oscillation. *Int. J. Climatol.* 23, 1185–1194. doi: 10.1002/joc.930

Vicente-Serrano, S. M., and López-Moreno, J. I. (2008). The nonstationary influence of the North Atlantic Oscillation on European precipitation. *J. Geophys. Res. Atmos.* 113, D20120. doi: 10.1029/2008JD010382

Conflict of Interest Statement: The author declares that the research was conducted in the absence of any commercial or financial relationships that could be construed as a potential conflict of interest.

frontiers
in Earth Science

ORIGINAL RESEARCH
published: 24 September 2015
doi: 10.3389/feart.2015.00055

The non-stationary influence of the Atlantic and Pacific Niños on North Eastern South American rainfall

Verónica Torralba[1]*, *Belén Rodríguez-Fonseca*[2,3], *Elsa Mohino*[2] *and Teresa Losada*[2]

[1] Climate Forecasting Unit, Institut Català de Ciències del Clima, Barcelona, Spain, [2] Departamento de. Física de la Tierra, Facultad Ciencias Físicas, Astronomía y Astrofísica I, Universidad Complutense de Madrid, Madrid, Spain, [3] Facultad Ciencias Físicas, Instituto de Geociencias (Consejo Superior de Investigaciones Científicas - Universidad Complutense de Madrid), Madrid, Spain

Edited by:
Anita Drumond,
University of Vigo, Spain

Reviewed by:
Fabio D'Andrea,
Laboratoire de Meteorologie Dynamique/Institut Pierre Simon Laplace, France
Janini Pereira,
Federal University of Bahia, Brazil

***Correspondence:**
Verónica Torralba,
Climate Forecasting Unit, Institut Català de Ciències del Clima, Doctor Trueta, 203, 08005 Barcelona, Spain
veronica.torralba@ic3.cat

Specialty section:
This article was submitted to Atmospheric Science, a section of the journal Frontiers in Earth Science

Received: *03 March 2015*
Accepted: *08 September 2015*
Published: *24 September 2015*

Citation:
Torralba V, Rodríguez-Fonseca B, Mohino E and Losada T (2015) The non-stationary influence of the Atlantic and Pacific Niños on North Eastern South American rainfall. Front. Earth Sci. 3:55. doi: 10.3389/feart.2015.00055

Rainfall variability over the tropical Atlantic region is dominated by changes in the surface temperature of the surrounding oceans. In particular, the oceanic forcing over Northeast of South America is dominated by the Atlantic interhemispheric temperature gradient, which leads its predictability. Nevertheless, in recent decades, the SST influence on rainfall variability in some tropical Atlantic regions has been found to be non-stationary, with important changes of the Atlantic and Pacific influence on Sahelian rainfall which appear to be modulated at multidecadal timescales. In this work, we revisit the SST influence over Northeast of South America including the analysis of the stationarity of this relationship at interannual timescales. Principal Component Analysis has been applied to the interannual component of rainfall during the March-April-May season. Results show how the SST forcing on the first mode of rainfall variability, which is a dipole-like pattern generated by the changes in the seasonal migration of the Intertropical Convergence Zone, is different depending of the considered period. The response to the SST anomalies in the Pacific basin is opposite to the Atlantic one and affects different areas. The Atlantic Niño influences rainfall variability at the beginning of the XX century and after 1970, while the Pacific Niño plays a major role in the variability of the rainfall in the Northeast of South America from 1970 onwards. The combined effect of both basins after the 1970s amplifies the anomalous rainfall response.

Keywords: multidecadal modulations, Northeastern South America rainfall, interannual variability, SST forced response, atmosphere general circulation models

Introduction

The northern South America is a complex region, because it is a large territory where different weather systems act. This region includes the Amazon region with one of the most intense convective activity areas in the world (Andreoli et al., 2012) and also the northeast of Brazil which is characterized by frequent and intense droughts due to its semiarid climate (Nobre and Shukla, 1996; Rao et al., 2006). The interaction between different atmospheric phenomena that appear in the whole region and local surface conditions (like topography, vegetation, and land use), generates a non-homogenous rainfall distribution that varies in a wide temporal and spatial range (Espinoza Villar et al., 2009; Sierra et al., 2015).

The present work focuses on the Northeast of South America (NESA) defined hereafter as the region between the 15 N–15 S and 30–75 W. The annual cycle of precipitation in that region is led by changes in the position of the Intertropical Convergence Zone (ITCZ), which suffers meridional shifts following the seasonal movement of insolation, producing bimodal or unimodal precipitation patterns over specific regions of South America and causing non-periodic events of droughts or floods in NESA region (Sperber and Palmer, 1996; Uvo et al., 1998; Poveda et al., 2006). The annual cycle of precipitation over NESA is not completely explained by the ITCZ excursions, the existence of regional processes strongly influences the amounts of precipitation over the region, defining local rainfall patterns (Sierra et al., 2015). The position of the ITCZ also plays an important role in the connection of the rainfall variations over the Northeast of South America with rainfall anomalies in the Sahel region (Rao et al., 2006). When the ITCZ is displaced to the south (north), higher than normal rainfall occurs over the Northeast of South America (Sahel).

The ocean is the main driver of interannual to decadal changes in rainfall in the NESA. At interannual timescales, anomalous rainfall is driven by changes in the tropical Atlantic sea surface temperatures (SST) and the remote influence of the tropical Pacific anomalous SSTs (Giannini et al., 2004; Grimm and Tedeschi, 2009). Rodrigues et al. (2011) have found how the tropical Pacific exerts influence over the tropical Atlantic in a way that El Niño has a positive effect on Atlantic Niños. Precipitation variability is thus driven by the two leading modes of variability of SST in the tropical belt: the Atlantic Niño (Zebiak, 1993) and the Pacific Niño (Philander, 1990). Although the separated influence of the tropical Atlantic and Pacific oceans on NESA has been documented, to our knowledge there is no work tackling on the stationarity of their relationship with NESA rainfall. Moreover, recent studies have found how the Atlantic and Pacific Niños appear anticorrelated in summer during the decades after the 1970s and at the beginning of the XX century (Polo et al., 2008, 2015; Rodríguez-Fonseca et al., 2009; Martín-Rey et al., 2012, 2014). The concomitant action of both basins on the NESA rainfall region has not been yet explored, although important impacts have been found for the Sahel (Losada et al., 2012; Rodríguez-Fonseca et al., 2015). Such studies have highlighted that the SST influence over West African region is not stationary. In this way, before the 1970s, the Pacific El Niño has a different impact over Sahelian rainfall than after that period. These works have demonstrated that this variability is due to the non-linear relationship between the precipitation in that region and the SST in the tropical Atlantic.

All these findings have encouraged us to explore the stationarity of the SST influence on the interannual variability of rainfall in some regions of the North of South America. The present study analyses the non-stationarity in the interannual variations of rainfall in NESA, as well as the associated influence of the Atlantic and Pacific tropical basins when they act together in opposite phases (Altantic El Niño and Pacific La Niña) as was observed after the 1970s.

The first part of this work presents an observational analysis which includes an assessment of the stationarity of precipitation anomalies and their relation with SST variability in the tropics. In the second part, we study the response obtained using sensitivity experiments that consider the concomitant influence of the Atlantic and Pacific main modes of interannual variability on the region.

This paper is divided as follows. Section Materials and Methods describes the used datasets and the methodology used. The results are shown in section Results and discussed in section Discussion and Conclusions.

Materials and Methods

Datasets

Precipitation

To undertake robust analyses, three high resolution land surface precipitation datasets are used. They are based on station data using different methods of spatial interpolation from the rain-gauge station locations to the nodes of the 0.5° grid. The interpolations are carried out with different versions of the Shepard's algorithm (Shepard, 1968; Willmott et al., 1985). The datasets are: Climate Research Unit version 3.1 (CRU TS 3.1, Harris et al., 2013; from 1901 to 2009), University of Delaware (UDel, Matsuura and Willmott, 2009, from 1900 to 2008); and Global Precipitation Climatology Center (GPCC, Schneider et al., 2008, from 1901 to 2007). These three data bases only have information over land which is a handicap for continuity studies of analysis of ITCZ-related variability.

Sea Surface Temperatures and Indices

Hadley Centre Sea Ice and Sea Surface temperature (HadISST) data is used (Rayner et al., 2003). This dataset provides reconstructed monthly SST and sea ice data on a horizontal grid with a resolution of 1° × 1° and spans from 1870 to 2011.

Two indices are calculated from this dataset at interannual scales: the ATL3 and NINO3 indices. The ATL3 index (Zebiak, 1993) is defined through the SST anomaly mean in the tropical Atlantic located between 3°N–3°S and 20°W–0°. The Niño3 index (Trenberth and Stepaniak, 2001) results from the SST anomalies averaged in the equatorial Pacific region (5°S–5°N, 150°W–90°W).

Methods

Statistical Analysis

To find out how the rainfall variability is organized in NESA region, Principal Component Analysis (PCA/EOF) has been applied to three different observational datasets. This discriminant analysis statistical technique is very useful to extract modes of variability explaining a high percentage of the field variance (Wilks, 2006). The analysis is applied to define the modes of precipitation variability for each of the three datasets considered. The study focuses on the assessment of the leading mode of variability with the aim of inferring the associated mechanisms involved in the origin of the anomalous rainfall in NESA.

The rainfall variability in the studied region has a strong variability at different timescales. In this paper we focus on interannual timescales. Therefore, in order to remove the decadal influence, the anomalous precipitation time series are filtered using a Butterworth filter (order 10, cut-off period of 13 years), which is applied at each grid point before the EOF analysis (Mann, 2008).

The statistical significance shown along this work has been obtained from a Student *t*-test with $\alpha = 0.05$.

Atmospheric General Circulation Model Experiments

AGCM simulations are used in this study to check the concomitant action of the Atlantic and Pacific tropical forcing on the NESA region. These simulations were carried out in Losada et al. (2012) to study the oceanic influence over West Africa. However, given the similarities between the SST variability modes that affect both tropical regions (Rao et al., 2006) and the fact that we want to verify the same hypothesis of the Atlantic and Pacific influence on NESA, we have considered their use in this study. The simulations were performed with the Atmospheric Global Coupled Model (AGCM) UCLA v.7.3 (Mechoso et al., 2000; Richter et al., 2008) with a horizontal resolution of 2.5° in longitude and 2° in latitude and a vertical resolution of 29 levels.

Three AGCM experiments have been analyzed. In the first experiment the SST anomalies prescribed are those from whole tropical region (Atlantic and Pacific) and they are added to the climatological SST values for the period 1979–2005, which is considered as the reference period. In these experiments, an Atlantic Niño appears together with a Pacific La Niña. In the second experiment the SST anomalies in the Tropical Atlantic (corresponding to an Atlantic Niño) are retained and they are added to the SST climatology in the Atlantic basin for the reference period. In the third experiment the anomalies in the Tropical Indo-Pacific are considered (Corresponding to a Pacific La Niña) and they are added to the mean SST values, for the reference period in the Indian and Pacific basins.

All the experiments are 14-month long (from February to April), 10-member ensemble integrations, in which the ensembles differ in a slight perturbation of the initial conditions. The control simulation is a 10-member ensemble integration with climatological, monthly-mean varying SST corresponding to the 1979–2005 period and the difference of the control simulation with the sensitivity experiments has been used to assess the response to the anomalous SST over the rainfall in the NESA region. We have focused our analysis in the rainy season (MAM) of the Northeast of South America.

Results

Seasonal Cycle and Variability Modes of Precipitation

The annual cycle of precipitation over tropical South America shows the characteristics of a monsoon system, with distinct wet and dry seasons for many areas (Gan et al., 2004). To explore the latitudinal evolution of rainfall throughout the year in the NESA region, a hövmoller diagram of the rainfall is presented (**Figure 1A**).

The hövmoller (**Figure 1A**) shows a maximum of the precipitation from February to April, between 5°S and the Equator. It is followed by a displacement to the north by mid-April and a strong reduction of rainfall south of the Equator. These features in the evolution of rainfall determine the rainy season in the region, which corresponds to the boreal spring (MAM, March-April-May). Horizontal maps in the NESA region have been also represented in **Figure 1B**, including the seasonal means in MAM (March-April-May and in SON (September-October-November). It can be seen how rainfall ranges from 18 mm/day during the boreal spring, to 0 mm/day during the autumn season. These abrupt changes in rainfall coincide with the meridional movements of the ITCZ, a result that has been highlighted by many authors (Moura and Shukla, 1981; Sperber and Palmer, 1996; Uvo et al., 1998; Giannini et al., 2004), who also deem the ITCZ as the main driver of the rainfall variability in the Northeast of South America.

To evaluate the precipitation variability at interannual timescales, the leading mode of MAM rainfall variability has been determined using Principal Components Analysis (**Figure 2**). This analysis has been carried out using the three datasets considered in the study which have been filtered using a Butterworth filter. The variance percentages explained by CRU, UDel, and GPCC are 23.8, 24.4, and 24.2%, respectively.

The spatial pattern of this mode of variability displays the same structure for the three datasets (**Figure 2A**). It corresponds with a dipole-like pattern, suggesting that the anomalies in the rainfall are linked to the meridional displacements of the ITCZ, which would increase rainfall in one side of the equator and decrease in the other. Therefore, when the ITCZ does not reach its most southern position (close to the northeast) droughts appears in northeast Brazil, but when the ITCZ stays longer in the south, heavy rains occur in the northeast of Brazil. The anomalies in the ITCZ shifts are mainly produced by variations in the SST interhemispheric gradient in the Atlantic (Uvo et al., 1998).

Principal components (PC) time series (**Figure 2B**) show remarkable changes in amplitude, from a [−1 1] range in the 1950–1970 period to a [−2 2] range in the previous and forthcoming decades. In fact, the variances in both periods have been compared and they display significant changes in amplitude in certain periods which could be due to the existence of external influences, as those given by the ocean, acting changing the amplitude of rainfall variability at those timescales.

In order to clarify the factors modulating these changes in amplitude (non-stationarities), in the next section, a study is done for separate periods including the analysis of the relation to the ocean.

Influence of SST on the Rainfall Interannual Variability

The regression map obtained from the projection of the PC associated with the first EOF of precipitation from the UDel dataset onto the SST anomalous field (**Figure 3A**) shows that lower precipitation (higher precipitation) in the northeast of Brazil region is connected with a warming (cooling) at the East of the tropical Pacific, together with positive (negative) anomalies of the SST over the tropical North Atlantic and negative (positive) anomalies over the tropical South Atlantic. The SST anomalies over the tropical Atlantic produce the strengthening (weakening)

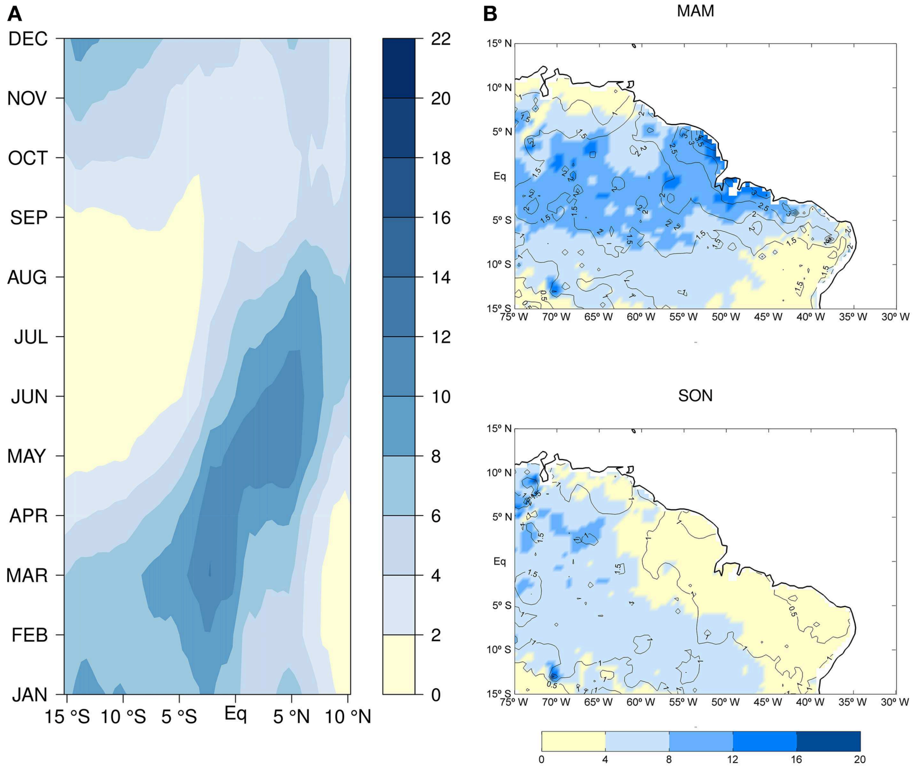

FIGURE 1 | (A) Hövmoller diagram with the evolution in time and latitude of the average precipitation per month in the region of 35–65 W. **(B)** Seasonal average of rainfall for UDel in the boreal spring months, March–May, (top panel) and autumn months September–November (bottom panel). Units are mm/day. Contours show the standard deviation.

of the SST interhemispheric gradient. This result agrees with those obtained previously by other authors (Harzallah et al., 1996; Chiang et al., 2000; Cazes-Boezio et al., 2003), who affirm that the dipole rainfall pattern over the NESA region is related to variability in the position of the ITCZ, which in turn is produced by SST anomalies.

The SST anomalous patterns related to rainfall variability in the NESA region include the two main modes of variability at interannual timescales in the Pacific and Atlantic basins, the Atlantic and the Pacific Niño, which agrees with those described by Hastenrath (2006) with an influence on the rainfall variability. To analyse the stationarity in the relationship between the rainfall and the Atlantic and Pacific Niño in the NESA, correlations have been computed between the leading PC of rainfall and the ATL3 and NINO3 indices using a 20-year sliding window (**Figures 3B,C**).

An interesting result arises when correlating the PC from UDel dataset with the ATL3 index (**Figure 3B**). The correlations are only significant in the periods 1905–1920 and 1965–1980 in agreement with changes in the PC amplitude. Similar behavior has been obtained when using CRU and GPCC datasets (not shown). The non-stationary relationship between ATL3 and the PCs seems to be robust and it means that the leading rainfall mode of variability is only modulated by the Atlantic Niño in certain periods (when the correlation is significant). This result is in agreement with the one obtained by Losada et al. (2012) for the Sahel and López-Parages and Rodríguez-Fonseca (2012) for Europe and demonstrates the importance of evaluating teleconnections with rainfall in a non-stationary way. Also the relationship between the Atlantic and Pacific Niños has been found to be modulated only during some decades, which coincides with those obtained in the present analysis (Martín-Rey et al., 2014; Polo et al., 2015). This absence of stationarity has been found to be related to changes in the background state of the ocean, for which different dynamical mechanisms operate and produce the emergence of different teleconnections (Martín-Rey et al., 2014).

Regarding the influence of the Pacific El Niño, **Figure 3C** displays the sliding windows correlations between NINO3 index and rainfall PC obtained with UDel dataset. From the 1970s the correlation between the PC and the NINO3 index is strong and statistically significant, while before the 1970s the correlation is weak and not statistically significant. Similar results were obtained with the other two long datasets (not shown). Hence, the relationship between rainfall in NESA and SST in the Pacific is also non-stationary.

The present results agree with a former study of Chiang et al. (2000), who showed that the Atlantic ITCZ variability is linked to that for the eastern Pacific in a non-stationary way through the Walker circulation as it respond to changes in equatorial Pacific

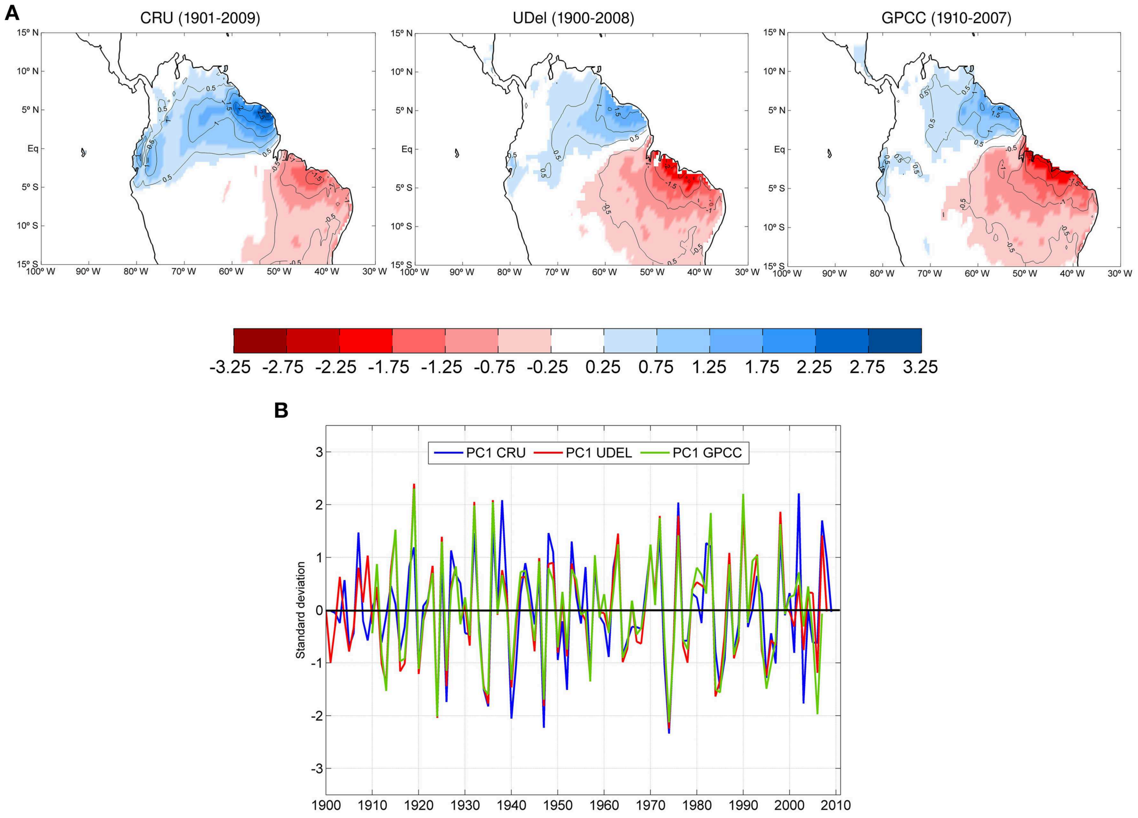

FIGURE 2 | (A) Leading empirical orthogonal function of the March-April-May (mm/day per std in the PC) anomalous rainfall. The regions with correlations significant at the 95% level are contoured. **(B)** Standardized principal component (PC1). They are associated with CRU (blue line), UDel (red line), and GPCC (green line) rainfall anomalies in March-April-May.

convection. We speculate that the Atlantic ITCZ variability, that is the main driver of the rainfall over the NESA region, can be modulated by the Atlantic-Pacific Niños connection. In that work the authors present graphical information (not interpreted) of this Atlantic-Pacific connection in relation to their findings, a fact that further encourage the importance of our results.

In summary, although the Atlantic has a significant influence at the beginning of the XX century and after the 1970s, both the Atlantic and Pacific main modes of interannual variability have a significant impact on the PC only after the 1970's, because at the beginning of the XX century the Pacific influence is not significant. Such change of impacts could be related to the late 1970s climate shift reported by Baines and Folland (2007), who argue that in the 1970s decade relevant characteristics of the climate changed. Such changes were particularly relevant over the Tropical regions, changing rainfall over the Amazon basin and northeast Brazil. In addition Chiang et al. (2000) indicated that the influence of the Pacific on the Atlantic as consequence of multidecadal changes in the ITCZ could be due to multidecadal changes in the ocean mean state and this could be responsible of enhancing convection in the western equatorial Atlantic. This multidecadal modulation will be further analyzed in the next section.

Multi-decadal Modulation of Precipitation: Before and After 1970

To confirm the relationship between the anomalous rainfall and the SST anomalies in the Atlantic and Pacific, the influence of NINO3 and ATL3 has been analyzed for two different periods 1900–1970 and 1970–2008 and rainfall composite analysis has been performed.

The composite maps which shows the relationship between the ATL3 index and the rainfall in the study region (**Figure 4A**) have been calculated as the difference between the composite map of the UDel rainfall (mm/day) for the event ATL3 > 1 minus the composite map for the event ATL3< -1 in the period before 1970 (left column) and after 1970 (right column).

The composite analysis suggests that before the 1970s, the effect of the positive phase of the Atlantic El Niño on anomalous rainfall on NESA is a dipole-like pattern of rainfall anomalies, with positive anomalies in the northeast of Brazil and negative anomalies in the north of NESA (**Figure 4A**). This pattern might be related to the significance relationship observed in the **Figure 3B** during the decades of 1910–1940. These composite maps have been also computed for CRU and GPCC datasets and they show a similar pattern (not shown). After 1970 the pattern is a dipolar structure (**Figure 4B**) as in the previous period

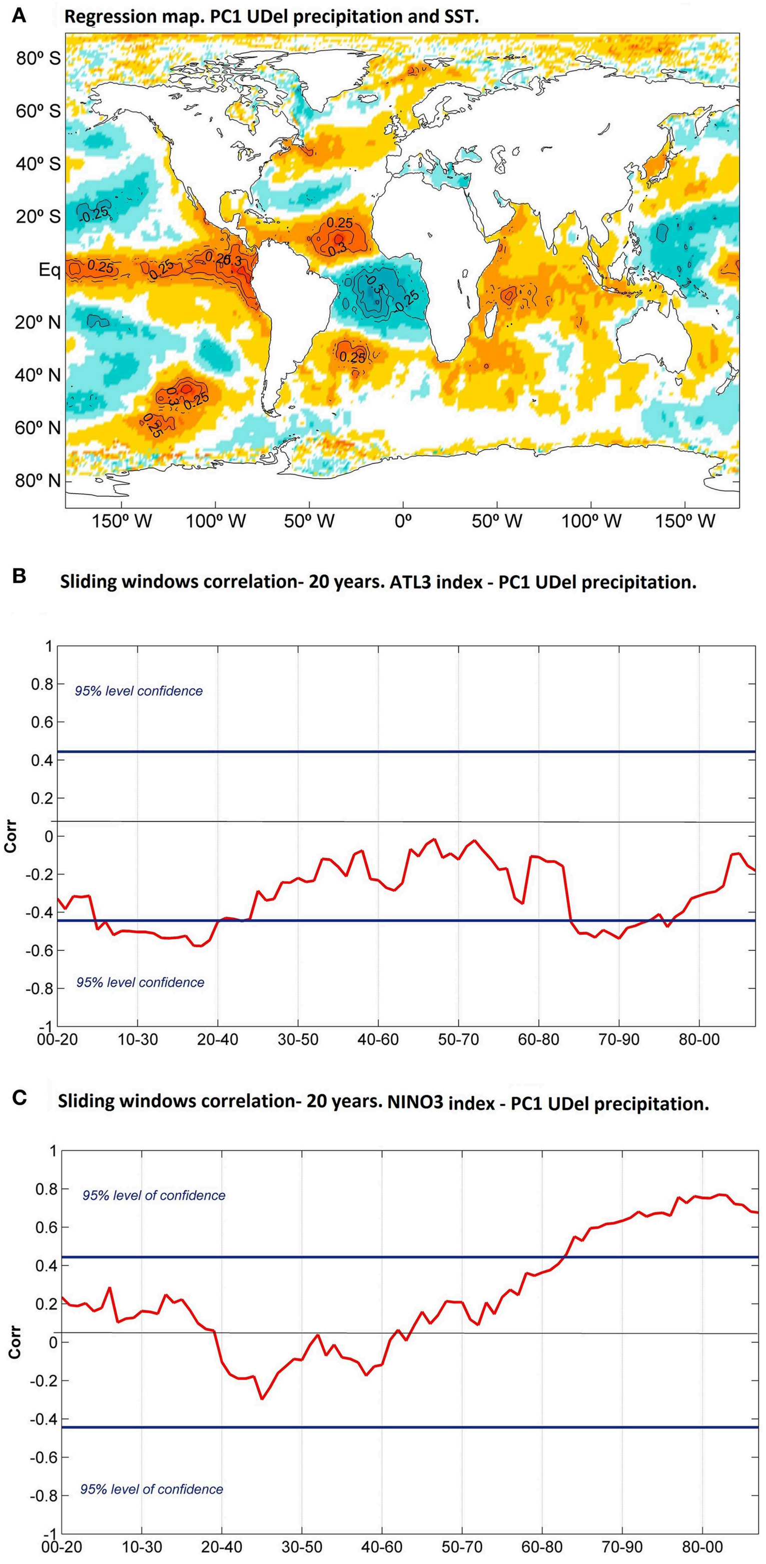

FIGURE 3 | (A) Regression map of anomalous SST onto the PC1 (°C/std in the PC) obtained for UDel dataset. The regions with correlations significant at the 95% level are contoured. **(B)** Twenty year moving window correlation between the standardized PC1 associated with the leading mode computed UDel and the ATL3 index (red line). In the horizontal axis, the year in which the period of 20 year starts is represented. **(C)** Twenty year moving window correlation between the standardized PC1 associated with the leading mode computed UDel and the NINO3 index (red line). In the horizontal axis, the year in which the period of 20 year starts is represented. The dark blue lines show the thresholds over which correlations are significant at 95% confidence level.

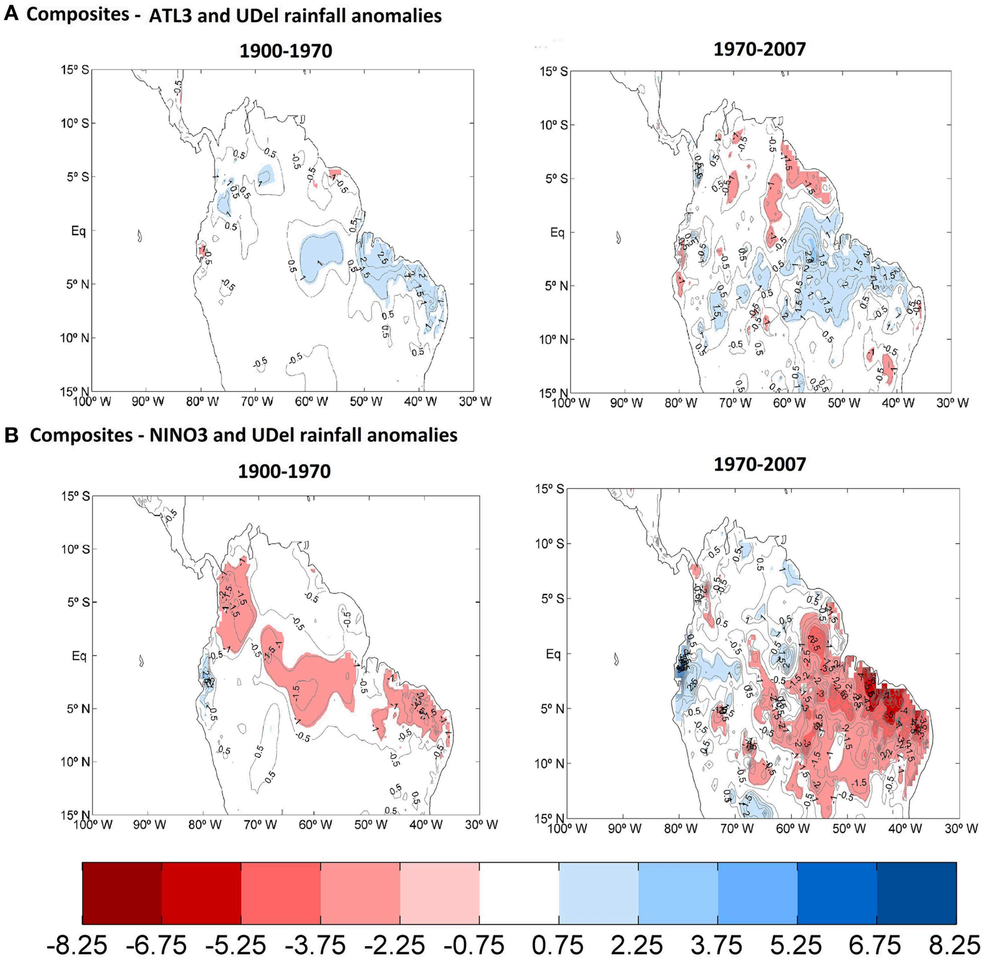

FIGURE 4 | Difference between the composite map of the UDel rainfall (mm/day) for the event. (A) ATL3 > 1 minus the composite map for the event ATL3 < −1 in the period before 1970 (left column) and after 1970 (right column). **(B)** NINO3 > 1 minus the composite map for the event NINO3 < −1 in the period before 1970 (left column) and after 1970 (right column). Contoured areas represent the values of the differences, expressed in mm/day, while the regions with correlations significant at the 95% level are shaded.

(**Figure 4A**), although the anomalies are slightly weaken, due to the shorter period (1970–1990) in which the observed correlation is significant (**Figure 3B**). The pattern coincides with the first mode of variability for the high frequency rainfall in NESA region. Some differences exist, however, as those significant anomalies located closer to the coast that could be explained for the higher vicinity of the Atlantic Ocean and, therefore, with a higher influence of this basin over the rainfall.

When an Atlantic Niño occurs, positive SST anomalies appear in the Tropical South Atlantic. These positive anomalies weaken the interhemispheric gradient of the Atlantic SST, and this fact enhances the shift of the ITCZ to the Southern Hemisphere and the appearance of rainfall in the northeast of Brazil region. This anomalous pattern, linked to the ATL3 index, suggests the Atlantic Niño as one of the essential phenomena explaining the interannual variability of the precipitation in the NESA region.

To ensure the robustness of this result, an AGCM simulation in which SST anomalies in the tropical Atlantic (TA experiment) with an Atlantic Niño configuration are prescribed is analyzed (see section Methods for description). **Figure 5A** presents the rainfall anomalies corresponding to the tropical Atlantic experiment, indicating a significant increase of precipitation in the equatorial rainfall with a decrease in the north of the NESA region, as a response of warm SST anomalies in the equatorial Atlantic.

Regarding the Pacific, the different response of the NESA rainfall to the Pacific El Niño before and after 1970 is examined by calculating the composite maps of anomalies. These maps have been calculated as the difference between the composite for Pacific Niño events minus the composite for Pacific Niña events in two different periods (**Figure 4B**). These composite maps have been computed based on the years with NINO3 > 1 (Pacific Niño) and years with NINO3 < −1 (Pacific Niña). Before 1970 (**Figure 4B**, left column) negative anomalies appear in the northwest of South America, but in the northeast of Brazil there are no significant anomalies in the rainfall. This result reveals

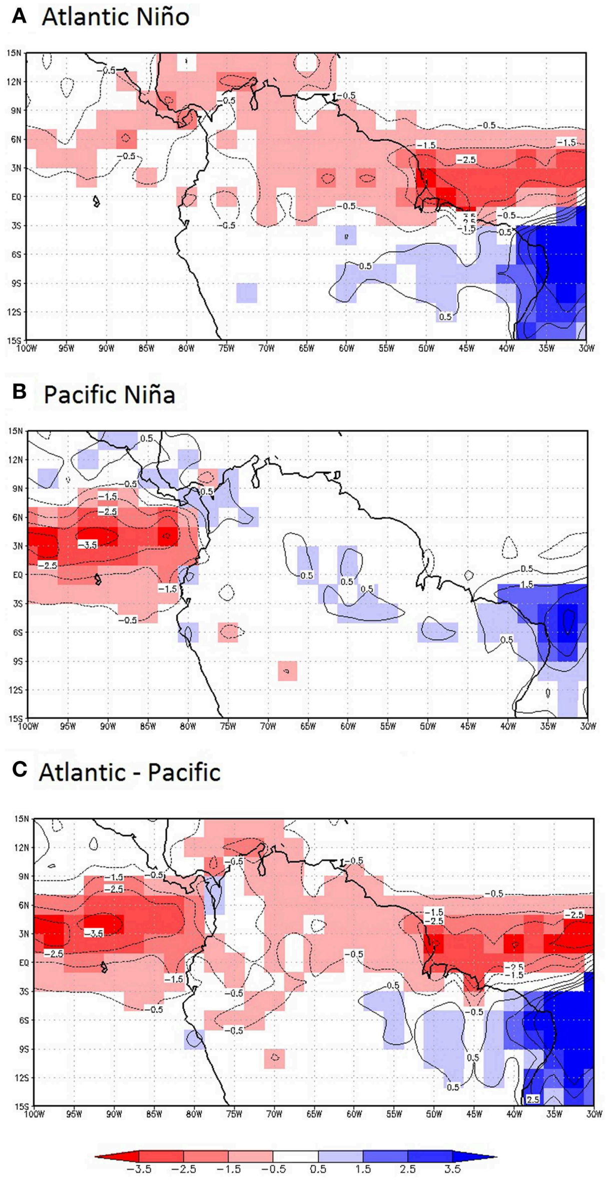

FIGURE 5 | (A) Rainfall anomalies for the Atlantic Niño simulation. **(B)** Rainfall anomalies for the Pacific Niño simulation. **(C)** Rainfall anomalies for the simulation in whole Tropical region (Atlantic Pacific). Contoured areas represent the values of the rainfall, expressed in mm/day, while the regions with correlations significant at the 95% level are shaded.

that the Pacific Niño events do not project on the interannual leading mode of variability of the rainfall in the NESA region during this period. However, after 1970 the anomalous pattern shows higher similarity with the leading mode of interannual rainfall variability over NESA (**Figure 2A**), especially over the southern centers of action of the mode. This result confirms the influence of the Pacific Niño in the interannual variability of the precipitation over the whole Amazonian basin during those decades (Rodrigues et al., 2011; Kayano et al., 2013).

To confirm this result, an AGCM sensitivity experiment for the tropical Indo-Pacific region is evaluated (see section Methods for description). Rodríguez-Fonseca et al. (2009) showed that after the 1970s, the Atlantic and Pacific El Niños were highly anticorrelated and Losada et al. (2012) performed AGCM sensitivity experiments to explore the influence of this interbasin connection on Sahelian rainfall. Therefore, to be consistent with the previous AGCM experiment, in which an Atlantic El Niño was simulated, we have chosen to analyse a simulation for the Pacific La Niña. The climatology used in both simulations starts after 1970, when the influence of the Pacific SST is higher (**Figure 3C**). It can be seen how the response to a cooling in the Pacific is an increase in rainfall over the Atlantic coast of South America, which extends to latitudes south of the Equator (**Figure 5B**).

If we assume a linear response of rainfall to the SST anomalies [as was found in Losada et al. (2012) for the Sahel], the sum of the Pacific and Atlantic response is a reinforcement of the signal over the northeast of Brazil, as shown in **Figures 5A,B**. To test such hypothesis, we plot in **Figure 5C** the rainfall response over NESA given by the simulation in which Atlantic El Niño and Pacific La Niña SST anomalies were used. The combined effect of the two basins produces a dipole-like pattern similar to the leading mode of variability. The positive anomalies in the north of equatorial region in the Atlantic coast of NESA region related to the Atlantic Niño are strengthen by the effect of the Pacific Niña which produce and increase of rainfall in the study region. Thus, contrary to the Sahel in which the concomitant action of both basins cancels the individual signals, over the NESA, the Atlantic-Pacific Niños connection adds their individual effects on rainfall. This novel result is very important for predictability issues and to better assess the SST influence on rainfall in the region.

Discussion and Conclusions

In this work the interannual rainfall variability in the Northeast of South America has been investigated in relation to the ocean forcing, with special emphasis in the non-stationarities of the found teleconnections. In particular, the different effect of the Pacific and Atlantic along time is explored together with the concomitant action of both basins on NESA rainfall.

The study focuses on the first mode of variability of the rainfall during the March-April-May season, which is characterized by a north-south dipole-like pattern which appears in response to the variability in the ITCZ shifts produced by SST anomalies. We show through observational and AGCM simulations how SSTs anomalies in the tropical basins can influence rainfall over NESA at interannual timescales. On the one hand, the anomalous heating in the equatorial Atlantic following an Atlantic El Niño configuration leads to increased rainfall over NESA through a southward shift of the ITCZ due to the subsidence north of the Equator. On the other, a cooling in the Pacific associated with a Pacific Niña event leads to rainfall increase over NESA through convergence in the Amazon region due to the compensation of surface divergence over the east tropical Pacific.

However, we also show that the impact of such SST interannual modes of variability on rainfall over NESA is non-stationary. While the Atlantic Niño produces rainfall variability at the beginning of the XX century and after 1970, the Pacific Niño does not have a big impact until the 1970s. In the period from 1920 to 1970 the rainfall variability in the NESA region could be attributed to the Atlantic interhemispheric mode. Our results also suggest that, after the 1970s, the response to concomitant anomalies of SST in the Pacific and Atlantic basins (Rodríguez-Fonseca et al., 2009) is of the same sign over NESA, producing an enhancement in the response when both basins act together.

More work is needed to identify the causes to this non-stationarity in the teleconnection between the Atlantic and the Pacific Niño with the rainfall variability. Why the Atlantic and Pacific exert a different impact on rainfall depending on the period is a question that remains open, although it could be related to the hypothesis posed in Rodríguez-Fonseca et al. (2015) for the Sahel, in which changes in the ocean background state related to the Atlantic Multidecadal Oscillation are identified as possible modulators of the interannual teleconnections. Also, it is necessary to analyse the relative impact of decadal variability over the rainfall in the northeast of South America.

Acknowledgments

We are grateful to the two anonymous reviewers whose comments have helped to improve this manuscript. The research leading to these results has received funding from the European Union Seventh Framework Programme (FP7/2007–2013) under grant agreement n° 603521 (PREFACE project) and the Spanish project CGL2012-38923-C02-01.

References

Andreoli, R. V., Ferreira de Souza, R. A., Kayano, M. T., and Candido, L. A. (2012). Seasonal anomalous rainfall in the central and eastern Amazon and associated anomalous oceanic and atmospheric patterns. *Int. J. Climatol.* 32, 1193–1205. doi: 10.1002/joc.2345

Baines, P. G., and Folland, C. K. (2007). Evidence for a rapid global climate shift across the late 1960s. *J. Climate* 20, 2721–2744. doi: 10.1175/JCLI4177.1

Cazes-Boezio, G., Robertson, A. W., and Mechoso, C. R. (2003). Seasonal dependence of ENSO teleconnections over South America and relationships with precipitation in Uruguay. *J. Climate* 16, 1159–1176. doi: 10.1175/1520-0442(2003)16<1159:SDOETO>2.0.CO;2

Chiang, J. C. H., Kushnir, Y., and Zebiak, S., E (2000). Interdecadal changes in eastern Pacific ITCZ variability and its influence on the Atlantic ITCZ. *Geophys. Res. Lett.* 27, 3687–3690. doi: 10.1029/1999GL011268

Espinoza Villar, J. C., Ronchail, J., Guyot, J. L., Cochonneau, G., Naziano, F., Lavado, W., et al. (2009). Spatio−temporal rainfall variability in the Amazon basin countries (Brazil, Peru, Bolivia, Colombia, and Ecuador). *Int. J. Climatol.* 29, 1574–1594. doi: 10.1002/joc.1791

Gan, M. A., Kousky, V. E., and Ropelewski, C. F. (2004). The South America monsoon circulation and its relationship to rainfall over west-central Brazil. *J. Climate* 17, 47–66. doi: 10.1175/1520-0442(2004)017<0047:TSAMCA>2.0.CO;2

Giannini, A., Saravanan, R., and Chang, P. (2004). The preconditioning role of tropical Atlantic variability in the development of the ENSO teleconnection: implications for the prediction of Nordeste rainfall. *Clim. Dyn.* 22, 839–855. doi: 10.1007/s00382-004-0420-2

Grimm, A. M., and Tedeschi, R. G. (2009). ENSO and extreme rainfall events in South America. *J. Climate* 22, 1589–1609. doi: 10.1175/2008JCLI2429.1

Harris, I., Jones, P. D., Osborn, T. J., and Lister, D. H. (2013). Updated high−resolution grids of monthly climatic observations–the CRU TS3. 10 Dataset. *Int. J. Climatol.* 34, 623–642. doi: 10.1002/joc.3711

Harzallah, A., Rocha de Aragao, J. O., and Sadourny, R. (1996). Interannual rainfall variability in North-east Brazil: observation and model simulation. *Int. J. Climatol.* 16, 861–878.

Hastenrath, S. (2006). Circulation and teleconnection mechanisms of Northeast Brazil droughts. *Progr. Oceanogr.* 70, 407–441. doi: 10.1016/j.pocean.2005.07.004

Kayano, M. T., Andreoli, R. V., and Ferreira de Souza, R. A. (2013). Relations between ENSO and the South Atlantic SST modes and their effects on the South American rainfall. *Int. J. Climatol.* 33, 2008–2023. doi: 10.1002/joc.3569

López-Parages, J., and Rodríguez-Fonseca, B. (2012). Multidecadal modulation of El Niño influence on the Euro-Mediterranean rainfall. *Geophys. Res. Lett.* 39:L02704. doi: 10.1029/2011GL050049

Losada, T., Rodríguez-Fonseca, B., Mohino, E., Bader, J., Janicot, S., and Mechoso, C. R. (2012). Tropical SST and Sahel rainfall: a non-stationary relationship. *Geophys. Res. Lett.* 39:L12705. doi: 10.1029/2012GL052423

Mann, M. E. (2008). Smoothing of climate time series revisited. *Geophys. Res. Lett.* 35:L16708. doi: 10.1029/2008gl034716

Martín-Rey, M., Polo, I., Rodríguez-Fonseca, B., and Kucharski, F. (2012). Changes in the interannual variability of the tropical Pacific as a response to an equatorial Atlantic forcing. *Sci. Mar.* 76, 105–116. doi: 10.3989/scimar.03610.19A

Martín-Rey, M., Rodríguez-Fonseca, B., Polo, I., and Kucharski, F. (2014). On the Atlantic–Pacific Niños connection: a multidecadal modulated mode. *Clim. Dyn.* 43, 3163–3178. doi: 10.1007/s00382-014-2305-3

Matsuura, K., and Willmott, C. J. (2009). *Terrestrial Precipitation: 1900–2008 Gridded Monthly Time Series*. Available online at: http://climate.geog.udel.edu

Mechoso, C. R., Yu, J. Y., and Arakawa, A. (2000). "A coupled GCM pilgrimage: from climate catastrophe to ENSO simulations," in *General Circulation Model Development: Past, Present and Future. Proceedings of a symposium in honor of Professor Akio Arakawa,* ed D. A. Randall (New York, NY: Academic), 539–575.

Moura, A. D., and Shukla, J. (1981). On the dynamics of drought in Northeast Brazil: observations, theory, and numerical experiments with a general circulation model, *J. Atmos. Sci.* 38, 2653–2675.

Nobre, P., and Shukla, J. (1996). Variations of sea surface temperature, wind stress, and rainfall over the tropical Atlantic and South America. *J. Climate.* 9, 2464–2479.

Philander, S. G. H. (1990). El Niño, La Niña, and the Southern Oscillation. *Int. Geophys*, 46, 293.

Polo, I., Martin-Rey, M., Rodriguez-Fonseca, B., Kucharski, F., and Mechoso, R. (2015). Processes in the Pacific La Niña onset triggered by the Atlantic Niño. *Clim. Dyn.* 44, 55–131. doi: 10.1007/s00382-014-2354-7

Polo, I., Rodríguez-Fonseca, B., Losada, T., and García-Serrano, J. (2008). Tropical Atlantic Variability modes (1979–2002). Part I: time-evolving SST modes related to West African rainfall. *J. Climate* 21, 6457–6475. doi: 10.1175/2008JCLI2607.1

Poveda, G., Waylen, P. R., and Pulwarty, R. S. (2006). Annual and inter-annual variability of the present climate in northern South America and southern Mesoamerica. *Palaeogeogr. Palaeoclimatol. Palaeoecol.* 234, 3–27. doi: 10.1016/j.palaeo.2005.10.031

Rao, V., Giarolla, B. E., Kayano, M. T., and Franchito, S. H. (2006). Is the recent increasing trend of rainfall over Northeast Brazil related sub-Saharan drought? *J. Climate* 19, 4448–4453. doi: 10.1175/JCLI3862.1

Rayner, N. A., Parker, D. E., Horton, E. B., Folland, C. K., Alexander, L. V., and Rowell, D. P. (2003). Global analyses of sea surface temperature, sea ice, and night marine air temperature since the nineteenth century. *J. Geophys. Res.* 108:4407. doi: 10.1029/2002jd002670

Richter, I., Mechoso, C. R., and Robertson., A. W. (2008). What determines the position and intensity of the South Atlantic anticyclone in Austral Winter? An AGCM study. *J. Climate.* 21, 214–229. doi: 10.1175/2007JCLI1802.1

Rodrigues, R. R., Reindert, J., Haarsma Campos, E. J. D., and Ambrizzi, T. (2011). The Impacts of Inter–El Niño variability on the Tropical Atlantic and Northeast Brazil climate. *J. Climate* 24, 3402–3422. doi: 10.1175/2011JCLI3983.1

Rodríguez-Fonseca, B., Mohino, E., Mechoso, C. R., Caminade, C., Biasutti, M., Gaetani, M., et al. (2015). Variability and Predictability of West African Droughts: a review of the Role of Sea Surface temperature Anomalies. *J. Climate* 28, 4034–4060. doi: 10.1175/jcli-d-14-00130.1

Rodríguez-Fonseca, B., Polo, I., García-Serrano, J., Losada, T., Mohino, E., Mechoso, C. R., et al. (2009). Are Atlantic Niños enhancing Pacific ENSO events in recent decades? *Geophys. Res. Lett*. 36, 67–74. doi: 10.1029/2009GL040048

Schneider, U., Fuchs, T., Meyer-Christoffer, A., and Rudolf, B. (2008). *Global Precipitation Analysis Products of the GPCC,* (Offenbach: Glob.Precip. Climatol. Cent.). Available online at http://gpcc.dwd.de

Shepard, D. (1968). A two-dimensional interpolation function for irregularly-spaced data. *Proc. 1968 A.C.M. Nat. Conf.* 68, 517–524. doi: 10.1145/800186.810616

Sierra, J. P., Arias, P. A., and Vieira, S. C. (2015). Precipitation over northern South America and its seasonal variability as simulated by the CMIP5 models. *Adv Meteorol*. 2015:634720. doi: 10.1155/2015/634720

Sperber, K. R., and Palmer, T. N. (1996). Interannual tropical rainfall variability in general circulation model simulations associated with the Atmospheric Model Intercomparison Project. *J. Climate* 9, 2727–2750.

Trenberth, K. E., and Stepaniak, D. P. (2001). Indices of El Niño Evolution. *J. Climate.* 14, 1697–1701. doi: 10.1175/1520-0442(2001)014<1697:LIOENO>2.0.CO;2

Uvo, C. B., Repelli, C. A., Zebiak, S. E., and Kushnir, Y. (1998). The relationships between tropical Pacific and Atlantic SST and Northeast Brazil monthly precipitation. *J. Climate* 11, 551–562.

Wilks, D. S. (2006). *Statistical Methods in the Atmospheric Sciences, 2nd Edn.* Amsterdam: Academic.

Willmott, C. J., Ackleson., S. G., Davis, R. E., Feddema, J. J., Klink, K. M., Legates, D. R., et al. (1985). Statistics for the evaluation and comparison of models. *J. Geophys. Res*. 90, 8995–8900.

Zebiak, S. E. (1993). Air-sea interaction in the Equatorial Atlantic region, *J. Climate* 6, 1567–1568.

Conflict of Interest Statement: The authors declare that the research was conducted in the absence of any commercial or financial relationships that could be construed as a potential conflict of interest.

ORIGINAL RESEARCH
published: 24 April 2015
doi: 10.3389/fenvs.2015.00029

Refinement of the daily precipitation simulated by the CMIP5 models over the north of the Northeast of Brazil

Gyrlene A. M. da Silva[1]* *and David Mendes*[2]

[1] *Department of Sea Sciences, University Federal of São Paulo, Santos, Brazil,* [2] *Department of Atmospheric Sciences and Climate, Centre for Exact and Earth Sciences, University Federal of Rio Grande do Norte, Natal, Brazil*

The ability of the Artificial Neural Network (ANN) and the Multiple Linear Regression (MLR) in reproducing the area-average observed daily precipitation during the rainy season (Feb–Mar–Apr) over the north of the Northeast of Brazil (NEB) is examined. For the present climate of Dec-Jan-Feb from 1963 to 2003 period these statistical models are developed and validated using the observed daily precipitation and simulated from the historical outputs of four models of the fifth phase of the Coupled Model Intercomparison Project (CMIP5). The simulations from all the models during DJF and FMA seasons have an anomalous intensification of the ITCZ and southward displacement in comparison with the climatology. Correlations of 0.54, 0.66, and 0.66 are found between the simulated daily precipitation of the CCSM4, GFDL_ESM2M, and MIROC_ESM models during DJF season and the observed values during FMA season. Only the CCSM4 model displays a slightly reasonable agreement with the observations. A comparison between the statistical downscaling using the nonlinear (ANN) and linear model (MLR) to identify the one most suitable for the analysis of daily precipitation was made. The ANN technique provides more ability to predict the present climate when compared to MLR technique. Based on this result, we examined the accuracy of the ANN model in project the changes for the future climate period from 2055 to 2095 over the same study region. For instance, a comparison between the daily precipitations changes projected indirectly from the ANN during Feb–Mar–Apr with those projected directly from the CMIP5 models forced by RCP 8.5 scenario is made. The results suggest that ANN model weights the CMIP5 projections according to the each model ability in simulating the present climate (and its variability). In others, the ANN model is a potentially promising approach to use as a complementary tool to improvement of the seasonal numerical simulations.

Keywords: artificial neural network, multiple linear regression, Intertropical Convergence Zone, sea surface temperature, precipitation, CMIP5 models

Edited by:
Anita Drumond,
University of Vigo, Spain

Reviewed by:
Meiry Sayuri Sakamoto,
Fundacao Cearense de Meteorologia
e Recursos Hidricos, Brazil
José Brabo Alves,
Ceará State University, Brazil

Correspondence:
Gyrlene A. M. da Silva,
Department of Sea Sciences,
University Federal of São Paulo, Av.,
Alm. Saldanha da Gama 89, Ponta da
Praia, Santos/SP 11030-400, Brazil
gyrlene@gmail.com

Specialty section:
This article was submitted to
Atmospheric Science,
a section of the journal
Frontiers in Environmental Science

Received: *10 November 2014*
Accepted: *25 March 2015*
Published: *24 April 2015*

Citation:
da Silva GAM and Mendes D (2015)
Refinement of the daily precipitation
simulated by the CMIP5 models over
the north of the Northeast of Brazil.
Front. Environ. Sci. 3:29.
doi: 10.3389/fenvs.2015.00029

Introduction

The Intertropical Convergence Zone (ITCZ) is the main meteorological system in large scale responsible for the rainy season over the north of the Northeast of Brazil (NEB) (Hastenrath et al., 1984; Xie and Carton, 2004 and references therein). This system is a semi-permanent low-pressure band of clouds that circle the globe near the equator on the confluence region of the southeasterly and northeasterly trade winds from the Southern and Northern Hemispheres, respectively.

Climatologically the ITCZ follows the seasonal march of the sun: the northernmost position occurs in July to September and the southernmost position is observed during December to February (Biasutti et al., 2003). As reported by Xie and Carton (2004) there is an apparent lag in the meridional excursion of the continental precipitation band. The possible causes are the heat reservoirs such as soil moisture and oceanic influences.

The rainy season over north of the NEB occurs due the meridional position of ITCZ closest to this region. The seasonality or persistence of warm waters over the Tropical South Atlantic favors the transport of the moisture into the interior of the NEB. In opposite, in periods in which the ITCZ is anomalously to the northward are expected drought conditions over the north of the NEB. As mentioned in Grodsky and Carton (2003) the anomalous displacement to the northward occurs in the presence of changes in inter-hemispheric Sea Surface Temperature (SST) gradient over the Atlantic Ocean. The development of the equatorial cold tongue in June persisting through September month maintains the ITCZ to the northward of the equator.

In general, the climate models show high degree skill in simulating the precipitation over the NEB region (Misra, 2004) in comparison with others regions of Brazil. Such characteristic is explained in part due the linear processes that dominate over the nonlinear processes in this region. The linear processes are influenced directly by the modifications in Hadley and Walker Cells in response to interannual variability in SST field over the Equatorial Eastern Pacific and the local impact of the South Tropical Atlantic Ocean. However, the nonlinear signal is influenced by SST variability that is found over others oceanic basins as the North Atlantic (Kayano and Andreoli, 2004) the North Pacific (Kayano and Andreoli, 2004; da Silva et al., 2011) and the Indian Ocean (Taschetto and Ambrizzi, 2012). The large SST anomalies over these oceanic basins seem to influence indirectly the linear impact and consequently the precipitation variability over the NEB. As mentioned in Silva et al. (2014) the precipitation field shows an inherent complexity determined by the global water cycle in association with the behavior of many factors such as moisture distribution over the continents, thermodynamics, and dynamical aspects, among others. This variable has an extreme relevance due the direct importance in many sectors of the society and environment. However, the spatial and temporal variability of the precipitation are not yet reproduced satisfactorily by the numerical models. This leads some questions that are addressed in present study:

(i) Are the CMIP5 models able to reproduce the main rainy season over the north of the NEB during the present climate?
(ii) What is the more adequate statistical downscaling approach to improve the model simulations during the present climate: the Artificial Neural Network (ANN) or the Multiple Linear Regression (MLR)?
(iii) Which one of these statistical models is more appropriate to project future scenarios of climate change based on CMIP5 runs?

It is worth mentioning that the scope of this paper is simple but efficient analyses relative to the performance of the ANN and MLR models to improve the General Circulation Models (GCMs) outputs. However, a brief discussion regarding the anomalous structure of the simulated ITCZ by these models is described to help in interpretation of the results. The statistical downscaling is used in this study as a refinement method to bridge the complex relationship between the large-scale and local atmospheric features for the present climate. The captured relationships are also designed to project regional climate change from direct outputs of the GCMs. The MLR have been introduced into meteorology and oceanography as a statistical model in a first stage in comparison with the ANN that is more recent at ends of 1990s approximately.

The ANN is able to learn and generalize the nonlinear relations between the predictor and predictand datasets. It also does not require a *priori* knowledge of the process. The disadvantage is that the relations learned are hidden in the structure not described in mathematical expression. The MLR captures the linear relations between these datasets that can be expressed in mathematical terms. The limitation of this model is the *priori* assumption about the consistency of this relationship.

The literature refers to the statistical downscaling through the ANN as an alternative to minimize the deficiencies of the GCMs (Gardner and Dorling, 1998). The technique allows the establishment of statistical links between the observed large-scale circulation and the precipitation or temperature fields by applying transfer functions to the GCMs outputs. Recently, Silva and Mendes (2013) elaborated a ANN model using as predictand variables the seasonal hindcasts of precipitation anomalies from the Climate Forecast System v2 (CFSv2) model and the observed dominant modes of anomalous SST over the South and North Atlantic to reproduce the precipitation during the rainy seasons over the south and north of the NEB region. The authors obtained fairly success in using the ANN approach as a complementary tool for the climate studies. However, there are few studies that explore the temporal downscaling by using the ANN method over the NEB region. The literature is focus mainly over the Amazon Basin (Mendes and Marengo, 2010; Mendes et al., 2014) and Southeast (Johnson et al., 2012) and South of Brazil (Ramírez et al., 2006).

The main objectives of the present study are twofold: to compare the performance of the temporal nonlinear (ANN) and linear (MLR) downscaling methods in predict the area-average observed daily precipitation during the rainy season over the north of the NEB for the present climate; and to examine the accuracy of the more adequate statistical method in project changes for the future climate over the same region. To investigate the future climate we use the CMIP5 model outputs forced by the Representative Concentration Pathways 8.5 (RCP8.5) scenario that is derived directly from the A2r scenario (Riahi et al., 2007). The choice for the RCP8.5 scenario is that in comparison with the others RCPs it corresponds to the pathway with the highest greenhouse gas emissions and concentrations leading to radiative forcing of 8.5 $\mathrm{W.m^{-1}}$ at the end of the century (Moss et al., 2010). The assumptions are summarized in Riahi et al. (2011): high population and relatively slow income growth with modest rates of technological change and energy intensity improvements, leading in the long term to high energy demand and greenhouse gas emissions in absence of climate change policies.

Section Materials and Methods describe the design of the statistical simulations. Section Results for the present and future climate analyses and the Section Summary refers to the main results.

Materials and Methods

The region of study is the north of the NEB that is detached by the red box between 2 and 7°S; 40 and 45°W as displayed in **Figure 1**. The 41 years of observed daily precipitation data for the present climate of 1963–2003 period derived from the South America 24 Gridded Precipitation dataset – SA24 (Liebmann and Allured, 2005) is obtained over this region. For the same period, we used the historical simulations of precipitation derived from the Coupled Model Intercomparison Project phase 5-CMIP5/IPCC (http://cmip-pcmdi.llnl.gov/cmip5). The projections of changes in precipitation field for the future climate of the 2055–2095 periods are obtained from the CMIP5 models forced with the high emission scenario RCP8.5 (940 ppm) as shown in **Table 1**.

For the observations the area-averaged daily precipitation is calculated over the study area during the rainy season from Feb–Mar–Apr (FMA) and for two previous lag months from Dec-Jan-Feb (DJF). The correlation between the observed daily precipitation during DJF and FMA is also calculated. Also, the differences between the normalized time series of the observed daily precipitation and the CMIP5 simulations during FMA season are shown. To explain such differences is calculated the anomalies of SST and precipitation over the Atlantic Ocean using as observations the ERSST version3b (Smith et al., 2008) and CAMS_OPI v0208 (Janowiak and Xie, 1999) datasets, respectively. All dataset are interpolated to a 1° lat-lon grid as in observations. Regarding the future climate period we also calculated the area-averaged daily precipitation during FMA season as derived from the CMIP5 runs.

FIGURE 1 | Location of the study region: North of the NEB delimited by the red box between 2 and 7°S; 40 and 45°W. The location is similar as in Silva and Mendes (2013). Adapted from http://mapas.ibge.gov.br.

The performance of the temporal downscaling through the ANN and MLR is compared with emphasis in ability to predict the tendency during present climate. Changes projected for the future climate derived directly from the grid box daily precipitation simulated by the CMIP5 models are compared with the changes simulated indirectly through the ANN. For the ANN and MLR methods the simulations are designed as in **Table 2**.

The ANN model is based in a learning technique in parallel. Through a sequence of predictors variables designed as input the network is trained to fit weights for those that can have contributed to the variability of predicted variables (target dataset). The learning technique has an advantages of generalization in which the input dataset should be divided in training (used to obtain the network weights), validation (used to obtain the accuracy of the model), and test (used to obtain the realistic estimative of the performance of the model). The network maps the predictors in a second set of output variables that are compared with the desired target and corrections are made until the model reaches the lowest possible error. In our study the skill model is analyzed through the Mean Squared Error (MSE), the linear correlation coefficient (corr) and the bias. The ANN has a capacity to identify approximate nonlinear relations between the predictor and predictand and their derivatives without a *prior* knowledge of a specific nonlinear function (Ramírez et al., 2006).

As in Silva and Mendes (2013) the Multilayer Perceptron architecture is used that is more adequate network for meteorological applications because the weather and the climate can repeat along the chronological time but never exactly in the same way (e.g., Cardoso and da Silva Dias, 2004). The **Figures 2, 3**

TABLE 1 | Observed and CMIP5 models daily precipitation dataset.

Daily Precipitation (all datasets are interpolated to 1° resolution)			
Observed	**Source**	**Spatial resolution (°)**	
SA24	NOAA/PSD/CIRES/CAB	1.0 × 1.0	
CMIP5 models		**Atmosphere**	**Ocean**
CCSM4	NCAR UCAR/USA	2.2 × 1.9	1.0 × 1.0
CNRM-CM5	CNRM-CERFACS/France	1.4 × 1.4	2.5 × 2.0
GFDL-ESM2M	NOAA GFDL/USA	2.5 × 2.0	1.0 × 0.9
MIROC_ESM	MIROC/Japan	2.8 × 2.8	1.4 × 0.9

TABLE 2 | Design of the statistical downscaling with the ANN model.

Predictors	Predictand	Forecast period
DJF CMIP5 runs and observed daily precipitation	FMA observed daily precipitation	1963–2003
FMA CMIP5 climate scenarios of daily precipitation	FMA climate scenarios of daily precipitation	2055–2095

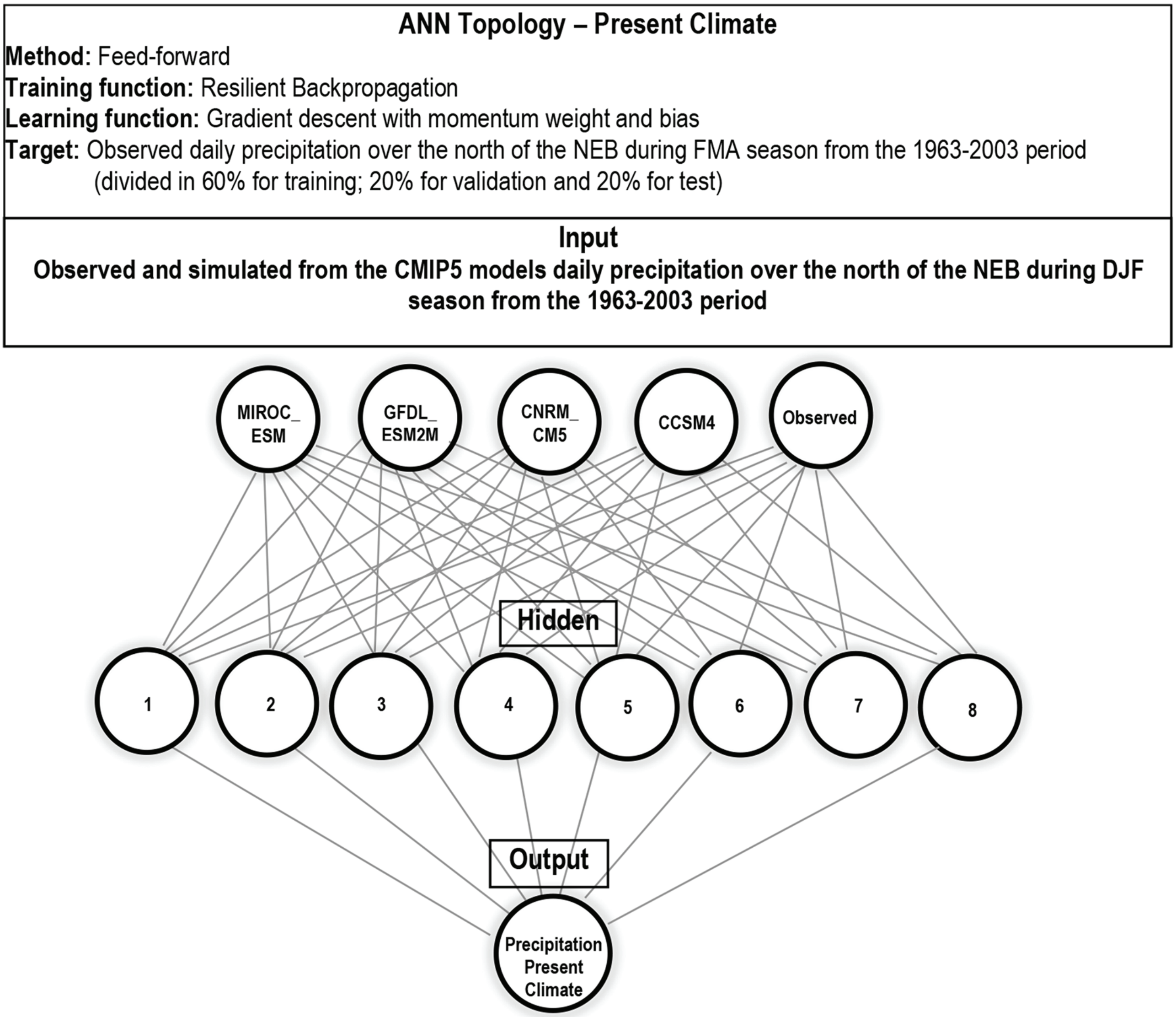
ANN Topology – Present Climate

Method: Feed-forward

Training function: Resilient Backpropagation

Learning function: Gradient descent with momentum weight and bias

Target: Observed daily precipitation over the north of the NEB during FMA season from the 1963-2003 period (divided in 60% for training; 20% for validation and 20% for test)

Input

Observed and simulated from the CMIP5 models daily precipitation over the north of the NEB during DJF season from the 1963-2003 period

FIGURE 2 | ANN topology used for the present climate simulations.

represent the topology of the ANN used in the present study for the present and future climate analyses, respectively. For both simulations the Multilayer Perceptron topology is interconnected in a feed-forward method. This method allows that the information of one hidden layer with the eight tangent sigmoid neurons be forward in direction of the input nodes to the output nodes.

The resilient backpropagation is the training function with a gradient descent, and the momentum weight and bias is the learning function. The training function used allows eliminating the effect of the sigmoid transfer function in the hidden layer. The effect surges when the input is large that forces to their gradient must approach zero tending to very small magnitude values favoring low changes in the weights and biases. To estimate the accuracy and reduce the effect of over-fitting, the cross-validation is applied. For instance, the training dataset is divided in 60% for training; 20% for validation; and 20% for test.

In **Figure 2** the target dataset is the observed daily precipitation during FMA season of 1963–2003 over the north of the NEB. The input is the daily precipitation during DJF season of the same period and region that are extracted from the observations and CMIP5 outputs. The result of the ANN model is the output relative to the daily precipitation simulated for the present climate during FMA season. In **Figure 3** for the future climate analyses the target is the daily precipitation during FMA season of the 1963–2003 previously predicted through the ANN. The input dataset are the values of precipitation for the FMA season of the 2055–2095 periods and the output is simulation of the ANN model relative to the precipitation scenario for the FMA season.

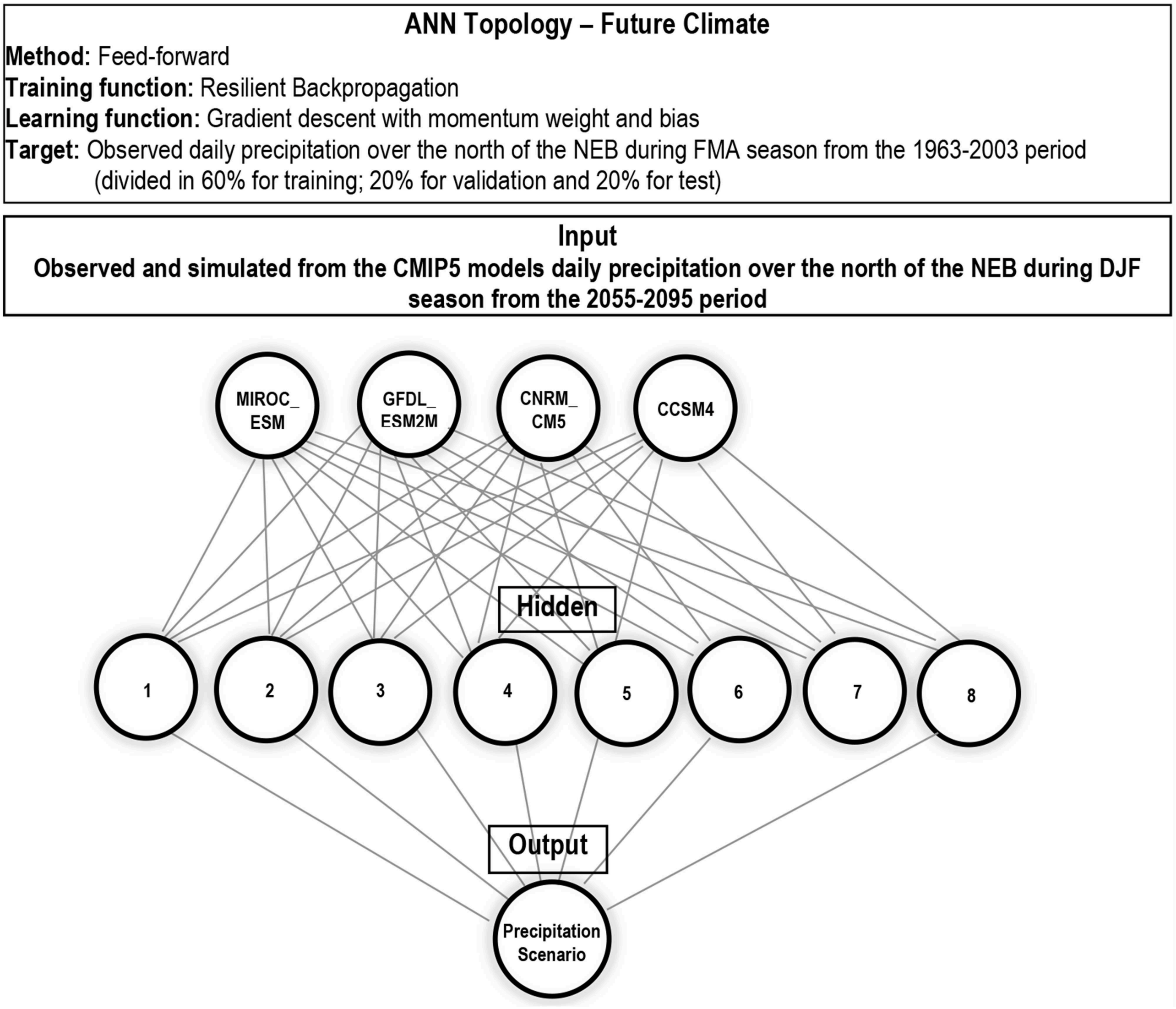

ANN Topology – Future Climate

Method: Feed-forward

Training function: Resilient Backpropagation

Learning function: Gradient descent with momentum weight and bias

Target: Observed daily precipitation over the north of the NEB during FMA season from the 1963-2003 period (divided in 60% for training; 20% for validation and 20% for test)

Input

Observed and simulated from the CMIP5 models daily precipitation over the north of the NEB during DJF season from the 2055-2095 period

FIGURE 3 | ANN topology used for the future climate simulations.

The Equation (1) express the MLR model in which a output y (predictand) is dependent of a set of input (predictors) that are independent variables $x_1, x_2, \ldots, x_p$ $(p > 1)$. The values α is the y-intercept, $\beta_k (k = 1, 2, \ldots, p)$ are the weights and ϵ is the forecast error.

$$y = \alpha + \sum_k \beta_k x_k + \in \tag{1}$$

The idea in using the MLR is to adjust predictors that are a set of daily precipitation during DJF season over the north of the NEB derived from the CMIP5 models to a predictand, the observed daily precipitation during FMA season over the same area. This implies in identify the lagged influence of each CMIP5 model in capture the most part of the variability in precipitation over the study region.

For the ANN and MLR models the predictors and predictand variables are normalized in interval [0, 1] by min-max formula similar as Sajikumar and Thandaveswara (1999):

$$v'(i) = \frac{v(i) - min_i v(i)}{max_i v(i) - min_i v(i)} \tag{2}$$

A posterior normalization in interval [−1,1] is assuming that

$$v'' = av' + b \tag{3}$$

So, when: $v' = 0,\ v'' = -1$; when $v' = 1,\ v'' = 1$ implying that $-1 = b$ and $1 = \mathrm{a} + \mathrm{b}'$ resulting in:

$$v'' = 2v' - 1 \tag{4}$$

Results

Present Climate

The observed and simulated normalized time series of daily precipitation for FMA season are displayed in **Figure 4**. The observed anomalies in **Figure 4A** are calculated in relation to the mean of 8.13 mm.day^{-1}. The median value of 8.21 mm.day^{-1} suggests that the extremes in normalized time series do not affect the mean value. The **Figure 4B** show high discrepancies between the CMIP5 outputs in modeling the present-day precipitation for FMA season. The MIROC_ESM model simulates the worst results overestimating the precipitation during the Feb–Mar months and underestimating in April. The GFDL_ESM2M model underestimates the daily precipitation amplitude along the time series and the CNRM_CM5 model shows a higher variability an extreme values. The differences between the models in modeling the large-scale precipitation patterns imply that is necessary to considerer the use of statistical techniques to improve the present simulation and future climate projections. In others, is relevant to apply the refinement methods in the GCMs outputs mainly in improving of their mean and variability.

The outputs from the CCSM4, GFDL_ESM2M, and MIROC_ESM models during DJF season are most correlated with the observed FMA season precipitation (**Table 3**). The correlations values are of 0.54, 0.66, and 0.66, respectively. However, only the CCSM4 model displays a slightly reasonable agreement in terms of variability in the normalized series. The considerable differences in the mean and the variability between the observed and modeled daily precipitation values justify the differences found in correlations observed in the **Table 3**.

In order to investigate these discrepancies we compare the simulated mean SST and precipitation from each model over the Equatorial Atlantic Ocean with the observed field (**Figures 5A,B**, **6A,B**, respectively) that results in the anomalous fields (**Figures 5C–J**, **6C–J**, respectively). The observed SST for the DJF season shows a warm pool in a region extending into the 5–8°S with values of 26–28°C and maximum magnitude on the eastern basin. The precipitation band is located over the equator region, between 5°S and 8°N onto which

TABLE 3 | Lagged correlation between the normalized daily precipitation time series derived from the CMIP5 models for the DJF season and observed for the FMA season during the 1963–2003 period.

Precipitation–FMA season	Precipitation–DJF season	corr
Observation	Observation	0.63
	CMIP5 models	
	CCSM4	0.54
	CNRM-CM5	0.27
	GFDL-ESM2M	0.66
	MIROC_ESM	0.66

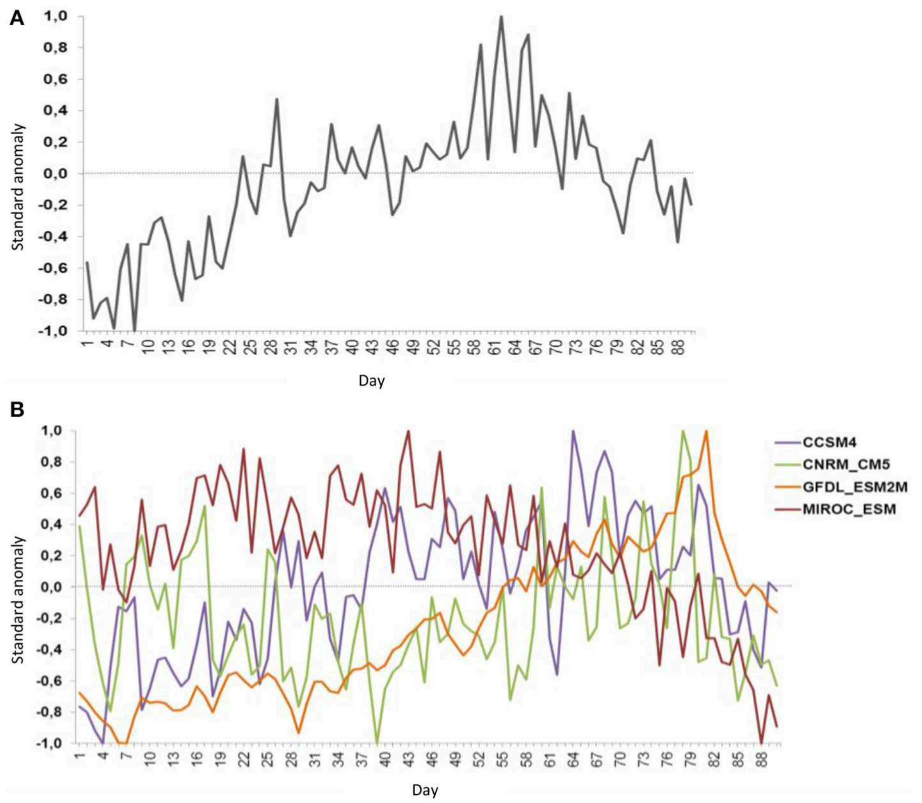

FIGURE 4 | Observed (A) and simulated from the CMIP5 models (B) daily precipitation over the north of the NEB during FMA season from the 1963–2003 period.

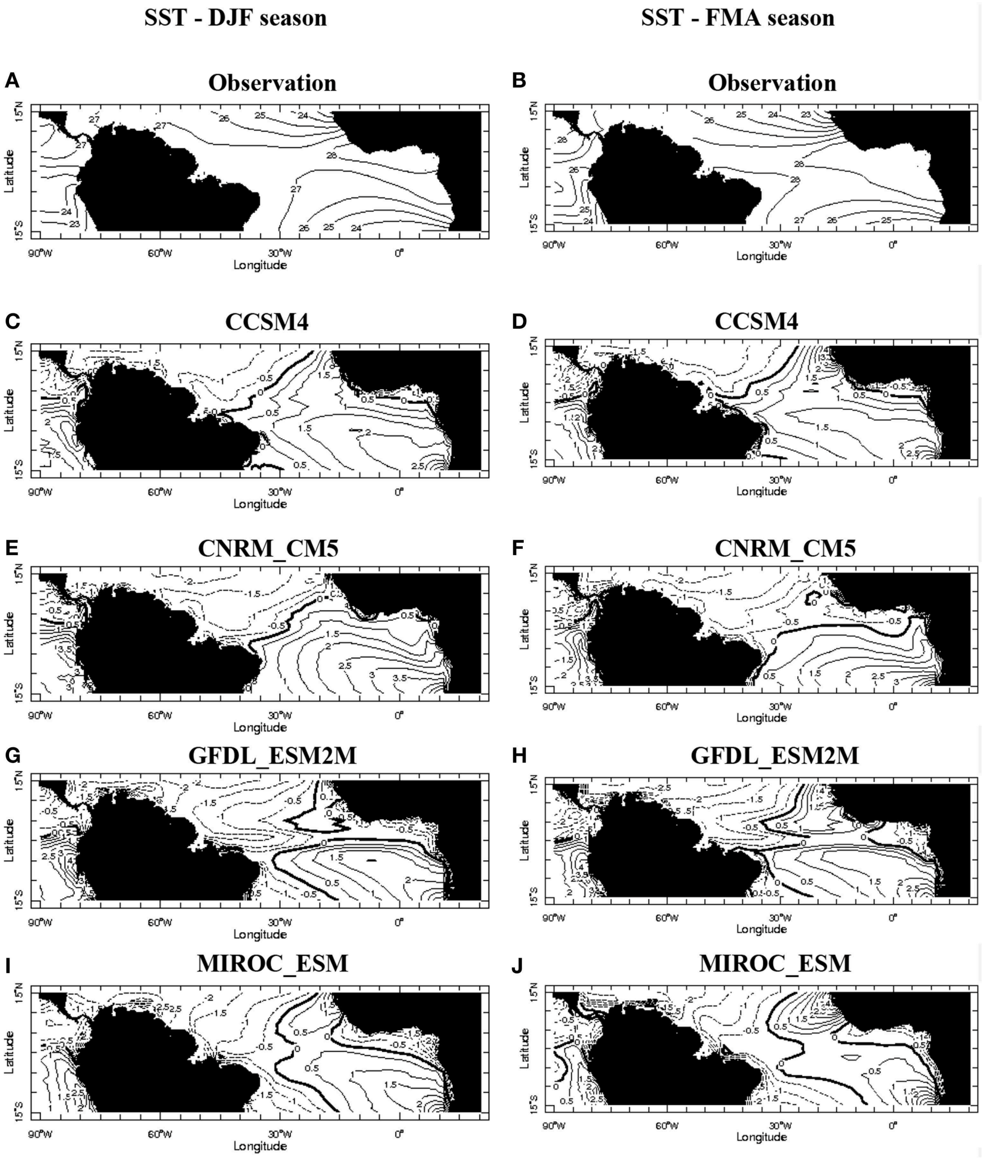

FIGURE 5 | On the left panel the DJF mean SST during 1963–2003 period along the equator area for the observation (letter A) and the DJF anomalies for the CCSM4, CNRM_CM5, GFDL_ESM2M e MIROC_ESM models (letters C, E, G, and I respectively). On the right panel the same sequence as on the left panel except for FMA (the mean in **B**, and the anomalies in **D**, **F**, **H**, **J**). All data are interpolated to a lat-lon grid with 1°. The respective maps were constructed from the IRI/LDEO Climate Data Library.

the trade winds converge from the North and South Hemispheres (**Figures 5A**, **6A**, respectively). During FMA season the warm pool intensifies along the central basin and coast of the NEB and vicinity of the Equatorial Atlantic Ocean. As response an intensification of the precipitation along these regions is observed during FMA season with a notable maximum nucleus over the north of the NEB (**Figures 5B**, **6B**, respectively).

Siongco et al. (2014) analyzed 24 of the CMIP5 models and found significant deficiencies in reproduction of the ITCZ structure with either the west or the east Atlantic bias and no model matches the observed precipitation distribution. Our analysis for the DJF and FMA seasons shows that the CCSM4, CNRM_CM5, GFDL_ESM2M,and MIROC_ESM models have a cooling (warming) bias over the western (eastern) basin with anomalies below −0.5°C (above 0.5°C). The more intense values are found on the eastern Equatorial Atlantic Ocean (**Figures 5C–J**, respectively). The anomalous precipitation fields shows that all the models suffer with deficiencies in representing the magnitude and mean position of the continental and oceanic ITCZ that is displaced to southward in comparison with the climatology (**Figures 6A,B**).

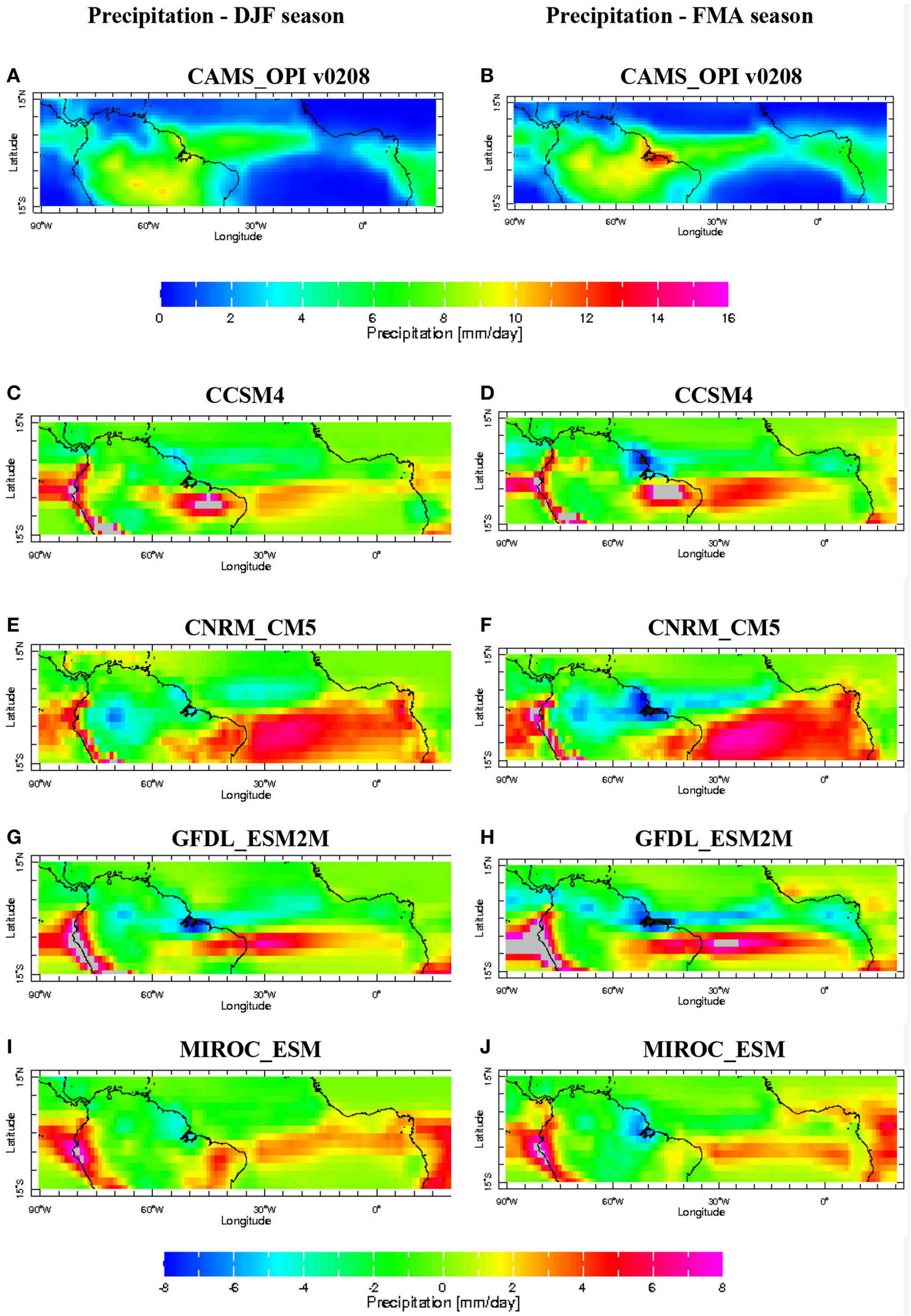

FIGURE 6 | On the left panel the DJF mean precipitation during 1963–2003 period along the equator area for the observation (letter A) and the DJF anomalies for the CCSM4, CNRM_CM5, GFDL_ESM2M e MIROC_ESM models (letters C, E, G, and I, respectively). On the right panel the same sequence as on the left panel except for FMA (the mean in **B**, and the anomalies in **D**, **F**, **H**, **J**). All data are interpolated to a lat-lon grid with 1°. The respective maps were constructed from the IRI/LDEO Climate Data Library.

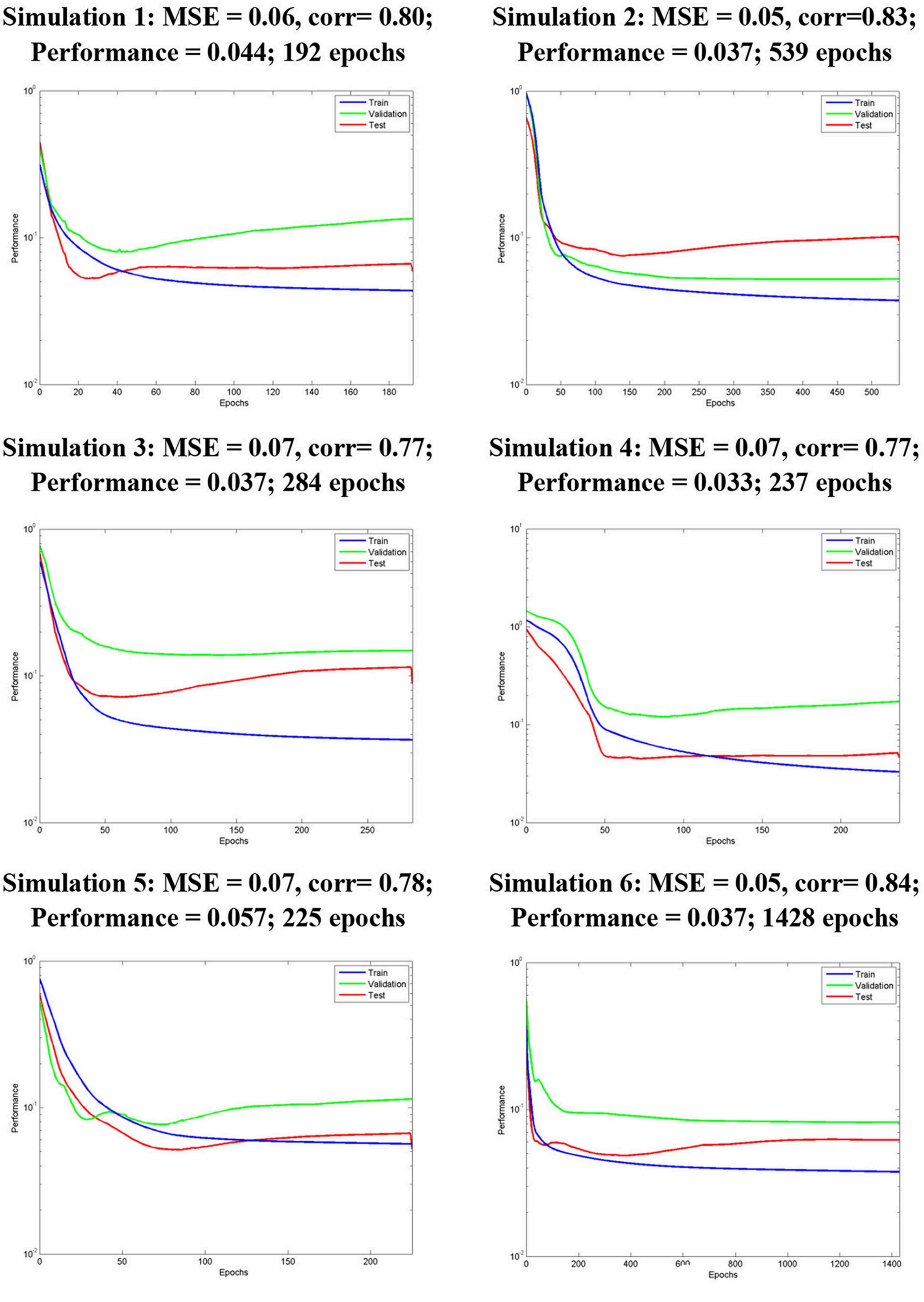

Simulation 1: MSE = 0.06, corr= 0.80; Performance = 0.044; 192 epochs

Simulation 2: MSE = 0.05, corr=0.83; Performance = 0.037; 539 epochs

Simulation 3: MSE = 0.07, corr= 0.77; Performance = 0.037; 284 epochs

Simulation 4: MSE = 0.07, corr= 0.77; Performance = 0.033; 237 epochs

Simulation 5: MSE = 0.07, corr= 0.78; Performance = 0.057; 225 epochs

Simulation 6: MSE = 0.05, corr= 0.84; Performance = 0.037; 1428 epochs

FIGURE 7 | Continued

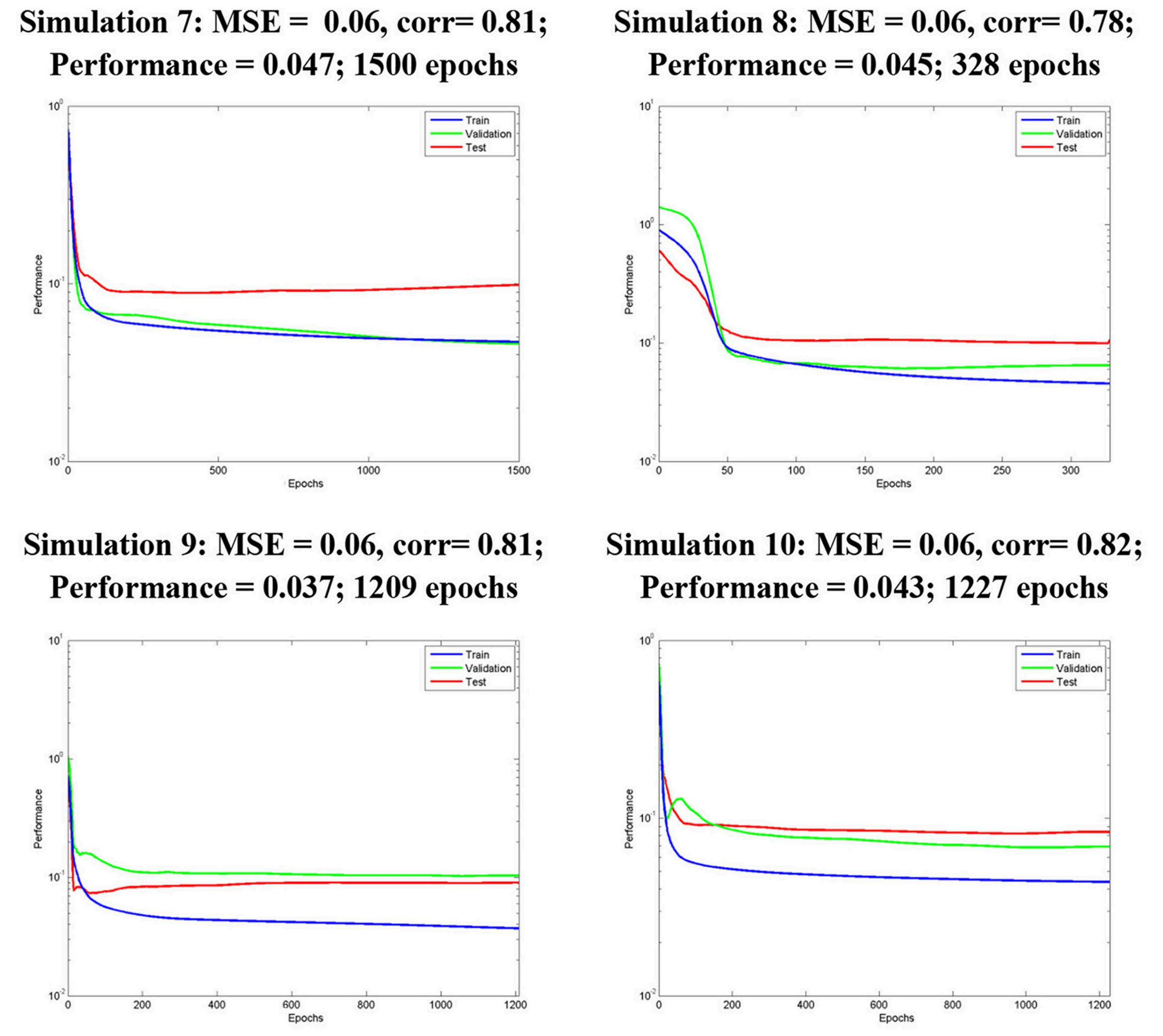

Simulation 7: MSE = 0.06, corr= 0.81; Performance = 0.047; 1500 epochs

Simulation 8: MSE = 0.06, corr= 0.78; Performance = 0.045; 328 epochs

Simulation 9: MSE = 0.06, corr= 0.81; Performance = 0.037; 1209 epochs

Simulation 10: MSE = 0.06, corr= 0.82; Performance = 0.043; 1227 epochs

FIGURE 7 | Simulations of the ANN model during the present climate period (1963–2003). In y-axis is the performance of each simulation divided in train (blue line), validation (green line), and test (red line) during different epochs (x-axis).

The CCSM4 model shows above mean precipitation in both seasons as indicative of Atlantic Niño mode (Richter et al., 2014) that may occurs in response to impact of inter-El Nino variability on the Tropical Atlantic over the Northeast Brazil (Rodrigues et al., 2011). The warmer SST anomalies in the eastern Equatorial and Tropical South Atlantic Ocean favor the southward ITCZ displacement and consequently the above average precipitation values over the NEB (**Figures 6C,D**). As seen in the **Table 3** the observed precipitation during FMA is more correlated with the outputs from GFDL_ESM2M, MIROC_ESM, and CCSM4 models. However, only the CCSM4 model displays a slightly reasonable agreement with observation in terms of variability on the daily precipitation.

In **Figures 6E,F** the CNRM-CM5 model simulates a more elongated southward ITCZ structure with above mean precipitation over the eastern than central Equatorial Atlantic basin in accordance with the simulated SST anomalies shown in **Figures 5E,F**. This model shows the more intense SST anomalous gradient along the Equatorial Atlantic Ocean in comparison with the others in analysis. As consequence the north of the NEB shows below average values mainly during FMA season that is the rainy season on this region. The consequence of this anomalous pattern is also noted in **Figure 4B** on the simulated daily precipitation time series of the CNRM-CM5 model and the low correlation value of 0.27, the lowest between the models, as shown in **Table 3**. In the GFDL-ESM2M model simulation there are two anomalous precipitation bands zonally elongated: to the north and to the south of the climatological position of the ITCZ that is considerably stronger than in observation leading above mean values over part of NEB (**Figures 6G,H**). The MIROC-ESM model shows more longitudinal elongated distribution of precipitation and above average values over the north of the NEB that is reflected in simulated time series shown in **Figure 4B**.

The results obtained from the best of 10 simulations from the ANN model are displayed in **Figure 7** that illustrates the performance of each simulation (y-axis) as function of the epochs (x-axis). The term performance refers to the ability of the network in generalize that is, the trained net is able to give correct outputs dataset from the same class as the learning dataset that it has never trained before. The epoch's term refers to the number of iterations for the input dataset in training. There is no rule to decide the number of simulations however 10 simulations are suggested as appropriate to visualize the differences in curves. The weights are reinitialized random in each simulation and the training iteration is initiated using the new target vectors and set of weights. The best simulation was chosen by analysis of the minimum Mean Square Error (MSE) and the maximum correlation coefficient between the predictors and predictand datasets. In addition, a maximum likelihood between the train, validation, test curves and their faster decay were also considered on choice of the best simulation.

The simulation 2 shows the best performance and estimated generalization error MSE $= |0.05|$and correlation coefficient of 0.83 (**Figures 7**, **8**). Although the values of MSE $= |0.05|$and corr $= 0.84$ in the simulation 6 it performance is not better than the simulation 2 which compromises the downscaled values. The explanation is that the purpose of training is to reduce the MSE to a low value using the few epochs as possible. The performance in simulation 6 is reached in 1426 epochs that is much long than in simulation 2 and also the respective test set (red line) is worst. Also, the variability of the output dataset obtained in the simulation 2 is better learned than in the simulation 6 (not shown). The **Figure 8** shows the cross-validation used to validate the network performance. This means that the network output with respect to target (observed daily precipitation during FMA season of 1963–2003 period over the north of the NEB) for training, validation and test datasets. The equation $Output = 0.7^{*} target + -0.051$ indicates how close the output is the target dataset. The fitting is reasonably good once the correlation coefficient is 0.83 and 70% of variability in output is explained by the target dataset The value of 0.051 represents the variability of the simulated output due the error term.

The Equation 4 is the result of the MLR model used in the prediction of normalized daily precipitation during FMA season being represented by the relationship between the predictors: the normalized daily precipitation for DJF season observed and simulated by the CMIP5 models. The MSE obtained is $|0.09|$and the correlation between the predictors and predictand dataset is 0.70. The equation of the MLR derived model is shown as follow:

$$
\begin{aligned}
\mathrm{Prec}_{FMA} &= -0.17 + 0.22 * \mathrm{Prec}_{MIROC\_ESMDJF} \\
&+0.22 * \mathrm{Prec}_{GFDL\_ESM2MDJF} + 0.20 * \\
&\mathrm{Prec}_{Obs\ DJF} - 0.07 * \mathrm{Prec}_{CCSM4\ DJF} \\
&+ 0.06 * \mathrm{Prec}_{CNRM\_CM5DJF} \qquad (5)
\end{aligned}
$$

This equation defines that -0.17 is the constant value at which the fitted line crosses the y-axis representing the expected response when the predictors are zero. Each predictor (output of each one of the CMIP5 model) is weighted, and the weights denote their relative contribution to the overall adjustment. It is interpreted that the precipitation simulated from the MIROC_ESM and GFDL_ESM2M models during DJF season captures 22% of the variability of the observed daily precipitation during FMA season over the study region. Additionally, the observed daily precipitation during DJF season captures 20% of the variability in precipitation during FMA season. Only a few part of the observed daily precipitation during the rainy season is captured by the simulations of DJF season from the CCSM4 and CNRM_CM5 models. The equation indicates that MLR model not represents the suitable adjustment between the observed daily precipitation during the rainy season of FMA trimester and those predicted in 2 months before during the DJF season.

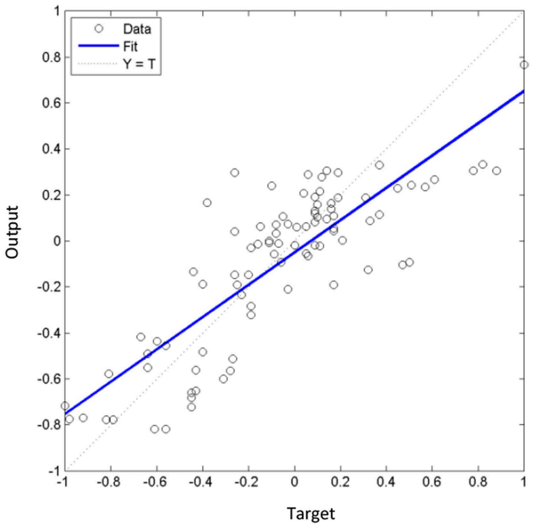

FIGURE 8 | Cross-validation result of the best fit obtained in the Simulation 2 with MSE = 0.05 and corr = 0.83. The output simulated using as target the observed daily precipitation during FMA season and input the simulations of this variable from the four CMIP5 models in analysis during DJF season of 1963–2003 period over the north of the NEB is: Output = 0.7*target + −0.051.

A comparison between nonlinear x linear methods illustrates that the downscaled values from the ANN model shows an improvement of 13% in terms of correlations coefficient values in comparison with the downscaled time series of the MLR model. This result is analyzed by subtracting the correlation coefficient value of 0.83 calculated between the observation and simulations values of the ANN model with those of the MLR model that is 0.70. Also, the ANN simulates a lesser generalized error of 0.05 in comparison with the obtained of the MLR model that is 0.09 and shows an improvement in the amplitude of the simulated time series.

The **Figure 9** shows that ANN and MLR techniques exhibit the same positive tendency as in observation however there are deficiencies to predict the extreme values. Nevertheless, the best prediction of these extremes is found in ANN time series. This means that the MLR model is poorly suited to modeling the complex nonlinear relationships inherent in climate variables. Also, the ANN is more able to capture features of the interannual

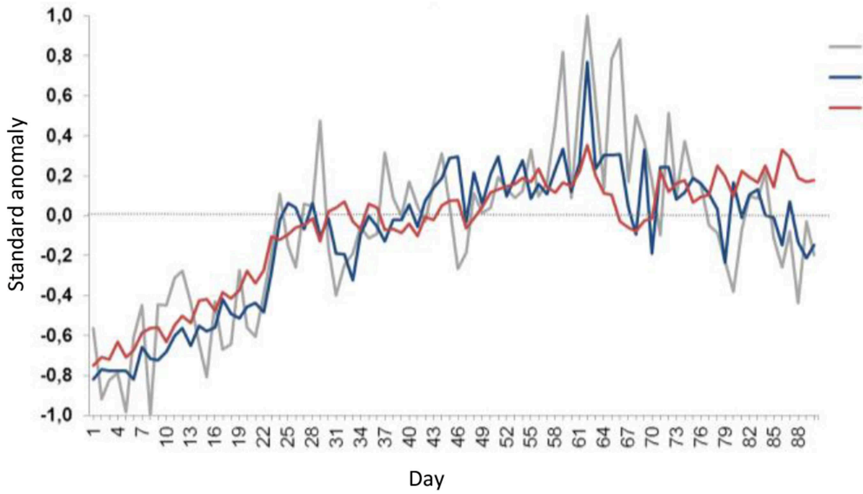

FIGURE 9 | Comparison between the observed (gray line) and simulated daily precipitation by the ANN (blue line) and MLR (red line) models during FMA season of the 1963–2003 period over the north of the NEB.

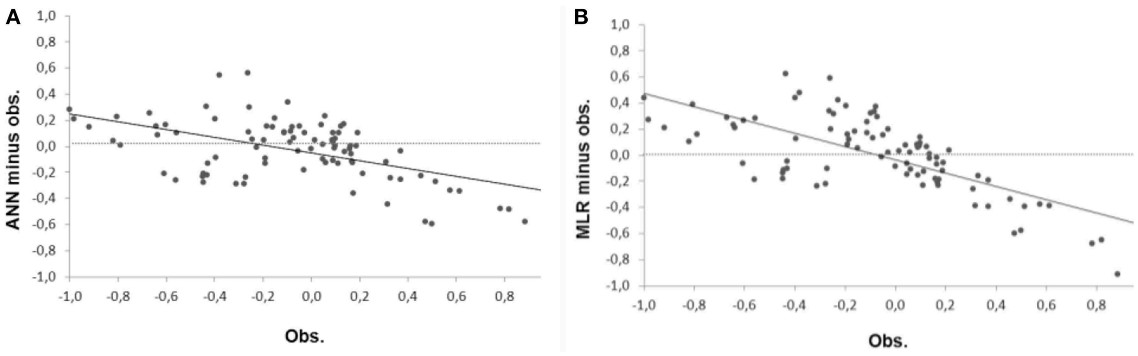

FIGURE 10 | Bias comparison between the simulated daily precipitation by the ANN (A) and MLR (B) models during FMA season of the 1963–2003 over the north of the NEB.

variability in the daily precipitation. In others, this is a useful tool to understanding of the main features of the precipitation in terms of large-scale atmospheric patterns.

The plot of the predictand bias (the simulated predictand values minus the observed values) shows that the distribution of errors with values close to zero being more frequent for nonlinear method than linear method (**Figures 10A,B**, respectively). It suggests that the ANN model is powerful to resolve the physical processes that are nonlinear in the precipitation dataset. However, the refinement methods show a tendency to underestimate high values of precipitation and to overestimate the low ones.

Through the box-plots is shown that the median is similar in the observed and the two downscaled times series (**Figure 11**). However, the dispersion is best represented in the ANN than in MLR model when compared to the observations. Also, the MLR has a considerably lesser symmetric distribution of values in the predictand time series with a negative tail and more outliers indicating values with an abnormal distance from the other. The downscaled times series show a decreasing of the variance compared to the observations that is also indicated in **Figure 9**. According the previous results it suggested that the MLR has no skill in simulating the present-day climate over the region probability due the non-linearity imposed between the input and output data. Based on this, we decided to use the ANN method in the next analyses for the future climate.

Future Climate

In the simulations for the future climate scenario we used the same ANN topology as those used in simulations for the present climate. The details about the design of the experiments are described in Section Results. We emphasize that the network projections criteria is different from those introduced in Boulanger et al. (2007). By comparing the 2055–2095 with the 1963–2003 periods is observed that all models project a positive tendency of daily precipitation over the north of the NEB (**Figures 12A–C**). An exception is found in the MIROC_ESM runs that projected a negative tendency and change from positive to negative on the rainy pattern (**Figure 12D**).

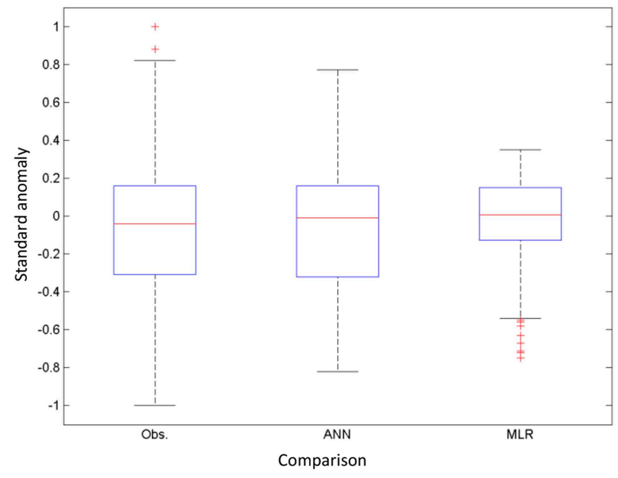

FIGURE 11 | Box-plots comparison between observed and simulated daily precipitation by the ANN and MLR models during FMA season of the 1963–2003 period over the north of the NEB.

The changes on the future climate projected by CMIP5 models for the 2055–2095 periods are validated with those obtained indirectly through the ANN model. The baseline is the predictand time series previously simulated for the present climate during the 1963–2003 period as shown in Section Present Climate. The best simulation results displayed in **Figure 13** reached the MSE = 0.02 and correlation of 0.88 between the predictors and predictand datasets (**Figure 13A**). The result of the cross-validation $Output = 0.74^{*}target + -0.02$ is interpreted as 74% variability of the output dataset is captured by all models and the uncountable part related to MSE = 0.02 is due the error in simulation. It means that the ANN model performs well in calibrating the climate model precipitation projections. The low MSE value may represent the local forcing as topography and local atmospheric processes that are smoothed in GCMs simulations due their low-resolution grid. We suggest the linear response that favors the relative high skill in predictability over the NEB in comparison with others regions of Brazil as mentioned in Introduction may be compromised when the models are forced by the greenhouse gas forcing RCP8.5. This suggests the importance of the RCP8.5 in change the large scale for the 2055–2095 periods. In **Figure 13B** the changes projected by ANN model exhibits near similar tendency as in GFDL_ESM2M model although the lower amplitudes.

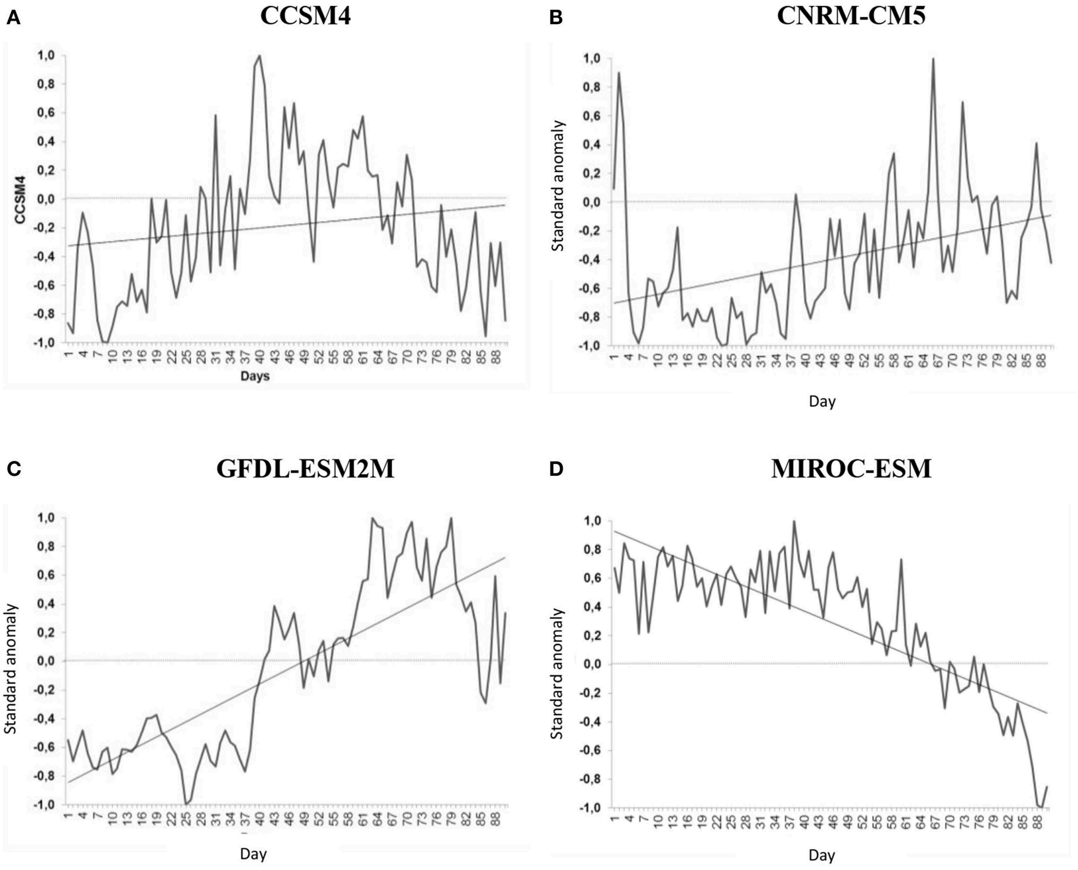

FIGURE 12 | Projections of the daily precipitation on the future climate during FMA season of 2055–2095 period over the north of the NEB simulated by the CMIP5 models: (A) CCSM4, (B) CNRM_CM5, (C) GFDL_ESM2M, (D) MIROC_ESM.

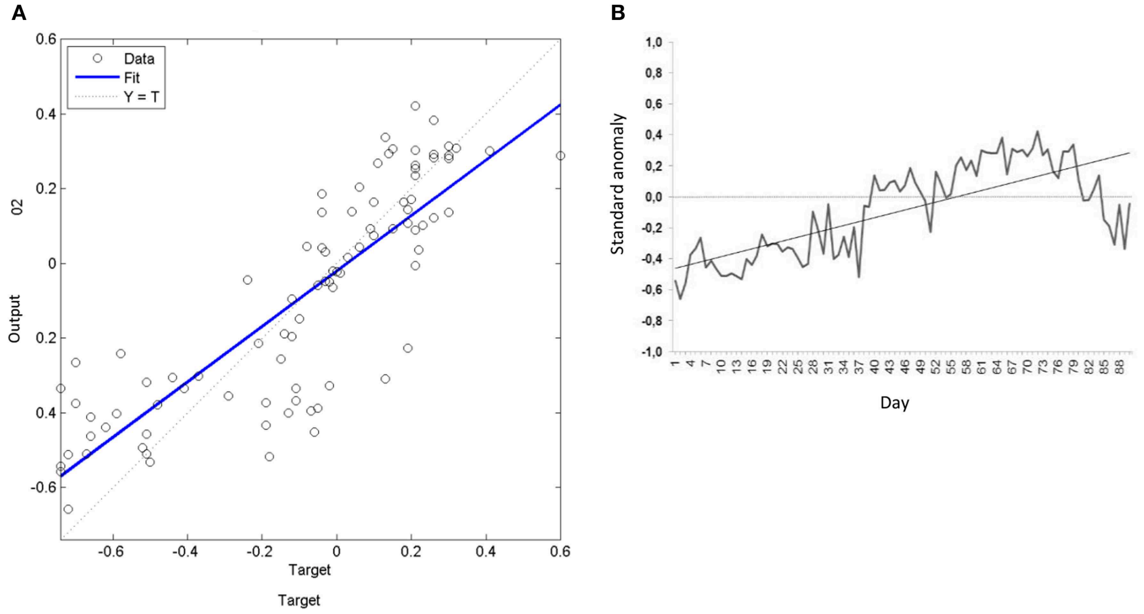

FIGURE 13 | Results of the future climate change scenario simulation during FMA season of the 2055–2095 period of the ANN model: (A) Cross-validation result from the best fit with MSE = 0.02 and corr = 0.84. The output simulated using as target the simulated daily precipitation during FMA season from the ANN model and input the simulations of this variable from the four CMIP5 models in analysis during FMA season of 2055–2095 period over the north of the NEB is: Output = 0.74*target + −0.02. The letter **(B)** exhibits the respective time series.

TABLE 4 | Correlation between the future scenarios for the 2055–2095 period projected direct from the CMIP5 models and indirect from the ANN model.

Correlation between future scenarios (2055–2095 period)	
CMIP5 model	**ANN model**
CCSM4	0.54
CNRM_CM5	0.36
GFDL_ESM2M	0.89
MIROC_ESM	−0.44

The **Table 4** shows the comparison through the correlation coefficient among the projected pattern from the ANN model and those from the CMIP5 models. It is clear that the ANN projection is more influenced by the GFDL_ESM2M response to RCP8.5 forcing. This model also shows a moderate correlation among the normalized daily precipitation during DJF and FMA seasons during the 1963–2003 period as seen in **Figure 4** and **Table 3**. However, in analysis of the **Figure 6** the mean structure of the ITCZ is better simulated in CCSM4 model that also show moderate correlation as displayed in **Table 3**. It suggests that a model may present a better simulation than another for the present-day climate but poorly respond to greenhouse gas forcing.

The results reinforce that serious uncertainty are still persists since the CMIP3 model version in projections of equatorial precipitation as an expected consequence of global climate change. Ceppi et al. (2013) and some references therein explained that the hemispheres not heat evenly: the north hemisphere warm more swiftly than the south and this imbalance will have a consequent effect on the structure of the ITCZ. This fact underscores the importance of studies as the present here by applying statistical downscaling approach to improve the estimation of the variability to the GCMs outputs.

Discussions

Regarding the complex task that the numerical models in reproduce the precipitation some questions are addressed in this study.

Are the CMIP5 Models Able to Reproduce the Main Rainy Season Over the North of the NEB During the Present Climate?

No, from the four CMIP5 models analyzed there is a high dispersion of the daily precipitation over the north of the NEB justifying the use of downscaling methods. Overall, the differences between the models are reflected mainly in the mean and variability values of the daily precipitation over this region. The simulated daily precipitation by the CCSM4, GFDL_ESM2M, and MIROC_ESM models during DJF season are most correlated with the observed daily precipitation during FMA season. The correlations are of 0.54, 0.66, and 0.66, respectively. These correlations are explained by deficiencies shown in configuration of the anomalies of SST along the Equatorial Atlantic Ocean that result in anomalies in simulated daily precipitation over the north of NEB. Only the CCSM4 model displays a slightly reasonable agreement with the observations.

Regarding this aspect a comparison between the nonlinear (ANN) and linear method (MLR) to identify the one most suitable for the analysis of daily precipitation is made. No additional post-processing is applied on the downscaled outputs and the statistical methods show a decreasing of the variance in the predictand time series. Such feature is commonly encountered in the results of the application of statistical downscaling in climate research (Silva and Mendes, 2013; among others).

What is the More Adequate Statistical Downscaling Approach to Improve the Model Simulations During the Present Climate: The Artificial Neural Network (ANN) or the Multiple Linear Regression (MLR)?

We compared the relative performance of ANN and MLR models in improve the normalized daily precipitation during FMA season over the north of the NEB derived from observed and the CMIP5 outputs during DJF 1963–2003 period. The comparison between the methods is based in analysis of the Mean Squared Error (MSE), the linear correlation coefficient and the variability of the downscaled time series.

The nonlinear downscaling with ANN is potentially promising method of improvement of the explained variance of dataset than linear downscaling with MLR. The temporal downscaling through the ANN appears relatively efficient in correct part of the deficiencies in CMIP5 runs though the improvement of the large scale observed patterns. In terms of correlation coefficient values the improvement is of 13% between the predictors and predictand values from the ANN model compared to those from the MLR model. Also, the estimated errors and the amplitude of downscaled time series is best performed by ANN model.

Which One of these Statistical Models is More Appropriate to Project Future Scenarios of Climate Change Based on CMIP5 Runs?

Excluding the MIROC_ESM model the others ones are relatively coherent in comparing their 2055–2095 climate scenarios pattern over the north of the NEB. They have a tendency of increase of the daily precipitation projected. The projections for the FMA season derived directly from the mean grid box precipitation simulated from the CMIP5 models are compared with those obtained indirectly through ANN method. The baseline is the predictand downscaled for FMA time series. The climate scenario projected by ANN model indicates that the unaccounted explained variance is $|0.02|$that is the lower possible and corresponding to local forcings that will not change in future warmer climate (Trigo and Palutikof, 2001). This local forcing may be associated with the topography and local convection that are not well incorporated in the numerical models but influence the occurrence of precipitation. It may be suggested that the heavy-emission scenario of CO_2 in RCP8.5 is an important forcing of large-scale circulation for the 2055–2095 period. A comparison of the precipitation change projected from the ANN and those from the CMIP5 models indicated that the statistical model weights the CMIP5 runs according to their skill in simulating present-day climate. Similar characteristic is also found by the Boulanger et al. (2007) by comparing the 2076–2100 SRES A2 annual mean precipitation change projected by the ANN with those simulated by the seven models from the IPCC AR4.

Through the obtained results we suggest that the ANN method is an important tool to allow the establishment of complex relationship between large-scale and local climate over the north of the NEB. The complex relationship in the precipitation pattern over this region refers to the influence of local and remote forcing's related to SST variability. The purpose of this study is to emphasize that the ANN method that is used in many operational centers around the world in improvement of the predictability of numerical models needs more studies and applications in Brazil.

Furthermore the similar methodology as the present here will be carry out in analysis of the temporal and spatial dependence of these results with those for the east and south grid boxes over the NEB. The east and south of the NEB are regions with stronger nonlinearity compared with the north region and it is possible that ANN results may vary according to the regions particularities. Another important feature that will be investigated is the improvement when the local forcing, as the microclimate, will be included as predictors in addition with the precipitation simulated by the CMIP5 models.

Funding

This work received financial support from the "Coordenação de Aperfeiçoamento de Pessoal de Nível Superior – CAPES" during the post-doctoral research at Post-Graduate Program in Climate Science PPGCC-UFRN/Brazil.

Acknowledgments

We thank the two anonymous reviewers that provided relevant suggestions to improve the quality of the manuscript and the "Coordenação de Aperfeiçoamento de Pessoal de Nível Superior–CAPES" for providing the financial support. We are also thankful to researchers Brant Liebmann and Dave Allured for providing the observational South America 24 gridded precipitation dataset, the Program for Climate Model Diagnosis and Intercomparison (PCMDI) and the Working Group on Coupled Modelling (WGCM) for availability of the CMIP5 model dataset and the International Research Institute for Climate and Society for providing the IRI/LDEO Climate Data Library.

References

Biasutti, M., Battisti, D. S., and Sarachik, E. S. (2003). The Annual Cycle over the Tropical Atlantic, South America, and Africa. *J. Climate* 16, 2491–2508. doi: 10.1175/1520-0442(2003)016<2491:TACOTT>2.0.CO;2

Boulanger, J. P., Martinez, F., and Segura, E. C. (2007). Projection of future climate change conditions using IPCC simulations, neural networks and Bayesian statistics. Part 2: precipitation mean state and seasonal cycle in South America. *Clim. Dyn.* 28, 255–271. doi: 10.1007/s00382-006-0182-0

Cardoso, A. O., and da Silva Dias, P. L. (2004). Variabilidade da TSM do Atlântico e Pacífico e temperatura na cidade de São Paulo no inverno. *Braz. J. Meteorol.* 19, 113–122 (Available in Portuguese). Available online at: http://www.rbmet.org.br/port/revista/revista_dl.php?id_artigo=78&id_arquivo=75

Ceppi, P., Hwang, Y. T., Liu, X., Frierson, D. M., and Hartmann, D. L. (2013). The relationship between the ITCZ and the Southern Hemispheric eddy-driven jet. *J. Geophys. Res. Atmos.* 118, 5136–5146. doi: 10.1002/jgrd.50461

da Silva, G. A. M., Drumond, A., and Ambrizzi, T. (2011). The impact of El Niño on South American summer climate during different phases of the Pacific Decadal Oscillation. *Theor. Appl. Climatol.* 106, 307–319. doi: 10.1007/s00704-011-0427-7

Gardner, M. W., and Dorling, S. R. (1998). Artificial neural networks (the multilayer perceptron)-a review of applications in the atmospheric sciences. *Atmos. Environ.* 32, 2627–2636. doi: 10.1016/S1352-2310(97)00447-0

Grodsky, S. A., and Carton, J. A. (2003). Intertropical Convergence Zone in the South Atlantic and the equatorial cold tongue. *J. Climate* 16, 723–733. doi: 10.1175/1520-0442(2003)016<0723:TICZIT>2.0.CO;2

Hastenrath, S., Wu, M. C., and Chu, P. S. (1984). Towards the monitoring and prediction of Northeast Brazil droughts. *Q. J. Roy. Meteorol. Soc.* 110, 411–425. doi: 10.1002/qj.49711046407

Janowiak, J. E., and Xie, P. (1999). CAMS_OPI: A Global Satellite-Rain gauge merged product for real-time precipitation monitoring applications. *J. Climate.* 12, 3335–3342.

Johnson, B., Kumar, V., and Krishnamurti, T. N. (2012). Rainfall anomaly prediction using statistical downscaling in a multimodel superensemble over tropical South America. *Clim. Dyn.* 43, 1731–1752. Available online at: http://diginole.lib.fsu.edu/cgi/viewcontent.cgi?article=6524&context=etd

Kayano, M. T., and Andreoli, R. V. (2004). Decadal variability of northern northeast Brazil rainfall and its relation to tropical sea surface temperature and global sea level pressure anomalies. *J. Geophys. Res. (1978–2012).* 109. doi: 10.1029/2004JC002429

Liebmann, B., and Allured, D. (2005). Daily Precipitation Grids for South America. *Bull. Am. Meteorol. Soc.* 86, 1567–1570. doi: 10.1175/BAMS-86-11-1567

Mendes, D., and Marengo, J. A. (2010). Temporal downscaling: a comparison between artificial neural network and autocorrelation techniques over the Amazon Basin in present and future climate change scenarios. *Theor. Appl. Climatol.* 100, 413–421. doi: 10.1007/s00704-009-0193-y

Mendes, D., Marengo, J. A., Rodrigues, S., and Oliveira, M. (2014). Downscaling statistical model techniques for climate change analysis applied to the Amazon region. *Adv. Artif. Neural Syst.* 2014:595462. doi: 10.1155/2014/595462

Misra, V. (2004). A Diagnosis of Skill in an AGCM over Northeast Brazil. *Cent. Ocean-Land Atmos. Stud.* 171. Available online at: ftp://grads.iges.org/pub/ctr/ctr_171.pdf

Moss, R. H., Edmonds, J. A., Hibbard, K. A., Manning, M. R., Rose, S. K., Vuuren, D. P., et al. (2010). The next generation of scenarios for climate change research and assessment. *Nature* 463, 747–756. doi: 10.1038/nature08823

Ramírez, M. C., Ferreira, N. J., and Velho, H. F. C. (2006). Linear and nonlinear statistical downscaling for rainfall forecasting over southeastern Brazil. *Weather Forecast.* 21, 969–989. doi: 10.1175/WAF981.1

Riahi, K., Gruebler, A., and Nakicenovic, N. (2007). Scenarios of long-term socio-economic and environmental development under climate stabilization. *Technol. Forecast. Soc. Change* 74, 887–935. doi: 10.1016/j.techfore.2006.05.026

Riahi, K., Shilpa, R., Volker, K., Cheolhung, C., Vadim, C., Guenther, F., et al. (2011). RCP 8.5— A scenario of comparatively high greenhouse gas emissions. *Clim. Change* 109, 33–57. doi: 10.1007/s10584-011-0149-y

Richter, I., Xie, S. P., Behera, S. K., Doi, T., and Masumoto, Y. (2014). Equatorial Atlantic variability and its relation to mean state biases in CMIP5. *Clim. Dyn.* 42, 171–188. doi: 10.1007/s00382-012-1624-5

Rodrigues, R. R., Haarsma, R. J., Campos, E. J. D., and Ambrizzi, T. (2011). The impacts of inter-El Niño variability on the tropical Atlantic and Northeast Brazil climate. *J. Clim.* 24, 3402–3422. doi: 10.1175/2011JCLI3983.1

Sajikumar, N., and Thandaveswara, B. S. (1999). A non-linear rainfall-runoff model using artificial neural network. *J. Hydrol.* 216, 32–55. doi: 10.1016/S0022-1694(98)00273-X

Silva, G. A., Dutra, L. M., da Rocha, R. P., Ambrizzi, T., and Leiva, É. (2014). Preliminary analysis on the global features of the NCEP CFSv2 seasonal hindcasts. *Adv. Meteorol.* 2014:695067. doi: 10.1155/2014/695067

Silva, G. A. M., and Mendes, D. (2013). Comparison results for the CFSv2 hindcasts and statistical downscaling over the northeast of Brazil. *Adv. Geosci.* 35, 79–88. doi: 10.5194/adgeo-35-79-2013

Siongco, A. C., Hohenegger, C., and Stevens, B. (2014). The Atlantic ITCZ bias in CMIP5 models. *Clim. Dyn.* 1–12. doi: 10.1007/s00382-014-2366-3

Smith, T. M., Reynolds, R. W., Peterson, C. T., and Lawrimore, J. (2008). Improvements to NOAA's Historical Merged Land-Ocean Surface Temperature Analysis (1880-2006). *J. Clim.* 21, 2283–2296. doi: 10.1175/2007JCLI2100.1

Taschetto, A. S., and Ambrizzi, T. (2012). Can Indian Ocean SST anomalies influence South American rainfall?. *Clim. Dyn.* 38, 1615–1628. doi: 10.1007/s00382-011-1165-3

Trigo, R. M., and Palutikof, J. P. (2001). Precipitation scenarios over Iberia: a comparison between direct GCM output and different downscaling techniques. *J. Clim.* 14, 4422–4446. doi: 10.1175/1520-0442(2001)014<4422:PSOIAC>2.0.CO;2

Xie, S. P., and Carton, J. A. (2004). Tropical Atlantic variability: Patterns, mechanisms, and impacts. *Earth Clim.* 121–142. doi: 10.1029/147GM07

Conflict of Interest Statement: The authors declare that the research was conducted in the absence of any commercial or financial relationships that could be construed as a potential conflict of interest.

frontiers in Environmental Science

ORIGINAL RESEARCH
published: 23 April 2015
doi: 10.3389/fenvs.2015.00023

An objective criterion for determining the South Atlantic Convergence Zone

Tércio Ambrizzi[1]* **and Simone E. T. Ferraz**[2]

[1] *Department of Atmospheric Sciences, University of São Paulo, São Paulo, Brazil,* [2] *Department of Physics, Federal University of Santa Maria, Rio Grande do Sul, Brazil*

The South Atlantic Convergence Zone (SACZ) is the dominant summertime cloudiness feature of subtropical South America and the western South Atlantic Ocean, having a significant influence on the precipitation regime of southeastern Brazil. This paper proposes an objective criterion based mainly on precipitation, as this variable is easily obtained on general circulation models simulating past, present and future climate. Usually most SACZ studies use emerging long wave radiation as a precipitation proxy. This is enough to describe event position at first, but using precipitation would allow for better quantification, especially for climate studies, where precipitation is indispensable. An assessment was carried out to find out if classical DJF period is ideal for determining the SACZ for the present climate and future scenarios. In general the SACZ event detection criterion showed quite satisfactory results when event dates were previously known. When it was applied to future climate scenario it identified a number of events compatible with the present climate. The SACZ was well defined for both the simulated and observed precipitation data.

Keywords: SACZ, objective criterion, precipitation

Edited by:
Anita Drumond,
University of Vigo, Spain

Reviewed by:
Mario Francisco Leal De Quadro,
Federal Institute of Santa Catarina, Brazil
Michel Nobre Muza,
Federal Institute of Santa Catarina, Brazil

***Correspondence:**
Tércio Ambrizzi,
Department of Atmospheric Sciences, University of São Paulo, Rua do Matão 1226, 05508-090, São Paulo, Brazil
ambrizzi@model.iag.usp.br

Specialty section:
This article was submitted to Atmospheric Science, a section of the journal Frontiers in Environmental Science

Received: *24 November 2014*
Accepted: *10 March 2015*
Published: *23 April 2015*

Citation:
Ambrizzi T and Ferraz SET (2015) An objective criterion for determining the South Atlantic Convergence Zone. Front. Environ. Sci. 3:23. doi: 10.3389/fenvs.2015.00023

Introduction

The South Atlantic Convergence Zone (SACZ) is the dominant summertime cloudiness feature of subtropical South America and the western South Atlantic Ocean. It is readily seen on maps of climatological summertime Outgoing Longwave Radiation (OLR) depicting high clouds and, due its high persistence, the SACZ exerts a significant influence on the precipitation regime of southeastern Brazil.

It was in the early 70's that the first studies about a convective persistent band over South America started to appear in the literature. Taljaard (1972) was probably the first to associate a cloud band over the eastern coast of South America and the convection over Amazonia. Streten (1973) and Krishinamurti et al. (1973) showed the importance of a quasi stationary wave associated with a persistent cloudiness in the SACZ region and the transport of momentum, heat and moisture from the tropics into higher latitudes. With the advent of satellite, Yassunary (1977) using averaged satellite images was one of the first works to emphasize the presence of three areas of persistent summer cloudiness in the Southern Hemisphere (SH), presently known as the Southern Pacific Convergence Zone (SPCZ), SACZ, and the Southern Indian Convergence Zone (SICZ).

Kodama (1992, 1993) noted an approximate 10-day half-period of convection in the convergence zones which may be associated with intraseasonal oscillations. For South America in particular, the results of Kodama suggest that the mean position of the SACZ may somehow be attributable to the deep convection of the Amazon Basin. Figueroa et al. (1995) were able to reproduce low-level convergence in the vicinity of the SACZ in an Eta-coordinate model using a heat source intended to mimic deep Amazonian convection, provided they used a realistic orography and background wind field. They also determined that a successful simulation was dependent on a heat source that varied diurnally. They found the SACZ to form 12–18 h after a peak in Amazon convection, suggesting that short-term variations in the cloud band may be influenced by deep convection in the Amazon. On the other hand, Lenters and Cook (1995) found a realistic SACZ in a general circulation model (GCM) that did not include diurnal variability. They also pointed out the importance of transient moisture flux from the Amazon, though it seems that the extratropical cyclones and fronts have an important role in maintaining the model SACZ.

General Characteristics and Determination of the ZCAS

Normally, the SACZ is a cloud band that appears to either emanate from or merge with the intense convection of the Amazon Basin, extending from tropical South America southeastward into the South Atlantic Ocean, in a NW-SE orientation that remains quasi stationary for several days. The definition of a SACZ event is based not only on satellite images but also on dynamic criteria. Quadro (1994) and Sanches and Silva Dias (1996) defined a SACZ event when the following minimum criteria were observed for at least 4 days:

- 850 hPa moisture convergence
- 500 hPa trough to the west of surface convergence
- Southerly winds to the south of the surface convergence zone
- persistent cloudiness in the satellite imagery

Some climatological characteristics of the SACZ include confluence in low levels well defined extending from central Brazil to the South Atlantic with southerlies and dry air to the south and northerlies in general and moist air to the north. The northerly sector actually may be divided in two different air masses separated by a north south confluence line: northwesterly from the Amazon Basin, very moist and northeasterly from the trade wind areas of the tropical Atlantic to the east. In upper levels the main feature is the Bolivian High to the west, mostly associated with the Amazon convective heat source. The Bolivian High extends to the southeast in accordance with the SACZ orientation. The upper level flow includes a trough off the coast of northeast Brazil, which occasionally closes into a cut off low (Figueroa et al., 1995; Carvalho et al., 2004).

A summary of the yearly occurrence in the summer season (December, January and February) from 1980/81 up to 1999/2000 obtained from Ferreira et al. (2004) may be seen in their Table 1. The duration and the number of SACZ occurrences are quite variable. It is interesting to observe that even during El Niño/Southern Oscillation (ENSO) years there is not any significant variability, though it seems that in El Niño years the frequency of occurrence is less variable than in La Niña (Quadro, 1994; Ferreira et al., 2004).

The relationship between SACZ intensity, position and underlying sea surface temperature (SST) anomalies has been discussed in many studies (e.g., Lenters and Cook, 1999; Robertson and Mechoso, 2000; Barreiro et al., 2002; Carvalho et al., 2004). However, the relationship between mean rainfall associated with SACZ activity and extreme events is not obvious (Liebmann et al., 2001). As discussed by Liebmann et al. (2001) while an intense SACZ may spawn extreme events, it may be short-lived. It seems that long lasting SACZ activity, while not intense enough to produce extreme events, may result in as much rainfall as the intense SACZ, by spread over time. They speculated that extreme precipitation events are related to intense squall lines. More recently, Siqueira and Machado (2004) and Siqueira et al. (2005) using satellite composites provided by the International Satellite Cloud Climatology Project (ISCCP) images and circulation fields from the National Centers for Environmental Prediction (NCEP) reanalysis described three different types of frontal system—tropical convection interaction.

From a global point of view the SACZ is part of a teleconnecting pattern that encompasses the whole SH with a few connecting paths to the Northern Hemisphere. The connection between the SPCZ and the SACZ was first suggested by Casarin and Kousky (1986) through observational data analysis. Later on, numerical simulations using simple barotropic (Ambrizzi et al., 1994; Grimm and Silva Dias, 1995) and baroclinic models (Ambrizzi and Hoskins, 1997) have confirmed the possibility of such relationship. Variations of the SACZ also seem to be linked to the Madden-Julian oscillation (MJO; Madden and Julian, 1994). Several studies have indicated that the SACZ varies as part of a dipole, with an enhanced SACZ being associated with anomalously high OLR (implying low rainfall) centered over Uruguay and extending into Argentina. This dipole, whose centers are elongated from northwest to southeast suggests forcing by a Rossby wave train propagating toward the equator (e.g., Kiladis and Weickmann, 1992, 1997), with negative OLR anomalies occurring in the region of expected uplift ahead of an upper-level trough and positive OLR anomalies in the subsidence region ahead of an upper ridge. This is one of the components of the Pacific-South American teleconnection pattern (PSA, Mo and Ghil, 1987; Kidson, 1988; Farrara et al., 1989). It has been suggested that this teleconnection pattern impacts the SACZ which results in a regional seesaw pattern of alternating dry and wet conditions (Paegle and Mo, 1997; Paegle et al., 2000, and others). Also, at higher frequencies, Kiladis and Weickmann (1992, 1997) and Liebmann et al. (1999) found evidence that SACZ variations are forced by wave activity originating in the extratropics on sub monthly (6–30 day) timescales.

To elucidate the relationship between SACZ and precipitation events, this paper will propose an objective criterion based mainly on precipitation, as this variable is easily obtained on general circulation models simulating past, present and future climate. Besides, most SACZ studies use emerging long wave radiation as a precipitation proxy. This is enough to describe event position at first, but using precipitation would allow for better quantification, especially for climate studies, where precipitation is indispensable. In addition, an assessment will be carried out to find out if classical DJF period is ideal for determining the SACZ for the present climate and future scenarios.

Materials and Methods

This study will use daily precipitation data available on a regular 1 × 1° grid over the area that encompasses the Brazilian Southeast. The timeframe ranges from 1989 to 2005. The gridded fields were constructed from about 7900 stations within 10,168 station data files. Most station records are shorter than the full 65-year period, with some missing observations within the available record. A given grid incorporates all station observations available for that day. With a sufficient density of stations, an occasional missing value will not substantially affect the gridpoint average (Liebmann and Allured, 2005). Henceforth, this dataset will be referred to as **LIB.**

Dynamic downscaling of HadGEM2-ES (Hadley Centre Global Environment Model version 2 – Earth System) data for two time periods:

1. Present Time: HadGEM2-ES—reference simulation from 1989 to 2005, henceforth, will be referred to as **PRE**.
2. Future Time: RCP4.5 Scenario simulation from 2079 to 2095, henceforth, will be referred to as **FUT.**

The dynamic downscaling of HadGEM-ES data was done using the regional model RegCM version 4 (Giorgi et al., 1993). **Figure 2** shows the topography of the RegCM. To avoid errors in the interface between the large scale and the region under consideration, we decided to use an area bigger than necessary. Dates when SACZ events happened from 1995 to 2005 were first selected through reference to the monthly climate report published by the Brazilian Center for Weather and Climate Prediction (Centro de Previsão de Tempo e Clima - http://www.cptec.inpe.br/). This showed that 48 SACZ events occurred in the referred timeframe and were distributed according to **Figure 1**. If the event started in a month and ended in another, it was considered the number of days in each month to determine what month he belonged. For example, 2 days at the end of January and 4 days in early February, the event will be accounted in February.

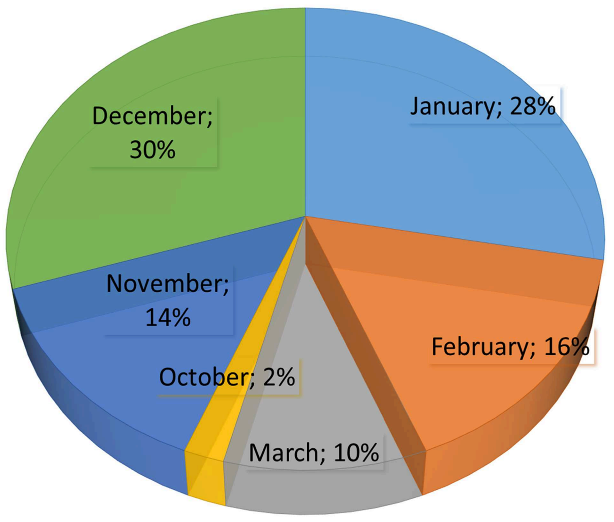

FIGURE 1 | SACZ event percentage from November to March.

SACZ studies usually cover the time period from December to February due to the increased number of events (for example Liebmann et al., 1999). As shown in **Figure 1** within the 10 years covered by this study, a higher number of events indeed occurred from December to February, but the number of SACZ events in November and March is significant, with a few occurrences in October as well. Therefore, the present study will consider the entire period from October to March to define the SACZ presence.

The study area (**Figure 2**) was based on the SACZ coastal influence region shown in Carvalho et al. (2002) (see their **Figure 3**). The choice of this region was due to its relation to summer rainfall during SACZ events and the availability of datasets with few series failures.

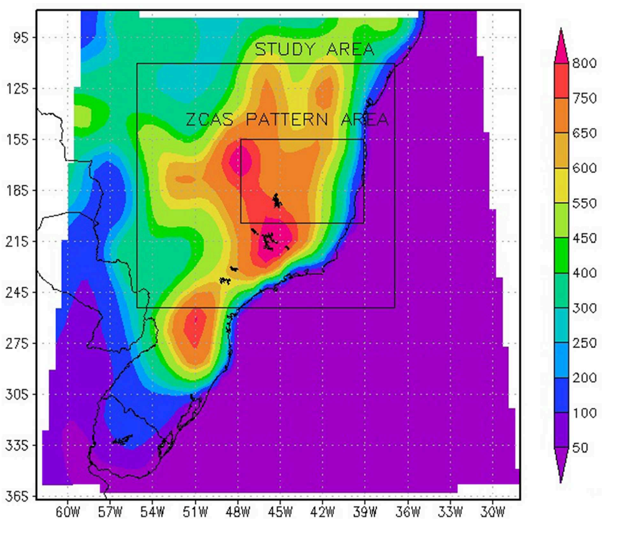

FIGURE 2 | Total region used with its regional topography. The two squares inside in the total region represent the study area and the main position of the SACZ pattern.

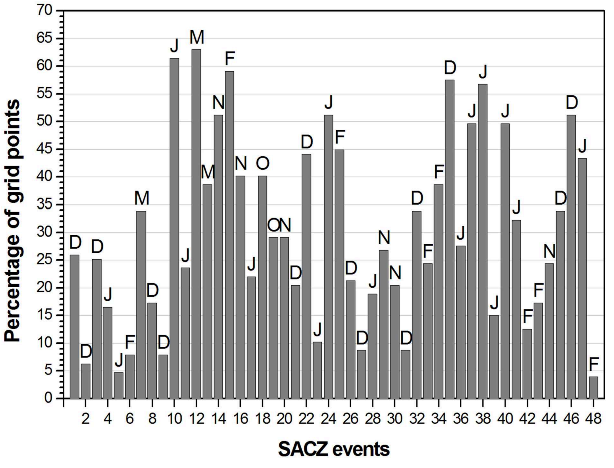

FIGURE 3 | Percentage of grid points where SACZ events happened when considered the period from October to March.

The monthly climatology of each grid point of the study area was calculated taking into account a 30-year average. A SACZ-related precipitation extreme event was defined as the set of 7 consecutive days with at least 1 day of 35% climatology precipitation or higher, and the sum of the precipitation in the two previous and two posterior days should be equivalent to, at least, 20% of the climatology. Also, the sum of the precipitation in the three previous and three posterior days should amount to 10% of the monthly climatology, and no values should be null.

The previously selected SACZ event dates were then confronted with the dates determined by the aforementioned criterion. Events that deviated up to 2 days of the original date were considered as coincident events. The 2-day gap was included because of future climate data, which in general a month have 30 days. This calendar does not contribute to exactly locate the correct date of the SACZ event.

The above analysis is suitable for real precipitation data, as shown in **Figures 3**, **4**. However, as numerical models do not always represent well the intra-seasonal variability, and as a consequence, systems such as SACZ (Ferraz et al., 2013), principal component analysis (PCA) was used in order to determine the mode more similar to SACZ and then the selection criterion was redefined based in the data rebuilt from the PCA series.

The new selection criterion consists of:

(1) Determining the mode maximum area and calculating an average for the period,
(2) Rebuilding the PCA series with this average,
(3) Selecting time periods when all of the following conditions are true:
    (a) $day(i) > 6\%CLIM$;
    (b) $\sum_{i=i-1}^{i+1} day(i) > 10\%CLIM$
    (c) $\sum_{i=i-2}^{i+2} day(i) > 12\%CLIM$
    (d) $\sum_{i=i-3}^{i+3} day(i) > 20\%CLIM$

The previously selected SACZ event dates were then confronted with the dates determined by the aforementioned criterion, in order to calibrate it and allow for its application to future data. This condition should be repeated for at least consecutive 3 days to be considered an event.

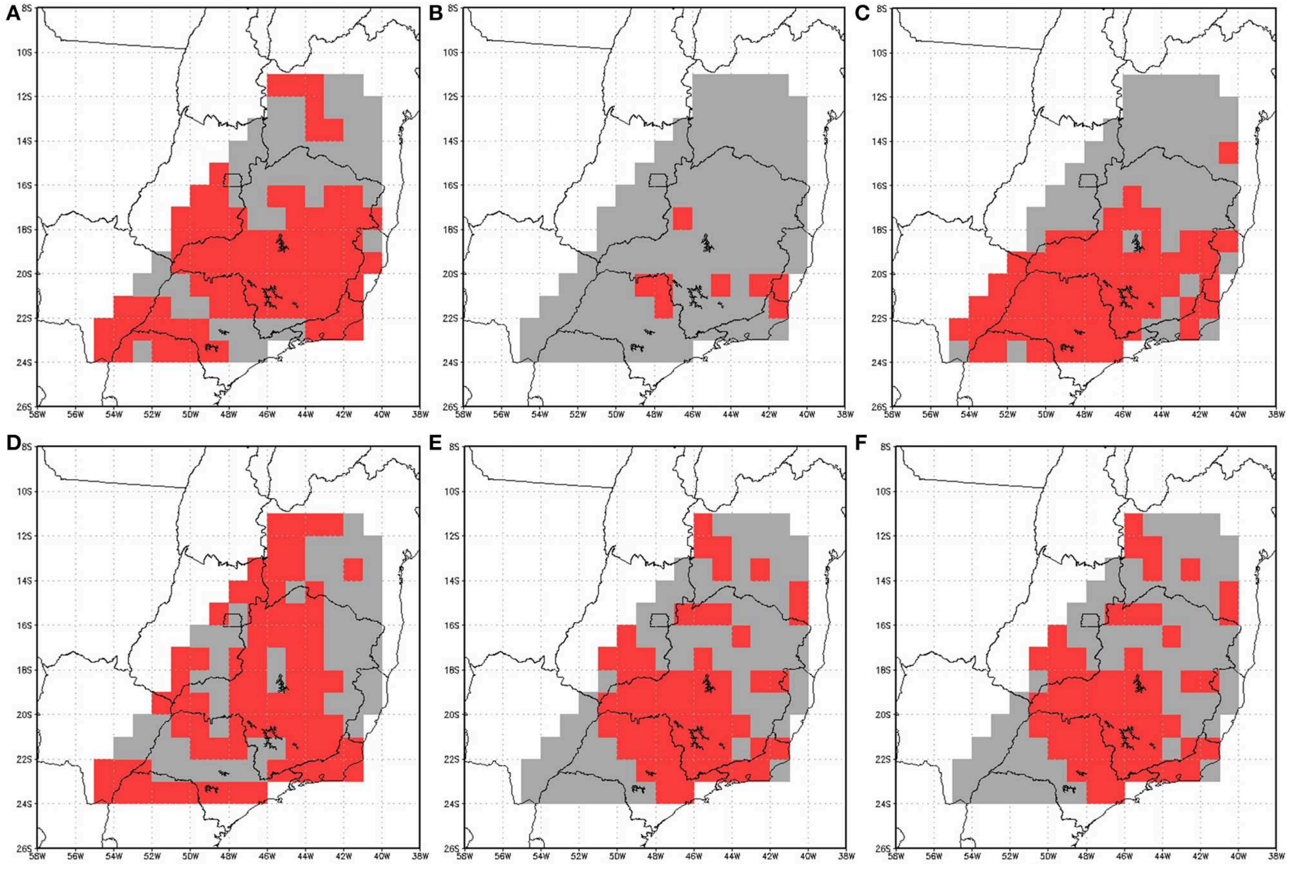

FIGURE 4 | Spatial distribution of events with increased date coincidence between the SACZ and a criterion-selected extreme. The light gray color represents the entire study area and the dark gray color shows the coincidence area. **(A)** Event 10 – January, **(B)** Event 12 – March, **(C)** Event 14 – November, **(D)** Event 15 – February, **(E)** Event 22, December and **(F)** Event 24, January.

Results

Figure 3 shows the event percentage per grid point, that is, on how many points in the study area grid each of the 48 events is shown. The letters above each bar represent the beginning of the month when the event happened. From this **Figure 1** can see that higher event frequency on a larger number of grid points (above 45%) occurred alternately in December and January, with fewer occurrences in February (2), March (1) and November (1).

As shown in **Figure 4**, the spatial distribution of increased coincidence grid points is set across clearly defined areas. From December to February there is an increased concentration on the states of Minas Gerais and Bahia (to the north of the Brazilian Southeastern Region), which reflects the results presented in Carvalho et al. (2002). In November, this distribution is more concentrated to the south, over São Paulo (event 14 – south of the Brazilian Southeastern Region) and in March it moves to the north, and covers part of Minas Gerais and Bahia (event 12), which suggests that the SACZ migrates from South to North throughout the summer. This variation may be related to event intensity or to the frequency period of the intra-seasonal oscillation that triggered the SACZ event. Ferraz (2004) showed differences in the oscillation periods for both areas. The southernmost area (which includes São Paulo) features

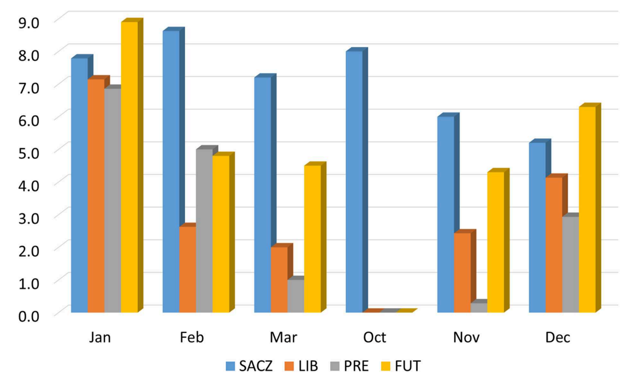

FIGURE 6 | Average duration of actual SACZ events (blue bar) detected by the criterion in the LIB (orange) and PRE series (gray), and events detected in the FUT series (yellow).

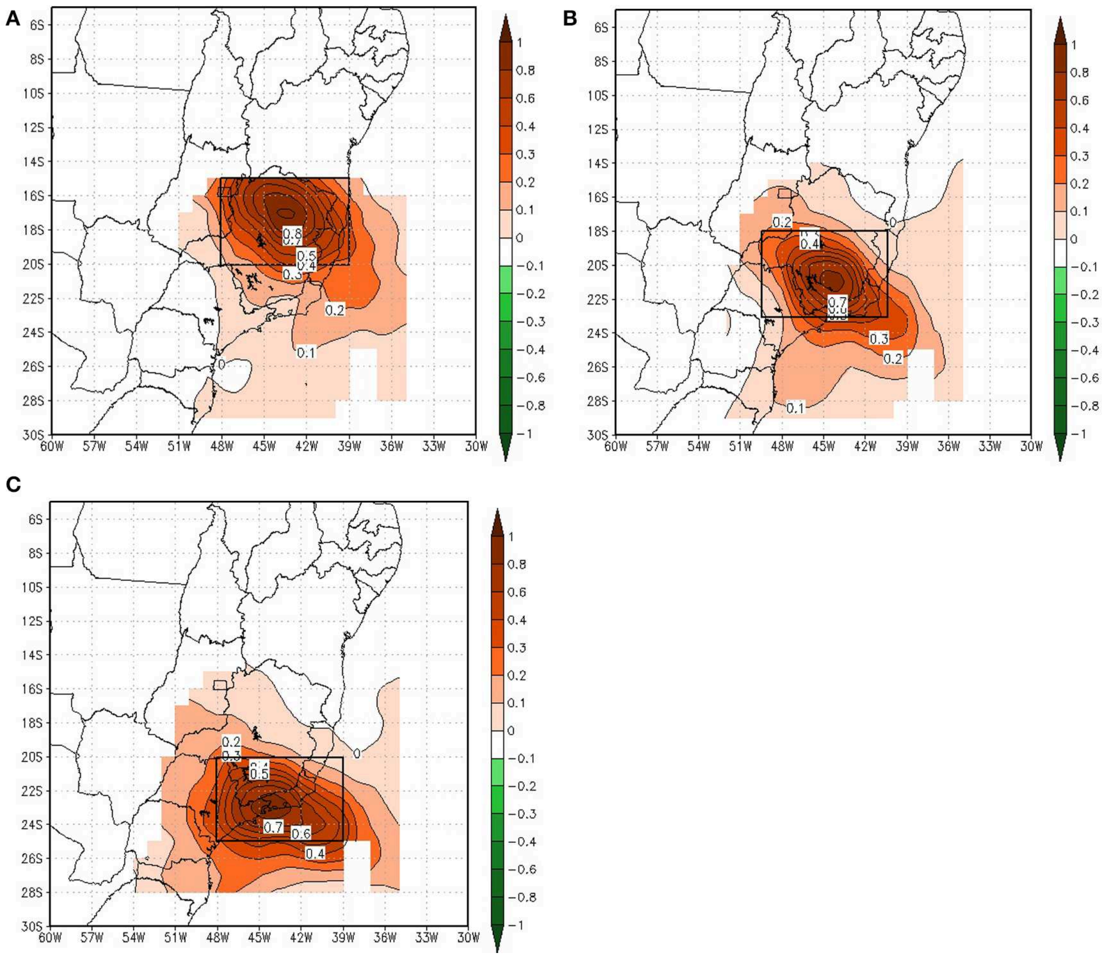

FIGURE 5 | SACZ-related variability methods using actual precipitation data (A - top left), present (B - top right) and future time RCP4.5 (C - bottom left).

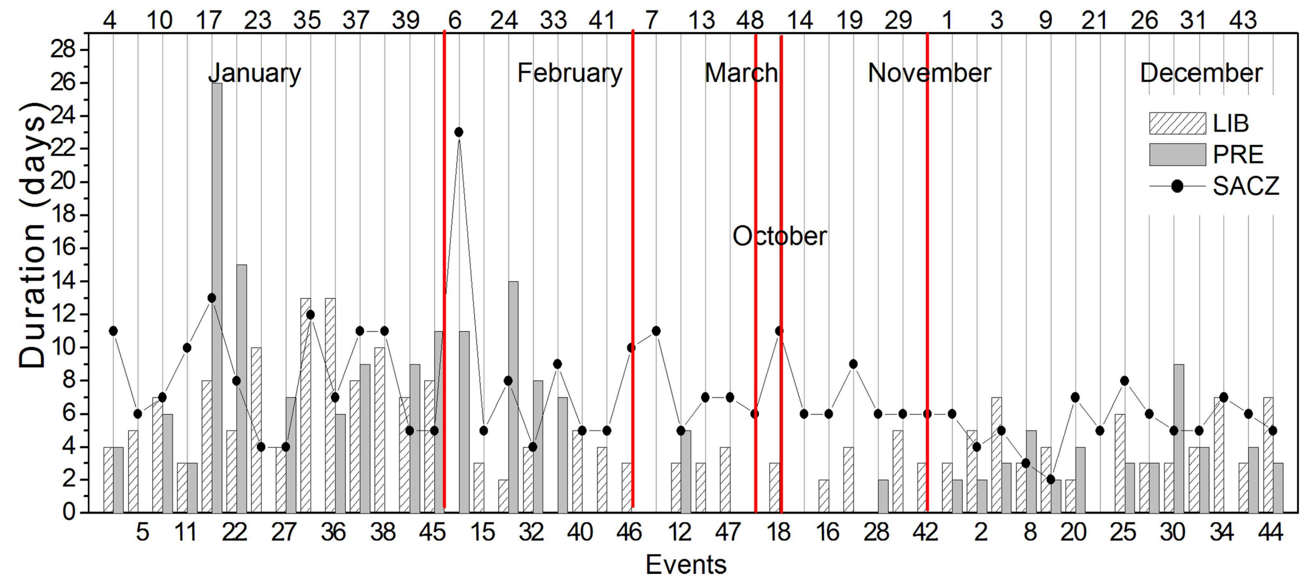

FIGURE 7 | Duration (in days) of each SACZ event: actual (line), and detected by the criterion for the LIB (hatched bar) and PRE (gray bar) series.

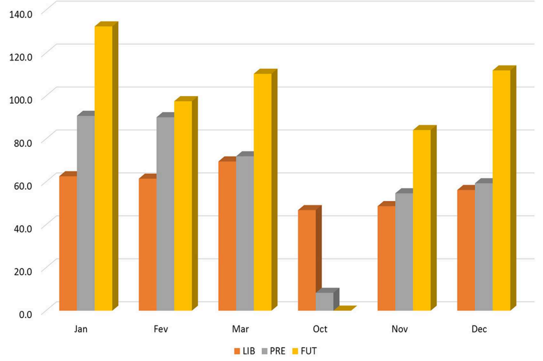

FIGURE 8 | Average precipitation in the method area, weighed by the number of events, during the 48 SACZ episodes for the LIB (orange) and PRE (green) series, and during the 73 episodes detected in the FUT series (violet).

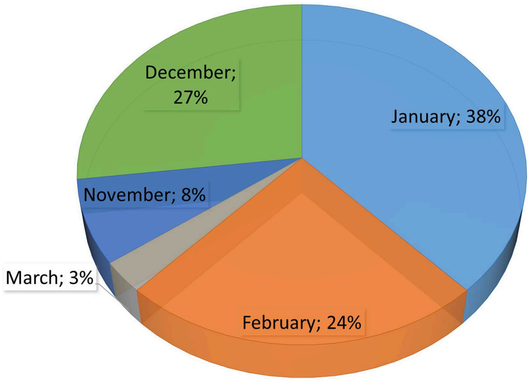

FIGURE 9 | SACZ event percentage from November to March for future time.

more frequent oscillation (10/20 days), whereas oscillation frequency is around 30/60 days further north. A thorough analysis of these events is required for a more comprehensive explanation.

A variability method with SACZ-attributable characteristics was found through principal component analysis. **Figure 5** shows the precipitation method for real data, and for present time and future climate scenarios (RCP4.5 Representative Concentration Pathways Emissions from the IPCC Fifth Assessment Report - **IPCC** AR5 WG1). The ZCAS position presented here agrees with that found by Lenters and Cook (1999) in their REOF 3 pattern.

The SACZ determination criterion was applied after the maximum precipitation area (marked by a rectangle on **Figure 5**) had been established. Variability methods were calculated using the 17 years period in each series, but the method was only calibrated with data from the known events timeframe (1995–2005).

Sixty extreme events were selected for the **LIB** series, and 40 of those are coincident with an actual SACZ event. Forty-five events were selected for the **PRE** series where 29 of those coincide with a SACZ event. This result indicates that the criterion was accurate for 83% the SACZ cases for the **LIB** series, but it overestimated the number of extreme events by 25%. For the PRE series, there was 61% accuracy, but the number of events was underestimated by 9%.

Figure 6 shows the average event duration for each month, where the SACZ column represents actual events found in the literature. For present time data, it can be seen that events last 7 days on average, and they last longer from January to March and in October, and shorter in November and December. For future time data (**FUT**), the average number of days is bigger in January (up to 9 days), followed by December (approximately 6 days). However, assessments of individual cases reveal very long events

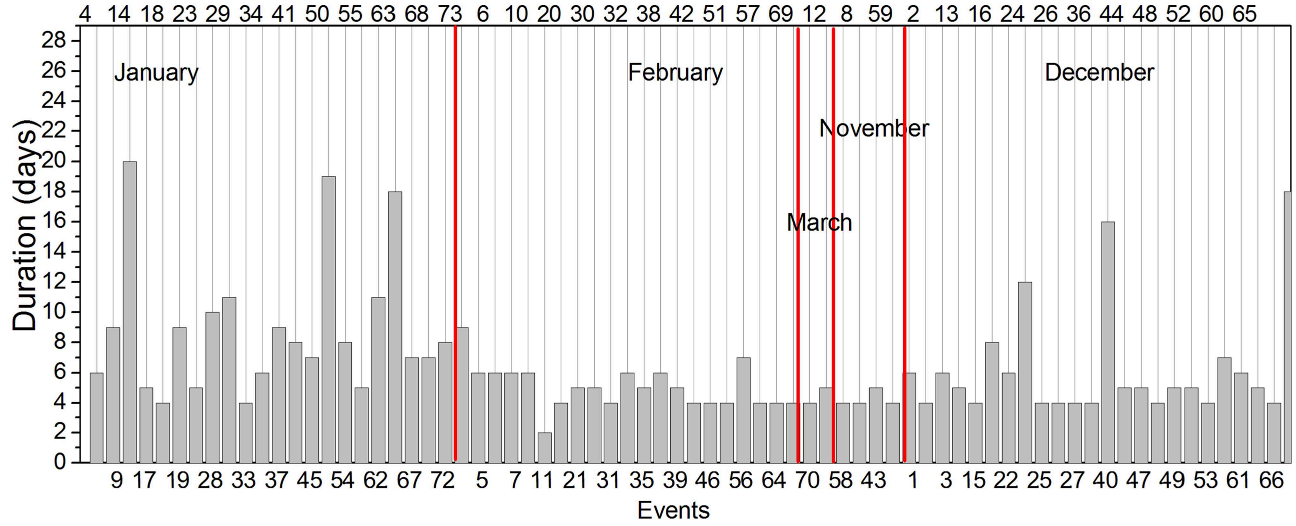

FIGURE 10 | Duration (in days) of every SACZ event simulated for the FUT series.

(lasting up to 25 days) that are generally overestimated by the PRE series, but overall both the **LIB** and the **PRE** series underestimate event duration (**Figure 7**). Several studies have shown that HADGEM-ES data underestimate the actual precipitation (Vogel, 2012; Zhang et al., 2013; Dike et al., 2014), in particularly over the SACZ, Cavalcanti and Shimizu (2012) showed a decrease in precipitation in this region in present time. The LIB gridded fields are made by averaging all available stations within a specified radius of each grid point. The radius was chosen to be 0.75 times the grid spacing, so as to ensure that every station was included in at least one grid point. In grid points with high station density benefit from spatial smoothing by blending numerous individual observations. In regions of low station density, however, there are many gridpoint values based on a single station report or a very small number of stations (Liebmann and Allured, 2005). In this way, Liebmann and Allured (2005) explain that extreme events (heavy storms) localized in areas smaller than the grid spacing will be considerably weaked by averaging with other stations. Such aspects may explain the decrease in intensity of events presented in **Figure 6**, in relation to real events.

When average precipitation in the maximum precipitation areas is compared for the 48 events (regardless how they were detected), it is clear that **PRE** data overestimates precipitation in the area (**LIB**), which may explain the increased number of events detected by the criterion in this data series (**Figure 8**). As for future climate scenario data (**FUT**), the increase is even more significant in every month. Cavalcanti and Shimizu (2012) showed an increase in precipitation in the SACZ region in the future data during Austral summer.

When applied to the 17 years of data available for the FUT series, the criterion revealed 73 events distributed according to **Figure 9**. Event distribution was similar to the present climate, with more events from December to February, whereas for the other months the number of events was slightly lower for the future climate. Looking at the event duration one can see a few long events in January and December; they are, however, shorter than the ones found in present climate (**Figure 10**).

Discussion

The SACZ event detection criterion proposed here showed quite satisfactory results when event dates were compared with previously known ones. When it was applied to future climate it identified a number of events compatible with the studied timeframe. The SACZ was well defined for both the simulated and observed precipitation data.

Considering the 60 months of data reviewed, 48 SACZ events were found (0.8 event/month); for future climate, there were 96 months of data and 73 events were found (0.76 events/month). This might suggest a slight reduction in the number of future events, however, there are a few points to consider: when this number is compared with the model simulation, 45 events were found, where 65% coincides with events that happened and 35% are coincident with method-detected events that did not happen. This means that, from the 73 events, only 49 would actually happen, which could suggest a significant reduction in the number of the events in the future when compared to the present time. On the other hand, even with the chance of a reduction in the number of events, this would not be directly related to precipitation numbers, as the accumulated average for event months reveals an increase of 55% in precipitation for future climate, which suggests fewer, but more intense events.

Despite being able to determine the characteristics of most of the SACZ events analyzed, the index presented in this study overestimated the number of events. It should be emphasized that we are proposing an objective criterion based only on precipitation, because this variable is easily obtained from general circulation models that simulates past, present and future climate, contrary to OLR and some other variables used nowadays. Of course, this is a first step to identify the SACZ through a simple objective analysis. Further work is still necessary to improve this method and it will be presented elsewhere.

Acknowledgments

The authors would like to acknowledge FAPESP (n° 08/58101-9) and CNPq for the financial support.

References

Ambrizzi, T., and Hoskins, B. J. (1997). Stationary Rossby wave propagation in a baroclinic atmosphere. *Q. J. Roy. Meteorol. Soc*. 123, 919–928. doi: 10.1002/qj.49712354007

Ambrizzi, T., Silva Dias, P. L., and Grimm, A. M. (1994). "A comparison between barotropic and baroclinic remote responses associated with the SPCZ and SACZ," in *II Congresso Latino-Americano e Ibérico de Meteorologia e VIII Congresso Brasileiro de Meteorologia, 1994, Belo Horizonte, MG. Anais do II Congresso Latino-Americano e Ibérico de Meteorologia e VIII Congresso Brasileiro de Meteorologia,* Vol. 2 (Belo Horizonte: Sociedade Brasileira de Meteorologia), 85–87.

Barreiro, M., Chang, P., and Saravanan, R. (2002). Variability of the South Atlantic Convergence Zone simulated by an atmospheric general circulation model. *J. Clim.* 15, 745–763. doi: 10.1029/2003GL018647

Carvalho, L. M. V., Jones, C., and Liebmann, B. (2002). Extreme precipitation events in Southeastern South America and large-scale convective patterns in the South Atlantic Convergence Zone. *J. Clim.* 15, 2377–2394. doi: 10.1175/1520-0442(2002)015<2377:EPEISS>2.0.CO;2

Carvalho, L. M. V., Jones, C., and Liebmann, B. (2004). The South Atlantic Convergence Zone: persistence, intensity, form, extreme precipitation and relationships with intraseasonal activity. *Clim. J.* 17, 88–108. doi: 10.1175/1520-0442(2004)017<0088:TSACZI>2.0.CO;2

Casarin, D. P., and Kousky, V. E. (1986). Anomalias de precipitacão no sul do Brasil e variaçõs na circulaçoes atmosférica. *Rev. Bras. Meteorol.* 1, 83–90. doi: 10.1175/1520-0442(2004)017<0088:TSACZI>2.0.CO;2

Cavalcanti, I. F. A., and Shimizu, M. H. (2012). Climate fields over South America and variability of SACZ and PSA in HadGEM2-ES. *Am. J. Clim. Change* 1, 132–144. doi: 10.4236/ajcc.2012.13011

Dike, V. N., Shimizu, M. H., Diallo, M., Lin, Z., Nwofor, O. K., and Chineke, T. C. (2014). Modelling present and future African climate using CMIP5 scenarios in HadGEM2−ES. *Int. J. Climatol.* doi: 10.1002/joc.4084. [Epub ahead of print].

Farrara, J. D., Ghil, M., Mechoso, C. R., and Mo, K. C. (1989). Empirical orthogonal functions and multiple flow regimes in the Southern Hemisphere winter. *J. Atmos. Sci*. 46, 3219–3223.

Ferraz, S. E. T. (2004). *Oscilações Intrasazonais no Sul e Sudeste do Brasil Durante o Verão*. Tese (Doutorado) - Instituto de Astronomia, Geofísica e Ciências Atmosféricas da Universidade de São Paulo, São Paulo.

Ferraz, S. E. T., Souto, R. P., Dias, P. L. S., Velho, H. F. C., and Ruivo, H. M. (2013). Analysis for precipitation climate prediction on south of Brazil. *Ciência e Natura* 496–500. doi: 10.5902/2179-460X12253

Ferreira, N. J., Sanches, M., Silva Dias, M. A. F. (2004). Composição da zona de convergência do atlântico sul em Períodos de el Niño e la Niña. *Rev. Bras. Meteorol.* 19, 89–98.

Figueroa, S. N., Satyamurty, P., Silva Dias, P. L. (1995). Simulation of the summer circulation over the South American region with an Eta coordinate model. *J. Atmos. Sci.* 52, 1573–1584.

Giorgi, F., Marinucci, M. R., and Bates, G. T. (1993). Development of a second generation regional climate model (RegCM2). Part I:Boundary layer and radiative transfer processes. *Mon. Wea. Rev.* 121, 2794–2813.

Grimm, A. M., and Silva Dias, P. L. (1995). Analysis of tropical—extratropical interactions with influence functions of a barotropic model. *J. Atmos. Sci.* 52, 3538–3555.

Kidson, J. W. (1988). Interannual variations in the Southern Hemisphere circulation. *J. Clim.* 1, 1177–1198.

Kiladis, G. N., and Weickmann, K. M. (1992). Circulation anomalies associated with tropical convection during northern winter. *Mon. Wea. Rev*. 120, 1900–1923.

Kiladis, G., and Weickmann, K. M. (1997). Horizontal structure and seasonality of large scale circulations associated with submonthly tropical convection. *Mon. Wea. Rev*. 125, 1997–2013.

Kodama, Y.-M. (1992). Large-scale common features of subtropical precipitation zones (the Baiu frontal zone, the SPCZ, and the SACZ), Part I: characteristics of subtropical frontal zones. *J. Meteorol. Soc. Jpn.* 70, 813–835.

Kodama, Y.-M. (1993). Large-scale common features of sub-tropical convergence zones (the Baiu frontal zone, the SPCZ, and the SACZ), Part II: conditions of the circulations for generating the STCZs. *J. Meteorol. Soc. Jpn.* 71, 581–610.

Krishinamurti, T. N., Kanamitsu, M., Koss, W. J., and Lee, J. D. (1973). Tropical east-west circulation during the Northern winter. *J. Atmos. Sci*. 30, 780–787.

Lenters, J. D., and Cook, K. H. (1995). Simulation and diagnosis of the regional South American precipitation climatology. *Clim. J.* 8, 2988–3005.

Lenters, J. D., and Cook, K. H. (1999). Summertime precipitation variability over South America: role of the large-scale circulation. *Mon. Wea. Rev*. 127, 409–431.

Liebmann, B., and Allured, D. (2005). Daily precipitation grids for South America. *Bull. Am. Meteorol. Soc*. 86, 1567–1570. doi: 10.1175/BAMS-86-11-1567

Liebmann, B., Jones, C., and Carvalho, L. M. V. (2001). Interannual variability of daily extreme precipitation events in the State of São Paulo. *J. Clim.* 14, 208–218. doi: 10.1175/1520-0442(2001)014<0208:IVODEP>2.0.CO;2

Liebmann, B., Kiladis, G. N., Marengo, J. A., Ambrizzi, T., and Glick, J. D. (1999). Submonthly convective variability over South America and the South Atlantic Convergence Zone. *J. Clim.* 12, 1877–1891. doi: 10.1175/1520-0442(1999)012<1877:SCVOSA>2.0.CO;2

Madden, R. A., and Julian, P. R. (1994). Observations of the 40-50 day oscillation —A review. *Mon. Wea. Rev*. 122, 814–837.

Mo, K. C., and Ghil, M. (1987). Statistics and dynamics of persistent anomalies. *J. Clim.* 44, 877–902.

Paegle, J. N., Byerle, L. A., and Mo, K. C. (2000). Intraseasonal modulation of South American summer precipitation. *Mon. Wea. Rev*. 128, 837–850. doi: 10.1175/1520-0493(2000)128<0837:IMOSAS>2.0.CO;2

Paegle, J. N., and Mo, K. C. (1997). Alternating Wet and Dry Conditions over South America during Summer. *Mon. Wea. Rev*. 125, 279–291.

Quadro, M. F. L. (1994). *South Atlantic Convergence (SACZ) Studies Over South America.* Master of Meteorology—National Space Agency Institute, São José dos Campos (available in Portuguese).

Robertson, A. W., and Mechoso, C. R. (2000). Interannual and interdecadal variability of the South Atlantic Convergence Zone. *Mon. Wea. Rev*. 128, 2947–2957. doi: 10.1175/1520-0493(2000)128<2947:IAIVOT>2.0.CO;2

Sanches, M. B., and Silva Dias, M. A. F. (1996). Summer Synoptic Analysis—South Atlantic Convergence Zone influence (SACZ). In: 9° Brazilian Congress of Meteorology, Campos do Jordão. *Ann. Braz. Meteorol. Soc.* 1, 439–443. [Available in Portuguese].

Siqueira, J. R., and Machado, L. A. T. (2004). Influence of the frontral systems on the day-to-day convection variability over South America. *J. Clim.* 17, 1758–1766. doi: 10.1175/1520-0442(2004)017<1754:IOTFSO>2.0.CO;2

Siqueira, J. R., Rossow, W. B., Machando, L. A. T., and Pearl, C. (2005). Structural characteristics of convective systems over South America related to cold-frontal incursions. *Mon. Wea. Rev*. 133, 1045–1064. doi: 10.1175/MWR 2888.1

Streten, N. A. (1973). Some characteristics of the satellite-observed bands of persistent cloudiness over the Southern Hemisphere. *Mon. Wea. Rev*. 101, 486–495.

Taljaard, J. J. (1972). The clouds bands of the South Pacific and Atlantic Oceans. *Meteorol. Monogr.* 13, 189–192.

Vogel, D. (2012). *Changes in Precipitation Characteristics and Extremes - Comparing Mediterranean to North-Western European Precipitation.* Master degree Thesis, Institute of Atmospheric and Climate Science, University of Reading.

Yassunary, T. (1977). Stationary waves in the Southern Hemisphere mid-latitude zonal revealed from average brightness charts. *J. Meteorol. Soc. Jpn.* 55, 274–285.

Zhang, H., Fraedrich, K., Blender, R., and Zhu, X. (2013). Precipitation extremes in CMIP5 simulations on different time scales. *J. Hydrometeorol.* 14, 923–928. doi: 10.1175/JHM-D-12-0181.1

Conflict of Interest Statement: The authors declare that the research was conducted in the absence of any commercial or financial relationships that could be construed as a potential conflict of interest.

frontiers in Physics

ORIGINAL RESEARCH
published: 15 September 2015
doi: 10.3389/fphy.2015.00076

A model study of the seasonality of sea surface temperature and circulation in the Atlantic North-eastern Tropical Upwelling System

Saliou Faye[1,2*], *Alban Lazar*[1,3], *Bamol A. Sow*[1,4] *and Amadou T. Gaye*[1]

[1] Laboratoire de Physique de l'Atmosphère et de l'Océan Simeon Fongung (LPAO-SF/ESP/UCAD), Dakar, Senegal, [2] Centre de Recherche Océanographique Dakar-Thiaroye (CRODT/ISRA), Dakar, Senegal, [3] Laboratoire d'Océanographie et du Climat: Expérimentations et Approches Numériques (LOCEAN/UPMC), Paris, France, [4] Laboratoire d'Océanographie, des Sciences de l'Environnement et du Climat (LOSEC/UASZ), Ziguinchor, Senegal

The climatological seasonal cycle of the sea surface temperature (SST) in the north-eastern tropical Atlantic (7–25°N, 26–12°W) is studied using a mixed layer heat budget in a regional ocean general circulation model. The region, which experiences one of the larger SST cycle in the tropics, forms the main part of the Guinea Gyre. It is characterized by a seasonally varying open ocean and coastal upwelling system, driven by the movements of the intertropical convergence zone (ITCZ). The model annual mean heat budget has two regimes schematically. South of roughly 12°N, advection of equatorial waters, mostly warm, and warming by vertical mixing, is balanced by net air-sea flux. In the rest of the domain, a cooling by vertical mixing, reinforced by advection at the coast, is balanced by the air-sea fluxes. Regarding the seasonal cycle, within a narrow continental band, in zonal mean, the SST early decrease (from September, depending on latitude, until December) is driven by upwelling dynamics off Senegal and Mauritania (15–20°N), and instead by air-sea fluxes north and south of these latitudes. Paradoxically, the later peaks of upwelling intensity (from March to July, with increasing latitude) essentially damp the warming phase, driven by air-sea fluxes. The open ocean cycle to the west, is entirely driven by the seasonal net air-sea fluxes. The oceanic processes significantly oppose it, but for winter north of ∼18°N. Vertical mixing in summer-autumn tends to cool (warm) the surface north (south) of the ITCZ, and advective cooling or warming by the geostrophic Guinea Gyre currents and the Ekman drift. This analysis supports previous findings on the importance of air-sea fluxes offshore. It mainly offers quantitative elements on the modulation of the SST seasonal cycle by the ocean circulation, and particularly by the upwelling dynamics.

Keywords: SST, upwelling, circulation, heat budget, observations, modeling

Edited by:
María Belén Rodríguez de Fonseca,
Universidad Complutense de Madrid,
Spain

Reviewed by:
Ana María Durán-Quesada,
University of Costa Rica, Costa Rica
Tomoki Tozuka,
University of Tokyo, Japan
Vincent Michel Echevin,
Laboratoire d'Océanographie et du
Climat: Expérimentations et
Approches Numériques, France

****Correspondence:***
Saliou Faye,
Laboratoire de Physique de
l'Atmosphère et de l'Océan Simeon
Fongung/École Supérieure
Polytechnique/Université Cheikh Anta
Diop, BP 5085 Dakar–Fann, Senegal;
Centre de Recherche
Océanographique Dakar-Thiaroye
(CRODT/ISRA), BP 2241 - Dakar,
Senegal
saliou.faye@ucad.edu.sn

Specialty section:
This article was submitted to
Atmospheric Science,
a section of the journal
Frontiers in Physics

Received: *28 February 2015*
Accepted: *24 August 2015*
Published: *15 September 2015*

Citation:
Faye S, Lazar A, Sow BA and Gaye AT
(2015) A model study of the
seasonality of sea surface
temperature and circulation in the
Atlantic North-eastern Tropical
Upwelling System. Front. Phys. 3:76.
doi: 10.3389/fphy.2015.00076

Introduction

The sea surface temperature (SST) is a crucial quantity for studies of both climate variability and marine ecosystem productivity. In the tropical Atlantic, as well as for the other tropical basins, SST exerts a significant influence on the climate of surrounding regions (e.g., [1, 2]). It is also a major indicator of the state of the marine environment relative to phytoplankton biomass needs, particularly for upwelling zone activity, and particularly for coastal upwellings [3]. One of the less studied zones is the Atlantic North-eastern Tropical Upwelling System (ANETUS, examined here from 7 to 25°N and 12 to 26°W). It is also one of the regions experiencing the largest SST seasonal cycle in the tropics. In this study, we propose to present and interpret the full spatial distribution of the processes driving the seasonal cycle of the SST, for the open ocean upwelling regime, as well as at the coasts.

Trade winds and the ITCZ generate large scale divergent Ekman transports, which force in the northern hemisphere a tropical upwelling system that continuously extends from Morocco to the mouth of the Guinea Gulf, and from the African coasts to mid and west Atlantic, depending on season [4, 5]. Considered from a basin-scale perspective, this system forces a cyclonic gyre circulation, the Guinea Gyre [e.g., 6], of which the Guinea Dome and the coastal West-African upwellings form the most eastern features [4, 7]. In this paper, we limit our study to the eastern part of the system, bounded in latitude by the Tropic of Cancer and the North Equatorial Counter-Current and in longitude by the Cape Verde Archipelago (CVA around 26°W) and African coasts. This area is marked by intense, seasonally dependent, off-shore and coastal primary production patterns of major economic importance. The coastal part of the upwelling system covers latitudes ranging from Morocco and Canary Islands to Senegal [8] and further south down to the Guinea Gulf. It forms the tropical part of the Canary Current Upwelling System (CCUS) down to Senegal, as well as the northern part of the Guinea Current Upwelling System that extends from Guinea coasts to the Gulf of Guinea. The CCUS is one of the four major eastern boundary upwelling systems with those of Peru-Chile, Benguela, and California.

Horizontal circulation is schematized **Figure 1**. To the west, the North Equatorial Current (NEC) and the Canary Current (CC) forms the eastern boundary of the North Atlantic subtropical gyre. Near-shore, a strong wind-induced coastal upwelling is active, its extension depending on season, and a density front develops that generates the coastal jet [9–11], also named Canary upwelling Current (CanUC) [12]. However, observations are lacking and its latitudinal extension to the south is uncertain, with some model studies showing it down to the Cape Verde peninsula (see dashed green arrow in **Figure 1**). South of the region, the circulation is dominated by the North Equatorial Counter-Current (NECC), which has a large seasonal cycle [13, 14]. It is located near 5°N in winter and reaches 10°N in summer. During this season, it continues north as the Mauritania Current (MC), which flows northward until about 20°N [15]. Offshore, the Guinea Dome (GD) is another important physical characteristic of the area, defined by a dome of the isotherms, and low hydrostatic pressure. It is centered in the southeast of the archipelago of Cape Verde, and intensifies in summer, at about 12°N, and 22–23°W. It is generated by upward Ekman pumping forced by the trade winds convergence [7, 17], and belongs to the Guinea Gyre, formed by the NEC and NECC in surface [4, 13]. It exist a link between the GD with the Atlantic Meridional Mode (AMM) which is related to the meridional migration of the Intertropical Convergence Zone (ITCZ) [18, 19].

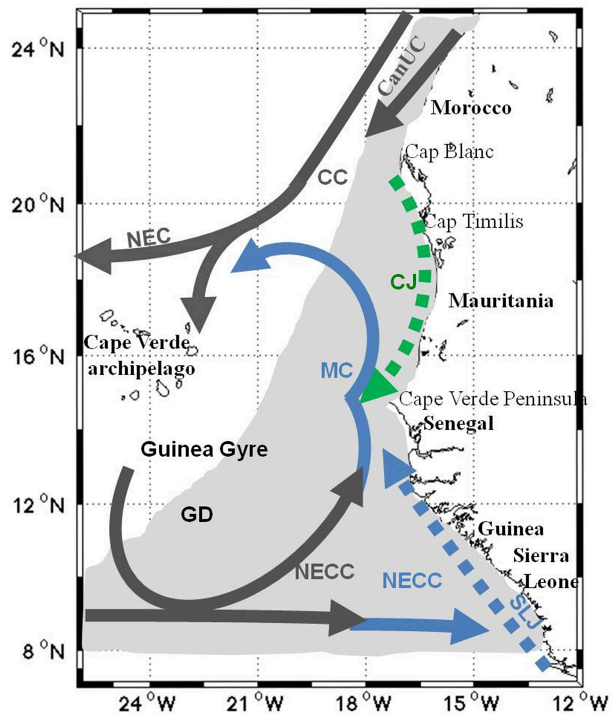

FIGURE 1 | Map of the schematic surface circulation in the Atlantic North-eastern Tropical Upwelling System characterized by permanent currents (dark gray), seasonal currents in winter-spring (green), another seasonal currents in summer-autumn (blue) and upwelling area (gray shading). Dash line corresponds to currents not evidenced by *in-situ* measurement, but visible in circulation derived from altimetry. (adapted from [16])

Regarding SST in our region, the mechanisms that drive its seasonal cycle are not yet certain. Carton and Zhou [20] ocean model sensitivity experiments show that air-sea flux and wind stress forcing are of comparable importance away from the continent, whereas within a few degrees of the African coasts, the meridional stress becomes the main forcing. Yu et al. [21] on the other hand evidenced the very high correlation at large scale in the region north of 10°N between the SST time derivative and the net air-sea flux. The first study can be interpreted as an indication that advection and associated Ekman pumping are important for the region, and dominant at the coast. The second may suggest that they do not drive the seasonal cycle. More specifically, the upper heat content at ∼12°N and few specific longitudes, within the Guinea Dome in particular, was studied by Yamagata and Iizuka [7]. They found that the summer subsurface cooling is explained comparably by horizontal and vertical advection. However, these results pertain to the upper thermocline doming, since SST increase in fact during the GD development. A proper (ML in the following) heat budget for the climatological SST seasonal cycle of the western part of our domain, was carried out by Foltz et al. [22] from observations and reanalysis products. They find also that air-sea fluxes drive the cycle, and suggest, from the heat budget residual, that vertical mixing damps it.

Regarding coastal patterns, their seasonal variability has been the subject of studies based on upwelling indices, calculated from *in situ* measurements [8] or satellite observations of SST [23]. They nevertheless often lack a robust heat budget analysis for the SST, that could provide clear physical interpretations of the SST changes. Along African coasts, an important issue for the system is how much upwelling forces SST, and how long does its effect last during the year. For example, Santos et al. [24], using a temperature-based estimate suggest that if the upwelling is persistent throughout the year, with a peak in autumn and spring, between 21 and 32°N, it would in contrast be restricted to winter-spring within the 12° and 20°N latitude band. These authors hypothesize that the turn of the summer monsoon winds would advect warm waters northward along-shore. One may wonder how much it contributes to the SST warming and what are the upwelling real cycle and effects, since a wind-derived proxy indicates rather that the latter persists in summer from 15 to 20°N, albeit weaker [e.g., 3]. Furthermore, air-sea heat fluxes could potentially also explain this summer evolution. In fact, within the coastal Mauritania and Senegal upwellings, even the first order balance between horizontal advection, subsurface heat fluxes and air-sea fluxes is unknown. This deserves to be checked in an Ocean Global Circulation Model (OGCM) and tested to the East, where the upwelling is stronger. A model study like the one we present here, despite its inherent uncertainties due to forcings and model errors, can offer complementary results. In this paper, we provide some quantitative elements of answer to the various uncertainties existing about the ocean dynamics and the control of the SST seasonal changes in the ANETUS, with observations and an OGCM. The focus is on the regimes of heat budget, and the processes that drive them, in particular the turbulent vertical mixing, hardly quantifiable from observations only and not yet analyzed *per-se* in the literature.

The article is structured as follows. The data and methods are presented in Section Data and Methods. In Section Choice of Relevant Time-average Periods, we present the general circulation features in observations and the simulation. Then we analyze in Section The Mixed Layer Heat Budget the spatial structures of oceanic and atmospheric contributions to the heat budget, and detail their temporal variations for continental and open-ocean sub-domains. Results are then summarized and discussed in Section Summary and Discussions.

Data and Methods

Observations

The NOAA AVHRR OISST SST at 25 km resolution is monthly averaged to produce the climatology for the period 1988–2000 that we use to evaluate model SST. For the circulation, OSCAR surface currents are used. They are representative of total geostrophic and wind-driven circulation over the first 15 m depth layer and are available on a horizontal grid of 1/3° × 1/3° [25]. Geostrophic currents are provided on a 1/3° × 1/3° spatial grid by AVISO. We constructed monthly-climatologies of surface circulation, with both products for the period 1993–2000, close to that of the climatological forcing used to run our model. Climatological wind stress is provided by the DFS4 forcing set (see further description in Numerical Model), and derived from the ERA40 reanalysis winds, which assimilated the QuickSCAT winds. The Ekman vertical velocities associated with the climatological winds are estimated using the Ekman transport divergence formula. Null cross-shore transport at the coast is enforced by setting the wind stress to zero at each land point. Note that both the coastal pumping and offshore Ekman pumping are computed with this formula. Mixed layer depth (hereafter MLD) is given by the monthly climatology from De Boyer Montégut et al. [26] on a 2° × 2° horizontal resolution. We retained the product based on a temperature threshold of 0.2°C, since the density-based product has a much less dense cover in our area of study. Thermocline depth is evaluated using the monthly climatological WOD05 hydrological dataset on a 1°× 1° latitude–longitude grid.

Numerical Model

The NEMO modeling system [27] is based on the global OGCM OPA, which solves the primitive equations on an Arakawa C grid, with a second-order finite difference scheme. It assumes the Boussinesq and hydrostatic approximations, and assumes incompressibility. In the present study, we use the regional configuration for the tropical Atlantic ATLTROP025, derived from the global DRAKKAR configuration ORCA025-G70 [28] with an extension limited to 30°N and 30°S. The horizontal resolution is 0.25° × 0.25°. Realistic bottom topography and coastlines are derived from ETOPO2. The vertical dimension is resolved by 46 z-levels with a vertical mesh size ranging from 5 m in the upper 30–250 m at depth. Most relevant elements of the parameterization are the following. A horizontal biharmonic operator is used for the diffusion of horizontal momentum, with a viscosity coefficient (background value of $-1.5\ 10^{-11}$ $m^4.s^{-2}$) varying as δx^3 (δx the horizontal grid size). Diffusion of temperature and salinity uses a Laplacian operator rotated along isopycnals, with a coefficient decreasing proportionally to the grid size (starting at 300 $m^2.s^{-1}$ at the equator). Vertical mixing of momentum and tracers is computed using a second-order turbulence kinetic energy closure model described in Madec [27]. Lateral boundary conditions are provided by the global run ORCA025-G70. For surface forcing, we use the DRAKKAR DFS4 6-hourly global forcing datasets [29]. To calculate latent and sensible heat fluxes, the CORE [30] bulk formulae algorithm is used, with surface atmospheric state variables derived from the ERA40 reanalysis and ECMWF analysis after 2002 (air temperature, humidity and winds at 10 m). Corrections are performed on these input fields to correct temporal discontinuities and yield better agreement with some recent high quality data. Radiation fluxes are based on the CORE v1 dataset, using a corrected ISCCP-FD radiation product [31]. For these experiments, we forced the model for thirteen years with climatological weekly fields averaged over the period 1988–2000. The 5-day mean outputs were averaged climatologically over the last year of simulation. It is worth to stress out that in order to study a climatological state closer to the observational one, it would be more rigorous to analyze a simulation of the same period as the observations, forced by the non-climatological fields. Such a simulation however, including heat budget diagnostics described below, was not yet realized at time of our study. It will be worth in the future to verify our conclusions with such a run.

For the present study, we derived off-line a number of quantities from the model outputs. In particular we estimated surface horizontal currents from the total SSH using the geostrophic equation and assumed they did not vary with depth over the ML. The model computes MLD using a density threshold of 0.01 $kg.m^{-3}$, and we use this output throughout the paper. For the validation section however, we also estimated MLD offline with the same threshold of 0.2°C, although the online computation (not available) would have been more comparable.

Diagnostics

In this study, we follow the approach used by Vialard and Delecluse [32] and by Peter et al. [33] and Jouanno et al. [34] where the ML temperature equation is partitioned as follows:

$$\partial_t \langle T\rangle = \underbrace{-\left\langle \overrightarrow{U_h}.\overrightarrow{\partial_h T}\right\rangle -}_{A} + \underbrace{\langle D_l\left(T\right)\rangle}_{B} - \underbrace{\langle w.\partial_z T\rangle}_{C} - \underbrace{\frac{1}{h}(K_z \partial_z T)_{z=h}}_{D} + \underbrace{\frac{Q^* + Q_s\left(1 - f_{z=h}\right)}{\rho_0 C_p h}}_{E} + res \qquad (1)$$

with $\langle . \rangle = \frac{1}{h}\int_{-h}^{0} .dz$

Here, the brackets represent a vertical integration over the MLD, T is the temperature, $\overrightarrow{U_h}$ and w are the horizontal and vertical currents, K_z is the vertical mixing coefficient, h is the MLD, and $D_l(T)$ is the lateral diffusion operator. Q^* and Q_s are the non-solar and solar components of the total heat flux, and $f_{z=h}$ is the fraction of the solar shortwaves that reaches below the MLD. Capital letters underneath terms are used, respectively, as short-hands for horizontal advection, horizontal diffusion associated with unresolved horizontal turbulent processes, vertical advection, vertical turbulent mixing at the ML base and air-sea fluxes. A last term *res*, computed as a residual, corresponds to the entrainment at the ML base. Note that we have checked that the latter is always largely negligible in our area.

In the following work, horizontal advection and vertical mixing always dominate the ocean contribution to the heat budget. For the sake of synthesis, we chose to group the ocean terms in horizontal and vertical processes terms. The first is the sum of lateral diffusion and horizontal advection contributions ($A+B$), and the second the sum of vertical advection, vertical mixing and entrainment ($C+D+res$). These group components have been checked individually relative to the others, and are discussed separately when they are significant. Term E corresponds to the net air-sea flux effect. To quantify the relative importance of terms, we compute their ratios. In the section dedicated to time-averages, we computed ratios of time-averaged group of terms, to emphasize their relative time-mean effects, whereas in the following section focusing on time-variations, we instead present the ratios of 5-day outputs. Differences between both computations are of second order and not relevant to discuss in this study.

Results

Choice of Relevant Time-average Periods

In order to distinguish time periods relevant for studying time-averages of the heat budget terms with a focus on the ocean contribution, **Figure 2** presents the Ekman upwelling and SST cycle averaged longitudinally from the coast to 18°W. The former is computed as the total Ekman transport divergence, including that of the alongshore grid-points. It first evidences the well-known latitudinal transition from a strongly varying upwelling at low latitudes to a more stable northern regime [e.g., 24, 35]. On both sides of approximately latitude 18°N, the Ekman pumping peaks occur out of phase, in agreement with Lathuilière et al. [3], due to the seasonal shift of the inter-tropical convergence. Low latitudes are marked by an intense winter regime, followed by a relaxation phase in summer, in particular off Senegal (10–16°N). North-Mauritania and south-Morocco latitudes (18–22°N) experience a peak in summer. Based on the strongest Ekman pumping and seasonal SST changes, we identify a first period from November to May, characterized globally by lowest or decreasing SST (so-called cooling period, (hereafter CP), and a warming period (hereafter WP) from June to October characterized by increasing or high SST. Next section, we describe the CP and WP general circulation and SST change patterns in the observation-derived products, and validate the simulation.

SST Variations and Mixed Layer Depth

Figure 3A displays observed SST variations for CP (computed as the SST difference between the end and the beginning of the period). They exhibit an extremum (-0.7°$C.month^{-1}$) located around (18°N, 18°W) off Mauritania coast. A second relative extremum (-0.6°$C.month^{-1}$) is located close to shore near 14.5°N, just south of the Cape Verde Peninsula in the southern Senegal upwelling center [36]. The model presents a more noisy structure (**Figure 3B**), due to the shorter length of average period relative to the observations. This being said, the large-scale patterns of the model are comparable to those of the observations, with only a slight underestimation of the cooling (∼0.2°$C.month^{-1}$) near the coast from 14° to 20°N. The large-scale structure of the temperature change during WP is very similar with a sign reversal and a somewhat more rapid evolution (maxima ∼1°$C.month^{-1}$, **Figure 3C**). The model is able to simulate this distribution although the area of largest warming tends also to be shifted a few degrees to the southwest. Nearshore, the highest differences reach comparable negative values as during CP (∼ -0.2°$C.month^{-1}$) from 15 to 22°N

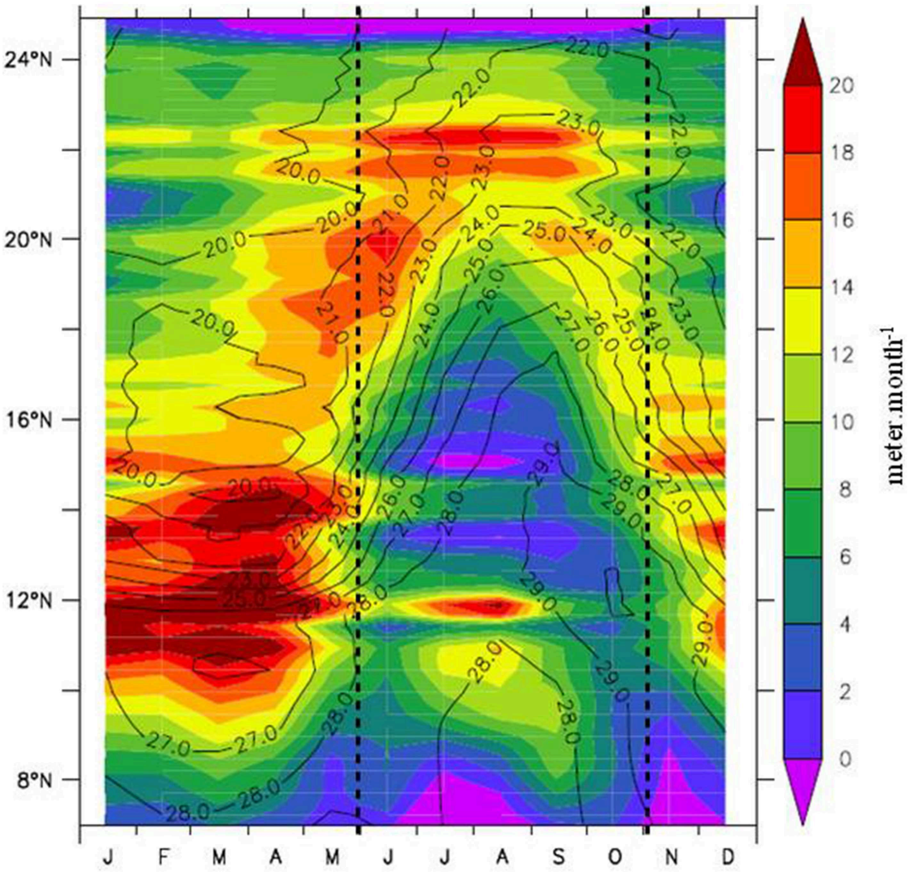

FIGURE 2 | Latitude-time Hovmöller plot along the coastal region (averaged from the coast to 18°W) of the seasonal cycles of Ekman pumping (shading, m.month^{-1}) and SST (contours, °C). Dash lines separate CP (November–May) and WP (June–October) periods.

(**Figures 3C,D**). **Figure 3** also shows the SST and MLD fields, which are essential to the heat budget analysis. The model SST suffers from a warm bias, generally between 0.5 and 1°C. The model MLD is 10–30 m too deep during CP and about 5 m too shallow during WP. Because there are little observations in the region, uncertainties are large particularly for MLD, and we consider the model sufficiently realistic.

Upwelling and Stratification

To better understand the effect of the wind-driven circulation on the ML heat budget, **Figures 4A,C** present the Ekman pumping patterns for CP and WP. To compare to the model, we present the maximum value of the model vertical velocities found between the surface and the base of the thermocline (**Figures 4B,D**). The spatial extent of the upwelling appears remarkably stable between the two seasons, and this is also verified with the monthly values (not shown). The strongest upwelling velocities are located nearshore north of ∼10°N, where they reach values of the order of 100 (resp. 50) m.month^{-1} during CP (resp. WP). Offshore, upwelling velocities display one order of magnitude lower values. They are associated with the trade winds curl and decrease gradually westward, more rapidly in the north than south, where they are responsible for the presence of the Guinea Dome. In the lee of the Cape Verde Islands, atmospheric island wake effect creates an upwelling–downwelling dipole patterns with typical scales of ∼100–200 km [37]. Regarding intensities derived from observations they most vary from CP to WP near the coasts, in the north (by a factor of ∼1.5), and much considerably south of 15°N (factor of ∼0.25) in support of Lathuilière et al. [3] estimate. For both periods the model is at large scale in good agreement with Ekman pumping estimates. This validates the model vertical dynamics, and indicates that Ekman pumping corresponds in general well to the maximum upper ocean vertical velocity. The most remarkable differences occurs nearshore over the wide shallow continental shelves of the Banc d'Arguin (∼20°N) and south of Senegal (∼14°N). Vertical velocities comparable to Ekman pumping are found west of the coast there. This is explained by the fact that, due to the shallow plateau there, bottom friction disturbs the surface Ekman layer and classical Ekman theory does not apply. The Ekman divergence is then fully developed further offshore where the plateau is deep enough [see 38, 39].

Since the thermocline depth reflects the stratification, which controls the turbulent heat fluxes at the ML base, it is important to validate its distribution. The 19°C isotherm depth is shown as a proxy. Modest differences in the position and shape of the GD

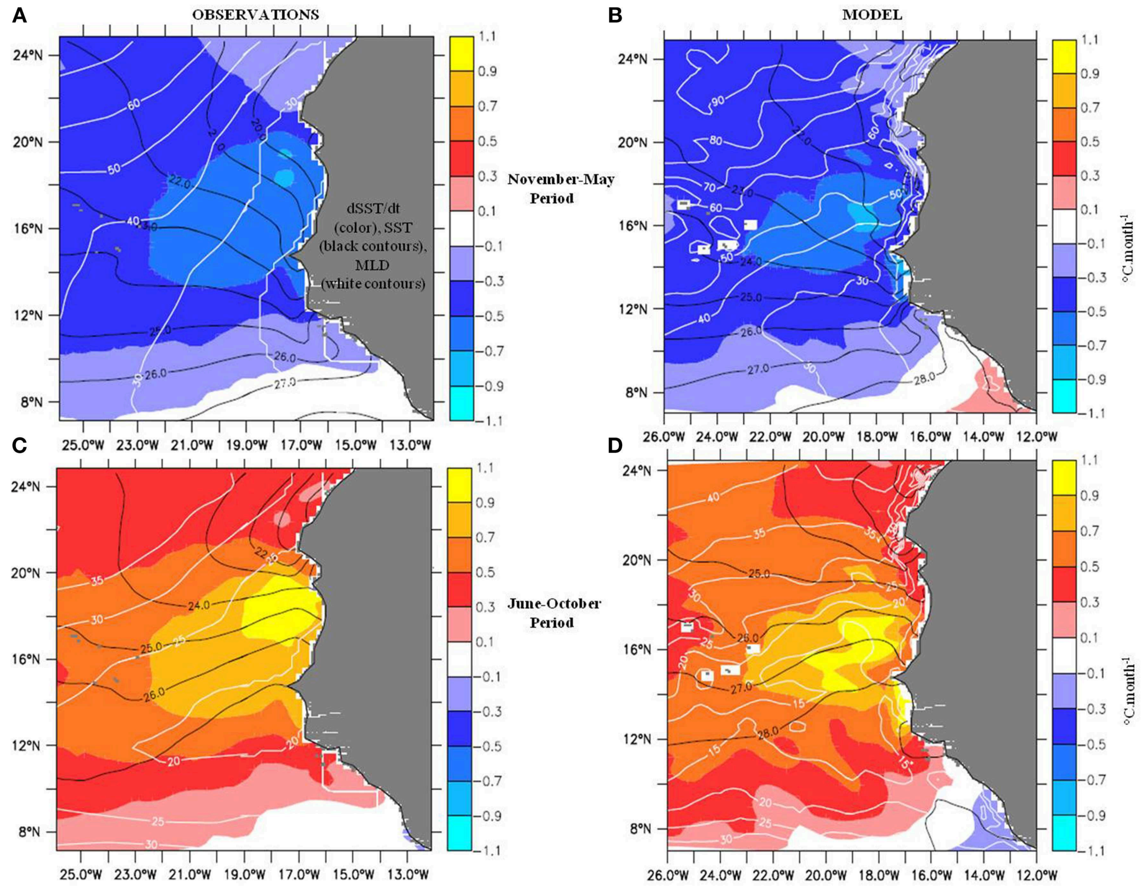

FIGURE 3 | SST trend (color, in °C.month^{-1}), SST (black contour, in °C) and mixed layer depth (white contour, in m), averaged over CP (November–May, top) and WP (June–October, bottom); left (A,C) for observations and right (B,D) for simulation.

(in subsurface, it is particularly visible near 100 m in observations (D15) and about 60 m in the model; **Figures 4A,B**) in particular are noticeable, and model values are deeper by about 20 m, possibly as a consequence of an overly diffuse thermocline, a common bias in OGCM.

Horizontal Surface Circulation

We present total and geostrophic surface currents on **Figure 5**. The major geostrophic currents in the region are well represented by the model (in black). The CC, NEC, CanUC, NECC and circulation around the GD are visible during the two periods. The CC exhibits an important seasonal variability with a strengthening during WP in association with stronger winds in the north (**Figures 5B,D**). A similar seasonal cycle is found in the observations but an important difference should be noted: the observation derived CC appears quite relatively patchy, as appear the total currents. The model westward circulation is comparatively less complex, in particular during CP where the westward flow is quite uniform north of 16°N. In the latitude range 7–16°N, the offshore flow is more seasonally variable. The MC and GD recirculation are both very clear in observed and simulated geostrophic currents. We also note the intense well-organized westward ageostrophic flow spanning 13–16°N east of the CVA in the model (note the weak geostrophic currents in both panels). This flow is coherent with the southward wind forcing (see **Figure 4A**). It is however not visible in the OSCAR reconstruction, which is weaker and noisy. During WP the NECC seems slightly reinforced by Ekman drift in the model and observations and turns into the Guinea Current to the South and into a northern circulation branch, particularly intense at the coast. The turning point appears to be the slope change of Sierra Leone coastline (~8.5–9°N). Before this northern current becomes the MC, we propose to name it the Sierra Leone Jet (SLJ). The difficulty for observations to represent the circulation features in this region is well-known and due to sparse measurements [40], which pose difficulties to validate satellite-derived products and in particular in regions of coastal distortions of the satellite estimates. We shall be cautious when presenting the advective terms in the heat budget, but do not *a priori* disqualify the modeled circulation where it disagrees with OSCAR and AVISO, particularly nearshore.

The Mixed Layer Heat Budget

In this section, we analyze the terms of the heat budget. We first analyze the spatial structures of the mains terms in order to evidence better their physical origins. The annual mean is

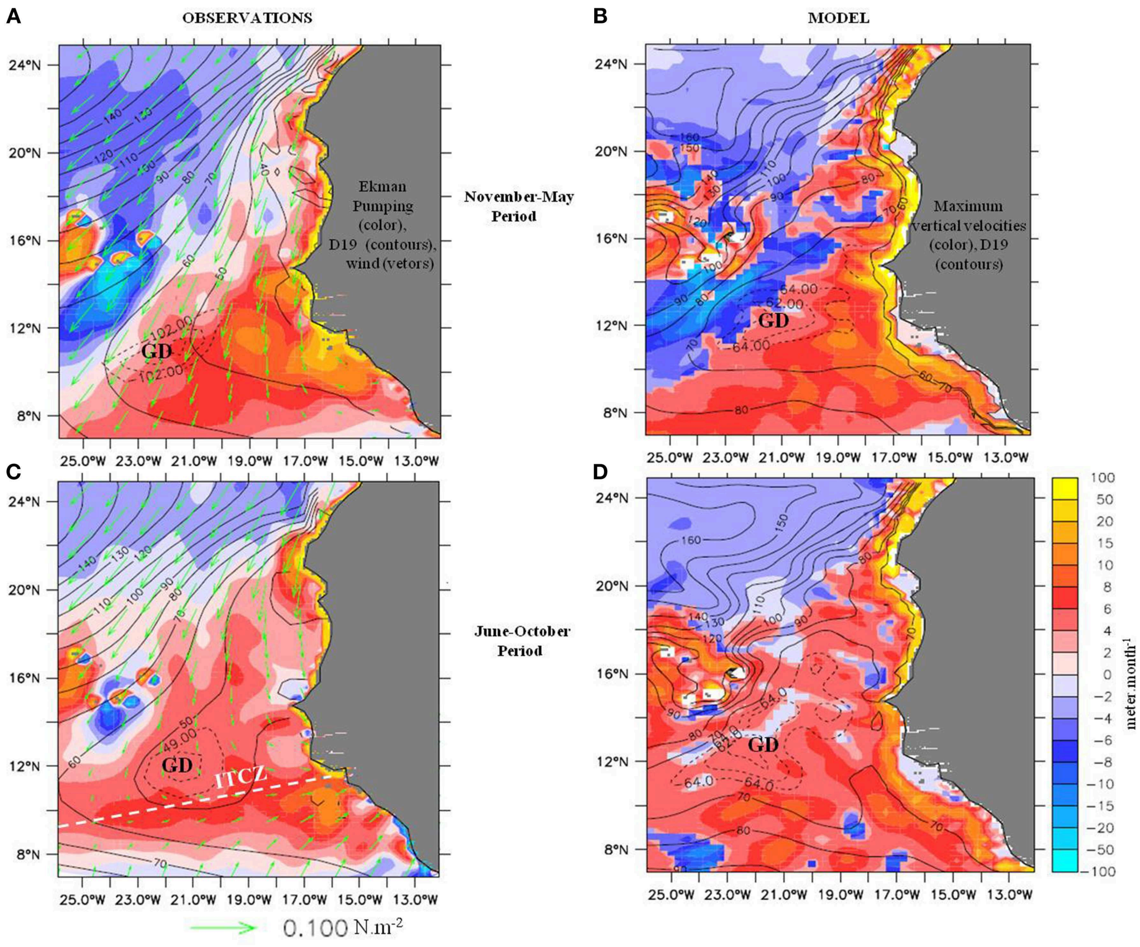

FIGURE 4 | Ekman pumping (shading, m.month^{-1}), 19°C isotherm depth (black contours, m) and wind stress (green vectors, N.m^{-2}) from observations, averaged over (A) the CP(November–May) period, and (C) WP (June–October) period. Maximum vertical velocities between surface and thermocline (shading, m.month^{-1}) and 19°C isotherm depth (black contours, m) for the simulation, averaged over (**B**) the November-May CP period, and **(D)** June–October WP period. GD, Guinea Dome.

presented, and then the CP and WP time-means, to take into account the cycle of the wind-driven upwelling activity, Then zonal averages are eventually examined for eastern and western sub-domains in function of time, in order to determine which processes are driving the time-variations of the SST.

Annual mean

Figure 6 shows the annual mean of ocean effects, and its two components, the horizontal and vertical processes. Since the sum of air-sea heat fluxes and ocean effects is equal to the annual heat storage, which is negligible in the model climatology, the net heat flux effect is the opposite of the ocean effect. Meridionally, there is a contrast between an ocean warming south of roughly parallel 12°N, and a cooling effect north of it. Zonally, contributions are maximum at the coast with values of up to -5°C.month^{-1}, and decrease abruptly westward by an approximate factor of five over a few degrees of longitude (**Figure 6A**). For the sake of differentiating sub-domains, we chose the longitude 18°W to separate regimes marked by high values dominated by coastal dynamics, and those with low values controlled by open-ocean circulation. In the west of the domain, CVA forms a specific sub-domain of intermediate or elevated intensities, which would require specific discussions out of scope of this paper.

Figures 6B,C show that the meridional contrast is explained by differences in the vertical and horizontal processes. North of ~12°N, vertical processes cause an expected general cooling through vertical exchanges with colder subsurface waters. It is worth noting that they prevail over the horizontal ones by a factor of about two in large parts of the domain, while both effects reach comparable amplitudes off Morocco and Cape Verde Islands. South of 12°N, a remarkably vast warming effect, albeit weak except along-shore, is sustained by vertical processes, which indicate the influence of temperature inversions, as it will be demonstrated in WP analysis. The location corresponds to patterns of barrier layers associated with ITCZ rainfall [41] that allow for the presence of temperature inversions. The ocean warming effect is however dominated by advection of warm waters poleward by the NECC (**Figure 6C**), except alongshore

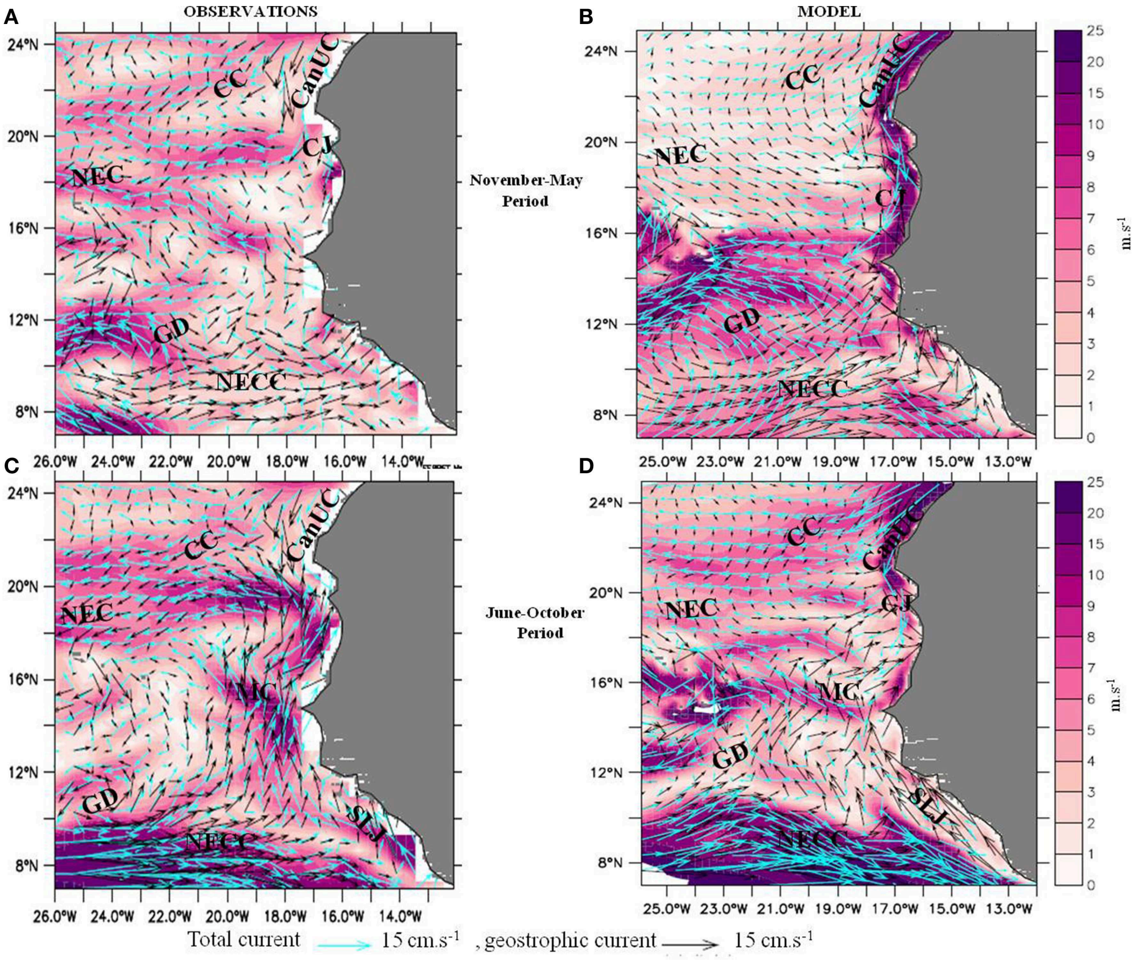

FIGURE 5 | Horizontal surface currents averaged over the CP (November–May, top) and WP (June–October, bottom) for observation-derived (A,C) and simulated (B,D); intensity of the total surface current (shading, m.s^{-1}), total (blue vectors) and geostrophic component (black vectors).

where currents are weak and SST is warmed up also by temperature inversions (**Figure 6B**). Note that 12°N corresponds to the GD latitude. This shows that, in annual mean, the ocean cools the GD SST in its northern half, but warms it in its southern part. Overall, south of 12°N, horizontal advection dominates vertical processes (**Figure 6C**), but for the remaining part of the region, heat exchanges with the thermocline cools the domain SST with a larger or comparable amplitude than horizontal currents effect (**Figure 6B**).

November–May Cooling Period

As we will see, during CP, the ocean contribution displays the larger negative signals, whereas during WP, it is the net air-sea flux contribution. Thus we start the CP analysis with the interpretation of the ocean terms, and then will study the WP starting with the investigation of the air-sea fluxes effects. During CP the total ocean contribution is close to its annual mean (**Figures 6A**, **7A**). The ratio of time-mean contributions of horizontal and vertical processes indicates that the latter have a larger effect on the SST cooling, next to the continent, as well as to the west in the latitude band 12–20°N. Compared to the annual mean, the vertical processes cause a stronger (weaker) cooling in the 12–18°N (18–24°N) coastal upwelling band (**Figure 7B**), evidently associated with the latitudinal structure of the seasonal Ekman pumping changes. It explains the same pattern in the total ocean contribution.

To detail further vertical cooling, we first note that it is by far dominated by vertical diffusion (not shown). Then by computing off-line the latter with model outputs of vertical diffusivity (K_z), temperature and MLD (see formula of D in Equation 1) we reproduced satisfyingly its pattern (not shown). Hence we examine diffusivity and vertical temperature gradient at the ML base. It appears that the maximum intensities along-shore is due to stronger vertical diffusivity there (**Figure 7C**), not to vertical temperature gradients which are weak compared to offshore (**Figure 7D**). We interpret this as a manifestation of coastal upwelling dynamics which generates intense current shear near the base of the mixed layer ML (**Figure 7C**, contours). It thereby enhances turbulence levels, simulated by large K_z. Intense coastal upwelling tends also to erode upper ocean stratification, relative

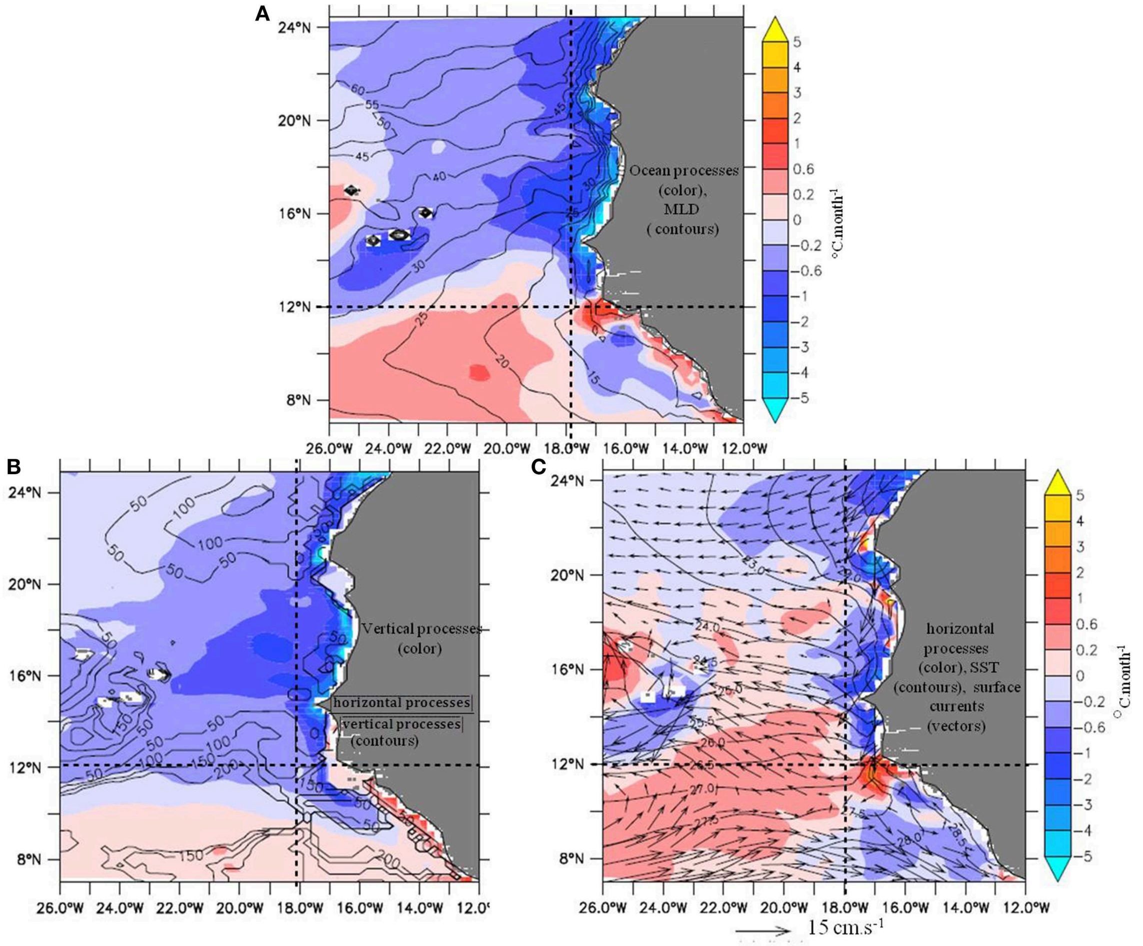

FIGURE 6 | Annual average of the various oceanic processes contributing to the mixed layer heat budget. (A) Total oceanic trend (shading, °C.month^{-1}), and mixed layer depth (MLD, black contours, m), **(B)** trend associated with vertical processes (sum of vertical advection, vertical diffusion at the base of the mixed layer and RES, shading, °C.month^{-1}) and ratio of horizontal processes over vertical processes (contour every 50, 100, 150, and 200%) and **(C)** horizontal processes (sum of the horizontal advection and lateral diffusion, shading, °C.month^{-1}), SST (black contour, °C) and surface currents (vectors). Vertical and horizontal dotted lines delimit regimes within the region.

to the moderate open-ocean upwelling to the west. To complete the explanation of this zonal variation, it is important to say that the MLD zonal pattern amplifies significantly the effect of the diffusive flux at the coast. Indeed, MLD, which enters the diffusive flux term in the denominator, is shallower at the coast by a factor of 1.5–2 relative to further west. Far from the continent, west of 18–19°W, the cause of relative high vertical diffusion is opposite. The vertical temperature gradients at the mixed layer ML base reach maximum intensities, about five times larger than nearshore (**Figure 7D**), explaining the vast and moderate diffusion pattern. The Guinea Gyre upwelling lifts gently the isotherms and maintains a strong stratification, maximal at the GD location. On the other hand, K_z is smaller (**Figure 7C**), in relation to weaker shear of horizontal current compared to nearshore.

Regarding the horizontal processes contribution (**Figure 8A**), it also appears similar to its annual mean (**Figure 6C**). It is essential to the model for redistributing heat horizontally, and modulating the 1D vertical upwelling dynamics. We first note that horizontal advection prevails largely over horizontal diffusion (not shown). Then in order to interpret advective effects, we estimated off-line the geostrophic and ageostrophic components of the horizontal advection term. To do so, surface geostrophic and ageostrophic currents were calculated (the latter as the total minus the geostrophic currents), and then used for computing scalar products with SST gradients. **Figures 8B,C** show that both contributions are most intense in the vicinity of coastlines, due to maximum SST gradients and generally more intense currents. They often partly oppose each-other, especially close to the continent, where geostrophic flow compensate partially, in addition to coastal upwelling, the mass imbalance generated by Ekman divergence.

Along African coasts, each advective contribution dominates alternatively the total in function of latitude. North of about

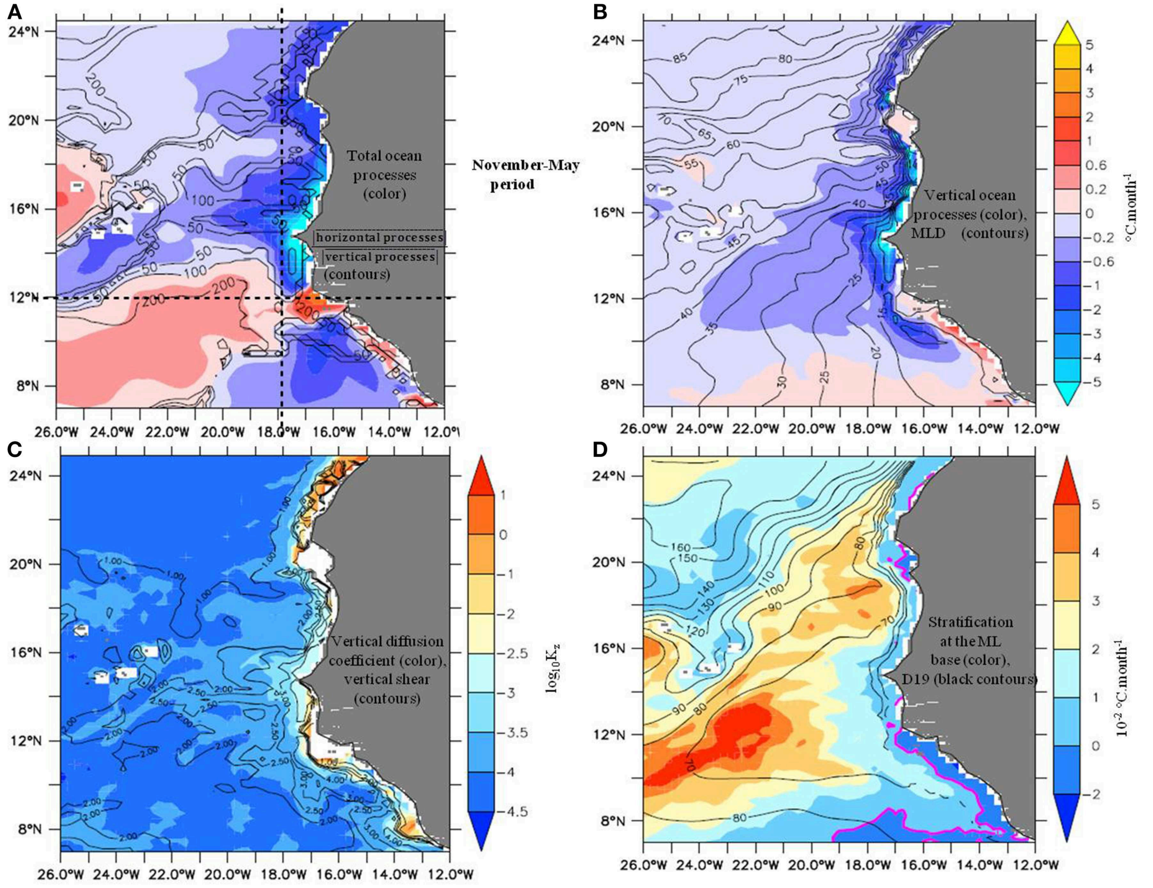

FIGURE 7 | Model oceanic trends averaged over CP averaged over the CP period. (A) Total ocean effect (shading, °C.month^{-1}) and ratio of contributions of horizontal processes over vertical processes, each in time-average (black contours), **(B)** Vertical processes effect (shading, °C.month^{-1}) and mixed layer depth (MLD, black contours, m), **(C)** vertical diffusion coefficient (shading, m^2.s^{-1}) and square of the vertical shear at the base of the ML (black contour, s^{-2}), and **(D)** vertical temperature gradient at the base of the ML (shading, °C.m^{-1}) and the 19°C isotherm depth (black contours, m).

17°N, the intense CJ, southward and geostrophic, dominates almost always the total effect. It advects upwelled waters and spread the cooling, particularly north of Cape Timiris (∼19.5°N). Interestingly, there within 100–200 km from the shore, the cross-shore component of the SST gradient is sometime reversed with warmer waters inshore, which explains the warming effect of the north-westward Ekman drift. To the south however, until the Cape Verde Peninsula, the CJ cross-shore component is sometimes eastwards and warms the coast, through advection of offshore waters. Hence along south Mauritania and northern Senegal from 20 to 15°N, the CJ is not systematically causing cooling, which instead results from the ageotrophic flow. From 15 to about 12.5°N, the balance is comparable to north of Cape Timiris. There is a net cooling effect explained essentially by the CJ. At 12°N, one remarks the Senegal-Mauritania meridional front [42], maintained by the upwelling and the CJ to the north, and the intense geostrophic poleward SLJ to the south, which transports warm water alongshore. South of 12°N, both the SLJ and the southward Ekman currents are flowing in large part along homogeneous warm SST, and become thus less important for the SST change.

Farther offshore, west of about 18°W, and on regional scales, the SST shows weaker fronts, and advection is hence less intense. North of the CVA in particular, weak SST gradients explain the weak effect of advection. To the contrary, around the CVA and south of about 15°N, the advection pattern explains in large part the net ocean contribution, with intensities generally larger than those of vertical processes. In particular, the maximum net cooling visible at latitudes 12–16°N appears to be due, to the east, to westward advection of coastal waters by Ekman drift (**Figure 8B**) and, to the west, to southward advection by the Guinea gyre geostrophic circulation (**Figure 8C**). Finally, to the south of ∼12°N, the warming longitudinal band is due to geostrophic MC and Ekman drift poleward transports, whereas the cooling pattern to the south-east is explained by the equatorward component of the NECC and the Ekman currents.

To complete the study of horizontal processes, it is worth saying that the diffusion term is significant nearshore with an

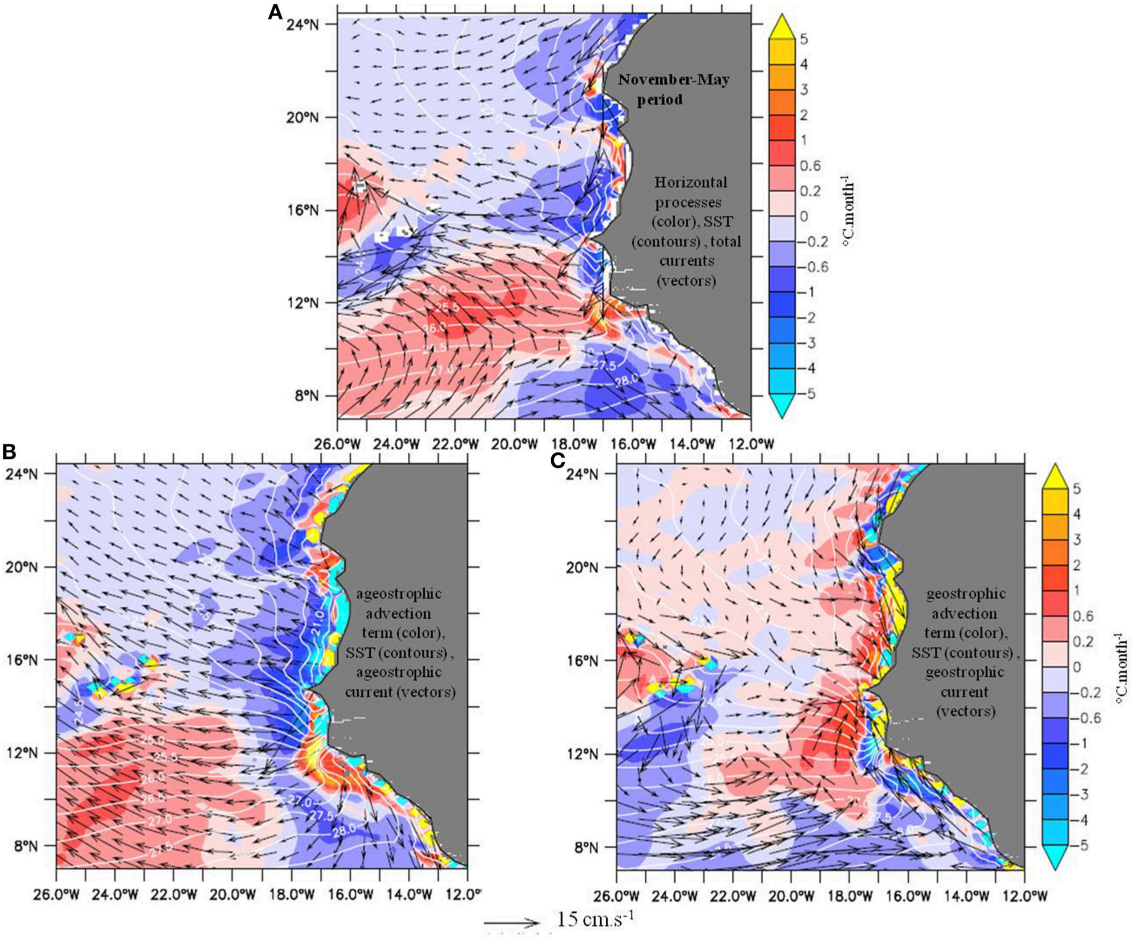

FIGURE 8 | Horizontal processes effect in the model averaged over the CP. (A) Sum of horizontal advection and lateral diffusion (shading, °C.month^{-1}), total currents (black vectors), **(B)** Ageostrophic advection term (shading, °C.month^{-1}), ageostrophic currents (black vectors), and **(C)** geostrophic advection term (shading, °C.month^{-1}), geostrophic currents (black vectors), and SST (white contours).

intensity reaching locally up to ∼1°C.month^{-1} between 10 and 19°N (not shown). Lateral temperature gradients and mesoscale eddies are stronger there. The warming tendency is consistent with the current understanding of the role of mesoscale turbulence [43] and with its manifestations in upwelling systems [44, 45]. Given our limited horizontal resolution, it is largely through lateral diffusion that these processes manifest themselves.

Now we proceed to the examination of the air-sea heat flux contribution (**Figure 9A**). Its structure is comparable to its annual mean (e.g., opposite to **Figure 6A**), except for a large domain of negative values, instead of positive, to the north-west of about (12°N, 19°W), and higher values along Mauritania and Morocco, as noted for all previous terms. The general structure is hence a coastal maximum, a rapid decrease until near 18°W where the sign changes, and a moderate decrease westward. Such a distribution is evidently due to that of the net heat flux (**Figure 9B**). The comparison of the radiative and turbulent components (**Figures 9B,C**) highlights that the second explains most of the pattern, since it varies zonally much more than the solar heat flux. Such variations east of about 18°W are explained in large part by the SST distribution. Close to the continent indeed, latent heat flux patterns are comparable to those of SST, due to a strong modulation of surface specific humidity. Similarly one observes minimum heat loss over cold coastal waters, north of the Senegal-Mauritania front (∼12°N), and larger loss over the warm SLJ to the south nearshore (**Figure 9C**). The large-scale tilt in the distribution of the trade winds speed explains the more regular decrease of the net heat flux west of about 18°W. At last it is important to note that the zonal decrease of the air-sea flux contribution between the continent and about 18°W is in large part also explained by the sharp increase of the MLD (see **Figure 7B**) since it is in the denominator of term D in Equation (1). In conclusion, in the vicinity of the continent east of ∼18°W, it is mainly SST and MLD structures, associated with coastal upwelling dynamics, which explain the intense damping of the oceanic processes by the air-sea fluxes. West of ∼18°W, the westward increase of the trade winds speed explains the progressive passage to a more classical winter cooling regime by air-sea fluxes, to the exception of the CVA where local wind reduction in the lee of islands generates a net heat gain by the ocean.

Overall, the comparison between ocean and air-sea fluxes contributions (see ratio of both contributions on **Figure 9A**) confirms that there are two main regimes for the region. East of 18°W, the ocean processes associated with coastal upwelling dynamics dominate the time-average cooling, whereas the air-sea fluxes damps it. West of this longitude band, the same opposition holds within the 12–18°N latitude band only, where the maximal net SST cooling centered at (16°N, 18°W) (**Figure 3B**) is due mainly to Ekman drift of cold coastal waters. North and south however, the air-sea fluxes dominate the ocean processes by at least a factor two. Note though that since the periods for time-averages were chosen to emphasize coherence in upwelling dynamics, ocean effect appears relatively intense. The net-air-sea flux in fact changes sign during CP, but explains month-to-month SST variations in large parts of the region, as we will see in Section The Sub-domain Next to the Continent.

June–October Warming Period

This period corresponds in time-average to a warming of the domain. The northward migration of the ITCZ causes a decrease of the coastal Ekman pumping south of 18°N, and an increase north of it (**Figure 2**). During WP, the contribution of the net air-sea heat flux is dominant over most of the domain as we will see, and we begin the analysis with it.

Figure 10 displays its time-mean contribution, and components. Overall the distribution resembles its annual mean. Compared to the CP mean, the structures of all quantities still display a rapid zonal variation of intensity from the coastline to about 18°W. Contrasts in longitude are weaker between 12 and 18°N, as expected from the lesser intensity of coastal dynamics associated with weaker Ekman pumping there. North of 15°N the air-sea flux effect decreases westward, first rapidly by a factor of ∼2 and then smoothly by ∼2 again (**Figure 10A**). It is due to the net air-sea flux distribution (**Figure 10B**), and also to the MLD westward increase (**Figure 3D**), both of them explaining the zonal change in roughly equal proportion. The net air-sea flux decrease arises from its turbulent component only, since solar radiation absorbed in the ML increases slightly westward (contours in **Figure 10B**). The turbulent heat loss is indeed rising to the west, due in main part, to SST distributions shaped by ocean circulation, in particular coastal dynamics associated with weak Ekman pumping (**Figure 2**). In the 15–20°N latitude band, it is also due to the wind speed increase to the west. To the north the wind speed decreases westward and effect on turbulent cooling is dominated by the SST increase. This result is consistent with the analysis by Foltz et al. [22] that also invokes the control by air-sea humidity gradients north of 20°N.

Regarding the abrupt meridional decrease of the net air-sea flux contribution in the south, it results from the combination of minimum incoming shortwave radiation (not shown) associated with the ITCZ cloud cover, and intensifying turbulent cooling due to equator-ward acceleration of the southern trade wind south of the ITCZ (white contours in **Figure 10C**). However the net air-sea flux is positive almost everywhere, and the net cooling contribution to the ML heat budget visible south of the ITCZ diagonal (**Figure 10A**) can only be due to the fraction of the solar flux that penetrates below the ML. This process will be confirmed by the examination of vertical processes contribution.

To conclude, it is worth noting the predominance in the net SST warming of the air-sea fluxes over the ocean processes north of the ITCZ region, whereas south of it, the weak SST variations are rather dominated by the ocean contribution.

Now we turn to the ocean contribution shown in **Figure 11A**. Its general structure is comparable to the annual mean, but for larger intensities to the north and south of the domain. The comparison with the contribution of vertical processes (**Figure 11B**) is striking and indicates that it explains most of the ocean contribution pattern. The ratio with the contribution of horizontal processes (contours in **Figure 11A**) shows however that north and south of the domain, horizontal processes are comparable contributors in terms of intensity. As during CP, the vertical processes contribution is dominated by far by vertical diffusion (not shown), but there are significant changes to this term compared to CP. First a domain scale latitudinal dipole appears on both sides of the ITCZ diagonal, and second the open-ocean diffusive cooling develops northward and westward, forming a relative maxima centered at (17°N, 19°W) (**Figure 11B**). Off-line reconstruction of the vertical diffusion effect indicates that is in large part explained by the vertical temperature gradient at the ML base, rather than by the vertical diffusion coefficient K_z (**Figures 11C,D**), except for the intensified Morocco upwelling. It is hence different than during CP. K_z is more homogeneous zonally and exhibits higher values far from the continent, possibly due to the weaker stratification at this period that is favorable to turbulence. Therefore the latitudinal variations of vertical stratification at the ML base become determining (**Figure 11D**), despite smaller values during this warming season. This relative weakness may seem surprising considering the intense seasonal surface warming, but during WP, a significant fraction of the solar radiation penetrates below the thin ML, and contributes to shaping smooth vertical profiles of temperature.

To explain the meridional structure of the subsurface stratification, it is first necessary to recall that the seasonal shift of the ITCZ is responsible of a northward shift of the open-ocean upwelling, which in turn lifts the thermocline (**Figure 4D**) and tends to enhance stratification north of about 15°N. Moreover, the ITCZ rainfall gives rise to barrier-layers, and associated temperature inversions at the ML base (**Figure 11D**) [41]. Consequently, vertical turbulence warms SST there. Looking at the diffusive warming and inversions distribution, it appears that it results from a combination of the large scale barrier layer distribution associated with the ITCZ and NECC [41], and from a narrow coastal band reaching further north up to the Cape Verde Peninsula, likely due to advection of equatorial fresh waters by the SLJ as well as local seasonal rainfall.

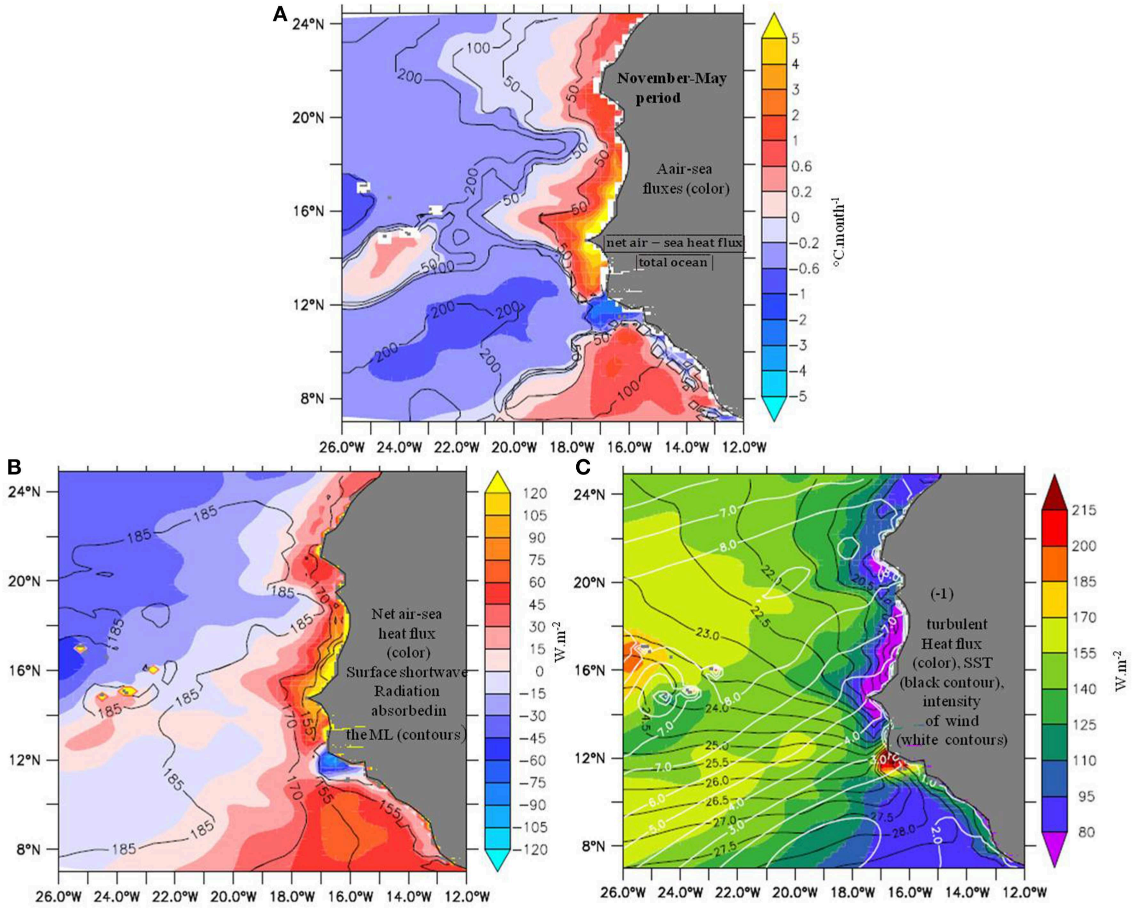

FIGURE 9 | Contribution of air-sea heat fluxes to the ML heat budget over the CP. (A) trend associated with the net air-sea heat flux (shading,°C.month^{-1}) and ratio of net air-sea heat fluxes effect over total ocean effect (black contours), **(B)** net air-sea heat flux (shading, W.m^{-2}) and surface shortwave radiation absorbed in the ML (black contours), **(C)** turbulent heat fluxes (latent+sensible) (shading, W.m^{-2}), SST (black contours, °C) and intensity of wind stress (white contours, N.m^{-2}). The sign of latent heat flux (<0) has been changed.

Note that in line with other coastal modifications between CP and WP described above, large horizontal diffusion effects are displaced northward offshore Mauritania and Morocco coasts (not shown). Their intensities reach up to 0.6°C.month^{-1}, corresponding to mesoscale eddy activities accompanying coastal upwelling.

During WP, horizontal advection still plays a significant role in the evolution of the SST, except for the zonal band located between 17 and 20°N. There it represents less than a quarter of the vertical oceanic processes (**Figure 11A**) due to currents largely parallel to the isotherms. Near-shore to the north of the domain, the cooling is essentially due to Ekman drift that follows the ITCZ migration (**Figures 12A,B**). It is shifted northward with a marked extreme and a large cross-shore extension north of 21°N. Around this latitude, warming occurs just at the coast because upwelling and SST minima are found at some distance offshore, as observed by Barton et al. [46], due to the wide plateau which affects structure and intensity of the upwelling. Interestingly, from Cape Timiris to the Cape Verde Peninsula within 100-300 km from the shore off Senegal and Mauritania, the imbalance between Ekman cooling and geostrophic warming by the MC (**Figure 12C**), is in favor of Ekman flow. This ageostrophic cooling reinforces the vertical processes cooling from the coastal upwelling (**Figures 11B**, **12A,B**). Hence the simulation suggests that the WP time-mean net current contribution is dominated by the MC warming effect only far off-shore, west of 18°W. To the opposite, just south of Cape Verde Peninsula, the advection of warm waters brought by the MC dominates the Ekman drift, which leads to net warming by advection (**Figures 12A–C**). On the continental shelf south of 12°N, a coastal SST maximum leads to the same type of compensation between geostrophic currents (cooling) and Ekman drift (warming), described above for southern Morocco, with overall a weak advective effect on SST. West of 18°W, the modulation of the advective effects associated with the Cape Verde islands is unchanged relative to CP (**Figures 8A**, **12A**). South of 12°N, the net warming by advection is due to the generally constructive contributions of Ekman and geostrophic

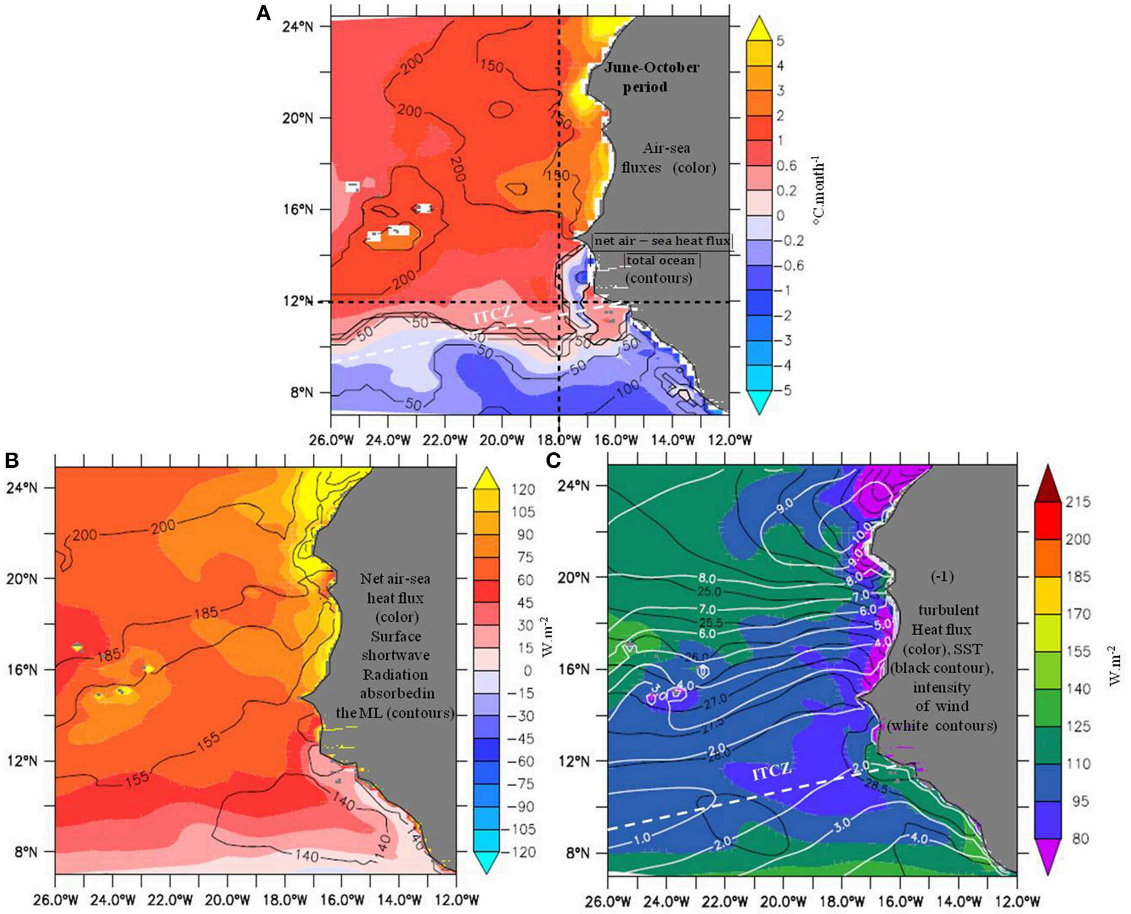

FIGURE 10 | Same as in Figure 9 but over WP (June–October).

(NECC) flows. Despite the high resulting velocities, the warming tendency remains modest because the temperature gradient in the area is weak.

Considering the insights provided by the above spatial analysis, a finer understanding of the leads and lags between processes of the heat budget can be obtained by latitude-time diagrams of the zonally averaged terms. In the following, we present one diagram for each sub-domain, first for the continental zone east of 18°W, and second for the open-ocean area to the west. We focus on time transitions between heat budget regimes. Note that averaging coastal data over a varying distance corresponding to the plateau width offers similar results.

The Sub-domain Next to the Continent

Two latitudinal sectors emerge from **Figure 13A**. North of 12°N the SST experiences an annual cycle, whereas to the south it is semi-annual and forced by the two passages of the ITCZ (**Figure 13A**). As seen before, the strongest SST variations ($>2°$C.month^{-1}) occur approximately from 12° to 20°N. At first sight the overall variations are in good phase with the net air-sea flux contribution (**Figure 13B**). We first study the cooling phases, which start early September north of the Cape Verde Peninsula, and later on further south (until December). North of ~20°N, the SST cooling phase is driven by the decrease of the net air-sea flux, warming effect, that become smaller than the cooling by upwelling dynamics. It is obviously due to the seasonal attenuation of solar radiations. The relative high intensity of the cooling effect by ocean processes is essential to the heat budget evidently, but not for its change from a net positive to net negative trend. It is not a driver since it entered a decreasing phase around this period, explained by the attenuation of the trade winds (**Figure 4**) and associated Ekman pumping (**Figure 2**). From ~20°N to the Cape Verde Peninsula (15°N), to the contrary the cooling effect by ocean processes strongly increases from early September to mid-October (from about −1 to ~ −2.5°C.month^{-1}, **Figure 13C**), due to intensification of vertical turbulent mixing and along-shore southward advection, generated by the strengthening of the winds (**Figures 2**, **4**, **13D,E**). Note that horizontal processes, largely dominated by advection, have a cooling effect generally more than half as intense as the vertical processes (contours in **Figure 13E**). During this period, the warming effect by air-sea fluxes decreases in smaller proportions (from about 1 to ~0.5°C.month^{-1}), thereby contributing slightly to the net cooling. The SST cooling peak

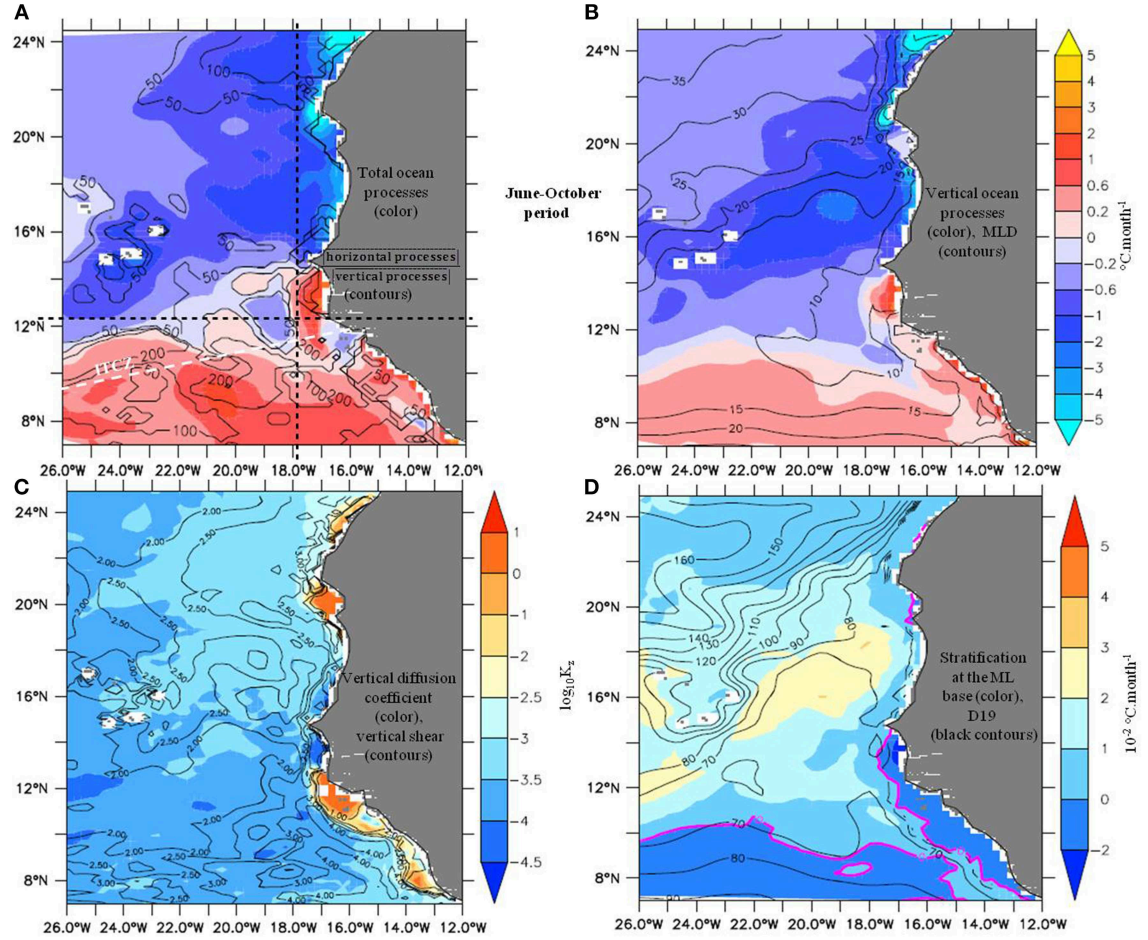

FIGURE 11 | Same as in Figure 7 but over WP (June–October).

in October is therefore explained by the constructive effects of both family of processes, dominated by the upwelling dynamics. From November to February, essentially the upwelling dynamics maintain the cooling rate. South of 15°N, it is clear that net air-sea flux again controls the early months of the cooling season. There, seasonal temperature inversion effects (**Figure 13D**) as well as northward advection of warm waters by the MC and SLJ (**Figure 13E**) warm the SST to the contrary.

The second period of particular interest is the period when SST has reached minimum annual values, and starts to increase again, in March-April at all latitudes. It is almost everywhere a period of cooling by oceanic processes, especially intense south of Cape Timilis (∼20°N) where Ekman pumping and upwelling velocities increase (**Figure 2** and contours in **Figure 13D**). Vertical turbulent processes dominate the cooling (see ratio in contours, **Figure 13C**), whereas coastal horizontal currents favor or oppose them depending on latitude, as discussed in previous sections. The only exception is over the Senegal-Mauritania front (11-12°N), where the SST warming appears to be due primarily to the poleward advection of warm waters along-shore by the SLJ and off-shore spreading by the Ekman drift. Nevertheless, it is overall the seasonal increase of the net air-sea flux that sets the start of the warming season, whereas ocean processes act to reduce or delay the warming.

The Open Ocean

We now focus on the area west of 18°W. The SST temporal changes are broadly similar to those next to the continent, but share a much stronger resemblance with the net air-sea flux term (**Figures 14A,B**). In more details, the air-sea fluxes contribution displays everywhere the same pattern as the SST change. It is more intense most of the time, though, since the oceanic processes oppose it quasi systematically (**Figures 14B,C**). Two regions of exception deserve attention: north of ∼18°N when the oceanic processes contribute weakly to the forcing of the SST decrease by the air-sea fluxes (October–February), and south of 10°N in September-October when the ocean forces mainly the second semi-annual warming. Overall, air-sea fluxes set the positive and negative trends in SST over most of the domain. Interestingly the ocean counter-action is not a mere passive damping. Indeed during WP, wind-driven vertical currents (contours in **Figure 14D**) amplify stratification and turbulent

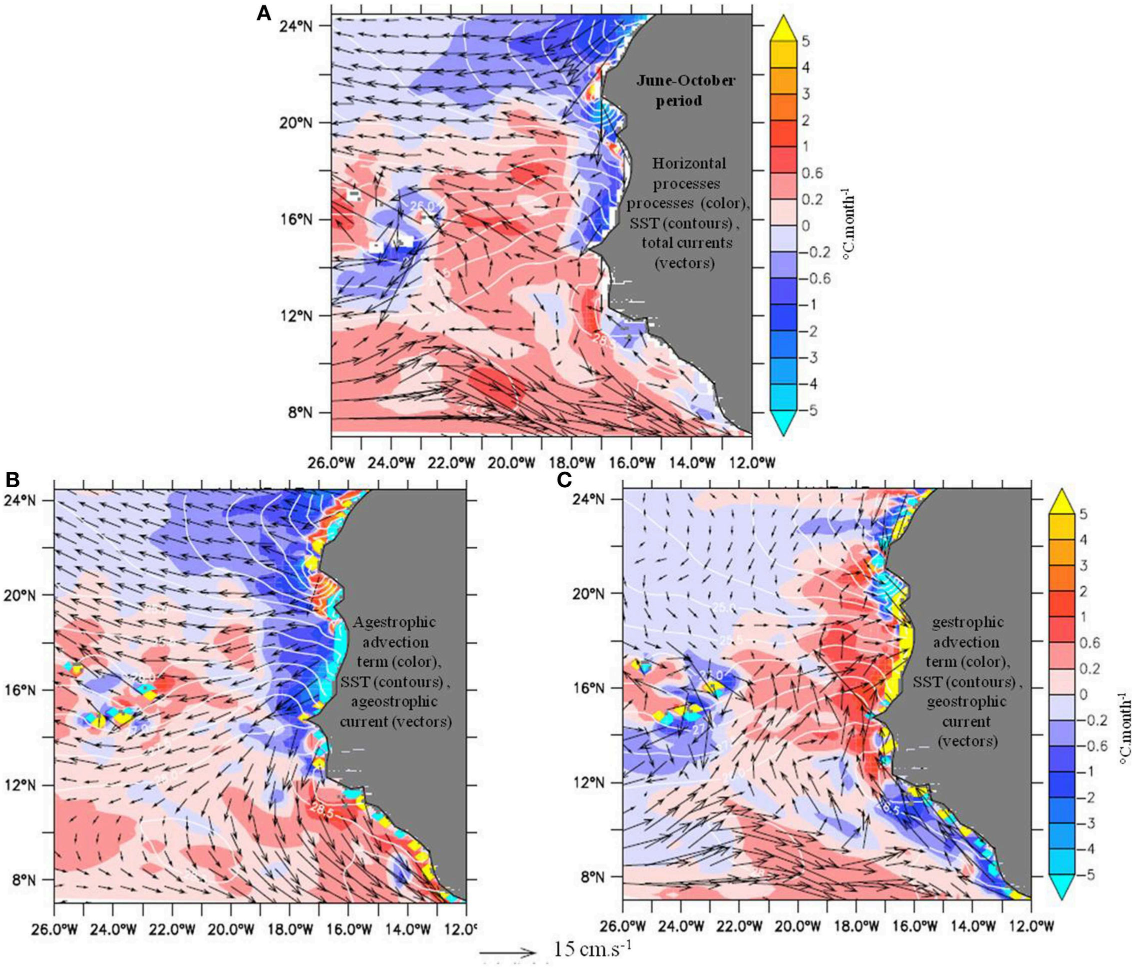

FIGURE 12 | Same as in Figure 8 but over WP (June–October).

cooling, especially near 16°N as discussed in **Figure 11**. To the south, temperature inversions associated with ITCZ barrier layers restore to the surface the heat from solar radiations that penetrate below the ML (see especially **Figure 11D**). From 8 to 10°N they oppose the July cooling, but set the following warming. Additionally throughout the year horizontal advection, discussed in previous sections, also contribute to oppose the net air-sea flux effect (**Figure 14E**). Considering the spatial distributions analyzed previously, these results, derived in average, are more representative of the western part of the sub-domain. Indeed, closer to the continent and the islands, oceanic effects have larger amplitudes relative to the net air-sea flux (see **Figures 9**, **10**). Also recall that the CP time-average had shown a positive mean contribution of the air-sea fluxes during the net SST cooling. This apparent contradiction, is due to the consistency of the sign of the ocean processes term over CP (negative during 4 out 6 months) relative to that of the net air-sea flux effect during the same period (half time negative, half time positive). Nevertheless, the main sign changes of the SST trend, in March and in September-October are driven by the net air-sea flux effect.

Summary and Discussions

In this study, the seasonal cycle of the SST in the Atlantic North-eastern Tropical Upwelling System (ANETUS) is examined using a ML heat budget, in a numerical simulation of the Tropical Atlantic. The ANETUS domain is characterized by the presence of the continent to the east, the Guinea upwelling gyre and Guinea Dome, and the presence of the ITCZ. The contribution of the ocean processes to the heat budget is the focus of our study, and particularly the heat fluxes at the base of the ML that is difficult to compute from existing observations. Two main heat budget regimes emerge in annual mean on both sides of schematically latitude 12°N (related to the mean ITCZ location) and are quite representative of the time-varying contribution of ocean processes. Roughly, to the north, the mean regime is characterized by a tendency to cool the ML by ocean processes, generally dominated by vertical turbulent mixing intensified by Ekman pumping. To the south, the ocean processes tend generally to warm the surface, through advection by NECC, MC or SLJ and temperature inversions, and against a time-mean

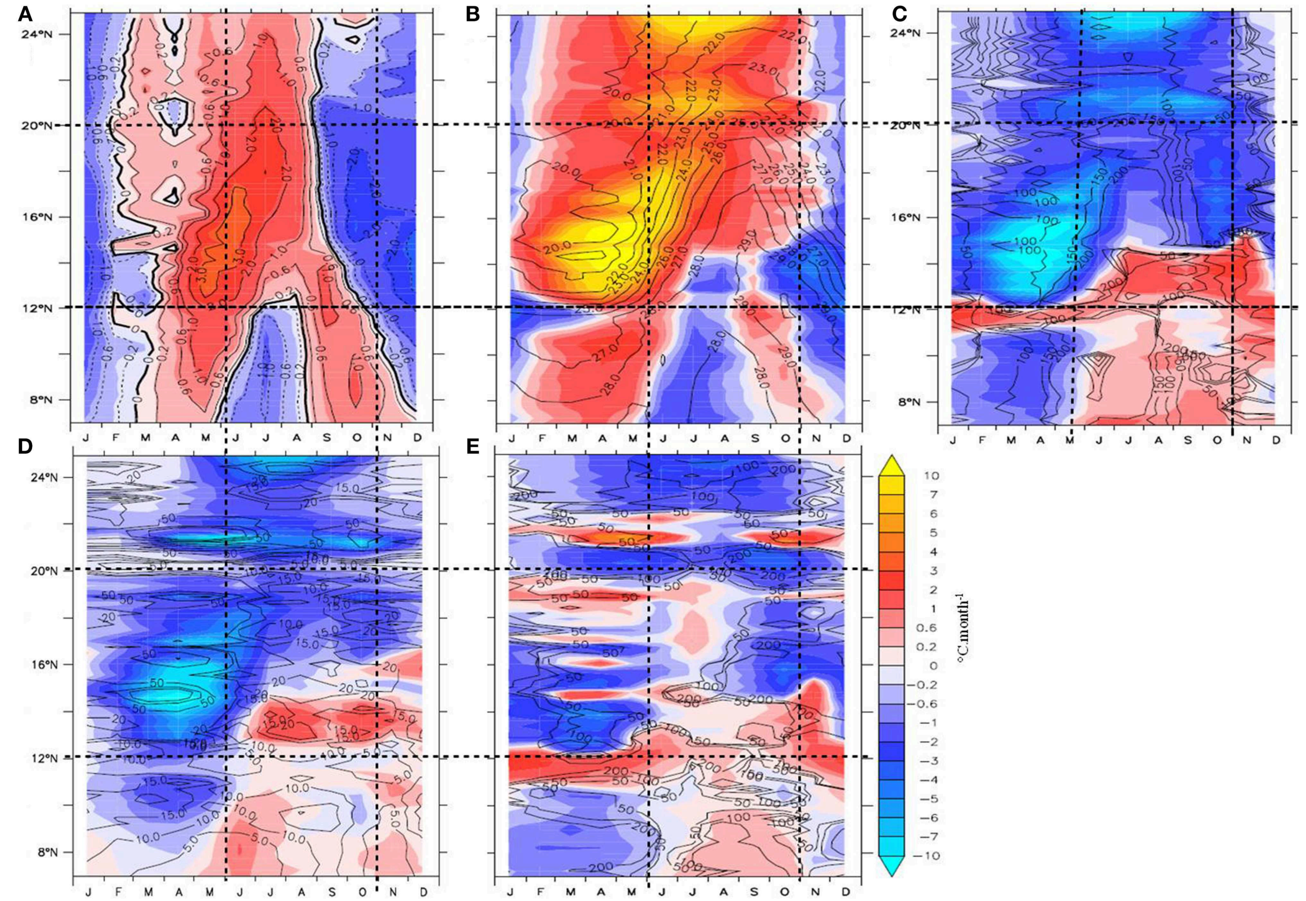

FIGURE 13 | Latitude-time Hovmöller plots along the coastal region (averaged from the coast to 18°W) of the mean seasonal cycles. (A) model total temperature trend (shading and contours, °C.month^{-1}), **(B)** air-sea heat vertical process (shading), and SST model (contours, °C), **(C)** total oceanic trend (shading, °C.month^{-1}) and ratio of net air-sea flux effect over ocean effect (contours, %), **(D)** trend associated with vertical processes (shading, °C.month^{-1}) and maximum vertical velocities between surface and thermocline (contours, m.month^{-1}) and **(E)** horizontal processes (shading, °C.month^{-1}) and ratio of horizontal processes over vertical processes (contours, %).

cooling by air-sea fluxes. The seasonal variations of the SST can be described by a CP of decreasing and then minimum SST (November-May), and a WP (June–October) of increasing SST reaching a maximum in summer. Both are, respectively, associated with maximum then minimum coastal upwelling south of ∼20°N (Cape Timilis), and vice-versa north of the Cape. Two sub-domains in terms of ocean circulation and heat budget are separated grossly by longitude 18°W: a narrow continental band of a few degrees of longitude next to West-Africa characterized by ocean frontal dynamics and intense signals, and a vast open ocean region to the west that displays smoother fields and weaker signals. The seasonal heat budget explaining the SST cycle is:

(1) *The continental band:* the cooling starts early September north of the Cape Verde Peninsula. North of Cape Timilis, it is driven by the decrease of the net air-sea flux warming effect, due to the seasonal attenuation of solar radiation. It is damped by the decrease of the upwelling-forced cooling trend, due to the seasonal Ekman pumping attenuation. South of 20°N, down to the Cape Verde Peninsula (15°N), the constructive effects of both air-sea fluxes and, in larger proportion, upwelling dynamics, explain the SST cooling and its October peak of intensity. Later on the latter dominates the cooling season. From 15 to 7°N and from October to December, the net air-sea flux negative trend triggers the cooling, whereas temperature inversion and warm geostrophic currents damp it. Regarding the second phase of the SST cycle, the start of the warming season, regardless of latitude, is forced by the net air-sea flux, and damped by upwelling dynamics.

(2) *The open ocean:* The cooling and warming phases are fundamentally driven by the seasonal net air-sea flux effect, against the oceanic processes that partly oppose it, except north of 18°N particularly. The March SST cooling is slightly amplified by the intensifying Guinea Gyre upwelling in summer-autumn, which tends to cool the surface by turbulent mixing, especially near 16°N. Further south,

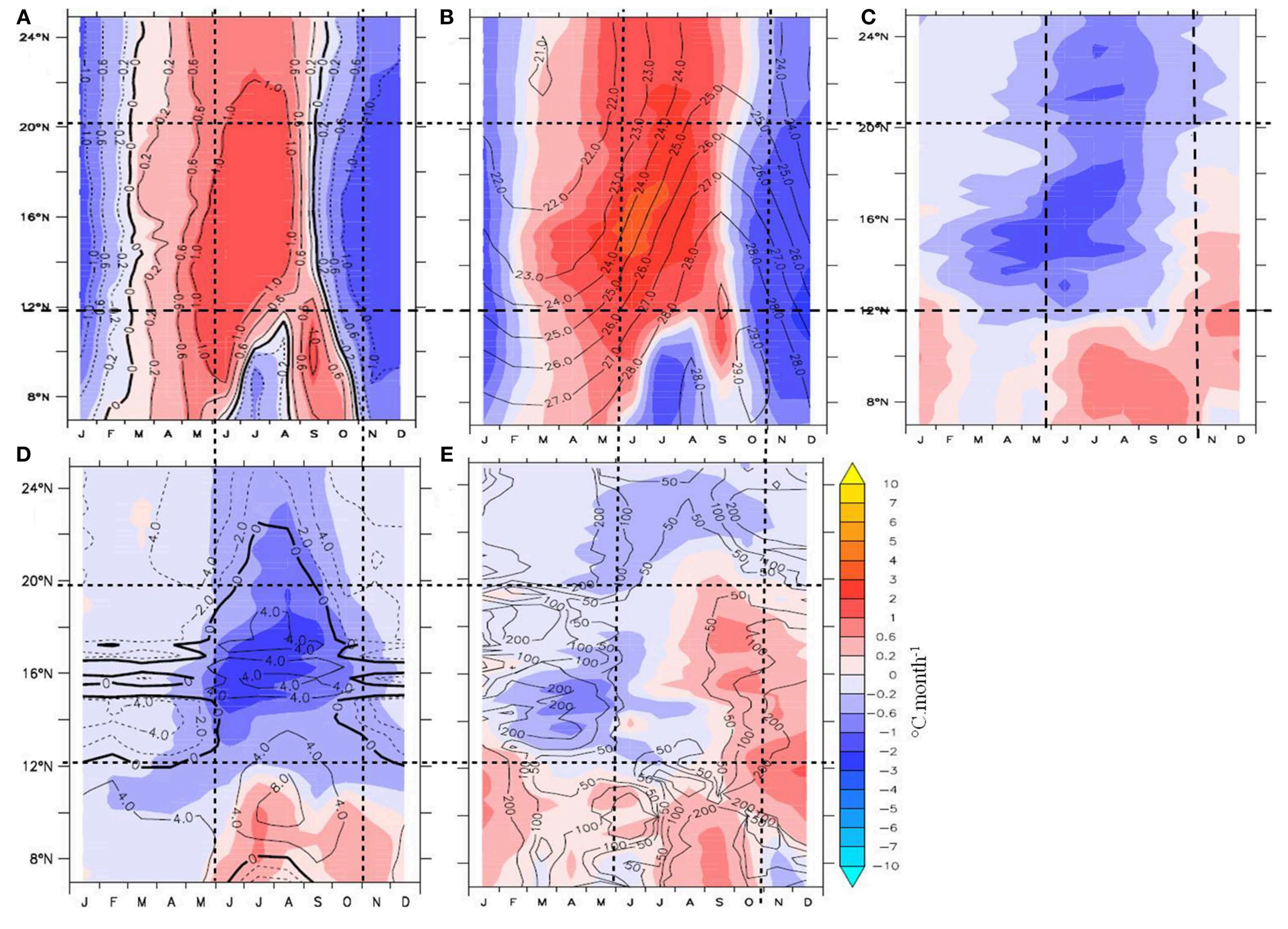

FIGURE 14 | Same as in Figure 13 but for the heat budget terms averaged between18°W and 26°W.

warming by temperature inversions and horizontal currents, opposes the net air-sea flux effect.

Near the continent, our results support the preliminary model study by Carton and Zhou [20] pointing out to the leading role of wind-driven coastal upwelling dynamics for the SST cycle from 10 to 20°N. It is however verified only for the cooling phase from September to early March. The warming phase starting in March-April in our simulation is driven instead by the seasonal increase of the solar radiations. The detailed analysis of the upwelling dynamics suggests that the total horizontal contribution represents more than 50% of the effect associated with vertical processes in general. North of 20°N and south of 12°N, it is often stronger than the effect of vertical processes. Advection of waters, especially from the north, is therefore an essential contributor to the coastal upwelling system heat budget, when SST is in its decreasing phase. Over the open ocean, west of ∼18°W, our result supports most of those of Foltz et al. [22]. South of the mean ITCZ location however, we could evidence warming by vertical turbulent processes associated with temperature inversions, found within barrier layers in the region. Due to these inversions, we found that the Guinea Dome upwelling is able to generate a surface cooling only in the northern half of the GD area. It clarifies the results from Yamagata and Iizuka [7], pertaining to the thermocline and not to the ML, which explained the decrease in heat content by horizontal and vertical divergence of the heat transport in all GD.

Our model results are limited by inherent errors due to the relatively low horizontal and vertical resolution near the coast, and uncertainties in air-sea fluxes. Despite the biases in the represented thermocline, ML and mesoscale structures, we hope that our paper can provide nevertheless a relevant basis for further studies of the variability of SST and currents in the ANETUS, in particular at other challenging time-scales, like intra-seasonal and interannual ones.

Important limitations in the present study are due to the scarcity of *in-situ* observations. Additional studies of ocean currents, upper ocean turbulence and mixing, and more robust estimates of air-sea heat fluxes are needed offshore West Africa. This will require the implementation of measuring instruments to monitor the coastal region over long time periods, such as fixed moorings performing oceanic and atmospheric measurements. Such measurements will allow us to better evaluate numerical models and improve our understanding of regional ocean-atmosphere exchanges and climate variability.

Acknowledgments

The research leading to these results has received funding from Centre de Recherche Océanographique Dakar-Thiaroye (CRODT/ISRA), Dakar-Sénégal and the International Joint Laboratory LMI ECLAIRS, as well as from the EU FP7/2007-2013 under grant agreement no. 603521. We thank B. Diaw, C. Ndour, H. Diadhiou, M. Fall, and Patrice Brehmer for their essential support throughout this study, and X. Capet. We are grateful to the anonymous reviewers for his helpful comments.

References

1. Carton J, Huang B. Warm events in the Tropical Atlantic. *J Phys Oceanogr.* (1994) **24**:888–903.
2. Chang P, Yamagata T, Schopf P, Behera SK, Carton J, Kessler WS, et al. Climate fluctuations of tropical coupled systems: the role of ocean dynamics. *J Clim.* (2006) **19**:5122–74. doi: 10.1175/JCLI3903.1
3. Lathuilière C, Echevin V, Lévy M. Seasonal and intraseasonal surface chlorophyll-a variability along the northwest African coast. *J Geophys Res.* (2008) **113**:C05007. doi: 10.1029/2007jc004433
4. Siedler G, Zangenberg N, Onken R, Molie're A. Seasonal changes in the tropical Atlantic circulation: observation and simulation of the Guinea Dome. *J Geophys Res.* (1992) **97**:703–15. doi: 10.1029/91JC02501
5. Lazar A, Inui T, Malanotte-Rizzoli P, Busalacchi AJ, Wang L, Murtugudde R. Seasonality of the ventilation of the tropical Atlantic thermocline. *J Geophys Res.* (2002) **107**:3104. doi: 10.1029/2000JC000667
6. Jiang H, Huang RX, Wang H. Role of gyration in the oceanic general circulation: Atlantic Ocean. *J Geophys Res.* (2008) **113**:C03014. doi: 10.1029/2007jc004134
7. Yamagata T, Iizuka S. Simulation of the tropical thermal domes in the Atlantic: a seasonal cycle. *J Phys Oceanogr.* (1995) **25**:2129–40.
8. Wooster, W, Bakun A, McLain D. The seasonal upwelling cycle along the eastern boundary of the North Atlantic. *J Mar Res.* (1976) **34**:131–41.
9. Allen JS. Upwelling and coastal jets in a continuously stratified ocean, *J. Phys Oceanogr.* (1973) **3**:245–57.
10. Hagen E. Mesoscale upwelling variations off the West African coast. In: Richardson FA, editor. *Coastal and Estuarine Sciences, Vol. I, Coastal Upwelling.* Washington, DC: AGU (1981). pp. 72–8. doi: 10.1029/co001p0072
11. Hagen E. Northwest Africa upwelling scenario. *Oceanol Acta* (2001) **24**(Suppl. 1):113–28. doi: 10.1016/S0399-1784(00)01110-5
12. Mason E, Colas F, Molemaker J, Shchepetkin AF, Troupin C, Sangrà P, et al. Seasonal variability of the Canary current: a numerical study. *J Geophys Res.* (2011) **116**:C06001. doi: 10.1029/2010jc006665
13. Mittelstaedt E. The ocean boundary along the northwest African coast: circulation and oceanographic properties at the sea surface. *Prog Oceanogr.* (1991) **26**:307–55. doi: 10.1016/0079-6611(91)90011-A
14. Stramma L, Huttl S, Schafstall, J. Water masses and currents in the upper tropical northeast Atlantic off northwest Africa. *J Geophys Res.* (2005) **110**:C12006. doi: 10.1029/2005JC002939
15. Lazaro C, Fernandes-Santos M, Oliveira P. Seasonal and interannual variability of surface circulation in the Cape Verde region from 8 years of merged t/p and ers-2 altimeter data. *Rem Sens Environ.* (2005) **98**:45–62. doi: 10.1016/j.rse.2005.06.005
16. Barton ED. Eastern boundary of the North Atlantic : Northwest Africa and Iberia. In: Robinson AR, Brink K, editors. *In The Sea*, Vol. 11. New York, NY: John Wiley and Sons, Inc. (1998). p. 633–57.
17. Mazeika PA. Thermal domes in the eastern tropical Atlantic Ocean. *Limnol Oceanogr.* (1967) **12**:537–9. doi: 10.4319/lo.1967.12.3.0537
18. Doi T, Tomoki T, Toshio Y. Interannual variability of the Guinea Dome and its possible link with the Atlantic Meridional Mode. *Clim Dyn.* (2009) **33**:985–98. doi: 10.1007/s00382-009-0574-z
19. Doi T, Tomoki T, Toshio Y. The Atlantic Meridional Mode and its coupled variability with the Guinea Dome. *J Clim.* (2010) **23**:455–75. doi: 10.1175/2009JCLI3198.1
20. Carton JA, Zhou ZX. Annual cycle of sea surface temperature in the tropical Atlantic Ocean. *J Geophys Res.* (1997) **102**:27813–24. doi: 10.1029/97JC02197
21. Yu LS, Jin, XZ, Weller, RA. Role of net surface heat flux in seasonal variations of sea surface temperature in the tropical Atlantic Ocean. *Clim J.* (2006) **19**:6153–69. doi: 10.1175/JCLI3970.1
22. Foltz G, Schmid C, Lumpkin R. Seasonal cycle of the mixed layer heat budget in the Northeastern Tropical Atlantic Ocean. *J Clim.* (2013) **26**:8169–88. doi: 10.1175/JCLI-D-13-00037.1
23. Nykjaer L, van Camp L. Seasonal and interannual variability of coastal upwelling along northwest Africa and Portugal from 1981 to 1991. *J Geophys Res.* (1994) **99**:14197–207. doi: 10.1029/94jc00814
24. Santos MP, Kazmin AS, Peliz A. Decadal changes in the Canary upwelling system as revealed by satellite observations: their impact on productivity. *J Mar Res.* (2005) **63**:359–79. doi: 10.1357/0022240053693671
25. Bonjean F, Lagerloef GSE. Diagnostic model and analysis of the surface currents in the Tropical Pacific Ocean. *J Phys Oceanogr.* (2002) **32**:2938–54. doi: 10.1175/1520-0485(2002)032<2938:DMAAOT>2.0.CO;2
26. de Boyer Montégut C, Madec G, Fischer AS, Lazar A, Iudicone D. A global mixed layer depth climatology based on individual profiles. *J Geophys Res.* (2004) **109**:C12003. doi: 10.1029/2004JC002378
27. Madec G. *NEMO Ocean Engine.* Note Pôle Modél. 77. Paris: Inst. Pierre-Simon Laplace (2008).
28. Molines JM, Barnier B, Penduff T, Brodeau L, Treguier AM, Theetten S, et al. *Definition of the Interannual Experiment orca025-g70, 1958 2004.* Technical Report, Laboratire des Ecoulements Geophysiques et Industriels, CNRS UMR 5519, Grenoble (2007).
29. Brodeau L, Barnier B, Tréguier A, Penduff T, Gulev S. An ERA40-based atmospheric forcing for global ocean circulations models. *Ocean Modell.* (2010) **31**:88–104. doi: 10.1016/j.ocemod.2009.10.005
30. Large W, Yeager S. *Diurnal to Decadal Global Forcing for Ocean and Seaice Models: The Data Sets and Climatologies.* Technical Report TN-460+STR. Boulder, CO: National Center for Atmospheric Research, Boulder (2004).
31. Zhang Y, Rossow WB, Lacis AA, Oinas V, Mishchenko MI. Calculation of radiative fluxes from the surface to top of atmosphere based on ISCCP and other global data sets: refinements of the radiative transfer model and the input data. *J Geophys Res.* (2004) **109**:D19105. doi: 10.1029/2003JD004457
32. Vialard J, Delecluse P. An OGCM Study for the TOGA Decade. Part I: role of salinity in the physics of the Western Pacific fresh pool. *J Phys Oceanogr.* (1998) **28**:1071–88
33. Peter A-C, Le Hénaff M, du Penhoat Y, Menkès C, Marin F, Vialard J, et al. A model study of the seasonal mixed layer heat budget in the equatorial Atlantic. *J Geophys Res.* (2007) **111**:C06014. doi:10.1029/2005JC003157
34. Jouanno J, Marin F, du Penhoat Y, Sheinbaum J, Molines J-M. Seasonal heat balance in the upper 100 m of the equatorial Atlantic Ocean. *J Geophys Res.* (2011) **116**:C09003. doi: 10.1029/2010jc006912
35. Roy C. Fluctuation of wind and upwelling variability off the Senegalese coast. *Oceanolo. Acta* (1989) **12**:361–9.
36. Ndoye S, Capet X, Estrade P, Sow, B, Dagorne D, Lazar A, et al. *SST Patterns and Dynamics of the Southern Senegal-Gambia Upwelling Center.* *J Geophys Res.* (2014) **119**:8315–35. doi: 10.1002/2014JC010242
37. Chelton DB, Schlax MG, Freilich MH, Milliff RF. Satellite measurements reveal persistent small-scale features in ocean winds. *Science* (2004) **303**:978–83. doi: 10.1126/science.1091901

38. Estrade P, Marchesiello P, de Verdiere AC, Roy, C. Cross-shelf structure of coastal upwelling: a two-dimensional extension of Ekman's theory and a mechanism for inner shelf upwelling shut down. *J Mar Res.* (2008) **66**:589–616. doi: 10.1357/002224008787536790
39. Austin JA, Lentz SJ. The inner shelf response to wind-driven upwelling and downwelling. *J Phys Oceanogr.* (2002) **32**:2171–93. doi: 10.1175/1520-0485(2002)032<2171:TISRTW>2.0.CO;2
40. Centurioni LR, Ohlmann JC, Niiler PP. Permanent meanders in the California Current System. *J Phys Oceanogr.* (2008) **38**:1690–710. doi: 10.1175/2008JPO3746.1
41. Mignot J, Lazar A, Lacarra, M. On the formation of barrier layers and associated vertical temperature inversions: a focus on the northwestern tropical. *J Atlantic Geophys Res.* (2012) **117**:C02010. doi: 10.1029/2011jc007435
42. Diakhaté M., de Coetlogon G., Lazar A., Gaye AT. Intra-seasonal SST variability within tropical Atlantic upwellings. *Soumis à Q J R Meteorol Soc.* (in press). doi: 10.1002/qj.2657
43. Gent PR, McWilliams JC. Isopycnal mixing in ocean circulation models. *J Phys Oceanogr.* (1990) 20, 150–5.
44. Capet X, Colas F, McWilliams JC, Penven P, and Marchesiello P. Eddies in eastern boundary subtropical upwelling systems. In: Hecht M, Hasumi H, editors. *Ocean Modeling in an Eddying Regime*. Geophysical Monograph Series, Vol. 177. Washington, DC: American Geophysical Union (2008). 131–48. doi: 10.1029/177GM10
45. Colas F, McWilliams JC, Capet X, and Kurian J. Heat balance and eddies in the Peru-Chile current system. *Clim Dyn.* (2012) **39**:509–29. doi: 10.1007/s00382-011-1170-6
46. Barton ED, Huyer A, Smith RL. Temporal variation observed in the hydrographic regime near Cabo Corveiro in the northwest African upwelling region, February to April 1974. *Deep Sea Res.* (1977) **24**:7–23. doi: 10.1016/0146-6291(77)90537-9

Conflict of Interest Statement: The Reviewer Vincent Michel Echevin declares that, despite having collaborated with the author Saliou Faye, and sharing an affiliation with the author Bamol A. Sow the review process was handled objectively. The authors declare that the research was conducted in the absence of any commercial or financial relationships that could be construed as a potential conflict of interest.

frontiers
in Earth Science

ORIGINAL RESEARCH
published: 24 July 2015
doi: 10.3389/feart.2015.00037

Growth and decay of the equatorial Atlantic SST mode by means of closed heat budget in a coupled general circulation model

Irene Polo[1,2]*, *Alban Lazar*[3,4], *Belen Rodriguez-Fonseca*[2,5] and *Juliette Mignot*[3,6]

[1] Department of Meteorology, University of Reading, Reading, UK, [2] Geophysis and Meteorology, Facultad de Ciencias Físicas, Universidad Complutense de Madrid, Madrid, Spain, [3] Laboratoire d'Océanographie et du Climat: Expérimentations et Approches Numériques Laboratory, Sorbonne Universités (UPMC, Université Paris IV)-Centre National de la Recherche Scientifique-IRD-MNHN, Paris, France, [4] Institut de Recherche Pour le Développement-Laboratoire de Physique de l'atmosphère et de l'océan Simeon Fongang, Dakar, Senegal, [5] Instituto de Geociencias (IGEO) UCM-CSIC, Madrid, Spain, [6] Climate and Environmental Physics, Physics Institute and Oeschger Centre of Climate Change Research, University of Bern, Bern, Switzerland

Edited by:
Anita Drumond,
University of Vigo, Spain

Reviewed by:
Ricardo De Camargo,
Universidade de Sao Paulo, Brazil
Rein Haarsma,
Koninklijk Nederlands Meteorologisch Instituut, Netherlands

***Correspondence:**
Irene Polo,
Department of Meteorology, University of Reading, Harry Pitt Building, 287, Earley Gate, Reading RG6 6BB, UK
i.polo@reading.ac.uk

Specialty section:
This article was submitted to Atmospheric Science, a section of the journal Frontiers in Earth Science

Received: *27 February 2015*
Accepted: *25 June 2015*
Published: *24 July 2015*

Citation:
Polo I, Lazar A, Rodriguez-Fonseca B and Mignot J (2015) Growth and decay of the equatorial Atlantic SST mode by means of closed heat budget in a coupled general circulation model. Front. Earth Sci. 3:37. doi: 10.3389/feart.2015.00037

Tropical Atlantic variability is strongly biased in coupled General Circulation Models (GCM). Most of the models present a mean Sea Surface Temperature (SST) bias pattern that resembles the leading mode of inter-annual SST variability. Thus, understanding the causes of the main mode of variability of the system is crucial. A GCM control simulation with the IPSL-CM4 model as part of the CMIP3 experiment has been analyzed. Mixed layer heat budget decomposition has revealed the processes involved in the origin and development of the leading inter-annual variability mode which is defined over the Equatorial Atlantic (hereafter EA mode). In comparison with the observations, it is found a reversal in the anomalous SST evolution of the EA mode: from west equator to southeast in the simulation, while in the observations is the opposite. Nevertheless, despite the biases over the eastern equator and the African coast in boreal summer, the seasonality of the inter-annual variability is well-reproduced in the model. The triggering of the EA mode is found to be related to vertical entrainment at the equator as well as to upwelling along South African coast. The damping is related to the air-sea heat fluxes and oceanic horizontal terms. As in the observation, this EA mode exerts an impact on the West African and Brazilian rainfall variability. Therefore, the correct simulation of EA amplitude and time evolution is the key for a correct rainfall prediction over tropical Atlantic. In addition to that, identification of processes which are responsible for the tropical Atlantic biases in GCMs is an important element in order to improve the current global prediction systems.

Keywords: tropical Atlantic variability, Atlantic Niño, GCM biases, heat budget, upwelling processes, West African rainfall, Brazilian rainfall

Introduction

Tropical Atlantic Variability (TAV) have important impacts over Africa and South America, where rain-fed agriculture is an important part of their economies (Xie and Carton, 2004;

Chang et al., 2006a; Kushnir et al., 2006; Rodríguez-Fonseca et al., 2015). However, historically major efforts have been done in understanding the Tropical Pacific which holds the most important inter-annual variability mode in terms of the global impacts: El Niño and the Southern Oscillation (ENSO, Philander, 1990). The Tropical Atlantic (TA) has received much less attention. Recently, scientific community is focusing attention in understanding model biases over the TA, which is systemic and common problem in coupled General Circulation Models (GCM). These biases could have important consequences in the ability of the models in simulating proper tele-connections which could lead to failure in seasonal to decadal forecasts. This paper is focused in understanding how a GCM simulates the main inter-annual variability mode with major impacts in surrounding areas and its systematic errors.

Inter-annual TAV has been described by two main modes: Equatorial Mode or Atlantic Niño and the Meridional Mode (Zebiak, 1993; Carton et al., 1996; Ruiz-Barradas et al., 2000; Kushnir et al., 2006; also see Xie and Carton, 2004; Chang et al., 2006a, for a revision). The Atlantic Niño presents anomalous SST over eastern equatorial Atlantic, it is phase-locked to the seasonal cycle, mainly occurring from June to September season, when the seasonal equatorial cold tongue develops over the eastern Atlantic associated with a northward Inter-Tropical Convergence Zone (ITCZ)-shift and the West African Monsoon (WAM) onset (Sultan et al., 2003; Okumura and Xie, 2004).

The Atlantic Niño mode is therefore tightly associated with the WAM inter-annual variability (Janicot et al., 1998; Ward, 1998; Giannini et al., 2003; Polo et al., 2008; Losada et al., 2010; Rodriguez-Fonseca et al., 2011; Rodríguez-Fonseca et al., 2015): positive (negative) SST anomalies influence the rainfall over the Gulf of Guinea through a decrease (increase) of the local surface temperature gradient, weakening (strengthening) the monsoon flow and the surface convergence over the Sahel (Vizy and Cook, 2001; Losada et al., 2010).

From observations, the origin of the mode has been mainly associated with anomalous equatorial winds over the western equatorial Atlantic (Zebiak, 1993; Latif and Grötzner, 2000; Keenlyside and Latif, 2007) and the evolution of the SST anomalies is related to positive Bjerknes feedback (Keenlyside and Latif, 2007) and Ekman processes (Hu and Huang, 2007). However, oceanic wave eastward propagation could also play a role in the evolution of the SST anomalies in the eastern Atlantic (Latif and Grötzner, 2000; Florenchie et al., 2003) although ocean waves could also be important in damping the mode (Polo et al., 2008). Finally, a recent study from Richter et al. (2012b) has pointed out other sources for the equatorial SST variability in the observations, such as the oceanic advection from the North Tropical Atlantic (NTA).

However, several studies have found that the Atlantic Niño usually starts over the South Atlantic via a weakening of the Sta Helena high pressure system, reaching the equator later on, where it evolves throughout Bjerknes feedback mechanism (Sterl and Hazeleger, 2003; Keenlyside and Latif, 2007; Trzaska et al., 2007; Polo et al., 2008; Lübbecke et al., 2010). In addition, some authors have highlighted the SST dipole pattern between the equator and the south Atlantic as part of a SST feedback trough changes in the Hadley circulation (Nnamchi and Li, 2011; Namchi et al., 2013).

In the observations, the Atlantic Niño generally appears associated with SST anomalies over the coastal Benguela upwelling region, which usually precedes the equatorial anomalies (Hu and Huang, 2007; Polo et al., 2008). Recently OGM studies have suggested that one season delay between the SST anomalies at the equator and the Benguela coast could be due to different seasonal cycle in the mixed layer depth over these regions (Lübbecke et al., 2010). However observations and models studies have suggested that the occurrence of anomalous SST over the coastal areas is due to alongshore wind anomalies (Richter et al., 2010), while the equatorial SST anomalies are produced by anomalous western equatorial winds together, perhaps, with Rossby wave propagation from the south Atlantic (Polo et al., 2008).

Finally, the equatorial Atlantic Niño could be remotely forced by tele-connections mainly from the Pacific, although the relationship is inconsistent. Chang et al. (2006b) have argued that the ENSO influences the equatorial Atlantic only under a specific ocean state in the Atlantic. Following the former argument, Lübbecke and McPhaden (2012) have discussed the different equatorial Atlantic responses from ENSO forcing and they have pointed out the conditions over the NTA as the responsible for a delayed feedback through Rossby wave propagation. De Almeida and Nobre (2012) have suggested from observations how ENSO weaken the equatorial Atlantic variability while Rodrigues et al. (2011) have confirmed the different impacts of Pacific El Niño-types over the Equatorial Atlantic.

Regarding the simulation of the TAV in the current GCMs, all of the models participating in the Coupled Model Inter-comparison Project (CMIP3, CMIP5) fail to reproduces both, the seasonal cycle and the inter-annual variability over the equatorial Atlantic (Breugem et al., 2006, 2007; Large and Danabasoglu, 2006; Chang et al., 2007; Richter and Xie, 2008; Wahl et al., 2011; Richter et al., 2012a; see also Tokinaga and Xie, 2011 additional material; Richter et al., 2014). The strong bias over the tropical Atlantic is a feature of the coupled models and it has been related to several processes: for instance, the complex land-sea interaction in the Atlantic basin, the oceanic coarse resolution for reproducing enough upwelling and the problems in simulating winds and clouds by the atmospheric model component (Large and Danabasoglu, 2006; Richter and Xie, 2008; Richter et al., 2012a; Toniazzo and Woolnough, 2014). In particular biases over the cold tongue region in several models have been attributed to the remote impact of erroneously weak zonal surface winds along the equator in boreal spring, due to a deficit of Amazon rainfall, which reverse the equatorial thermocline tilt and prevent cold tongue formation the following season (Collins et al., 2006; Chang et al., 2007; Richter and Xie, 2008; Richter et al., 2012a). Wahl et al. (2011) have also emphasized the role of weak equatorial winds and the stratocumulus clouds in producing warm water in the Benguela region. Similar biases diagnosis over the tropical Atlantic with CCSM4 model by Grodsky et al. (2012) have concluded that a sufficient ocean horizontal resolution and adequate modeled alongshore winds are necessary for simulating northward transport of cold water along the coast. Otherwise, the error propagates westward by advection and positive feedback involving stratocumulus clouds (Mechoso et al., 1995; Grodsky et al., 2012). In addition, another potential source of bias is the impact of errors in the atmospheric hydrologic cycle on the ocean stratification through its effects on ocean salinity (Breugem et al., 2008). Recently, Toniazzo and Woolnough (2014) have analyzed the growth of the error in several CGMs and each model has its particular processes for creating the bias, for instance, HadCM3 has a too passive ocean which prevents the advection of heat from upwelling areas.

As a result of an inadequate seasonal cycle over the equatorial Atlantic, coupled models also fail in reproducing the proper leading mode of the inter-annual variability (i.e., Atlantic Niño, Breugem et al., 2006, 2007; Richter et al., 2014). Nevertheless, most of the CMIP models show variability over the equatorial Atlantic associated with a Bjerknes feedback (Breugem et al., 2007; Richter et al., 2014), suggesting that they are able to produce some thermocline feedbacks even when the mean thermocline is much more deeper in the eastern equatorial Atlantic compared with the observations (i.e., see variability of HadCM3 Figure 2 in Polo et al., 2013).

In particular, the IPSL-CM4 model used along this work, shows a wrong annual mean of SST along the equator but less bias of equatorial surface winds compared with the rest of the CMIP3 models (see Figures 2, 10 in Richter and Xie, 2008). Besides, IPSL-CM4 model displays a very reasonable seasonality of the Atlantic Niño variability (see **Figure 1B** and compare with the variance for rest of the models in Breugem et al. (2006, 2007) and the next version of the model IPSL-CM5 (part of the CMIP5) has not improved neither the mean state nor the variability over the equatorial Atlantic (i.e., Richter et al., 2014). Biases in the inter-annual TAV are poorly studied (Ding et al., 2015), however, the model community needs an appropriate tool to improve the SST bias in both, seasonal cycle an inter-annual variability in the next model generations and to be able to represent a more accurate way the tropical tele-connections. This is a "*sine qua non*" condition for better assessing interpretation about future climate.

Here we want to understand the mechanisms behind the Atlantic Niño-like in IPSL-CM4 coupled model. The way the model produces its own Atlantic Niño mode will give more insights in the understanding of the coupled model biases in the inter-annual variability. We will answer the following questions; how is IPSL-CM4, a state-of-the-art coupled model, generating inter-annual TAV? how does the model simulate the main mode of inter-annual variability? What are the processes governing the origin and damping of this mode, in particular the ocean heat fluxes? And finally, are vertical subsurface turbulent processes as important as for the seasonal cycle of the stand- alone ocean model (Peter et al., 2006; Jouanno et al., 2011) and the observations (Foltz et al., 2003; Hummels et al., 2014)? The last interrogation justify by itself the modeling approach we chose, instead of observation derived one, since subsurface mixing observations are far too sparse to allow constructing a reasonably closed heat budget at basin scale.

The article is organized as followed, firstly the model and data used are described with a discussion of the seasonal cycle and the variability in the model, in the results section the mode is described together with the associated heat budget and the main processes are explained. Finally, a discussion and the main conclusions are summarized.

Model and Methods

Although this work is devoted to understand the variability in the coupled model, some observational data has been used throughout the work in order to validate the model (**Figures 1–3**). For the SST, HadISST (Rayner et al., 2003) and ERSST (Smith and Reynolds, 2003) has been used. For the Mixed Layer Depth (MLD), data from de Boyer Montegut et al. (2004) has been used. Near-surface ocean current estimates come from Ocean Surface Current Analysis (OSCAR) merged satellite dataset (Bonjean and Lagerloef, 2002); surface wind from ERA-Interim reanalysis (Dee et al., 2011) and precipitation CMAP dataset (Xie and Arkin, 1997). In the following section the IPSL-CM4 coupled model is described.

Description of the Model

Fully coupled climate model developed at the Institut Pierre-Simon Laplace, IPSL-CM4 v2 (Marti et al., 2010) has been used. This model is composed of the LMDz4 atmosphere GCM (Hourdin et al., 2006), the OPA8.2 ocean model (Madec et al., 1997), the LIM2 sea-ice model (Fichefet and Maqueda, 1997) and ORCHIDEE 1.9.1 for continental surfaces (Krinner et al., 2005). The coupling between the different parts is done by OASIS (Valcke et al., 2000). The resolution in the atmosphere is $96 \times 71 \times 19$, i.e., 3.75° in longitude, 2.5° in latitude, and 19 vertical levels. The ocean and sea-ice are implemented on the ORCA2 grid (averaged horizontal resolution ∼2°, refined to 0.5° around the equator, 31 vertical levels). This model was intensively used during the CMIP3. Properties and variability of the large scale oceanic circulation in the model was investigated by Msadek et al. (2010) in the North Atlantic and Marini et al. (2011) in the Southern Ocean. Mignot and Frankignoul (2010) studied the sensitivity of the Thermohaline Circulation to anomalous freshwater input in the Tropics. Representativity of tropical features was investigated in particular in Braconnot et al. (2007) and Lengaigne et al. (2004, 2006), as well as in some multi-model studies (Richter and Xie, 2008; Richter et al., 2014). However, the TAV in this model was not investigated *per se*.

In addition to the 500 year control simulation, with constant pre-industrial GHG concentration, the heat and salinity budgets in the mixed layer are available over an extra 50 years period. This period, which will be used to investigate TAV, has thus beneficiated from an adjustment of more than 500 years (Marti et al., 2010). Notice that the version of the model used in CMIP5 (IPSL-CM5) does not show an improvement over the tropical Atlantic, therefore we will make use of the available simulations of IPSL-CM4 for understanding processes in the TAV.

Seasonal Cycle in the Model

Figures 1A,B shows the seasonal cycle of the SST over the Atl3 region [20W-0E, 3S-3N]. The observations and the model show

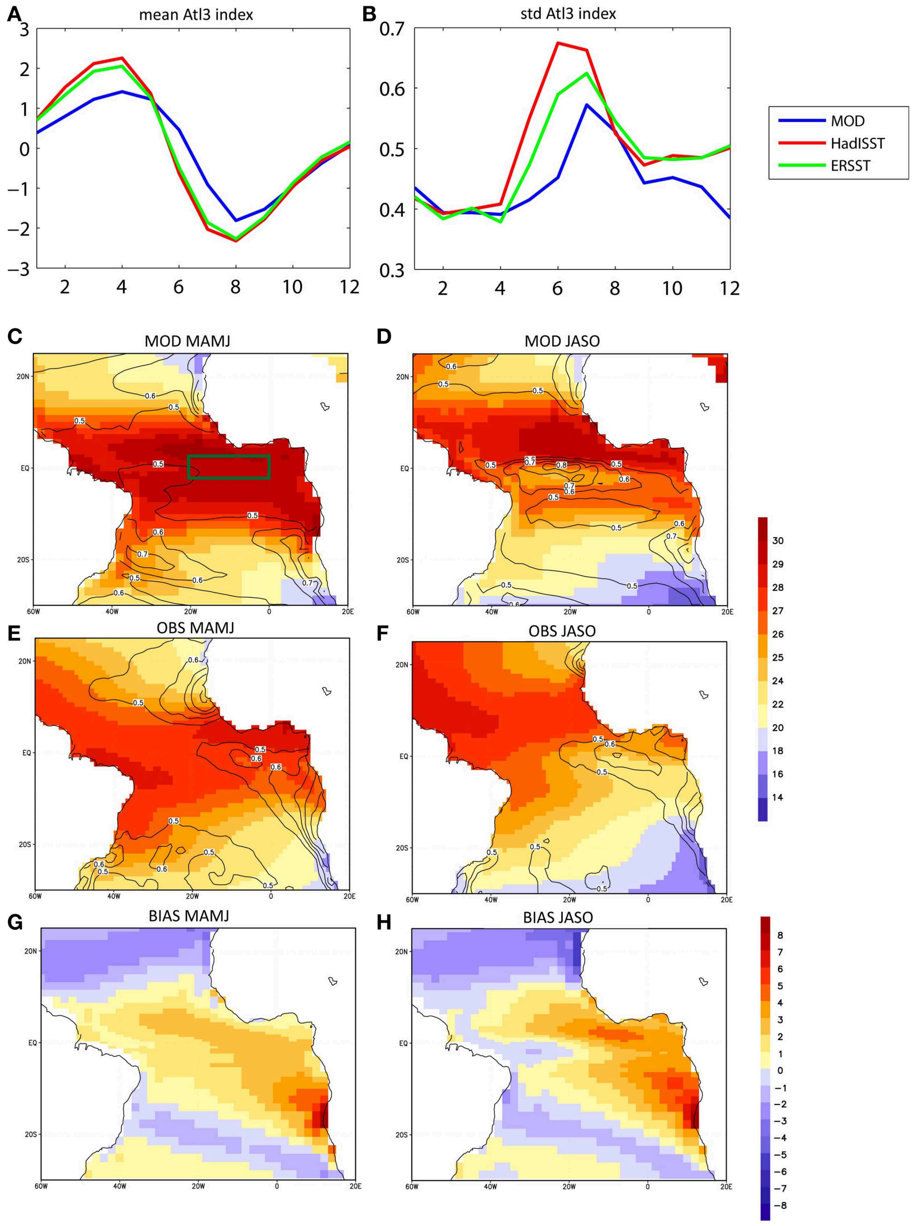

FIGURE 1 | Tropical Atlantic SST bias. Seasonal cycle for the Atl3 index [SST averaged over 20W–0E 3N–3S], **(A)** mean (minus the long-term mean) and **(B)** standard deviation for each month for the model (blue) and observations from HadISST dataset (red) and ERSST dataset (green). The IPSL-CM4 model simulates variability over summer season over the eastern equatorial Atlantic. **(C)** Mean SST (shaded in **C**) and standard deviation of SST (contours) for MAMJ season for the model. The green square is the Atl3 region **(D)** same as **(C)** but for the JASO season. **(E,F)** same as **(C,D)** but for the observations (HadISST dataset). **(G)** SST BIAS (model minus observations, in **C)** for MAMJ 4-months seasons **(H)** same as **(G)** but for JASO.

in general a good agreement with the timing in the seasonal cycle and its variability. Although the peaks of both, the mean and the variance in the model are delayed by 1 month with respect to the observations, the model seems to be reliable to reproduce the Atlantic Niño seasonality, which is important in terms of tele-connections and impacts (García-Serrano et al., 2008; Losada et al., 2010, 2012). Nevertheless, the model shows an important bias of the annual mean SST over the equatorial region from MAMJ to JASO season (**Figures 1C,D**).

Correct representation of the timing in the cold tongue evolution is important. **Figures 1C–F** illustrates the SST in MAMJ and in JASO seasons when the origin and damping of Atlantic Niño occurs respectively. A strongest bias is seen in JASO, and it exceeds 4C, although in the previous MAMJ season the bias is also presented with 2–3C of differences with respect to the observations.

Maximum SST biases are found along the eastern oceanic borders (**Figure 1H**), in the well-known regions of coastal upwelling. Such biases are very common in coarse resolution coupled models (e.g., Large and Danabasoglu, 2006) or even forced oceanic models (Richter et al., 2012a). Note that the SST bias is maximum during the summer of each hemisphere, which is the season of maximum upwelling (not shown). The SST variability is also biased in the model; maximum variability from MAMJ to JASO occurs over western-central equator, while in the observations the standard deviation shows the cold tongue shape over the eastern-central equator. Strong variability for both, model and observations is found in the Angola/Benguela front.

In summary, **Figures 1G,H** shows the typical bias in the state-of-the-art models consistent in a dipole pattern of cooling in the north and warming in the south (Grodsky et al., 2012). The northern cooling is related to an excess of wind-induced latent heat loss while the southern warming has been related to both weak winds over the western equator and the related air-sea feedbacks together with reduced alongshore upwelling in the Angola-Benguela region. The later could induce, in turn, an erroneous ocean heat advection (Large and Danabasoglu, 2006; Richter and Xie, 2008; Grodsky et al., 2012; Toniazzo and Woolnough, 2014; Xu et al., 2014).

Figures 2A,B shows the seasonal transition (from MAMJ to JASO) of the mixed layer depth and the surface currents. The modeled mean circulation shows strong westward surface currents at the equator. The strengthening of the North Brazil Current (NBC) along the American coast and the retroflection at 5N in MAMJ-JASO, leading to the eastward North Equatorial Counter Current (NECC), which extends into the Guinea Current in the Gulf of Guinea are satisfyingly simulated. The amplitude of the NECC in the model matches the observed one; however the intensity of NBC is overestimated in the model as well as the westward surface currents at the equator (i.e., -0.4 m/s in the model vs -0.1 m/s in the observations from OSCAR dataset in MAMJ). This bias in the equatorial surface currents can be seen as a northward shift and extension of the South Equatorial Current (SEC), which is present in MAMJ when all the equatorial flow is westward (**Figure 2A**). The North Equatorial Current (NEC) which has its maximum at 10N-20N is less representative from MAMJ to JASO in the model. Finally, the Equatorial Under-Current (EUC) is also well-simulated by the model with a strengthening from boreal spring to late-summer at 80–120 m (not shown), as it is observed (Bourlès et al., 2002; Arhan et al., 2006; Brandt et al., 2006).

MLD in the model shows an equatorial minimum with a large westward extension in comparison with the observations (**Figures 2A,C**). A maximum dome in the west equatorial Atlantic at 3N appears in JASO season (**Figure 2B**) forming a dipole pattern a both side of the equator. However, mixed layer off-equatorial band is quiet well-represented in the model. Additionally, **Figure 2** includes the comparison modeled-observed MLD for the four seasons at the equator (**Figure 2E**). The striking feature is that the model has a reduced MLD all along the year and in particular: (i) in MAM the MLD minimum ($\sim$11 m) is found at 30W-20W and in JJA the slope east-west is substantially reduced and the MLD at the west equator is 20 m in the model vs. 40 m in the observations. This westward displacement of the minimum MLD could explain the maximum standard deviation of the SST in **Figure 1**. Besides, this difference would be important to explain the shape of the variability mode described in the following section.

Figure 3 shows the seasonal transition for the wind stress and precipitation (form MAMJ to JASO). The northward ITCZ-shift is quite well-represented in the model, although the modeled precipitation is located southward compared with the observations especially over West Africa, presumably associated with the warm SST bias over the equatorial Atlantic (**Figures 1C,D**) and the weaken cross-equatorial surface winds (toward land) in comparison with observations (**Figures 3B–D**). Next section describes the main Tropical Atlantic variability mode in the model which is related to the rainfall variability over the surrounding land areas.

Methods for Finding the Mode

Previously to determine the leading mode of the equatorial SST inter-annual variability, we have removed the seasonal cycle of the variables and we have applied an inter-annual filter to all the data. To this end, we have subtracted the previous year to the actual year, removing the low-frequency variability and just allowing the inter-annual variability to arise (Stephenson et al., 2000). This is very useful since the equatorial Atlantic has a strong decadal signal which could be mixed with the higher frequencies (see also **Figure 4**). We are using monthly mean anomalies for all variables.

The leading co-variability mode between SST over the TA and the rainfall over West Africa is related to a strong ENSO signal (not shown). It shows a warming over the whole tropical basin from MAMJ to JASO associated with anomalous positive rainfall over Sahel region in JJAS (not shown). This mode reflects the excess of tele-connection of El Niño in most of the coupled models (Lloyd et al., 2009) due to atmospheric feedbacks and it is not investigated further here. To this end, we thus have removed the ENSO influence on the Tropical Atlantic following the methodology by Frankignoul and Kestenare (2005). We have reconstructed the global SST with the two leading Principal Components of the tropical Pacific, which is the region [120E-90W, 10S-10N]. The two PC constitute 56% of the total variance. The reconstructed data has been removed from the original data and the tropical SST has been retained.

In order to extract the variability modes, we have computed EOF over the TA monthly mean SST anomalies. Note that the SST-WAM co-variability modes calculated from Extended Maximum Covariance Analysis (EMCA, Polo et al., 2008) do not change substantially from SST EOF modes (not shown). Although the EOF method is simpler than EMCA, it also allows discriminating the variability mode that is phase-locked with the seasonal cycle and in our case, locked within the JJASO season.

Hereafter in the manuscript, the regression and correlation maps are the result of projecting the different model outputs onto the PC time-series of the Equatorial Atlantic (EA) mode, which is associated with the first EOF of TA after pre-processing the data. Ninety percent of confidence level has been used to test the significance of the correlation with a *t*-test.

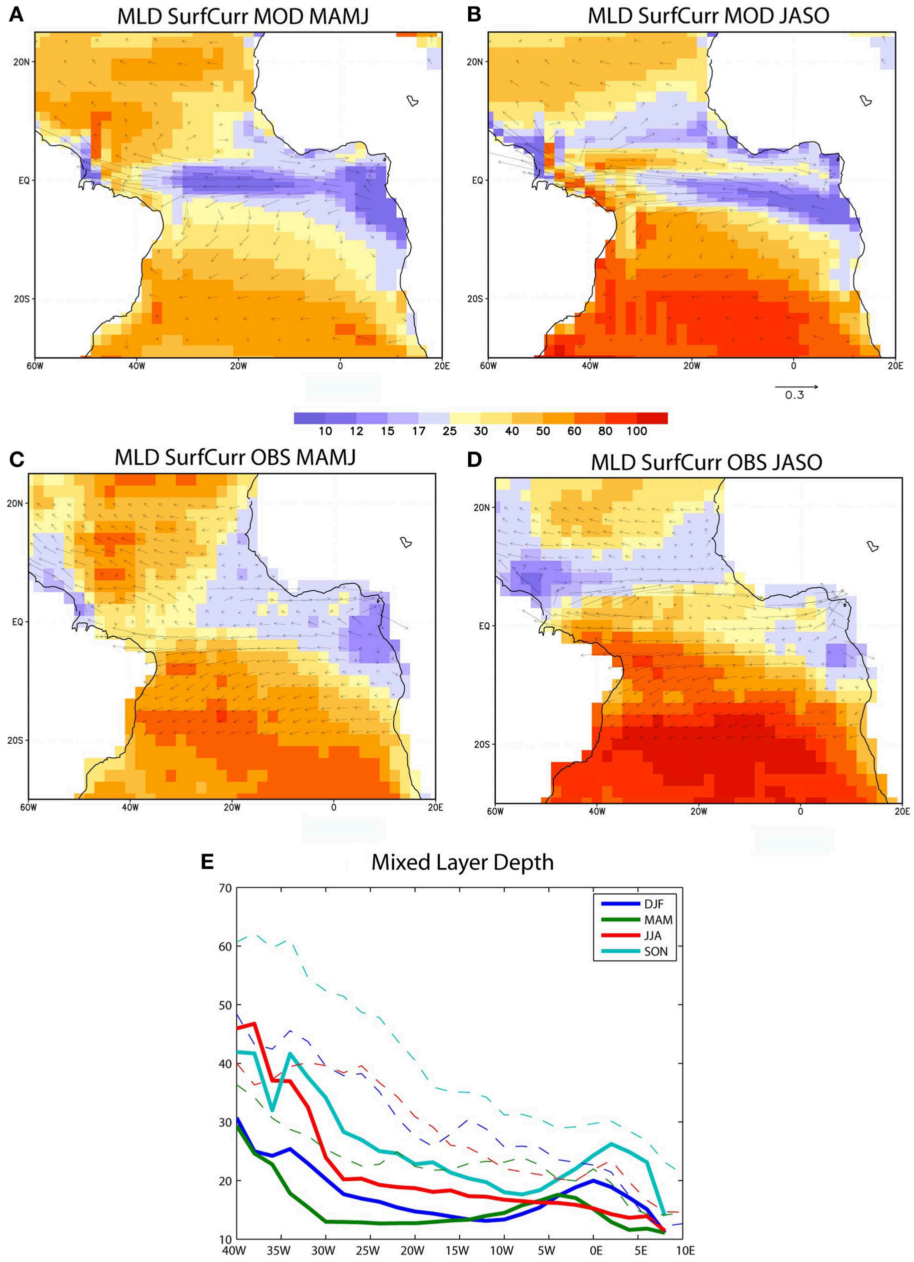

FIGURE 2 | Biases in the TA ocean. (A) Mean Mixed layer depth (shaded in m) and horizontal currents (vectors in m/s) from the model for the MAMJ **(B)** same as **(A)** but for JASO 4-months season. **(C,D)** Same as **(A,B)** but for the observations. **(E)** Mixed layer depth in meters for the model (bold lines) and the observations (dashed lines) along the equatorial Atlantic [3N–3S] for the four seasons.

Results

Equatorial Atlantic (EA) Mode

The leading mode of SST inter-annual variability over the Tropical Atlantic shows an anomalous warming over the equatorial Atlantic explaining 37% of the variance (**Figure 4A**). **Figures 4B,C** shows the time-series of the mode (JJAS mean), together with the Atl3 index for the observations. Seasonality of the EA mode shows a peak in JJASO (not shown).

The power spectra of these time-series are shown in **Figure 4D**. We have used Multi Tapper Method (Thomson, 1982) to allow more degrees of freedom and significance. The mode highlights maximum of energy in [2–5] year period band, consistent with the observational data (maximum around 2–7 year period band). Peak at 3–4 years is very well-simulated. Next section describes the evolution of the SST pattern and the associated impacts in JJAS precipitation.

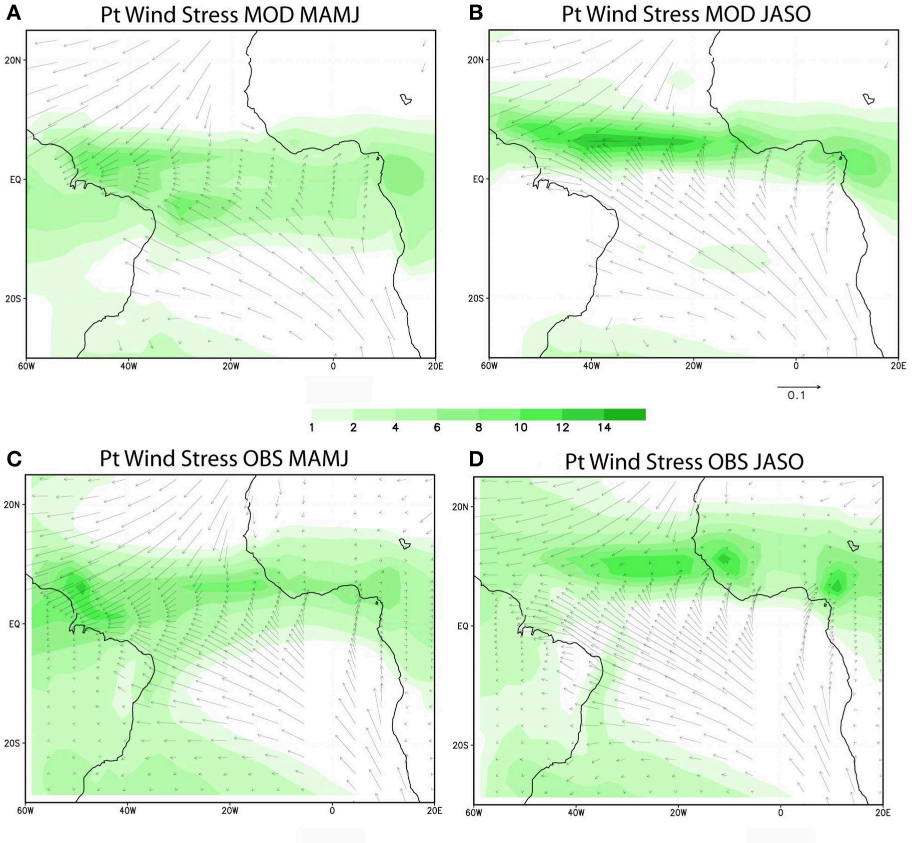

FIGURE 3 | Biases in the TA atmosphere. (A) Precipitation (shaded in kg/day) and wind stress (vectors in N/m2) from the model over Tropical Atlantic for MAMJ **(B)** same as **(A)** but for JASO 4-months seasons. **(C,D)** Same as **(A,B)** but for the observations.

Impacts of the EA Mode

Figure 5 shows the regression of the precipitation and SST over the EA time-series for JJAS season. The EA mode is associated with an anomalous southward shift of the rainfall belt during JJAS also related to anomalously warm SSTs covering the whole tropical Atlantic basin (**Figure 5**, since the EA-mode has a linear nature, the same is true for the opposite case). Warm SST is associated with increased precipitation over the equator, more relevant over the western equatorial Atlantic, suggesting that convection is dislocated westward as an atmospheric response. Rainfall over Brazil and Peru are highly anomalous positive. Associated with the equatorial increase in rainfall, a clear negative anomalous precipitation signal appears over 5-10N in the tropical Atlantic which represents 20% of the precipitation variability of the region in the model. Therefore the onset of West African Monsoon is affected by this EA mode: the evolution of the anomalous negative rainfall shows a latitudinal shift with a maximum over JJAS (not shown), when the rainfall reaches its northernmost position over West Africa. Another significant area of anomalous precipitation is South Africa which could be related to anomalous negative inland flow due to the warming along the Benguela/Namibia coast.

EA Mode Evolution

The evolution of the mode (SST together with the time-derivative of SST) is illustrated in **Figure 6** and it is the focus of this study. Since the ENSO effect has been removed, this mode is assumed to be an intrinsic mode of the TA system in the model. The evolution of the mode shows a warming over the equator and the African coast from MJJA to JJAS seasons, with a maximum of about 0.15°C per month over the west equatorial Atlantic in MAMJ and a resulting SST anomaly peaking in size and value in JASO (about 0.2°C over the eastern half equator). Notice that the amplitude of the SST anomalies (0.15°C) corresponds to the filtered data, which is ∼0.5°C of the non-filtered data in the model from composites of the highest events (i.e., SST >0.5 in the index). This anomaly represents 0.5°C in the central equatorial Atlantic in JJAS, which is roughly 1 standard deviation in the model (**Figure 1**). The damping of the anomalies at the equator becomes maximum in JASO season (**Figure 6F**).

The equatorial Atlantic warming is associated with a relaxation of the equatorial and trade-winds: southward cross-equatorial anomalous winds are developed as the subtropical winds are also reduced from AMJJ to JASO (**Figures 6C–F**).

Regarding the similarity of the EA mode from the model and the one found in the observations with the EMCA method (Polo

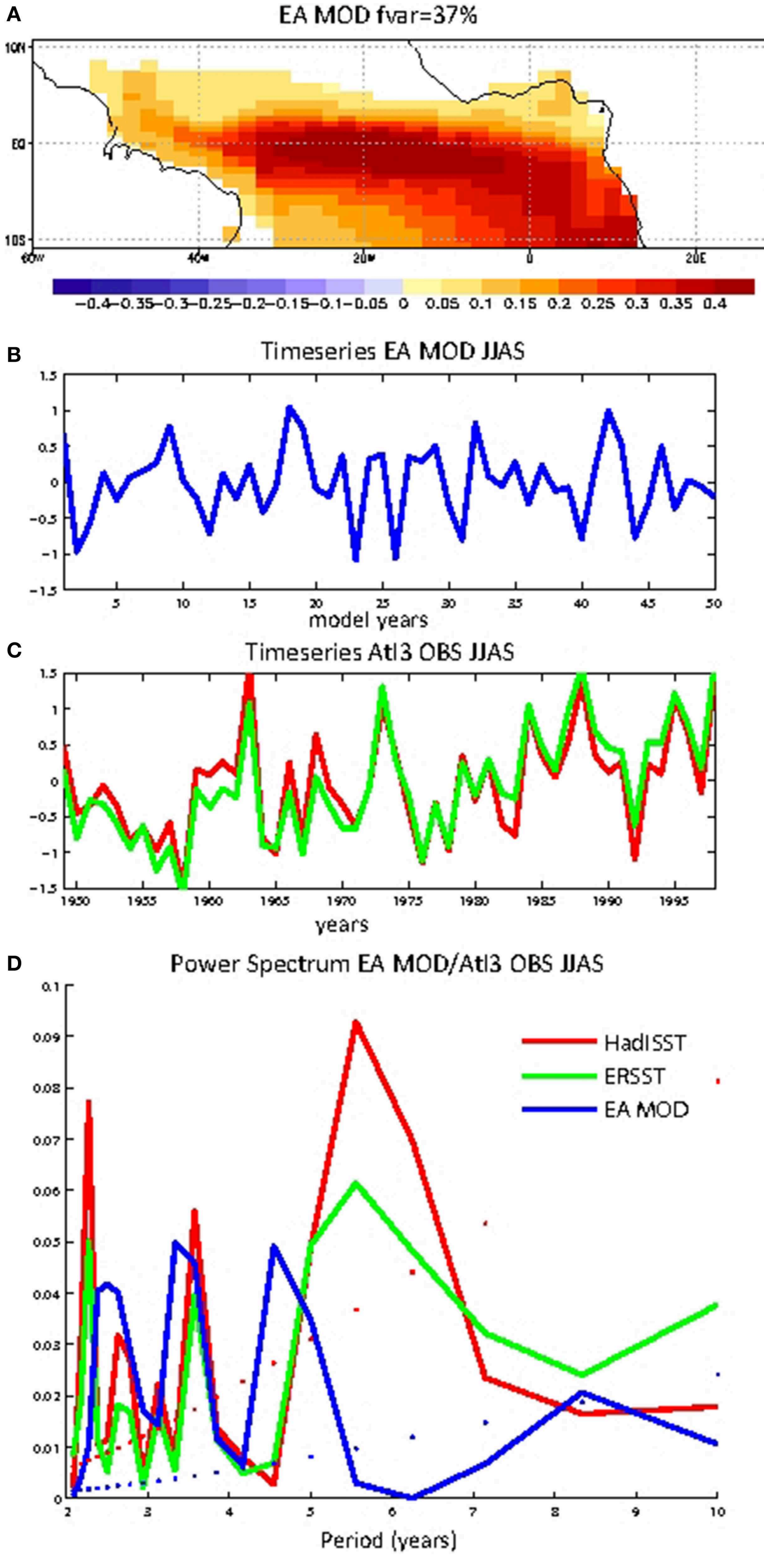

FIGURE 4 | The EA mode: spatial pattern and time-series. (A) spatial pattern of the EA mode **(B)** Standardized time series for the EA-mode (JJAS mean) **(C)** Standardized time series for JJAS Atl3 index for the observations, from HadISST dataset (red) and ERSST dataset (green). For the observations the period 1949–2000 has been chosen. **(D)** Power Spectrum for the time series above-mentioned (50 years). The observations and model have a common peak in [3–4] years band. Multi Tapper method has been used to perform the spectrum and the significance corresponds to 95% confidence level for AR(1) fitting.

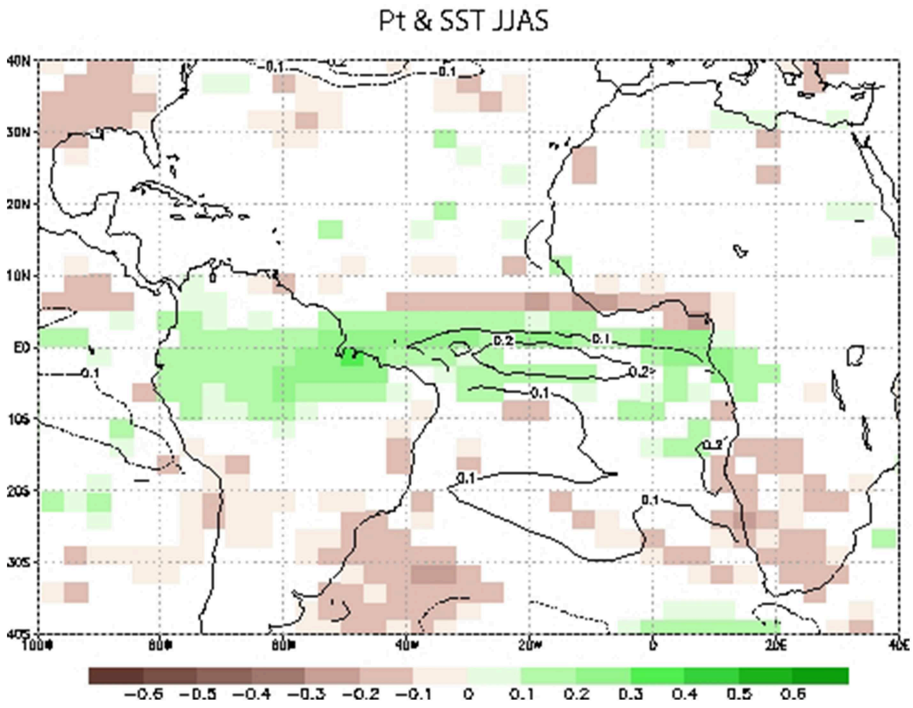

FIGURE 5 | Impacts of the EA mode over TA. Regression map of the anomalous precipitation (shaded in standard deviations) and SST (contour lines in C) onto the EA-mode for JJAS season.

et al., 2008), the model is consistent in amplitude. The amplitude of Atlantic Niño from observations is ~0.4°C over the central equatorial Atlantic in JJAS (see Figure 3 in Polo et al., 2008), which corresponds to half standard deviation.

The main difference between the EA mode in the model and the observational Atlantic Niño is the geographical evolution. Polo et al. (2008) have found the mode starts in MAMJ at the southwest African coast over the upwelling region and the SST anomalies seem to propagate westward and equatorward reaching the whole equatorial band in JASO, consistent with many studies with EOF (i.e., Ruiz-Barradas et al., 2000). The evolution of the SST anomalies in the model is mainly from west equatorial Atlantic to South African coast. The fact that the mode starts ~30W in the simulation could be due to differences in the mean seasonality of the mixed layer depth (**Figure 2**). The mixed layer in the model results too shallow compared with the observations, especially in the west and thus impacts of surface wind anomalies are integrated by the ocean nearly simultaneously over the whole equatorial Atlantic basin. Despite the differences, the observed warming over the equatorial Atlantic is simulated. Next section investigates this origin from previous winter regressions.

Origin of the EA Mode

Associated with the EA mode, there is anomalous SST around 20S co-varying with the equatorial warming. These SST anomalies are present from FMAM (contour lines in **Figure 6A**) and are persistent and related to anomalous trades over south Atlantic. In order to understand these preceding anomalies, **Figure 7** shows global SST and wind stress projected onto EA mode from previous seasons SOND(-1) to FMAM(0). The subtropical–extra-tropical features related to the mode from previous SOND season are consistent with the observations: SST anomalies over the subtropical South Atlantic in a dipolar-like pattern are presented from previous seasons (SOND), associated with anomalous winds of the South subtropical high pressure system (**Figure 7A**).

This dipole-like structure in the model develops (**Figures 7A–D**) increasing both, the wind anomalies and the SST response, and persists almost stationary in the following MAMJ to JASO (contour lines in **Figure 6**). Tropical/extra-tropical structure over Atlantic in **Figure 7A** is quite similar to the pattern reported by observational studies (Trzaska et al., 2007; Polo et al., 2008; Nnamchi and Li, 2011). Global pattern in **Figure 7D** resembles the tele-connection patterns from the Southern Pacific basin via extra-tropical Rossby wave train (Penland and Matrosova, 1998; Barreiro et al., 2004; Huang, 2004) with an associated SST dipolar pattern at both sides of 25S.

Although La Niña pattern is developing the previous NDJF season, the wind anomalies over the south Atlantic seems to appear previously to the Pacific anomalies (**Figure 7A**), suggesting that the ENSO could enhance anomalous wind structure over south Atlantic via Rossby wave-train but the source in SOND (year-1) rather is intrinsic variability

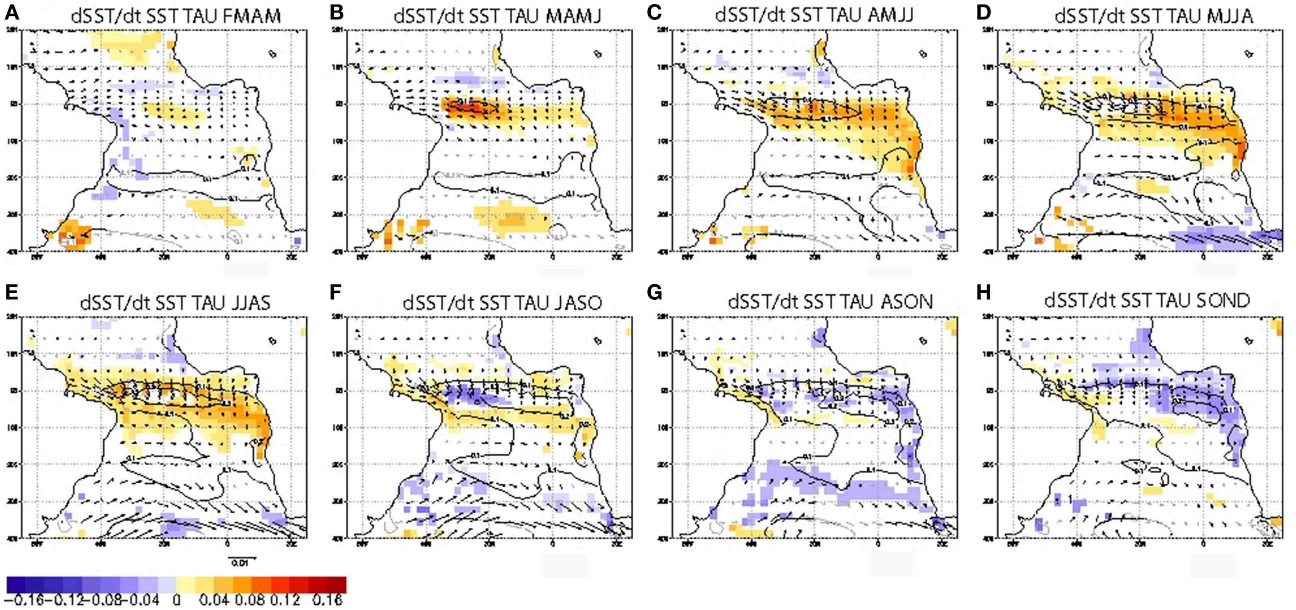

FIGURE 6 | Evolution of the EA mode. Regression map of SST anomalies (contours in C), dSST/dt (shaded in C/month) and wind stress (vectors in N/m2) from FMAM **(A)** to SOND **(H)** 4-months seasons onto time-series of the EA mode. Only significant areas have been plotted from a *t*-test at 90% confidence level.

over southern hemisphere in the model (**Figure 7**). The associated global structure shows an austral hemispheric pattern similar to the Southern Annular mode (Terray, 2011). Although it is difficult to explain why the equatorial SST and the anomalous subtropical SST co-vary from SOND(-1) to ASON (0), the covariance between anomalous equatorial winds and the austral extra-tropical wind (southern 40S) is significant.

In summary, the development of the tropical SST anomalies associated with the EA mode is intrinsic to the tropical Atlantic basin through local feedbacks, but the SST anomalies over the subtropical/extra-tropical basin from the previous seasons (SOND-DJFM) are explained by atmospheric forcing from extra-tropical southern hemisphere and, perhaps, enhanced by ENSO tele-connections.

We will concentrate in understanding how the equatorial SST anomalies are formed and damped. Projections of the surface variables onto EA mode index allow us to understand how the coupled model reproduces an Atlantic Niño-like. The evolution of the EA has a maximum growth in MAMJ and the decay starts in June with a minimum in JASO season (**Figure 6**). In the next section we will analyze how these SST changes are simulated in the model and what are the associated processes.

The Heat Budget

From the closed heat budget over the mixed layer depth, we have illustrated the components responsible for the formation of the SST anomalies of the EA mode described in **Figure 6**. Mixed layer temperature equation is decomposed as described by Vialard et al. (2001) and also by Peter et al. (2006). Equation (1) describes the SST tendency integrated over the mixed layer depth h as:

$$\partial_t T = \underbrace{-\frac{1}{h}\int_{-h}^{0} u\partial_x T dz - \frac{1}{h}\int_{-h}^{0} v\partial_y T dz - \frac{1}{h}\int_{-h}^{0} D_l}_{a} \quad (1)$$

$$\underbrace{-\frac{1}{h}(T - T_h)(\nabla hu + \partial_z h) - \frac{1}{h}[\kappa_z \partial_z T]_{-h}}_{b}$$

$$\underbrace{-\frac{Q_{rad}(1 - F_{-h}) + Q_{tur}}{\rho_o C_p h}}_{c}$$

Integrals represent the quantity integrated over the mixed layer. In Equation (1), T is the temperature in the mixed layer, T_h is the temperature below the mixed layer; u, v and w are the zonal, meridional and vertical currents, respectively, and D_l the lateral diffusion and K_z the vertical mixing coefficient. Q_{net} is the total net heat flux with the atmosphere and it is divided in radiative Q_{rad} and turbulent Q_{tur}heat fluxes. F is the function that describes the fraction of shortwave fluxes penetrating the mixed layer, ρ_0 is the sea water density and C_p is the sea water specific heat capacity coefficient.

The heat budget can be divided into oceanic components and air-sea fluxes forcing (atmospheric components). The total air-sea fluxes forcing is the term (c) on the right hand side and it is the sum of the surface turbulent and radiative heat fluxes. The oceanic part has all the horizontal and vertical terms [a and b on the right hand side of Equation (1)]. Horizontal ocean components (a) are the sum of the horizontal advection plus horizontal diffusion. The vertical terms (b) are the turbulent

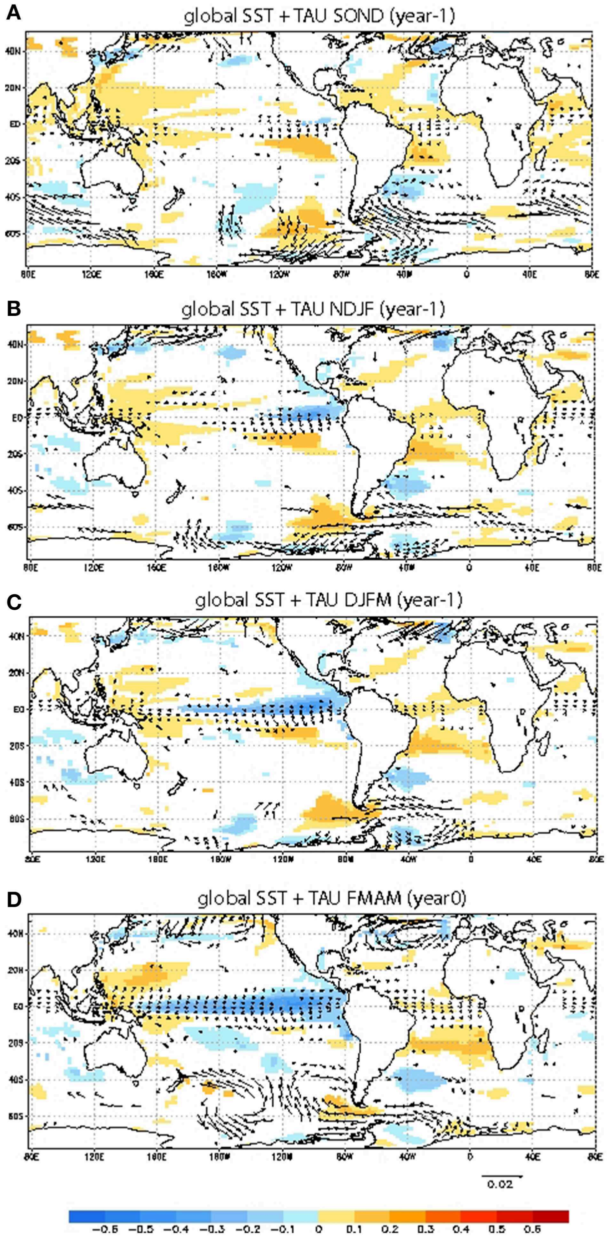

FIGURE 7 | Origin of EA mode. **(A)** Regression map of the global anomalous SST (shaded in **C**) and wind stress (vector in N/m2) onto the time-series of the EA mode for the previous SOND (year -1) season. **(B)** Same as **(A)** but for NDJF (year -1). **(C)** same as **(A)** but for DJFM (year 0). **(D)** same as **(A)** but for the FMAM (year 0).

mixing, vertical advection and an entrainment term computed as the residual following Vialard et al. (2001).

In order to understand the evolution of the EA mode, regression of the terms in the SST tendency equation onto the time-series of the EA mode are analyzed in this section. Note that the regression operator respects the linear partitioning of Equation (1) and that the sum of the regressed terms equals the regressed SST time derivative.

Development of the EA Mode

Figure 8 shows the main components for the MAMJ season, when the warming is maximum in the central equatorial basin. At the equator, there is a large-scale structure which is an intensification of anomalous westerly winds, already seen from previous seasons (i.e., FMAM in **Figure 6A**). These wind anomalies induce an equatorial positive warming by the oceanic contribution in the mixed layer budget, with a primary maximum in the west and a secondary one in the east (**Figure 8A**). Noticeably, air-sea fluxes above are negative and principally reduce the ocean dynamics impacts (**Figure 8B**). Hence the trade reduction is not warming the equator through negative latent heat loss anomalies, as one could have expected, but through its frictional effect on the ocean dynamics. Considering the dependence of the latent heat loss to SST through both, sea level humidity gradient and wind speed, we can conclude that the trade reduction influence on the SST is countered and dominated by the surface humidity increase, itself triggered by the oceanic warming. A similar pattern was found by Sterl and Hazeleger (2003) and Polo et al. (2007) in the observations. Additionally, anomalous positive precipitation and thus anomalous cloud cover over the western-central equatorial Atlantic (especially from AMJJ, not shown) can affect the radiative fluxes by cooling the surface. In summary, air-sea fluxes over the equator merely damp the oceanic warming. In contrast with the climatological seasonal cycle, where air-sea fluxes participate to the cold tongue development through a decrease of their warming effect (not shown), their inter-annual role for the EA mode of variability is only destructive.

When searching for the details of the equatorial warming mechanisms, the partitioning of the oceanic contribution point out to the anomaly of vertical fluxes at the base of the mixed layer (**Figure 8D**), largely associated with turbulent mixing (not shown), which appear as the only cause of the warming, while the horizontal oceanic fluxes contributions are essentially negative. In other words, the net SST anomaly in MAMJ is driven by an upwelling intensity decrease. In coherence with the general behavior of the upwelling systems, the pattern of the vertical component shows a warming also along the African coasts and in particular over both the Ivory Coast and the Angola-Benguela upwelling systems (respectively near 5N-5S, and from the equator down to 20S) reminding the seasonal cold tongue structure (see also **Figure 1D**). The associated cooling by horizontal oceanic contribution displays a very comparable in amplitude but opposite sign pattern, which anomalous currents are reminiscent in opposite of the seasonal mean South Equatorial Current (see **Figure 2A**). Considering the net oceanic contribution and the total SST change in MAMJ season, it appears that horizontal dynamics is only able to drive a significant SST anomaly very locally at the Angola-Benguela front, where lie two intense horizontal SST gradient, that is the mean front and an anomalous one (see respectively **Figures 1C**, **8B**).

From MAMJ to JASO, the anomalous equatorial warming on **Figure 6** seems to propagate eastward along the equator. Anomalous eastward currents at the Equator in MAMJ (**Figure 8C**) are wind-driven (vectors in **Figure 8B**). The

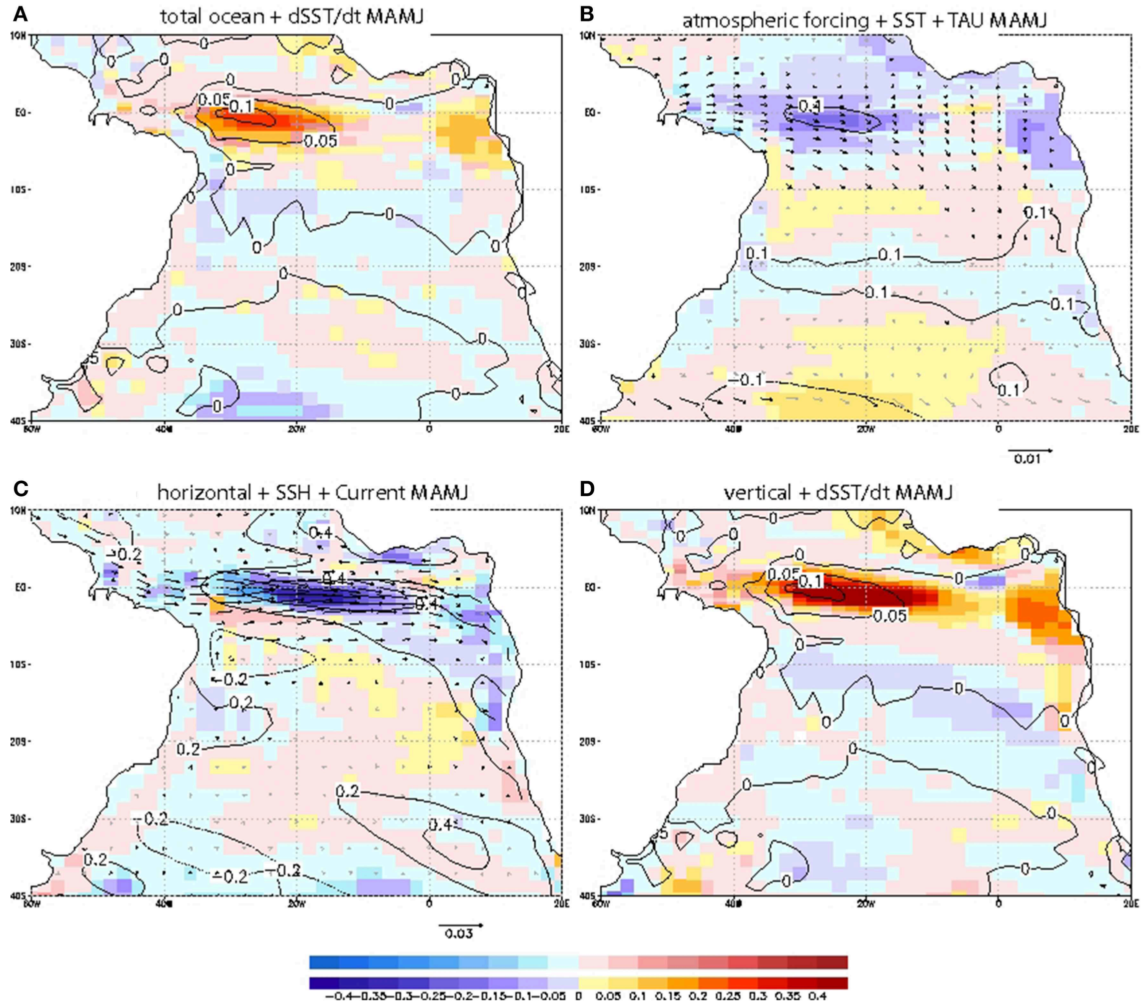

FIGURE 8 | Processes in the development of the EA mode. Heat budget for the mixed layer regressed onto the time-series of the EA mode for the growth season MAMJ. **(A)** Total Ocean component (shaded in C/month) and total SST tendency (contour, in C/month) **(B)** Atmospheric component (shaded in C/month), SST (contour in C) and wind stress (vector in N/m2) **(C)** Horizontal ocean component (shaded in C/month) and SSH (contour in cm) and horizontal surface currents (vectors in m/s) **(D)** Vertical ocean component (shaded in C/month) and total SST tendency (contour in C/month). The colorbar of purple/red colors are significant areas for the SST tendency at 90% confidence level. Bolded contours and vectors are significant areas.

SSH anomalies are positive and present along the equatorial and the African coast (contours in **Figure 8C**), these SSH anomalies suggest that oceanic waves could be interacting by changing the vertical stratification (and thus mixed layer depth *h*) which would affect the vertical terms (**Figure 8D**). These vertical terms are the dominated processes in the warming of the equator and African coast associated with the EA mode.

The ocean horizontal component shows a damping pattern eastward of the maximum SST anomaly in MAMJ (**Figure 8C**), suggesting that horizontal advection (both terms, the mean horizontal currents over the anomalous SST gradient ($u_m$gradT'), and anomalous currents under mean temperature gradients (u'gradT_m) are responsible for this local cooling (while u'gradT' and $u_m$gradT_m would warm the surface). Together with horizontal terms, the atmosphere is instantaneously damping the excess of anomalous SST over the region of maximum SST change.

Finally, the Benguela area shows similar behavior although with less intense anomalies than the equatorial band: in FMAM, the wind is reduced over this region, both coastal upwelling cooling and latent heat loss are reduced and act together to warm the surface (not shown). Afterwards (from MAMJ), the SST anomaly becomes important and the atmospheric fluxes turn into a damping term (**Figure 8B**). Anomalous vertical terms are the main responsible for the warming over the African coast (**Figure 8D**).

Damping of the EA Mode

The mode terminates with a reduction of the large-scale equatorial wind anomaly (centered on 5S-5N) and a weakening of the Santa Helena pressure system 40S (JASO, **Figures 6**,

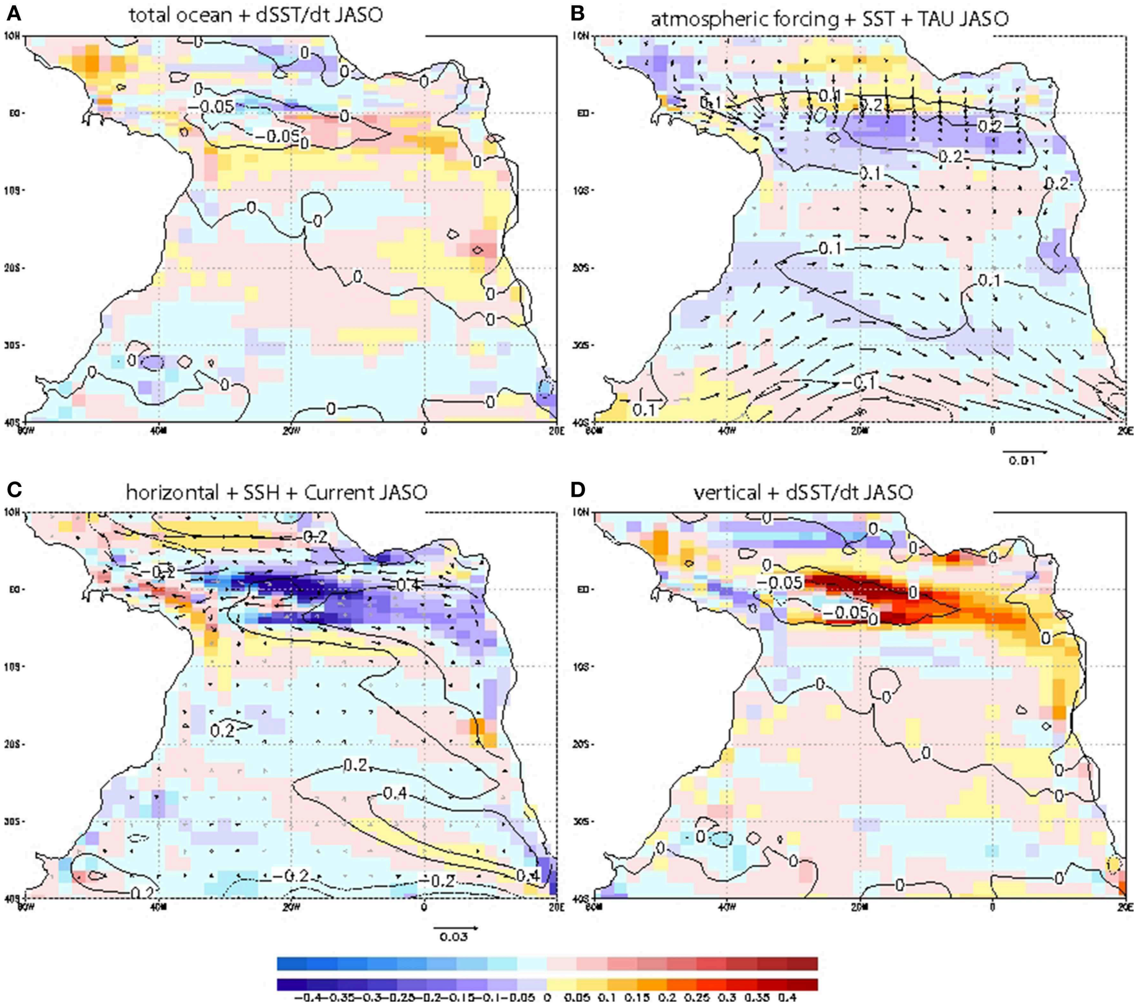

FIGURE 9 | Processes in the damping of the EA mode. Same as **Figure 8** but for the decay season JASO.

9A,B). In JASO, when the mode enters its vanishing phase, the equatorial SST anomalies are damped between 35W and 10W. **Figure 9** shows that it is caused by the oceanic contribution from 35W to 20W, and by the air-sea fluxes effects from 20W to 10W. Whereas there is no other important role for ocean dynamics, the air-sea fluxes also control the damping over almost the whole tropical south Atlantic. As explained above, this suggests that the change in air-sea temperature and humidity gradients are the main components since the wind stress is still anomalously weak (**Figure 9B**). The damping by vertical humidity surface gradient was a damping mechanism also pointed out by Sterl and Hazeleger (2003) for the tropical-subtropical southern dipole.

At the equator, the partitioning of the oceanic terms allows realizing that the total ocean contribution is dominated again by the vertical terms, which warm the eastern half of the change in SST visible on **Figure 9A**, and cools its western half, helped by the horizontal terms (**Figures 9C,D**). This reversed sign is probably caused by the reduction of the wind anomaly and the fact that mean vertical currents are now acting in a more stratified ocean. In addition, as in the previous seasons, the important oceanic contribution for the cooling comes from the horizontal component at the eastern of 20W (**Figure 9C**).

In summary; the ocean is the responsible of the warming over the western part of the equatorial basin and along the African coast by anomalous vertical entrainment while the atmospheric forcing is responsible for warming the South Atlantic region from the previous seasons (not shown) until MAMJ (**Figure 8**). The atmosphere is damping from the beginning of the SST anomaly formation at the equator and along the African coast.

Discussion and Conclusions

In the IPSL-CM4 coupled model, the leading mode of SST variability is found at the equator and along the African coast in the southern hemisphere. This mode is described and referred here as Equatorial Atlantic (EA) mode. Anomalous westerly winds are associated with an anomalous downwelling pattern along the equator and the African coast, while horizontal terms and the atmosphere are damping the resulting SST anomalies.

It is found that the EA mode is part of the internal TAV in the model, however the EA mode is found to covary with an austral hemispheric mode during previous seasons (from internal extra-tropical atmospheric variability) and possibly enhanced by tele-connection from Pacific La Niña throughout Rossby waves impacting the Sta Helena high pressure system.

Regarding the observations, the mode starts over the Benguela region in boreal spring and then reaches the eastern equator, with a stronger SST signal than the EA mode in the model. The opposite situation occurs in the model; the SST anomalies seem to propagate from the western equator to the African coast. The delayed SST anomalies at the equator have been explained by the different mixed layer depth seasonality in Angola/Benguela region and the eastern equator (Lübbecke et al., 2010). Following the similar reasoning, the reversed propagation in the model (i.e., the SST anomalies start first at the western-central equator and later on at the eastern equator) could be due to the fact that the mixed layer depth seasonality is not well reproduced in the model. Maximum SST variability in MAMJ season is found at 40W-30W at the equator (**Figure 1C**). This SST variability maximum is also found in the entrainment and vertical diffusion terms (not shown). The fact that the region of maximum variability in SST (and vertical oceanic terms) corresponds to a minimum in MLD in MAM (**Figure 2E**) suggests that the seasonality of MLD could be tightly linked to the SST changes. Additionally, the model sub-estimates the MLD along the equator but especially west to 20W in MAM season (**Figures 2A,C**). If the MLD is very shallow, vertical terms will be more effective in changing the temperature, which could result in a positive feedback. Nevertheless, in order to deeply understand how important the MLD bias is for the formation of the SST anomalies and its seasonal evolution, associated with the EA mode, we would need to perform sensitivity experiments and further analysis would be required.

The vertical terms are the major contributor to generate SST anomalies over the equator and along the African coast in IPSL-CM4 (also in other models as CCSM4 see Muñoz et al., 2012). Tropical Atlantic SST variability in models is very sensitive to details in the upper ocean vertical mixing scheme. Hazeleger and Haarsma (2005) investigated the sensitivity of the climate models to the mixing scheme and they found that when the entrainment efficiency is enhanced, the mean and variability over the TA are improved. More work is needed for understanding these processes and the different mixing schemes, which will help to comprehend and reduce biases in coupled models. More investigation could be done using coupled simulation with reduced bias to better discriminate the Atlantic Niño-like mode and the processes involved.

The main results are summarized in this section as follows:

- Even though the IPSL-CM4 model presents a strong mean SST bias over the Atlantic cold-tongue region in JJAS season, the model is able to reproduce the amplitude and the seasonality of the Atlantic Niño inter-annual variability quite well (**Figure 1**).
- Equatorial Atlantic inter-annual SST variability mode (EA mode) has been identified to occur in the IPSL-CM4 coupled model control experiment. EA mode consists in an anomalous SST over the equatorial Atlantic and African south coast (from MAMJ to JASO) in a cold-tongue shape. This mode is considered as Atlantic Niño-like in the model (**Figures 5**, **6**).
- EA-SST pattern is related to anomalous rainfall in JJAS in a dipole-like structure over the equator and 10N. Anomalous precipitation is found over North Brazil, West Africa and South Africa (**Figure 5**).
- An anomalous SST dipole over the south West Atlantic (from previous SOND (year-1) to FMAM) occurs to co-vary with equatorial SST anomalies. The SST dipole over south Atlantic in boreal fall-winter preceding the equatorial boreal summer SST anomalies is due to anomalous Sta Helena High pressure system, which seems to be part of the atmospheric extra-tropical internal variability over austral hemisphere and, perhaps, enhanced by the Indo-Pacific tele-connection (**Figure 7**).
- In the EA mode, the warming (cooling) at the equator and along the African coast is due to anomalous vertical upwelling processes from MAMJ to JASO. Horizontal terms tend to damp the SST anomalies at the east of the maximum SST anomaly. From JASO, the anomalous eastward (westward) currents start to reverse and the vertical ocean starts to cool (warm) at 30W (**Figures 8**, **9**).
- Despite the anomalous wind stress over the equatorial Atlantic, the atmosphere forces the damping of the SST anomalies throughout anomalous turbulent heat fluxes (wind-driven) and radiative heat fluxes (cloud-cover) from MAMJ to JASO.
- EA-SST evolution is found to be weaker and opposite in the model in comparison with the observations: from west equator to the southeast Atlantic. This could be related to the wrong mixed layer depth along the equator in the model which allows the ocean to easily integrate the changes from an anomalous forcing in the western equator. In addition, the model bias of a strong westward surface current at the equator in MAMJ could act to damp in excess the SST anomalies, resulting in decreasing the amplitude of the equatorial SST anomalies of the mode with respect to the observations.

Acknowledgments

Irene Polo has been supported by a postdoctoral fellowship funded by the Spanish Government. This work has been also possible thanks to the Spanish projects: Tropical Atlantic Variability and the Climate Shift (TRACS-CGL2009-10285), MOVAC and MUL CLIVAR (CGL2012-38923-C02-01) and the European project PREFACE. PREFACE is the research leading to these results received funding from the EU FP7/2007-2013 under grant agreement no. 603521.

References

Arhan, M., Treguier, A. M., Bourlès, B., and Michel, S. (2006). Diagnosing the annual cycle of the equatorial undercurrent in the Atlantic Ocean from a general circulation model. *J. Phys. Oceanogr*. 36, 1502–1522. doi: 10.1175/JPO2929.1

Barreiro, M., Giannini, A., Chang, P., and Saravanan, R. (2004). On the role of the South Atlantic atmospheric circulation in tropical Atlantic variability. *Earth Clim.* 147, 143–156. doi: 10.1029/147gm08

Bonjean, F., and Lagerloef, G. S. E. (2002). Diagnostic model and analysis of the surface currents in the tropical Pacific Ocean. *J. Phys. Oceanogr*. 32, 2938–2954. doi: 10.1175/1520-0485(2002)032<2938:DMAAOT>2.0.CO;2

Bourlès, B., D'Orgeville, M., Eldin, G., Gouriou, Y., Chuchla, R., DuPenhoat, Y., et al. (2002). On the evolution of the thermocline and subthermocline eastward currents in the equatorial Atlantic. *Geophys. Res. Lett.* 29, 1785. doi: 10.1029/2002GL015098

Braconnot, P., Hourdin, F., Bony, S., Dufresne, J. L., Grandpeix, J., Marti, O., et al. (2007). Impact of different convective cloud schemes on the simulation of the tropical seasonal cycle in a coupled ocean–atmosphere model *Clim. Dyn.* 29, 501–520. doi: 10.1007/s00382-007-0244-y

Brandt, P., Schott, F., Provost, C., Kartavtseff, A., Hormann, V., Bourlès, B., et al. (2006). Circulation in the central equatorial Atlantic: mean and intraseasonal to seasonal variability. *Geophys. Res. Lett*. 33, L07609. doi: 10.1029/2005GL025498

Breugem, W. P., Hazeleger, W., and Haarsma, R. J. (2006). Multimodel study of tropical Atlantic variability and change. *Geophys. Res. Lett*. 33, J23706. doi: 10.1029/2006GL027831

Breugem, W. P., Hazeleger, W., and Haarsma, R. J. (2007). *Multimodel Study of Tropical Atlantic Variability and Change*. Available online at: http://www.knmi.nl/samenw/tameet/ipcc_ar4_comp

Breugem, W. P., Chang, P., Jang, C. J., Mignot, J., and Hazeleger, W. (2008). Barrier layers and tropical Atlantic SST biases in coupled GCMs. *Tellus* 60A, 885–897. doi: 10.1111/j.1600-0870.2008.00343.x

Carton, J. A., Cao, X., Giese, B. S., and Da Silva, A. M. (1996). Decadal and interannual SST variability in the tropical Atlantic Ocean. *J. Phys. Oceanogr*. 26, 1165–1175.

Chang, P. T., Yamagata, P., Schopf, S. K., Behera, J., Carton, W. S., Kessler, G., et al. (2006a). Climate fluctuations of tropical coupled systems – the role of the ocean dynamics. *Clim. J.* 19, 5122–5174. doi: 10.1175/JCLI3903.1

Chang, P., Fang, Y., Saravanan, R., Ji, L., and Seidel, H. (2006b). The cause of the fragile relationship between the Pacific El Niño and the Atlantic Niño. *Nature* 443, 324–328. doi: 10.1038/nature05053

Chang, C. Y., Carton, J. A., Grodsky, S. A., and Nigam, S. (2007). Seasonal climate of the tropical Atlantic sector in the NCAR Community Climate System Model 3: error structure and probable causes of errors. *Clim. J.* 21, 1053–1070. doi: 10.1175/JCLI4047.1

Collins, W. D., Bitz, C. M., Blackmon, M. L., Bonan, G. B., Bretherton, C. S., Carton, J. A., et al. (2006). The Community Climate System Model Version 3 (CCSM3). *Clim. J.* 19, 2122–2143. doi: 10.1175/JCLI3761.1

De Almeida, R. A. F., and Nobre, P. (2012). On the Atlantic cold tongue mode and the role of the Pacific ENSO. *Ocean Sci. Discuss*. 9, 163–185. doi: 10.5194/osd-9-163-2012

de Boyer Montégut, C., Madec, G., Fischer, A. S., Lazar, A., and Iudicone, D. (2004). Mixed layer depth over the global ocean: an examination of profile data and a profile-based climatology. *J. Geophys. Res.* 109:C12003. doi: 10.1029/2004JC002378

Dee, D. P., Uppala, S. M., Simmons, A. J., Berrisford, P., Poli, P., Kobayashi, S., et al. (2011). The ERA-Interim reanalysis: configuration and performance of the data assimilation system. *Q. J. R. Meteorol. Soc*. 137, 553–597. doi: 10.1002/qj.828 doi: 10.1002/qj.828

Ding, H., Keenlyside, N., Latif, M., Park, W., and Wahl, S. (2015). The impact of mean state errors on equatorial Atlantic interannual variability in a climate model. *J. Geophys. Res. Oceans* 120, 1133–1151. doi: 10.1002/2014JC010384

Fichefet, T., and Maqueda, M. A. M. (1997). Sensitivity of a global sea ice model to the treatment of ice thermodynamics and dynamics. *J. Geophys. Res. Oceans* 102, 12609–12646. doi: 10.1029/97JC00480

Florenchie, P., Lutjeharms, J. R. E., Reason, C. J. C., Masson, S., and Rouault, M. (2003). The source of Benguela Niños in the South Atlantic Ocean. *Geophys. Res. Lett*. 30, 1505. doi: 10.1029/2003GL017172

Foltz, G. R., Grodsky, S. A., Carton, J. A., and McPhaden, M. J. (2003). Seasonal mixed layer heat budget of the tropical Atlantic Ocean. *J. Geophys. Res*. 108, 3146. doi: 10.1029/2002JC001584

Frankignoul, C., and Kestenare, E. (2005). Air–sea interactions in the tropical Atlantic: a view based on lagged rotated maximum covariance analysis. *Clim. J.* 18, 3874–3890. doi: 10.1175/JCLI3498.1

García-Serrano, J., Losada, T., Rodríguez-Fonseca, B., and Polo, I. (2008). Tropical Atlantic variability modes (1979–2002). Part II: time-evolving atmospheric circulation related to SST-forced tropical convection. *Clim. J.* 21, 6476–6497. doi: 10.1175/2008JCLI2191.1

Giannini, A., Saravannan, R., and Chang, P. (2003). Oceanic forcing of Sahel rainfall on interannual to interdecadal time scales. *Science* 302, 1027–1030. doi: 10.1126/science.1089357

Grodsky, S. A., Carton, J. A., Nigam, S., and Okumura, Y. (2012). *Tropical* Atlantic biases *in CCSM4. J. Clim*. 25, 3684–3701. doi: 10.1175/JCLI-D-11-00315.1

Hazeleger, W., and Haarsma, R. J. (2005). Sensitivity of tropical Atlantic climate to mixing in a coupled ocean-atmosphere model. *Clim. Dyn*. 25, 387–399. doi: 10.1007/s00382-005-0047-y

Hourdin, F., Musat, I., Bony, S., Braconnot, P., Codron, F., Dufresne, J. L., et al. (2006). The lmdz4 general circulation model: climate performance and sensitivity to parametrized physics with emphasis on tropical convection. *Clim. Dyn*. 27, 787–813. doi: 10.1007/s00382-006-0158-0

Hu, Z. Z., and Huang, B. (2007). Physical processes associated with the Tropical Atlantic SST gradient during the anomalous evolution in the Southeastern Ocean. *Clim. J.* 20, 3366–3378. doi: 10.1175/JCLI4189.1

Huang, B. (2004). Remotely forced variability in the Tropical Atlantic Ocean. *Clim. Dyn*. 23, 122–152. doi: 10.1007/s00382-004-0443-8

Hummels, R., Dengler, M., Brandt, P., and Schlundt, M. (2014). Diapycnal heat flux and mixed layer heat budget within the Atlantic Cold Tongue. *Clim. Dyn*. 43, 3179–3199. doi: 10.1007/s00382-014-2339-6

Janicot, S., Harzallah, A., Fontaine, B., and Moron, V. (1998). West African monsoon dynamics and eastern equatorial Atlantic and Pacific SST anomalies (1970–1988). *Clim. J.* 11, 1874–1882. doi: 10.1175/1520-0442-11.8.1874

Jouanno, J., Marin, F., du Penhoat, Y., Sheinbaum, J., and Molines, J.-M. (2011). Seasonal heat balance in the upper 100 m of the equatorial Atlantic Ocean. *J. Geophys. Res.* 116:C09003. doi: 10.1029/2010JC006912

Keenlyside, N. S., and Latif, M. (2007). Understanding equatorial Atlantic interannual variability. *Clim. J.* 20, 131–142. doi: 10.1175/JCLI3992.1

Kushnir, Y., Robinson, W. A., Chang, P., and Robertson, A. W. (2006). The physical basis for predicting Atlantic sector seasonal- to-interannual climate variability. *Clim. J.* 19, 5949–5970. doi: 10.1175/JCLI3943.1

Krinner, G., Viovy, N., de Noblet-Ducoudré, N., Ogée, J., Polcher, J., Friedlingstein, P., et al. (2005). A dynamic global vegetation model for studies of the coupled atmosphere-biosphere system. *Global Biogeochem. Cycles* 19:GB1015. doi: 10.1029/2003GB002199

Large, W. G., and Danabasoglu, G. (2006). Attribution and Impacts of Upper Ocean Biases in CCSM3. *Clim. J.* 19, 2325–2346. doi: 10.1175/JCLI3740.1

Latif, M., and Grötzner, A. (2000). On the equatorial Atlantic oscillation and its response to ENSO. *Climate Dyn*. 16, 213–218. doi: 10.1007/s003820050014

Lengaigne, M., Guilyardi, E., Boulanger, J. P., Menkes, C., Delecluse, P., Inness, P., et al. (2004). Triggering of El Nin Þ*o by Westerly wind events in a coupled general circulation model. *Clim. Dyn*. 23, 601–620. doi: 10.1007/s00382-004-0457-2

Lengaigne, M., Boulanger, J. P., Menkes, C., and Spencer, H. (2006). Influence of the seasonal cycle on the termination of El Niño events in a coupled general circulation model. *J. Clim*. 19, 1850–1868. doi: 10.1175/JCLI3706.1

Lloyd, J., Guilyardi, E., Weller, H., and Slingo, J. (2009). The role of atmosphere feedbacks during ENSO in the CMIP3 models. *Atmos. Sci. Lett*. 10, 170–176 doi: 10.1002/asl.227

Losada, T., Rodriguez-Fonseca, B., Janicot, S., Gervois, S., Chauvin, F., and Ruti, P. (2010). A multi-model approach to the Atlantic Equatorial mode: impact on the West African monsoon. *Clim. Dyn*. 35, 29–43. doi: 10.1007/s00382-009-0625-5

Losada, T., Rodriguez-Fonseca, B., and Kucharski, F. (2012). Tropical Influence on the Summer Mediterranean Climate. *Atmos. Sci. Lett*. 13, 36–42. doi: 10.1002/asl.359

Lübbecke, J. F., Böning, C. W., Keenlyside, N. S., and Xie, S.-P. (2010). On the connection between Benguela and equatorial Atlantic Niños and the role of the South Atlantic Anticyclone. *J. Geophys. Res*. 115, C09015. doi: 10.1029/2009JC005964

Lübbecke, J., and McPhaden, M. (2012). On the inconsistent relationship between Pacific and Atlantic Niños. *J. Clim*. 25, 4294–4303. doi: 10.1175/JCLI-D-11-00553.1

Madec, G., Delecluse, P., Imbard, M., and Levy, C. (1997). *OPA Version 8.1 Ocean General Circulation Model Reference Manual*. Technical Report, LODYC, Paris.

Marini, C., Frankignoul, C., and Mignot, J. (2011). Links between the southern annular mode and the Atlantic meridional overturning circulation in a climate model. *J. Clim*. 24, 624–640. doi: 10.1175/2010JCLI3576.1

Marti, O., Braconnot, P., Bellier, J., Benshila, R., Bony, S., Brockmann, P., et al. (2010). *The New IPSL Climate System Model: IPSL-CM4, Note du Pôle de Modélisation n 26, Institut Pierre Simon Laplace des Sciences de l'Environnement Global*. Paris: IPSL Global Climate Modeling Group.

Mechoso, C. R., Robertson, A. W., Barth, N., Davey, M. K., Delecluse, P., Gent, P. R., et al. (1995). The seasonal cycle over the tropical Pacific in coupled ocean-atmosphere general circulation models. *Mon. Weather Rev*. 123, 2825–2838.

Mignot, J., and Frankignoul, C. (2010). Local and remote impacts of a tropical Atlantic salinity anomaly. *Clim. Dyn*. 35, 1133–1147. doi: 10.1007/s00382-009-0621-9

Msadek, R., Frankignoul, C., and Li, Z. X. (2010). Mechanisms of the atmospheric response to North Atlantic multidecadal variability: a model study. *Clim. Dyn*. 36, 1255–1276. doi: 10.1007/s00382-010-0958-0

Muñoz, E., Weijer, W., Grodsky, S., Bates, S. C., and Wagner, I. (2012). Mean and Variability of the Tropical Atlantic Ocean in the CCSM4. *J. Clim*. 25, 4860–4882. doi: 10.1175/JCLI-D-11-00294.1

Nnamchi, H. C., and Li, J. (2011). Influence of the South Atlantic Ocean Dipole on West African summer precipitation. *Clim. J*. 24, 1184–1197. doi: 10.1175/2010JCLI3668.1

Namchi, H. C., Li, J., Kang, I. S., and Kucharski, F. (2013). Simulated impacts of the South Atlantic Ocean Dipole on summer precipitation at the Guinea Coast. *Clim. Dyn*. 4, 677–694 doi: 10.1007/s00382-012-1629-0

Okumura, Y., and Xie, S. (2004). Interaction of the Atlantic Equatorial cold tongue and the African monsoon. *Clim. J*. 17, 3589–3602. doi: 10.1175/1520-0442(2004)017<3589:IOTAEC>2.0.CO;2

Penland, C., and Matrosova, L. (1998). Prediction of Tropical Atlantic Sea Surface temperatures using linear inverse modeling. *Clim. J*. 11, 483–496.

Peter, A.-C., Le He'naff, M., du Penhoat, Y., Menkes, C. E., Menkes, F., Marin, J., et al. (2006). A model study of the seasonal mixed layer heat budget in the equatorial Atlantic. *J. Geophys. Res*. 111, C06014. doi: 10.1029/2005JC003157

Philander, S. G. H. (1990). *El Niño, La Niña, and the Southern Oscillation. International Geophysics Series, Vol. 46*. San Diego; New York; Berkeley; Boston; London; Sydney; Tokyo; Toronto: Academic Press.

Polo, I., Rodriguez-Fonseca, B., Garcia-Serrano, J., and Losada, T. (2007). "Interannual West African rainfall-tropical atlantic SST covariability modes during the dry Sahel period (1979-2001)," in *Poster Presentation in 2nd International AMMA Conference* (Karlsruhe).

Polo, I., Rodriguez-Fonseca, B., Losada, T., and Garcia-Serrano, J. (2008). Tropical Atlantic variability modes (1979-2002). Part I: time-evolving SST modes related to West African rainfall. *J. Clim*. 21, 6457–6475. doi: 10.1175/2008JCLI2607.1

Polo, I., Dong, B. W., and Sutton, R. T. (2013). Changes in tropical Atlantic interannual variability from a substantial weakening of the meridional overturning circulation. *Clim. Dyn*. 41, 2765–2784. doi: 10.1007/s00382-013-1716-x

Rayner, N., Parker, D., Horton, E., Folland, C., Alexander, L., Rowell, D., et al. (2003). Global analyses of sea surface temperature, sea ice, and night marine air temperature since the nineteenth century. *J. Geophys. Res*. 108, 4407. doi: 10.1029/2002JD002670

Richter, I., Behera, S. K., Masumoto, Y., Taguchi, B., Komori, N., and Yamagata, T. (2010). On the triggering of Benguela Niños: remote equatorial versus local influences. *Geophys. Res. Lett*. 37, L20604. doi: 10.1029/2010GL044461

Richter, I., Behera, S. K., Masumoto, Y., Taguchi, B., Sasaki, H., Yamagata, T., et al. (2012b). Multiple causes of interannual sea surface temperature variability in the equatorial Atlantic ocean. *Nat. Geosci*. 6, 43–47. doi: 10.1038/ngeo1660

Richter, I., and Xie, S. P. (2008). On the origin of equatorial Atlantic biases in coupled general circulation models. *Clim. Dyn*. 31, 587–598. doi: 10.1007/s00382-008-0364-z

Richter, I., Xie, S. P., Behera, S. K., Doi, T., and Masumoto, Y. (2014). Equatorial Atlantic variability and its relation to mean state biases in CMIP5. *Clim. Dyn*. 42, 171–188. doi: 10.1007/s00382-012-1624-5

Richter, I., Xie, S.-P., Wittenberg, A. T., and Masumoto, Y. (2012a). Tropical Atlantic biases and their relation to surface wind stress and terrestrial precipitation. *Clim. Dyn*. 38, 985–1001. doi: 10.1007/s00382-011-1038-9

Rodrigues, R. R., Haarsma, R. J., Campos, E. J. D., and Ambrizzi, T. (2011). The impacts of inter-El Niño variability on the Tropical Atlantic and Northeast Brazil climate. *Clim. J*. 24, 3402–3342. doi: 10.1175/2011JCLI3983.1

Rodriguez-Fonseca, B., Janicot, S., Mohino, E., Losada, T., Bader, J., Caminade, C., et al. (2011). Interannual and decadal SST-forced responses of the West African monsoon. *Atmos. Sci. Lett*. 12, 67–74. doi: 10.1002/asl.308

Rodríguez-Fonseca, B., Mohino, E., Mechoso, C. R., Caminade, C., Biasutti, M., Gaetani, M., et al. (2015). Variability and predictability of West African droughts: a review of the role of sea surface temperature anomalies. *J. Clim*. 28, 4034–4060. doi: 10.1175/JCLI-D-14-00130.1

Ruiz-Barradas, A., Carton, J. A., and Nigam, S. (2000). Structure of interannual-to-decadal climate variability in the tropical atlantic sector. *Clim. J*. 13, 3285–3297. doi: 10.1175/1520-0442(2000)013<3285:SOITDC>2.0.CO;2

Smith, T. M., and Reynolds, R. W. (2003). Extended reconstruction of global sea surface temperatures based on COADS data (1854–1997). *Clim. J*. 16, 1495–1510. doi: 10.1175/1520-0442-16.10.1495

Stephenson, D. B., Pavan, V., and Bojariu, R. (2000). Is the North Atlantic oscillation a random walk? *Int. J. Climatol*. 20, 1–18. doi: 10.1002/joc.1003

Sultan, B., Janicot, S., and Diedhiou, A. (2003). The West African Monsoon Dynamics. Part I: documentation of the intraseasonal variability. *Clim. J*. 16, 3389–3406. doi: 10.1175/1520-0442(2003)016<3389:TWAMDP>2.0.CO;2

Sterl, A., and Hazeleger, W. (2003). Coupled variability and air-sea interaction in the South Atlantic Ocean. *Clim. Dyn*. 21, 559–571. doi: 10.1007/s00382-003-0348-y

Terray, P. (2011). Southern Hermisphere extratropical forcing: a new paradigm for El Niño- Southern Oscillation. *Clim. Dyn*. 36, 2171–2199. doi: 10.1007/s00382-010-0825-z

Thomson, D. J. (1982). Spectrum estimation and harmonic analysis. *Proc. IEEE* 70, 1055–1096. doi: 10.1109/PROC.1982.12433

Tokinaga, H., and Xie, S. P. (2011). Weakening of the equatorial Atlantic cold tongue over the past six decades. *Nat. Geosci*. 4, 222–226. doi: 10.1038/ngeo1078

Toniazzo, T., and Woolnough, S. (2014). Development of warm SST errors in the southern tropical Atlantic in CMIP5 decadal hindcasts. *Clim. Dyn*. 43, 2889–2913. doi: 10.1007/s00382-013-1691-2

Trzaska, S., Robertson, A. W., Farrara, J., and Mechoso, C. R. (2007). South Atlantic variability arising from air-sea coupling: local mechanisms and tropical–subtropical interactions. *Clim. J*. 20, 3345–3365. doi: 10.1175/JCLI4114.1

Valcke, S., Terray, L., and Piacentini, A. (2000). *The Oasis Coupler User Guide Version 2.4*. Technical Report, TR/CMGC/00–10, Paris.

Vizy, E. K., and Cook, K. H. (2001). Mechanisms by which Gulf of Guinea and eastern North Atlantic sea surface temperature anomalies can influence African rainfall. *Clim. J*. 14, 795–821. doi: 10.1175/1520-0442(2001)014<0795:MBWGOG>2.0.CO;2

Vialard, J., Menkes, C., Boulanger, J.-P., Delecluse, P., Guilyardi, E., McPhaden, M. J., et al. (2001). Oceanic mechanisms driving the SST during the 1997–1998 El Nino. *J. Phys. Oceanogr*. 31, 1649–1675. doi: 10.1029/2001JC000850

Ward, M. N. (1998). Diagnosis and short-lead time prediction of summer rainfall in tropical North Africa at interannual and multidecadal timescales. *Clim. J*. 11, 3167–3191.

Wahl, S., Latif, M., Park, W., and Keenlyside, N. (2011). On the Tropical Atlantic SST warm bias in the Kiel climate model. *Clim. Dyn*. 36, 891–906 doi: 10.1007/s00382-009-0690-9

Xie, S.-P., and Carton, J. A. (2004). "Tropical Atlantic variability: patterns, mechanisms, and impacts," in *Earth Climate: The Ocean-Atmosphere*

Interaction, Geophysical Monograph Series, Vol. *147*, eds C. Wang, S.-P. Xie, and J. A. Carton (Washington, DC: AGU), 121–142.

Xie, P., and Arkin, P. A. (1997). Global precipitation: a 17-year monthly analysis based on gauge observations, satellite estimates, and numerical model outputs. *Bull. Am. Meteorol. Soc*. 78, 2539–2558.

Xu, Z., Li, M., Patricola, C. M., and Chang, P. (2014). Oceanic origin of southeast tropical Atlantic biases. *Clim. Dyn*. 43, 2915–2930. doi: 10.1007/s00382-013-1901-y

Zebiak, S. E. (1993). Air–sea interaction in the equatorial Atlantic region. *Clim. J.* 6, 1567–1586. doi: 10.1111/j.1600-0870.2008.00343.x

Conflict of Interest Statement: The authors declare that the research was conducted in the absence of any commercial or financial relationships that could be construed as a potential conflict of interest.

frontiers in Environmental Science

ORIGINAL RESEARCH
published: 31 March 2015
doi: 10.3389/fenvs.2015.00022

Moisture contribution of the Atlantic Warm Pool to precipitation: a Lagrangian analysis

Rogert Sorí[1], **Anita Drumond**[2]* **and Raquel Nieto**[2]

[1] Grupo Científico del Centro Meteorológico, Instituto de Meteorologia, Ciego de Ávila, Cuba, [2] EPhysLab, Departamento de Física Aplicada, Facultad de Ciencias, Universidad de Vigo, Ourense, Spain

In this work we use a Lagrangian model (FLEXPART) to investigate the contribution of moisture from the Atlantic Warm Pool (AWP) to the atmospheric hydrological budget during the period from 1982 to 1999, and to identify which regions are affected by the moisture transport from this source. FLEXPART computes budgets of evaporation minus precipitation by calculating changes in the specific humidity along 10-day forward trajectories. A monthly analysis was made for May–October, the typical development period of the AWP. Climatologically, the moisture transported from the AWP to North and Central America increases from June onwards. Humidity is also transported toward western Europe from July to October, probably favored by the positioning of the North Atlantic Subtropical High and its associated flows. The largest moisture sinks associated with transport from the AWP were found from August to October, when the warm pool can extend to the north-western coast of Africa. The technique of composites was used to analyse how the interannual variability of moisture contribution from the AWP depends on changes in the pool's areal extension, and on the El Niño Southern Oscillation (ENSO). The results indicate that during episodes when the AWP is at its maximum extent, its moisture contribution increased to the Caribbean, to the region of the Inter-tropical Convergence Zone (ITCZ), and to the North Atlantic. By contrast, less moisture was transported to southeastern North America during July and August, or to central North America during September and October. The differences in moisture sink regions for extreme ENSO episodes suggest that there are favored sinks in the Caribbean and in the ITCZ region during La Niña events.

Keywords: Atlantic Warm Pool, transport of moisture, Lagrangian analysis

Edited by:
Silvina A. Solman,
Centro de Investigaciones del Mar y la Atmósfera, Argentina

Reviewed by:
Alexandre M. Ramos,
University of Lisbon, Portugal
Juan José Taboada,
MeteoGalicia, Spain

***Correspondence:**
Anita Drumond,
EPhysLab, Departamento de Física Aplicada, Facultad de Ciencias, Universidad de Vigo,
Campus As Lagoas, S/N,
32004 Ourense, Spain
anitadru@uvigo.es

Specialty section:
This article was submitted to Atmospheric Science, a section of the journal Frontiers in Environmental Science

Received: *20 September 2014*
Accepted: *06 March 2015*
Published: *31 March 2015*

Citation:
Sorí R, Drumond A and Nieto R (2015) Moisture contribution of the Atlantic Warm Pool to precipitation: a Lagrangian analysis.
Front. Environ. Sci. 3:22.
doi: 10.3389/fenvs.2015.00022

Introduction

The understanding and quantification of the link between evaporation of water in one region and precipitation in another, and of the connecting processes, is one of the main problems in hydrometeorology (Gimeno et al., 2010). However, moisture transport between different regions of the Earth is difficult to quantify because it involves all components of the hydrological cycle (Stohl and James, 2004, 2005). By considering a moisture source as an area of maximum divergence of the vertically integrated moisture flux (VIMF) (Trenberth and Guillemot, 1998), Gimeno et al. (2010) identified both the major oceanic source areas of moisture and the continental regions significantly influenced by the humidity transported from each source through a Lagrangian approach.

Applying the same methodology and focusing on tropical latitudes, Drumond et al. (2011) studied the moisture contribution of the Western Hemisphere Warm Pool (WHWP) to northern hemisphere precipitation. The WHWP is the world's second largest warm pool, and is defined by the sea surface temperature (SST) isoline of 28.5°C (Weisberg, 1996; Wang and Enfield, 2001). At various stages of development, the WHWP comprises the eastern North Pacific and eastern Pacific, the Gulf of Mexico, the Caribbean Sea, and the Western Tropical North Atlantic (TNA). The Central American land mass divides the WHWP into two oceanic regions: the eastern North Pacific Warm Pool and the Atlantic Warm Pool (AWP) (Wang et al., 2008). As the WHWP develops, higher SSTs drive a number of linked phenomena: increased temperature and moisture in the local troposphere, decreased sea level pressure (SLP), light winds from the east, and decreased vertical wind shear (Gray, 1968; Knaff, 1997).

Drumond et al. (2011) showed that during the WHWP's development, it is a source of moisture for precipitation in Central and North America, the North Atlantic, and Western Europe. However, they did not investigate contributions from the Atlantic and the Pacific subregions of the WHWP separately, and their 5-year analysis did not allow an investigation of interannual variations in moisture transport from the pool.

The AWP, as a component of the WHWP, is a large body of water warmer than 28.5°C, which may comprise the Gulf of Mexico, the Caribbean Sea, and the Western TNA (Wang and Enfield, 2001). The AWP reaches its maximum extension in the boreal summer (Wang and Enfield, 2001) and affects rainfall variability in the Western Hemisphere (Wang et al., 2006). A relationship with the tropical Atlantic SST is evident, because large (small) AWPs are associated with warm (cold) SST anomalies in the TNA. This anomalous pattern induces a low-level moisture flux convergence (divergence) and an anomalous ascending (descending) motion, enhancing (inhibiting) local precipitation. The intensification (reduction) of precipitation leads to negative (positive) "evaporation minus precipitation" ($E - P$) budget, and to anomalies in sea surface salinity across the pool. In this way, the atmospheric moisture transport from the Atlantic to the Pacific basin plays an important role in regulating North Atlantic salinity, and thus the strength of the thermohaline circulation (Richter and Xie, 2010).

The AWP tends to weaken the summertime North Atlantic Subtropical High (NASH), particularly at its south-western edge, which in turn weakens the easterly Caribbean Low Level Jet (CLLJ). The westward CLLJ's moisture transport has a semi-annual cycle: two maxima during the summer and winter, and two minima in the spring and fall (Wang and Lee, 2007). In addition to increasing the Caribbean precipitation (Martin and Schumacher, 2011), the weakening of the CLLJ associated with the AWP-induced changes in the upper-level winds also reduces the tropospheric vertical wind shear over the AWP region, and favors the development of hurricanes during August–October (Wang et al., 2007).

The AWP's warming on inter-annual time scales is associated with an anomalous tripolar SST pattern in the north Atlantic, and leads to more rainfall in the central and eastern United States (Liu et al., 2015). Additionally, the ($E - P$) anomalies in the AWP are also influenced remotely by the climatic variability modes of the El Niño-Southern Oscillation (ENSO) and of the North Atlantic Oscillation (NAO), as well as by anomalous conditions in the Tropical South Atlantic (TSA) (Liu et al., 2012; Zhang and Wang, 2012). Stephenson et al. (2014) verified some influence of the North Atlantic Ocean through the Atlantic Multi-decadal Oscillation (AMO) on Caribbean precipitation during boreal summer. Sea breezes in north-western Florida can be affected by changes in the size of the AWP: during years characterized by large AWP extensions, the NASH becomes weaker and moves further eastwards. At the same time, a large part of southeast North America including Florida is affected by relatively strong anomalous low-level northerly flow and large-scale subsidence, which suppress diurnal convection over the coast of the Florida panhandle (Misra et al., 2011).

Evidence for the importance of the AWP in modulating the climate system is also provided by studies of past and future conditions. For instance, reconstructed paleoclimatic data indicate that the persistence of the AWP during summer is responsible for increased precipitation and temperature detected in Florida during Heinrich events (Donders et al., 2011). Boer et al. (2011) suggest that the AWP may have played a key role in the glacial climate, by acting as a gatekeeper to regulate atmospheric moisture transport from the Atlantic across the Central American isthmus toward the Pacific. They also indicate that a decrease in the area of the AWP may enhance the cross-isthmus moisture transport, whereas extratropical North Atlantic cooling and a larger AWP may decrease it. Additionally, the Intergovernmental Panel on Climate Change's (IPCC) simulations of future climate suggest that atmospheric moisture will increase globally, increasing the moisture transport by 0.25 Sverdrups from the Atlantic to the Pacific (Richter and Xie, 2010).

Focusing on the Atlantic subregion of the WHWP, the aim of the present work is to analyse the role of the AWP as a source of moisture during its development, and to investigate the interannual variability of moisture transport across the region during the period 1982–1999 associated with changes in the warm pool's areal extension and with the ENSO.

Materials and Methods

Our method is based on the Lagrangian FLEXPART model developed by Stohl and James (2004, 2005) to calculate the variability of moisture along tracks of air particles and to identify regions where they gain and loss moisture. The methodology proposed here has been successfully applied to study moisture transport on the American continent in South America (Drumond et al., 2008) and Central America (Durán-Quesada et al., 2010), as well as other regions of the world (e.g., Gimeno et al., 2010).

In this approach, the atmosphere is divided into N evenly distributed "particles" or "parcels", and their advection is described by the expression:

$$\frac{dx}{dt} = v\left[x\left(t\right)\right] \quad (1)$$

where x is the position of the parcel and $v\,[x(t)]$ is the wind speed, interpolated in space and time, of the corresponding analysis grid. The gain (through evaporation from the environment, e) or loss (through precipitation, p) of specific humidity (q) by each parcel is calculated using the formula:

$$(e - p) = m\frac{dq}{dt} \tag{2}$$

The value of mass (m) is constant for every parcel. Integrating the $(e - p)$ values of all parcels in a vertical column of unit horizontal area over the depth of the atmosphere gives $(E - P)$, where E represents the evaporation and P the precipitation per unit area. Regions where $(E - P) < 0$ indicate moisture loss, so that precipitation exceeds evaporation in those areas, and the opposite is true where $(E - P) > 0$. The air parcel trajectories can be integrated backwards or forwards in time.

The AWP's extent was defined for every month from 1982 to 1999 and the area was computed at a monthly scale by applying the 28.5 isotherm definition proposed by Wang and Enfield (2001, 2003) to the SST dataset.

The Lagrangian data used in this work were obtained from a FLEXPART experiment run on a global domain, in which the atmosphere was divided in 1.9 million uniformly distributed particles. The model was fed by the ERA-40 reanalysis data set (Uppala et al., 2005) available at 6 h intervals (00, 06, 12, and 18 UTC) at a resolution of 1° × 1° in 60 vertical levels, from 0.1 to 1000 hPa, with approximately 14 model levels below 1500 m, and 23 between 1500 and 5000 m. FLEXPART needs five three-dimensional fields: horizontal and vertical wind components, temperature, and specific humidity in the ECMWF vertical hybrid coordinate system. The model also needs the two-dimensional fields: surface pressure, total cloud cover, 10 m horizontal wind components, 2 m temperature and dew point temperature, large scale and convective precipitation, sensible heat flux, east/west and north/south surface stress, topography, land-sea-mask, and subgrid standard deviation of topography.

Because we want to investigate the role of the AWP as a moisture source, we analyse the forward trajectories. We tracked the movement of parcels leaving the area of the AWP for 10 days forwards in time, which is the average residence time of water vapor in the atmosphere (Numaguti, 1999). The climatology covered the months from May to October for the years 1982–1999. We used data from the Global Precipitation Climatology Project (GPCP) (Adler et al., 2003) with a horizontal resolution of 2.5°, and the NOAA Optimum Interpolation SST V2 data (Reynolds et al., 2002) at a horizontal resolution of 1°. Both monthly data sets were provided by the NOAA/OAR/ESRL

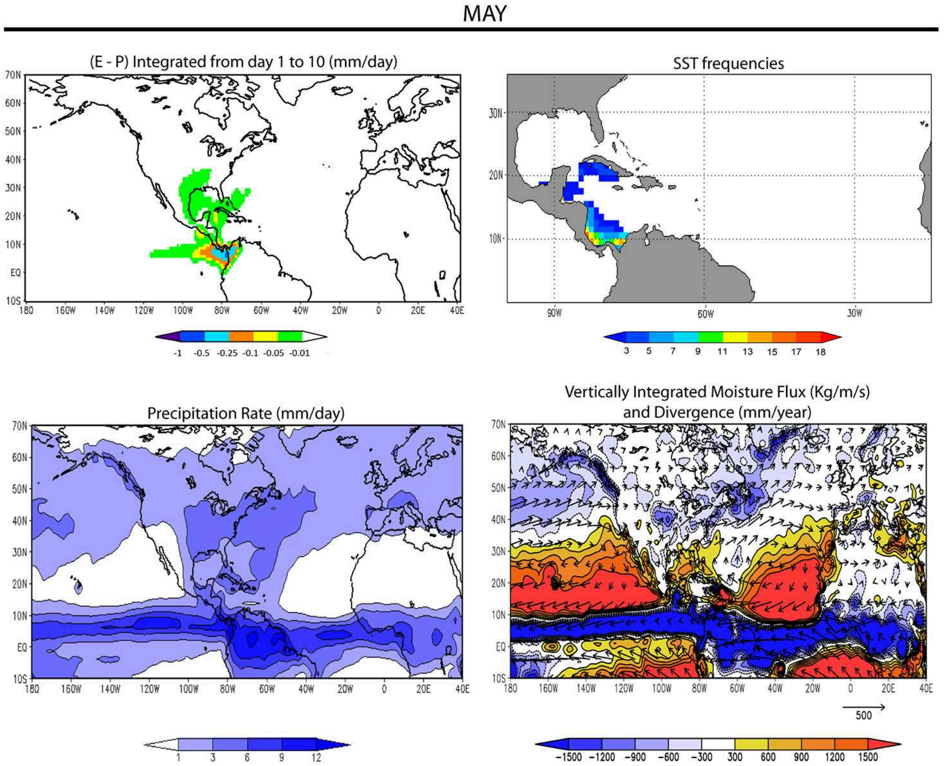

FIGURE 1 | Top left: Mean value of the $(E - P)$ field, forward integrated over a 10 day period from the AWP source defined for every May from 1982 to 1999. Only negative values of $(E - P)$ are shown, in order to emphasize the sink regions. **Top right**: Absolute frequency of monthly SST above the threshold 28.5°C. **Bottom left**: Precipitation rate. **Bottom left**: Vertically integrated moisture flux (VIMF) and its divergence. Units of $(E - P)$ and precipitation rate are mm d^{-1}, units of SST frequency are number of months, vectors of moisture flux are in kg m^{-1} s^{-1}, and units of contours of divergence of moisture are mm yr^{-1}.

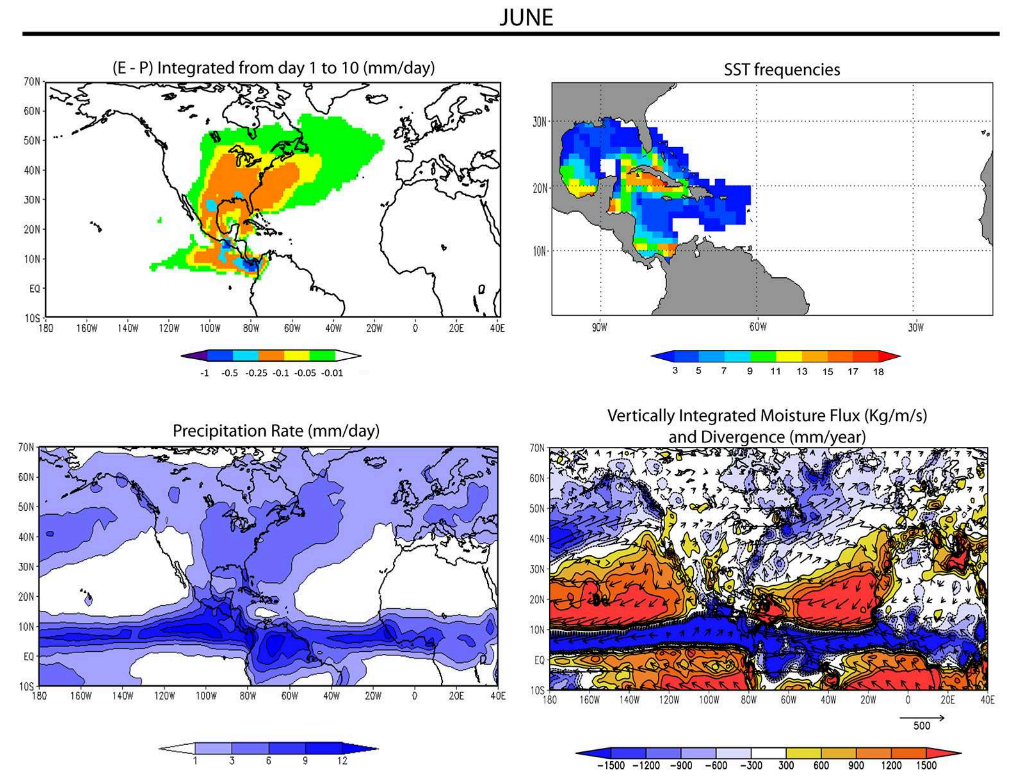

FIGURE 2 | As Figure 1, for June.

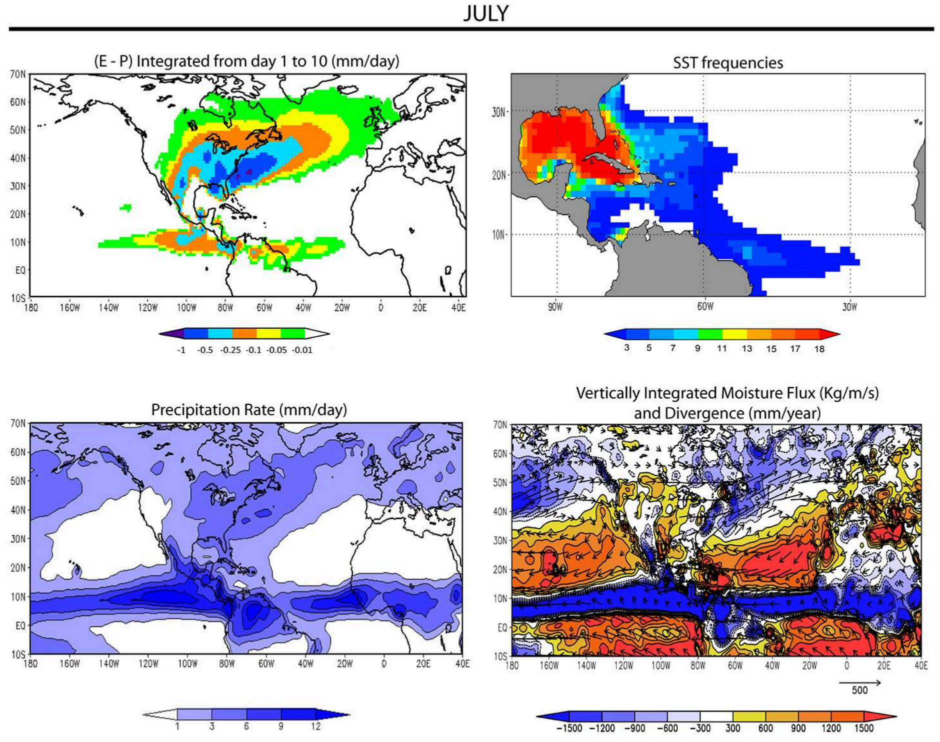

FIGURE 3 | As Figure 1, for July.

PSD via their website (http://www.esrl.noaa.gov/psd/). The vertical integral (over all levels available at ECMWF) of eastward and northward water vapor flux components were also obtained from the ERA-40 data with resolution of 1°, and they were used to compute the divergence of moisture flux.

ENSO events were obtained using the Oceanic Niño Index (ONI) from the NOAA Climate Prediction Center (www.cpc.noaa.gov/products/analysis_monitoring/ensostuff/ensoyears.shtml). The ONI has become the standard that NOAA uses for identifying El Niño and La Niña events in the tropical Pacific for the Niño 3.4 region (5°N–5°S, 120°W–170°W). The index values were calculated as the 3-month running mean of Extended Reconstructed Sea Surface Temperature (ERSST) v3b SST anomalies (Smith et al., 2008) in the Niño 3.4 region, and the ONI is based on climatology for the period 1981–2010. Extreme ENSO episodes occur when the threshold of ±0.5°C for the ONI is exceeded on a minimum of five consecutive overlapping seasons. To select an ENSO episode, we considered those periods when the threshold was exceeded a minimum of five consecutive times between June in year 0 and May in year 1 (defining an ENSO cycle). Five El Niño episodes (1982/83, 1986/87, 1987/88, 1991/92, 1994/95) and six La Niña events (1984/85, 1988/89, 1995/96, 1998/99, 1999/00) were selected for analysis. Our analyses of composites refer to anomalous patterns during the development stage of an ENSO cycle, before the winter's peak.

Analysis of the composite differences was carried out using a qualitative comparison of the results. The availability of a short period of data (18 years) limits both the selection of episodes (each composite contains around five cases) and the application of any statistical evaluation. The scope of our study is therefore to provide an overview of the regional climate characteristics of the AWP and to suggest how variability of the moisture transport from this source is associated with changes in its area and with the ENSO. Nevertheless, we argue that a longer period of data would be necessary to increase the number of elements in the composites, which is crucial for a more meaningful statistical evaluation of the results.

Results and Discussion

Figure 1 shows the mean climatological fields for May of (a) $(E - P) < 0$ (sinks of moisture), (b) the number of months for which SST values are above 28.5°C ('SST frequency'), (c) rainfall, and (d) VIMF and its divergence. The $(E - P)$ results indicate the presence of moisture sinks over the Pacific coast of Central America. It is interesting to note the low contribution of transported moisture to the precipitation over North America. This pattern may be explained by the presence of high moisture flux divergence values over the Gulf of Mexico and the west coast of North America, which inhibit precipitation over the area. It

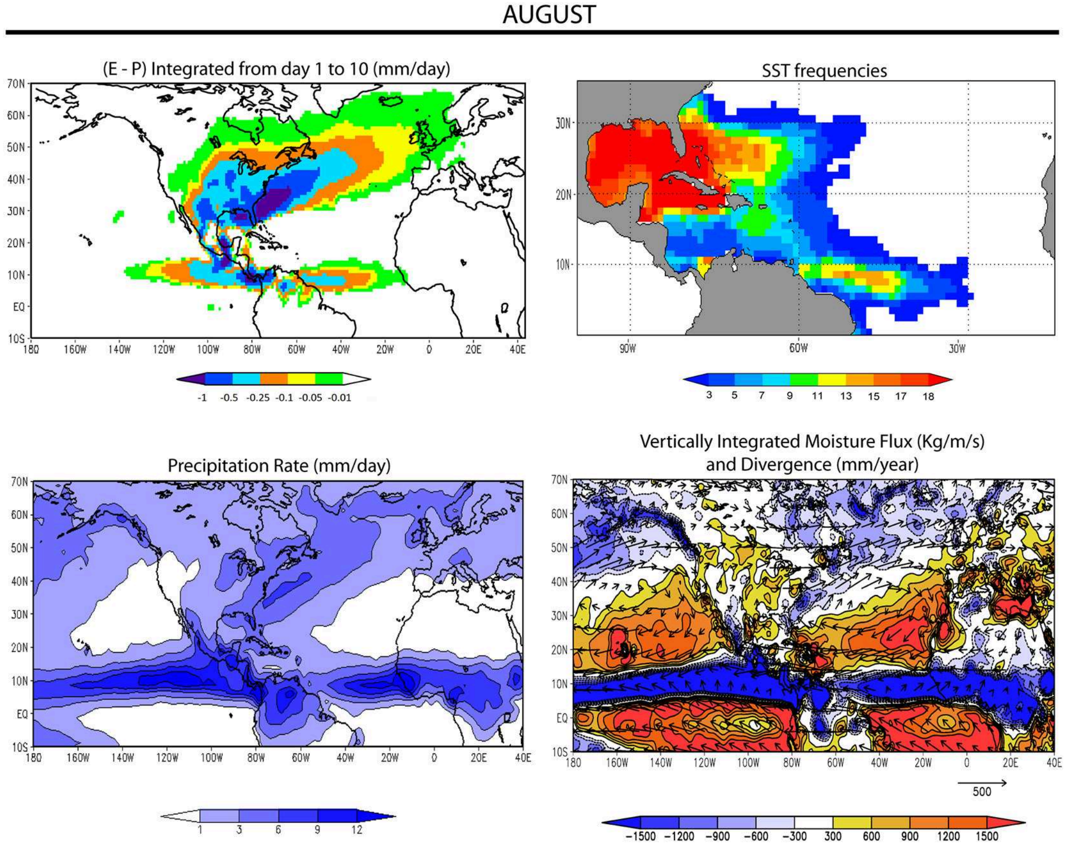

FIGURE 4 | As Figure 1, for August.

is known that the Caribbean rainy season is during the months May-November, in the boreal summer (Gouirand et al., 2014). Nevertheless, it is important to take into account that precipitation in North America is derived not only from large scale transport, but also from tropical cyclones during summer (Larson et al., 2005) and from cold surges (which are particularly important for the Gulf of Mexico) (Colle and Mass, 1995). Because the methodology proposed here focuses on identifying the precipitation generated by large-scale moisture transport, the $(E - P)$ and precipitation fields do not necessarily have to agree if the rainfall is produced through other mechanisms. The SST frequencies for May illustrate the positioning of the AWP restricted by the south of Cuba and the Central American coast. According to Mestas et al. (2005), the Intra-American Sea (IAS) may be considered a moisture source in which the moisture surplus is exported mainly to the west and north. A joint analysis of the maxima in the precipitation and in the convergence of the VIMF provides a rough estimate of the positioning of the Inter-tropical Convergence Zone (ITCZ) (Žagar et al., 2011), and $(E-P)$ suggests some moisture contribution from the AWP toward the eastern Pacific ITCZ region.

In June (**Figure 2**), the SST frequency field shows that the AWP has expanded to cover the whole Gulf of Mexico and the Caribbean Sea. The $(E - P)$ field shows the moisture contribution toward a region covering a small area in the Pacific, as well as central-eastern North America and the Western Atlantic, agreeing qualitatively with the observed precipitation patterns. Anomalies in $(E - P)$ are mainly balanced by the change in moisture flux divergence at time scales of a month and longer, while the contribution from transient eddies occurs at on a much shorter time scale (Wang et al., 2013). Chan et al. (2011) reported the importance of the Lesser Antilles in modulating regional atmospheric circulation, and the impact of AWP variations on the islands' climate. During June the moisture flux penetrates into south-eastern North America associated with the Great Plains Low Level Jet (GPLLJ). The GPLLJ is a mechanism which transports moisture from the IAS to the North American continent during summer, and enhances precipitation over the central United States (Ropelewski and Yarosh, 1998).

During July (**Figure 3**), the region with higher SST frequencies covered the northern Gulf of Mexico and the seas around Cuba, including near La Española. In August (**Figure 4**) it expanded toward the Gulf of Mexico and part of the Caribbean Sea. During these months the moisture contribution to south-eastern North America increased strongly, while weakening to the sink regions over the Caribbean. In August the sinks expanded over south-eastern North America, Central America, and the Atlantic and Pacific oceans between approximately 3° and 6°N, coinciding with the region where the ITCZ develops (Žagar et al., 2011). The moisture contribution from the AWP also reached Western

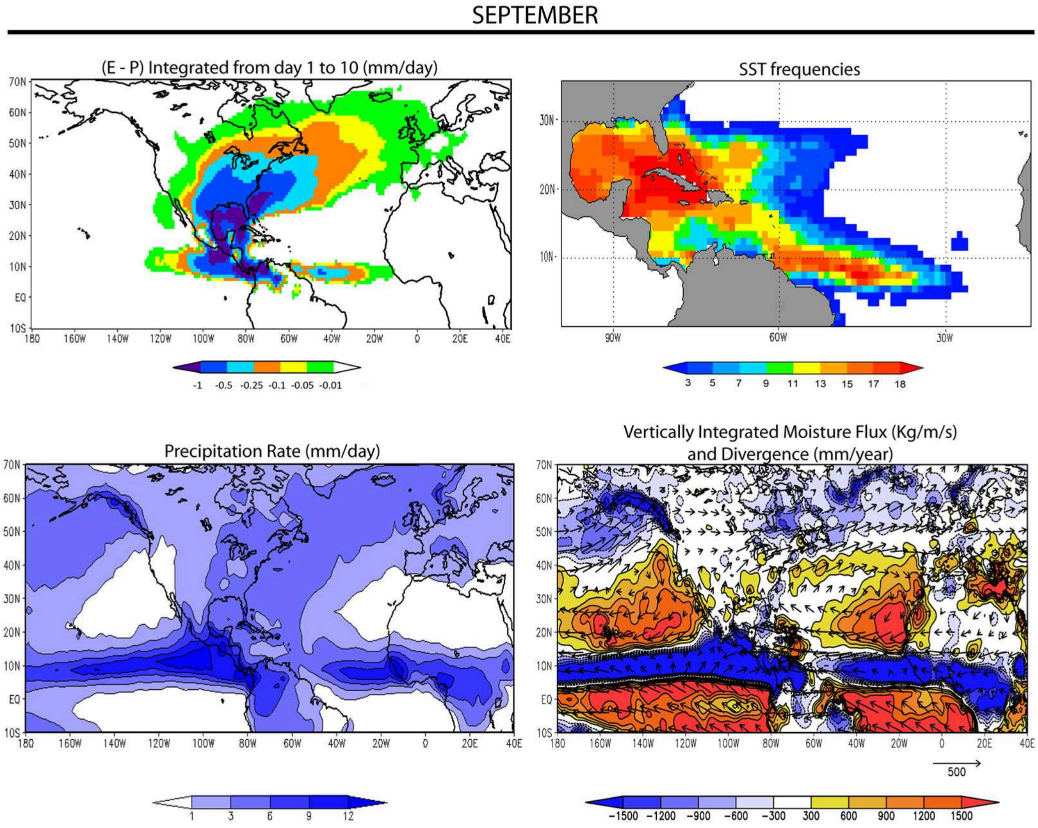

FIGURE 5 | As Figure 1, for September.

Europe during these months. The sink areas coincided with moisture flow convergence regions. A qualitative comparison between $(E-P)$ and patterns of precipitation rate can be used to help to assess the results, suggesting that moisture from the AWP contributed to precipitation in these areas.

In September (**Figure 5**) the AWP reached the central Atlantic, and in October (**Figure 6**) it reached the western coast of Africa and extended southwards. The temporal evolution of the AWP matches the previous results of Wang and Enfield (2001) and Drumond et al. (2011). In September, the moisture sink regions appear to cover a larger area than in previous months, and according to **Table 1** this is also the month when the extent of the AWP reaches its maximum. In September and October the size of the moisture sinks increased over central and southeastern North America, and over the Atlantic and Pacific ITCZ regions. A visual analysis indicates that zones of precipitation in both months increased significantly in size over these regions. Areas of moisture flux divergence weakened and were displaced eastwards over the tropical Atlantic during September, and in October they appeared over the Gulf of Mexico and the east coast of North America.

Drumond et al. (2011) used only a five year period (2000–2004) and considered the whole WHWP to explain an $(E-P)$ pattern extending further westwards into the Pacific. Our separate analysis of the AWP shows that it provides moisture to the Pacific, Central and North America, and tropical and North Atlantic, confirming the interhemispheric influence of moisture transport from the AWP (Wang et al., 2009).

($E-P$) during Times of Largest and Smallest AWP Area

Table 1 shows the values of the monthly climatological AWP area during the extended summer season. The minimum area of 0.5×10^{12} m^2 occurs in May, and it reaches its maximum in September with a value of about 13.6×10^{12} m^2. **Figure 7** shows the monthly evolution of the AWP area during the period of interest, 1982–1999. The area was at a maximum during August and September 1998, with values up to 21.6×10^{12} m^2, while the minima occurred during May 1984, 1986, and 1992. It is important to note that

TABLE 1 | Climatological monthly average area of AWP ($\times$ 10^{12} m^2) for 1982–1999.

Month	Average area
May	0.5
June	0.9
July	7.2
August	11.9
September	13.6
October	8.9

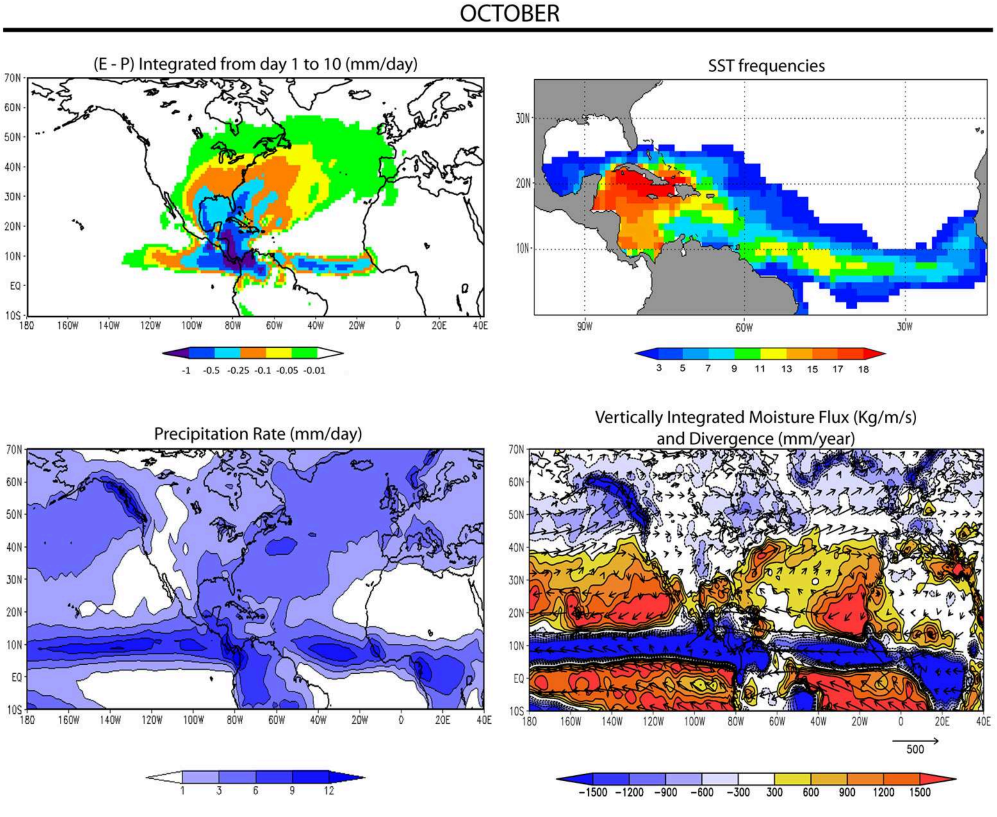

FIGURE 6 | As Figure 1, for October.

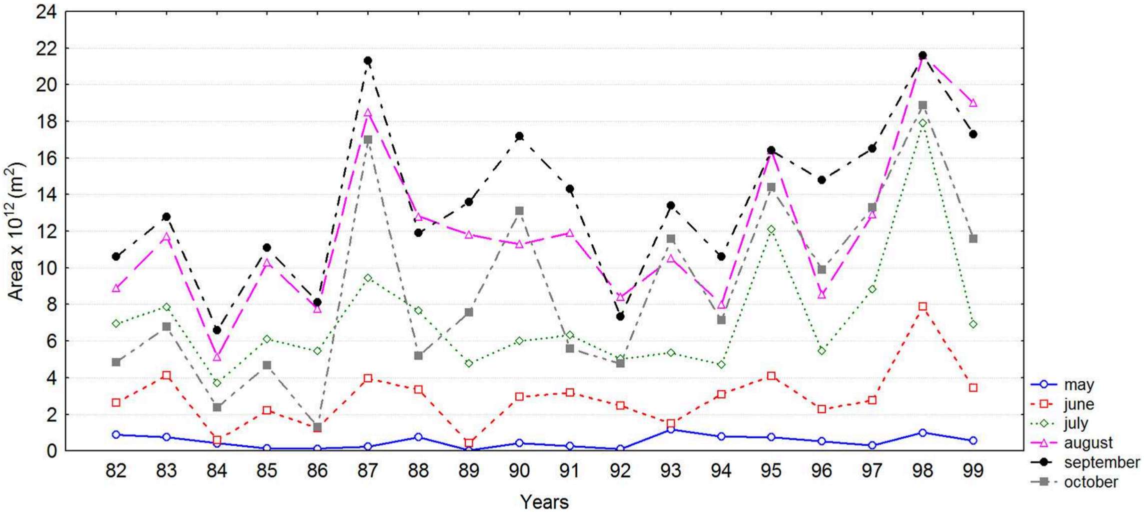

FIGURE 7 | Annual time series of AWP area, 1982–1999.

there are some years for which the AWP area was a local maximum or minimum in almost all months. For example, in 1984, 1986 and 1992, for at least 5 of the 6 months analyzed, the area of the AWP was less than during the same month in the years before and after: in **Table 2**, these years are shaded gray, green and blue, respectively. By contrast, in 1987, 1995, 1997 and 1998, the AWP was larger than in the same months in the years before and after: these years are marked in **Table 3**. **Tables 2**, **3** show the five years that contain the smallest and largest AWP areas for each month respectively. The monthly differences in moisture sink patterns for the composite of the highest and lowest AWP areas (**Figure 8**) shows the impact of AWP extension on moisture transport. During May and June, negative values of $(E - P)$ (blueish colors) prevailed over Central America, the Pacific ITCZ region, and southern North America, suggesting that the moisture contribution of the AWP increases when the AWP is at its largest. The moisture contribution to the climatological sinks during these periods is also enhanced during the other months, except for parts of south-eastern and central North America during July–August and September–October, respectively. The main reason is that an anomalously large (small) AWP weakens (strengthens) the southerly GPLLJ, which reduces (enhances) northward moisture transport from the Gulf of Mexico and thereby decreases (increases) summer rainfall over central North America (Wang et al., 2008). The direct relationship between larger AWPs and warmer North Atlantic temperatures from August to October described by Wang et al. (2006) is also associated with increased rainfall over the Caribbean, Mexico, eastern subtropical Atlantic, and the southeast Pacific, and decreased rainfall in northwest North America and eastern South America. In the warm season, warmer TNA conditions induce a local increase in atmospheric convection and a reduction of precipitation over western North America (Kushnir et al., 2010). From July to October there is an enhanced moisture contribution from the AWP to Western Europe during years when the AWP is larger than average.

TABLE 2 | Years of smallest AWP area for 1982–1999.

Smallest AWP extension					
May	**Jun**	**Jul**	**Aug**	**Sept**	**Oct**
1985	1984	1984	1984	1982	1982
1986	1985	1989	1986	1984	1984
1987	1986	1992	1992	1986	1985
1989	1989	1993	1994	1992	1986
1992	1993	1994	1996	1994	1992

Highlighted years indicate when a local minimum is reached for the majority of months.

TABLE 3 | Years of highest AWP area for 1982–1999.

Largest AWP extension					
May	**Jun**	**Jul**	**Aug**	**Sept**	**Oct**
1982	1983	1983	1987	1987	1987
1988	1987	1987	1995	1990	1990
1993	1995	1995	1997	1997	1995
1994	1998	1997	1998	1998	1997
1998	1999	1998	1999	1999	1998

Highlighted years indicate when a local maximum is reached for the majority of months.

The Monthly Influence of the Evolution of the ENSO Cycle

The ENSO is the most powerful coupled ocean-atmosphere mode on the planet (Trenberth and Caron, 2000; Trenberth and Stepaniak, 2001). It originates in the Pacific Ocean where the major environmental changes occur; however, its influence extends to the whole climatic system, with effects detected in precipitation patterns, SST, pressure, wind, and specific humidity among others (e.g., Peixoto and Oort, 1992; Giannini et al., 2001; Moron and Plaut, 2003; Wagner et al., 2005).

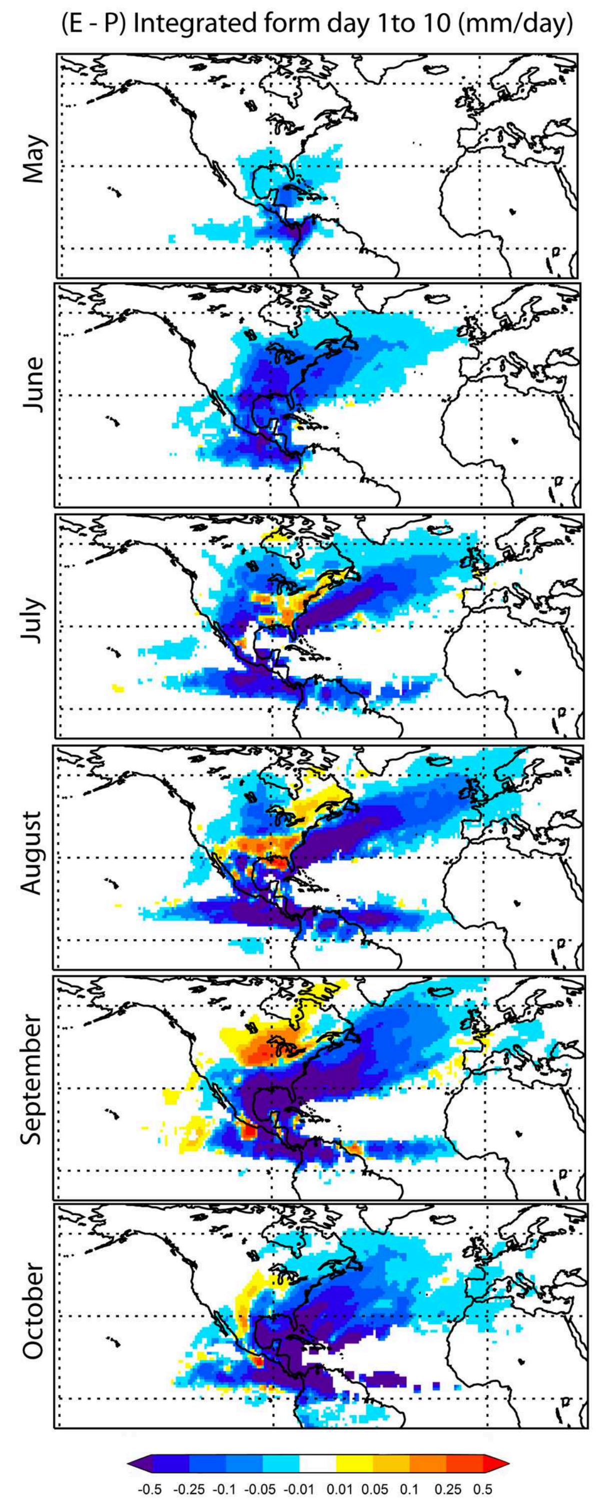

FIGURE 8 | Monthly composite differences of moisture sinks (only $E - P < 0$ values) between years with the largest and smallest AWP areas during the period 1982–1999 (Tables 2, 3, respectively). Units are mm d^{-1}.

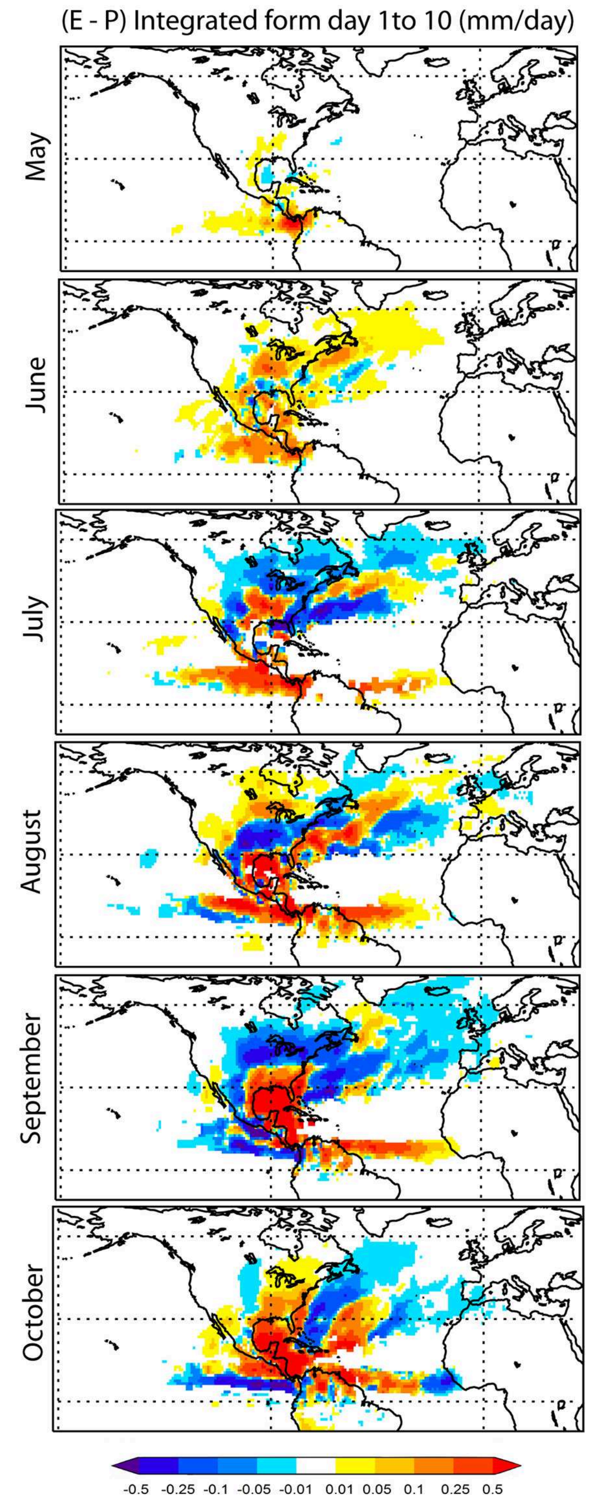

FIGURE 9 | Monthly composite differences of moisture sinks (only $E - P < 0$ values) between El Niño and La Niña events for 1982–1999. Units are mm d^{-1}.

The direct effect of the size of the AWP's area on moisture transport was described in the previous section. In this section, we examine the effect of ENSO phase on the variability of moisture transport from the AWP. Wang et al. (2006) found that about two-thirds of the overall variability of warm pool size in the summer following a winter with a peak ENSO event appears to be unrelated to the ENSO. On the other hand, during the summer a strong (weak) easterly CLLJ is associated with warm (cold) SST anomalies in the tropical Pacific (Wang, 2007). Wang (2001) reported that ENSO can affect the TNA through the Walker and Hadley circulations, favoring the TNA warming in the subsequent spring of the El Niño year. According to the methodology explained in the Section Materials and Methods, five El Niño episodes (1982/83, 1986/87, 1987/88, 1991/92, 1994/95) and six La Niña events (1984/85, 1988/89, 1995/96, 1998/99, 1999/00) were selected during the period 1982–1999.

The variations in the AWP's moisture contribution during ENSO warm phases (El Niño) and cool phases (La Niña) were analyzed by subtracting sink patterns of composites of El Niño and La Niña episodes observed during the period of interest (**Figure 9**). In contrast to Wang et al. (2006), the composites in this work refer to the extended summer season preceding a mature ENSO phase, because we want to check whether the development of an extreme ENSO episode is associated with anomalies in the AWP region. Accordingly, in **Figure 9** the reddish (blueish) colors indicate enhanced sinks for moisture transported from the AWP during La Niña (El Niño) events. During May and June, it seems that the moisture contribution to areas surrounding the AWP is higher during La Niña episodes. In July the bluish colors in parts of Central America, the Pacific, Atlantic, and central-eastern North America indicate enhanced moisture contribution during El Niño events. In August, September, and October the reddish colors over the Caribbean and TNA suggest that moisture sinks are intensified over these regions during la Niña events. Giannini et al. (2001) verified that Caribbean rainfall may be affected by extreme ENSO conditions, and indicated that dry conditions prevail over the Caribbean during the development stage of an El Niño episode.

Conclusions

The FLEXPART model allows air parcels, and the water vapor they contain, to be tracked for up to 10 days after they leave the area of the AWP. Visual analysis of $(E - P)$ suggests that May and September are the months presenting the smallest and largest sink regions respectively, which agrees with the variations in the AWP's measured area. Higher moisture contributions to continental precipitation occur from June onwards, with sink regions mainly over Colombia, Central America, México, and the eastern United States and Canada. From July to October the sinks expand toward Western Europe, probably associated with flow conditioned by the North Atlantic Subtropical High. Although the contribution of moisture to the Pacific ITCZ region is lower than the results obtained by Drumond et al. (2011) for all WHWP extension, there is some moisture transport from the AWP toward the Pacific.

In respect of the climatological positioning of the AWP and its interannual variability, the pool is limited to the coast of Central America in May and expands toward the east and south covering the whole Caribbean in the months that follow, reaching the west coast of Africa in October. The number of months with SST above 28.5°C indicates the Gulf of Mexico and the Caribbean Sea surrounding Cuba as the most constant location of the AWP.

The composite analysis suggests that the largest warm pools found during the 18 year dataset accounted for most of the increased contribution of humidity to the climatological sinks. Differences between El Niño and La Niña suggest that during La Niña events the moisture loss increases in the Caribbean and TNA regions, particularly from August to October. It is important to stress that analysis of the composite differences was carried out using a qualitative comparison of the results. The availability of a short period of data limits both the selection of more episodes and the application of any significant statistical evaluation.

Although the present work analyzes the variations of the moisture contribution from the AWP during the development stage of the extreme ENSO episodes, a more detailed analysis on the links (including dynamical mechanisms) between ENSO and the WHWP is necessary and it will be considered in further studies. It was noted that the moisture transport within the region is not only dominated by the Atlantic component of the warm pool, but also by the Pacific one, which will be the focus of a future subsequent paper.

Acknowledgments

This work is based on the final project of the first author's Master degree. RS thanks the Spanish Agency of International Cooperation and Development (AECID) for the scholarship. The authors gratefully acknowledge the support of the Spanish Government through their funding of the TRAMO ("TRAnsport of MOisture") project (CGL-2012-35485), which is also cofunded by FEDER (in Spanish European Regional Development Fund-ERDF).

References

Adler, R. F., Huffman, G. J., Chang, A., Ferraro, R., Xie, P., Janowiak, J., et al. (2003). The Version 2 Global Precipitation Climatology Project (GPCP) monthly precipitation analysis (1979-Present). *J. Hydrometeor.* 4, 1147–1167. doi: 10.1175/1525-7541(2003)004<1147:TVGPCP>2.0.CO;2

Boer, H. J., Roche, D. M., Renssen, H., and Dekker, S. C. (2011). Two-signed feedback of cross-isthmus moisture transport on glacial overturning controlled by the Atlantic warm pool. *Clim. Past Discuss.* 7, 3859–3893. doi: 10.5194/cpd-7-3859-2011

Chan, S. C., Misra, V., and Smith, H. (2011). A modeling study of the interaction between the Atlantic Warm Pool, the tropical Atlantic easterlies, and the Lesser Antilles. *J. Geophys. Res.* 116, D00Q02. doi: 10.1029/2010JD015260

Colle, B. A., and Mass, C. F. (1995). The structure and evolution of could surges east of the Rocky mountains. *Mon. Wea. Rev.* 123, 2577–2610.

Donders, T. H., de Boer, H. J., Finsinger, W., Grimm, E. C., Dekker, S. C., Reichart, G. J., et al. (2011). Impact of the Atlantic Warm Pool on precipitation and temperature in Florida during North Atlantic cold spells. *Clim. Dyn.* 36, 109–118. doi: 10.1007/s00382-009-0702-9

Drumond, A., Nieto, R., and Gimeno, L. (2011). On the contribution of the Tropical Western Hemisphere Warm Pool source of moisture to the Northern Hemisphere precipitation through a Lagrangian approach. *J. Geophys. Res.* 116, D00Q04. doi: 10.1029/2010JD015397

Drumond, A., Nieto, R., Gimeno, L., and Ambrizzi, T. (2008). A Lagrangian identification of major sources of moisture over central Brazil and La Plata Basin. *J. Geophys. Res.* 113, D14128. doi: 10.1029/2007JD009547

Durán-Quesada, A. M., Gimeno, L., Amador, J. A., and Nieto, R. (2010). Moisture sources for Central America: Identification of moisture sources using a Lagrangian analysis technique. *J. Geophys. Res.* 115, D05103. doi: 10.1029/2009JD012455

Giannini, A., Kushnir, Y., and Cane, M. A. (2001). Seasonality in the impact of ENSO and the North Atlantic High on Caribbean Rainfall. *Phys. Chem. Earth* 26, 143–147. doi: 10.1016/S1464-1909(00)00231-8

Gimeno, L., Drumond, A., Nieto, R., Trigo, R., and Stohl, A. (2010). On the origin of continental precipitation. *Geophys. Res. Lett.* 37, L13804. doi: 10.1029/2010GL043712

Gouirand, I., Moron, V., Hu, Z.-Z., and Jha, B. (2014). Influence of the warm pool and cold tongue El Niños on the following Caribbean rainy season rainfall. *Clim. Dyn.* 42, 919–929. doi: 10.1007/s00382-013-1753-5

Gray, W. M. (1968). A global view of the origin of tropical disturbances and storms. *Mon. Wea. Rev.* 96, 669–700.

Knaff, J. A. (1997). Implications of summertime sea level pressure anomalies in the tropical Atlantic region. *J. Clim.* 10, 789–804.

Kushnir, Y., Seager, R., Ting, M., Naik, N., and Nakamura, J. (2010). Mechanisms of tropical Atlantic SST influence on North American precipitation variability. *J. Clim.* 23, 5610–5628. doi: 10.1175/2010JCLI3172.1

Larson, J., Zhou, Y., and Higgins, R. W. (2005). Characteristics of landfalling tropical cyclones in the United States and Mexico: climatology and interannual variability. *J. Clim.* 18, 1247–1262. doi: 10.1175/JCLI3317.1

Liu, H., Wang, C., Lee, S.-K., and Enfield, D. (2012). Atlantic warm-pool variability in the IPCC AR4 CGCM simulations. *J. Clim.* 25, 5612–5628. doi: 10.1175/JCLI-D-11-00376.1

Liu, H., Wang, C., Lee, S.-K., and Enfield, D. (2015). Inhomogeneous influence of the Atlantic Warm Pool on United States precipitation. *Atmos. Sci. Lett.* 16, 63–69. doi: 10.1002/asl2.521

Martin, R. E., and Schumacher, C. (2011). The Caribbean low-level jet and its relationship with precipitation in IPCC AR4 models. *J. Clim.* 24, 5935–5950. doi: 10.1175/JCLI-D-11-00134.1

Mestas, N. A. M., Zhang, C., and Enfield, D. B. (2005). Uncertainties in estimating moisture fluxes over the Intra-Americas Sea. *J. Hydrometeorol.* 6, 696–709. doi: 10.1175/JHM442.1

Misra, V., Moeller, L., Stefanova, L., Chan, S., O'Brien, J. J., Smith, T. J. III, et al. (2011). The influence of the Atlantic warm pool on the Florida panhandle sea breeze. *J. Geophys. Res.* 116, D00Q06. doi: 10.1029/2010JD015367

Moron, V., and Plaut, G. (2003). The impact of El Niño-southern oscillation upon weather regimes over Europe and the North Atlantic during boreal winter. *Int. J. Climatol.* 25, 363–379. doi: 10.1002/joc.890

Numaguti, A. (1999). Origin and recycling processes of precipitating water over the Eurasian continent: Experiments using an atmospheric general circulation model. *J. Geophys. Res.* 104, 1957–1972. doi: 10.1029/1998JD200026

Peixoto, J. P., and Oort, A. H. (1992). *Physics of Climate*. New York, NY: Springer–Verlag New York Press.

Reynolds, R. W., Rayner, N. A., Smith, T. M., Stokes, D. C., and Wang, W. (2002). An improved *in situ* and satellite SST analysis for climate. *J. Clim.* 15, 1609–1625. doi: 10.1175/1520-0442(2002)015<1609:AIISAS>2.0.CO;2

Richter, I., and Xie, S.-P. (2010). Moisture transport from the Atlantic to the Pacific basin and its response to North Atlantic cooling and global warming. *Clim. Dyn.* 35, 551–566. doi: 10.1007/s00382-009-0708-3

Ropelewski, C. F., and Yarosh, E. S. (1998). The observed mean annual cycle of moisture budgets over the central United States (1973–1992). *J. Clim.* 11, 2180–2190.

Smith, T. M., Reynolds, R. W., Peterson, T. C., and Lawrimore, J. (2008). Improvements to NOAA's historical merged land-ocean surface temperature analysis (1880–2006). *J. Clim.* 21, 2283–2296. doi: 10.1175/2007JCLI2100.1

Stephenson, T. S., Vincent, L. A., Allen, T., Van Meerbeeck, C. J., McLean, N., Peterson, T. C., et al. (2014). Changes in extreme temperature and precipitation in the Caribbean region, 1961–2010. *Int. J. Climatol.* 34, 2957–2971. doi: 10.1002/joc.3889

Stohl, A., and James, P. (2004). A Lagrangian analysis of the atmospheric branch of the global water cycle. Part 1: Method description, validation, and demonstration for the August 2002 flooding in central Europe. *J. Hydrometeorol.* 5, 565–678. doi: 10.1175/1525-7541(2004)005<0656:ALAOTA>2.0.CO;2

Stohl, A., and James, P. (2005). A Lagrangian analysis of the atmospheric branch of the global water cycle. Part 2: Earth's river catchments, ocean basins, and moisture transports between them. *J. Hydrometeorol.* 6, 961–984. doi: 10.1175/JHM470.1

Trenberth, K. E., and Caron, J. M. (2000). The Southern oscillation revisited: sea level pressures, surface temperatures and precipitation. *J. Clim.* 13, 4358–4365.

Trenberth, K. E., and Guillemot, C. J. (1998). Evaluation of the atmospheric moisture and hydrological cycle in the NCEP/NCAR reanalysis. *Clim. Dyn.* 14, 213–231. doi: 10.1007/s003820050219

Trenberth, K. E., and Stepaniak, D. P. (2001). Indices of El Nino evolution. *J. Clim.* 14, 1697–1701. doi: 10.1175/1520-0442(2001)014<1697:LIOENO>2.0.CO;2

Uppala, S. M., Kallberg, P. W., Simmons, A. J., Andrae, U., da Costa Bechtold, V., Fiorino, M., et al. (2005). The ERA-40 re-analysis. *Q. J. R. Meteorol. Soc.* 131, 2961–3012. doi: 10.1256/qj.04.176

Wagner, T., Beirle, M., Grzegorski, M., Sanghavi, S., and Platt, U. (2005). El Niño induced anomalies in global data sets of total column precipitable water and cloud cover derived from GOME on ERS-2. *J. Geophys. Res.* 110:D15104. doi: 10.1029/2005jd005972

Wang, C. (2001). Atlantic climate variability and its associated atmospheric circulation cells. *J. Clim.* 15, 1516–1536. doi: 10.1175/1520-0442(2002)015<1516:ACVAIA>2.0.CO;2

Wang, C. (2007). Variability of the Caribbean low-level jet and its relations to climate. *Clim. Dyn.* 29, 411–422. doi: 10.1007/s00382-007-0243-z

Wang, C., and Enfield, D. B. (2001). The tropical hemisphere warm pool. *Geophys. Res. Lett.* 28, 1635–1638. doi: 10.1029/2000GL011763

Wang, C., and Enfield, D. B. (2003). A further study of the tropical Western Hemisphere Warm Pool. *J. Climate*, 16, 1476–1493. doi: 10.1175/1520-0442-16.10.1476

Wang, C., Enfield, D. B., Lee, S. K., and Landsea, W. (2006). Influences of the Atlantic warm pool on Western summer rainfall and Atlantic Hurricanes. *J. Clim.* 19, 3011–3028. doi: 10.1175/JCLI3770.1

Wang, C., and Lee, S.-K. (2007). Atlantic warm pool, Caribbean low-level jet, and their potential impact on Atlantic hurricanes. *Geophys. Res. Lett.* 34, L02703. doi: 10.1029/2006GL028579

Wang, C., Lee, S.-K., and Enfield, D. B. (2007). Impact of the Atlantic Warm Pool on the summer climate of the Western Hemisphere. *J. Clim.* 21, 5021–5040. doi: 10.1175/JCLI4304.1

Wang, C., Lee, S.-K., and Enfield, D. B. (2008). Climate response to anomalously large and small Atlantic warm pools during the summer. *J. Clim.* 21, 2437–2450. doi: 10.1175/2007JCLI2029.1

Wang, C., Lee, S.-K., and Mechoso, C. R. (2009). Interhemispheric influence of the Atlantic Warm Pool on the Southeastern Pacific. *J. Clim.* 23, 404–416. doi: 10.1175/2009JCLI3127.1

Wang, C., Zhang, L., and Lee, S.-K. (2013). Response of freshwater flux and sea surface salinity to variability of the Atlantic warm pool. *J. Clim.* 26, 1249–1267. doi: 10.1175/JCLI-D-12-00284.1

Weisberg, R. H. (1996). "On the evolution of SST over the PACS region," in American Meteorological Society, *76th Annual Meeting* (Atlanta, GA).

Žagar, N., Skok, G., and Tribbia, J. (2011). Climatology of the ITCZ derived from ERA Interim reanalyses. *J. Geophys. Res.* 116, D15103. doi: 10.1029/2011JD015695

Zhang, L., and Wang, C. (2012). Remote influences on freshwater flux variability in the Atlantic warm pool region. *Geophys. Res. Lett.* 39, L19714. doi: 10.1029/2012GL053530

Conflict of Interest Statement: The authors declare that the research was conducted in the absence of any commercial or financial relationships that could be construed as a potential conflict of interest.

frontiers
in Environmental Science

ORIGINAL RESEARCH
published: 27 May 2015
doi: 10.3389/fenvs.2015.00024

Tropical south east Atlantic warm events and associated rainfall anomalies over southern Africa

Chris J. C. Reason and Sandi Smart*

Oceanography Department, University of Cape Town, Cape Town, South Africa

Moisture flux and rainfall anomalies over southern Africa that have occurred during strong warm SST events off the coast of Angola since 1950 are considered. These events typically occur during February-April (FMA), the main rainy season for Angola/northern Namibia. Eleven of these events have occurred in this 60 year period and each experiences increased rainfall somewhere in coastal Angola, and in 10 cases, somewhere in northern Namibia. Attention is focussed on the five events with the largest and most widespread positive rainfall anomalies over Africa south of 10°S; namely, 1963, 1986, 2001, 2006, 2011. All of these five events experienced increased moisture flux from the western tropical Indian Ocean, warm SST anomalies also in the south west Indian Ocean, and most also showed increased westerly moisture flux from the tropical south east Atlantic. The events also showed strong weakening of the mid-level anticyclonic conditions that occur over southern Africa during summer. This factor together with the distribution of anomalous uplift through the middle/upper troposphere appeared to match the areas of increased rainfall better than the areas of low level moisture convergence. Reported experiments with an atmospheric GCM forced with idealizations of the observed SST anomalies show rainfall anomalies consistent with the observed patterns.

Keywords: south east Atlantic, warm events, southern African rainfall, climate variability, moisture flux

OPEN ACCESS

Edited by:
Anita Drumond,
University of Vigo, Spain

Reviewed by:
Michelle Simoes Reboita,
Federal University of Itajubá, Brazil
Isabel Iglesias,
Ciimar, Portugal

****Correspondence:***
Chris J. C. Reason,
Oceanography Department, University of Cape Town, Private Bag X3,
7701 Cape Town, South Africa
chris.reason@uct.ac.za

Specialty section:
This article was submitted to Atmospheric Science,
a section of the journal
Frontiers in Environmental Science

Received: *18 December 2014*
Accepted: *10 March 2015*
Published: *27 May 2015*

Citation:
Reason CJC and Smart S (2015) Tropical south east Atlantic warm events and associated rainfall anomalies over southern Africa.
Front. Environ. Sci. 3:24.
doi: 10.3389/fenvs.2015.00024

Introduction

Most of southern Africa is an austral summer rainfall region. This summer precipitation is associated with three major oceanic sources of moisture; traditionally the tropical western Indian Ocean has been thought to be the most important with the subtropical southwest Indian Ocean also being a substantial contributor of moisture for rain over the subtropical regions (e.g., D'Abreton and Lindesay, 1993). The third source is the South Atlantic basin but, historically, not much work has been done on its influences on southern African climate (Reason et al., 2006). However, Hirst and Hastenrath (1983) drew attention to the existence of warm events in the tropical South East Atlantic and rainfall over Angola and Namibia. These rainfall linkages were further explored by Rouault et al. (2003) while Vigaud et al. (2007) highlighted the importance of tropical Atlantic moisture flux for Congo Basin rainfall. South Atlantic moisture flux anomalies associated with SST dipole events in the midlatitudes (Fauchereau et al., 2003; Hermes and Reason, 2005) may also contribute to summer rainfall over subtropical southern Africa (Vigaud et al., 2009).

A warm pool (SST 26–29°C) develops in the tropical South East Atlantic Ocean, off the central and northern coast of Angola and north of the Angola Benguela Frontal Zone (ABFZ), during the austral summer and lasts until at least April. As the trade winds north of the ABFZ relax after spring and through summer, latent heat fluxes and upper ocean mixing reduce in this region, leading to the development of warm SSTs here (Reason et al., 2006; Rouault et al., 2007, 2009). Within the equatorial wave guide which includes the northern part of the warm pool, this seasonal relaxation of the easterly winds reduces the zonal pressure gradient, flattens the thermocline and leads to warming across the equatorial Atlantic (Philander and Pacanowski, 1986). Moisture emanating from the warm pool region is a secondary source for the summer rainfall region (Reason et al., 2006), but can make larger contributions during some summer wet spells (e.g., Cook et al., 2004). This tropical South East Atlantic moisture flux also feeds into the Angola low, a heat low that exists over northern Namibia / southern Angola during the summer half of the year, and which acts as the source region for the main synoptic summer rainfall producing system over subtropical southern Africa, the tropical temperate trough or tropical extra-tropical cloud band (Harrison, 1984; Hart et al., 2010).

Figure 1 shows schematically the locations of the Angola low, the cloudbands and the low level tropical convergence zones over southern Africa in the austral summer as well as the ABFZ which separates the warm tropical Angolan Current waters from the northern Benguela Current upwelling system off the coast of northern Namibia. Also apparent in **Figure 1** is the narrow peninsula-like distribution of the southern African landmass and its termination in the subtropics in mid-ocean. It is this geography that enables the South Atlantic and Indian Oceans to play a very strong role in its climate.

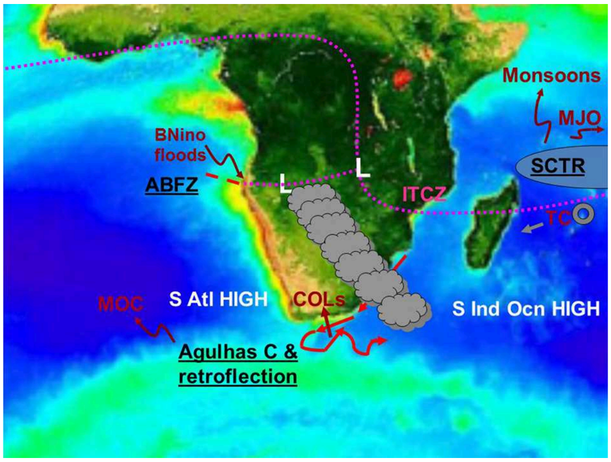

FIGURE 1 | Schematic showing the main circulation features important for southern African rainfall during summer (Angola low denoted L, subtropical anticyclones, tropical convergence zones denoted as magenta dotted lines, cloud bands), unique regional oceanic features (Angola Benguela Frontal Zone denoted ABFZ, Agulhas Current and retroflection region, Seychelles-Chagos Thermocline Ridge denoted SCTR) and their climate impacts (Meridional Overturning Circulation denoted MOC, cut-off low induced flooding denoted COLs, tropical cyclones denoted TC, Madden Julian Oscillations denoted MJO, Benguela Niño induced floods denoted BNino).

In addition to the ABFZ, there are two other rather unique regional ocean features that strongly impact on southern African weather and climate. These are the Agulhas Current and its retroflection which sheds rings of warm, salty water into the South East Atlantic and the Seychelles Chagos Thermocline Ridge (SCTR) northeast of Madagascar. The Agulhas retroflection region has been implicated in many of southern South Africa's flooding disasters through moisture-laden low level wind jets impacting on the coastal mountains during severe cut-off low events (Singleton and Reason, 2007). SST anomalies here and in the South Atlantic regions west and southwest of South Africa also impact on winter rainfall over southwestern South Africa (Reason and Jagadheesha, 2005). While not an Atlantic feature, for completeness, it is mentioned that the SCTR is important for tropical cyclones, MJO activity and rainfall in the South West Indian Ocean / southeastern African region.

On the seasonally averaged scale, **Figure 2** (derived from NCEP re-analyses, Kalnay et al., 1996) shows the 850 hPa level late summer (February to April) moisture flux and its convergence over the southern African region. This figure implies that the South Atlantic is less important than the South Indian Ocean for rainfall over the landmass. Note that the 850 hPa level is just above the height of the interior plateau that exists over much of southern Africa. Over this landmass, the cyclonic circulation and strong convergence over tropical southwestern Africa marks the Angola Low and its connection to the meridional arm of the Inter-tropical Convergence Zone (ITCZ) through the eastern Congo Basin, schematically shown in **Figure 1**. Further east in the southern Mozambique Channel, there is another cyclonic area of low level moisture convergence which may also act as a source region for cloud bands. Moisture flux from the subtropical South West Indian Ocean feeds into this feature and over subtropical southeastern Africa. This cyclonic feature is associated with the adjustment of the easterly trade winds to the Madagascan topography. Relative divergence and anticyclonic flow occurs over most of South Africa and southern Botswana / southern Zimbabwe, some of this due to the adjustment of the flow to the high lying areas over eastern South Africa. Northeast of Madagascar and stretching across the tropical South Indian Ocean is the low level convergence associated with the ITCZ. Another area of moisture convergence, fed by the northeast monsoonal flow from the tropical western Indian Ocean and a weaker westerly flow from the tropical South East Atlantic/Congo Basin, is apparent over equatorial East Africa, just to the south of Lake Victoria.

On this seasonal scale, it is apparent that most of the low level moisture flux over southern Africa emanates from the western Indian Ocean with the tropical South East Atlantic Ocean playing rather a minor role since the anticyclonic circulation of the South Atlantic High essentially exports moisture away from the landmass. However, on synoptic and intraseasonal scales, as well as on seasonal scales during certain years, moisture from the South Atlantic plays an important role (Cook et al., 2004; Vigaud et al., 2007, 2009; Hart et al., 2010). It is the latter case that is the main focus in this study; namely, late summer (February-April) warm events over the tropical South East Atlantic Ocean and their associated rainfall and moisture flux anomalies.

An association between SST anomalies off the Angolan / Namibian coast during austral summer and rainfall over the adjacent land has been known for some time (Hirst and Hastenrath, 1983). However, in recent decades, most attention has focussed on the warm events, called Benguela Niños (Shannon et al., 1986; Florenchie et al., 2003, 2004) for strong cases where they tend to be caused by wind anomalies in the equatorial Atlantic and subsequent Kelvin wave adjustment. These Benguela Niños are typically thought to be associated with above average rainfall in austral summer over western Angola and northwestern Namibia (Rouault et al., 2003). These authors examined four events (1984, 1986, 1995, 2001) and found that while there was evidence of increased rainfall along the coast, the magnitude of the rainfall anomalies varied markedly, and in some cases, there were also substantial anomalies over large inland areas. The suggested mechanism for the increased rainfall was increased evaporation off the warm SST anomaly and re-circulation of the regional moisture flux transport (mainly from the western Indian Ocean) over the tropical South East Atlantic leading to local moisture flux convergence over the coastal region.

A strong warm event also occurred in 2011 together with devastating floods in Namibia and Angola which displaced several hundred thousand people. During this period, the ephemeral Kuiseb River was able to flow as far as the Namibian coast near Walvis Bay for the first time since 1963. Thus, one of the aims here is to document the rainfall and SST anomalies during the very strong 2011 warm event and compare these to other recent warm events. The circulation anomalies associated with the strong warm events with large and widespread rainfall anomalies (five events) are then analyzed to better understand the rainfall patterns.

Data and Methodology

Extended re-constructed SST (ERSST) V3b data (Smith and Reynolds, 2004) are used to assess anomalies in the tropical South East Atlantic Ocean of interest here. Warm events are defined as those showing February-April (FMA) SST standardized anomalies about or greater than one standard deviation in a box off Angola (8–15°E, 10–20°S), the so-called ABA index (Rouault et al., 2009). Using this definition, strong warm events occurred in 1959, 1963, 1965, 1984, 1986, 1995, 1998, 1999, 2001, 2006, 2011—**Table 1**.

The FMA season is chosen since it is when Angola / northwest Namibia receive much of their annual rain and it corresponds to the time of maximum SST off their coasts. Global Precipitation Climatology Centre (GPCC) gridded data (Schneider et al., 2008) are used to assess rainfall anomalies because station data for some large areas in southern Africa, especially Angola, were not available to us. For the purposes of this study, southern Africa is defined as Africa south of 10°S. NCEP re-analyses (Kalnay et al., 1996) are used to compute moisture fluxes and atmospheric circulation anomalies. Unless otherwise stated, climatologies are constructing use a base period of 1980–2010.

TABLE 1 | Indices for tropical South East Atlantic warm events (ABA), and the subtropical South Indian Ocean dipole (°C) for the FMA season.

Warm events	ABA index (°C)	Niño 3.4 (°C)	SIOD (°C)
1959	0.70	0.3	−1.72
1963	0.54	0.0	−1.72
1965	0.78	−0.3	−1.55
1984	1.86	−0.2	−1.02
1986	1.12	−0.3	0.96
1995	2.77	0.7	−0.78
1998	0.82	1.5	−1.13
1999	1.42	−0.9	1.60
2001	1.53	−0.4	1.34
2006	1.28	−0.4	2.10
2011	2.27	−0.9	0.51

The ABA index is the standardized SST anomaly for 8–15°E, 10–20°S. The SIOD index is the standardized SST anomaly difference between the western (55–65°E, 37–27°S) and eastern (90–100°E, 28–18°S) South Indian Ocean. The 5 events analyzed in detail are denoted in bold italics.

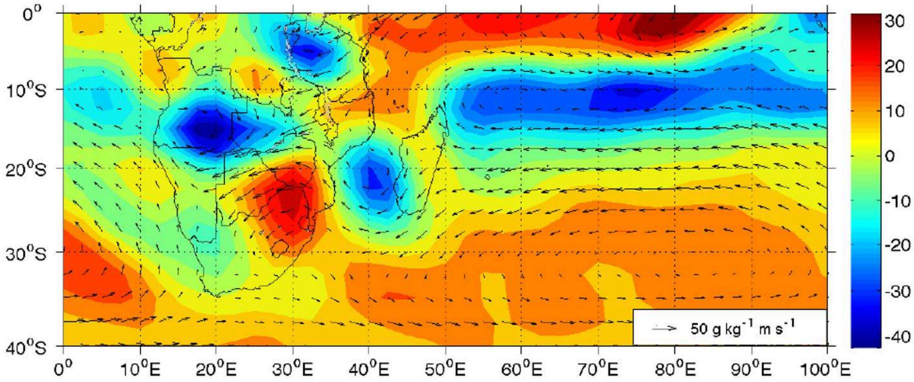

FIGURE 2 | Climatological moisture flux and divergence for February–April at the 850 hPa level computed from NCEP re-analyses for 1980–2010. A scale moisture flux vector is given.

Rainfall Anomalies

Figure 3 which shows the standardized rainfall anomalies for all warm events since 1950 suggests that the events with the strongest and most widespread positive rainfall anomalies over southern Africa are 1963, 1986, 2001, 2006, and 2011. Although for completeness **Figure 1** plots data to the equator, in this study southern Africa is considered to be Africa south of 10°S. Consistent with earlier work (e.g., Hirst and Hastenrath, 1983; Rouault et al., 2003), there are positive rainfall anomalies somewhere in coastal Angola in each event and somewhere in northern Namibia for 10 of the 11 events. In terms of Angola, the most consistent region of increased rainfall is the south, particularly the southwest, although the positive anomalies are weak for the 1984, 1998, and 1999 events. These three events are also accompanied by large areas of drier conditions over southern Africa. Thus, although it is generally accepted in the literature that the strong warm events are associated with large positive FMA rainfall anomalies in Angola and Namibia, **Figure 3** indicates that there is substantial variation in the magnitude and spatial extent of the rainfall anomalies. For the remainder of this study, attention is focused on the five events with largest and most widespread rainfall anomalies over Africa south of 10°S; namely, 1963, 1986, 2001, 2006, and 2011.

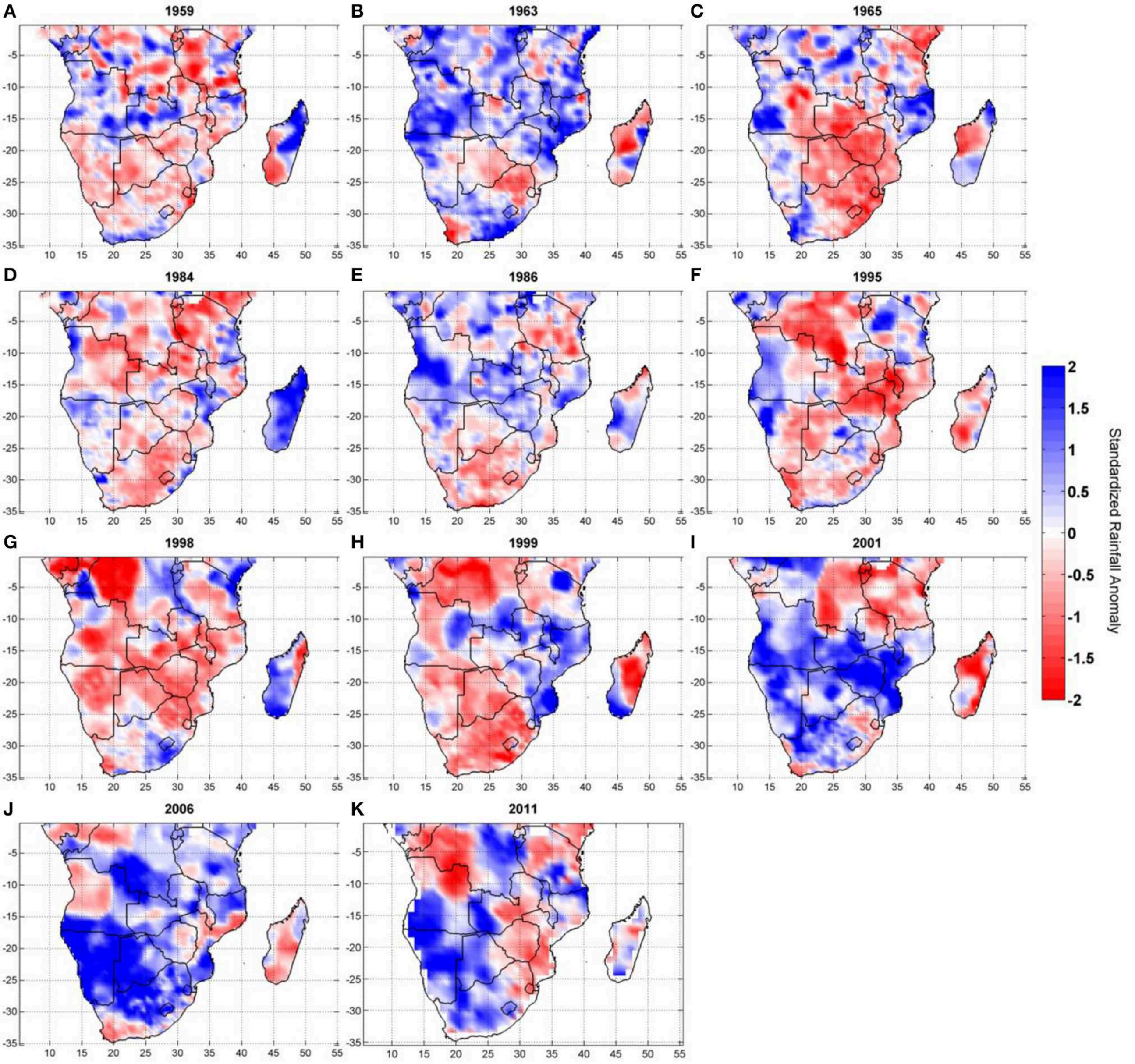

FIGURE 3 | FMA rainfall anomalies (contour interval 10 mm) occurring during all warm SST events since 1950 using GPCC data (A) 1959, (B) 1963, (C) 1965, (D) 1984, (E) 1986, (F) 1995, (G) 1998, (H) 1999, (I) 2001, (J) 2006, and (K) 2011.

Evolution of SST Anomalies

In addition to the tropical South East Atlantic, there is evidence that SST anomalies in the South West Indian Ocean can influence southern African summer rainfall (e.g., Reason and Mulenga, 1999; Behera and Yamagata, 2001; Reason, 2001). **Figure 4** therefore plots the regional SST anomaly for the 1963, 1986, 2001, 2006, and 2011 events which had the largest and most widespread rainfall anomalies. It is evident that, off Angola, the 2011 case has the strongest FMA SST expression and that the first two events are weaker than the more recent three. A Hovmoller analysis of SST in the coastal South Atlantic along 10°E (**Figure 5**) for these five events confirms that 2011 was the strongest event, it also began earlier than the other cases and had peak SST anomaly in JFM rather than FMA. In the 1963 case, the FMA anomaly is relatively weak but then grows to become one of the strongest in winter. SST anomalies off Angola can last well into the winter (2001, 2006), or almost die away by April before re-generating in May (1963), and can occur before (2006) or after (1986) warming in the lower latitudes. Note that strong warm events further west in the equatorial zone in the central eastern Atlantic are known as Atlantic Niños and typically occur in austral winter (e.g., Chang et al., 2006).

A common feature to all the events except 1963 in **Figure 4** is the presence of warm SST anomalies in the South West Indian Ocean. This event is also the only one that occurred prior to the 1976–1977 climate shift in the Pacific Ocean which may also have impacted on southern Africa and the South Indian Ocean (Miller et al., 1994; Baines and Folland, 2007; Manatsa et al., 2012). Based on observational analyses and experiments with an atmospheric GCM, Reason and Mulenga (1999) showed that warm SST anomalies in the South West Indian Ocean are associated with increased summer rainfall over southern Africa. There are also some similarities between the SST anomaly patterns in the South Indian Ocean in **Figure 4** with the South Indian Ocean subtropical dipole, a climate mode peaking in

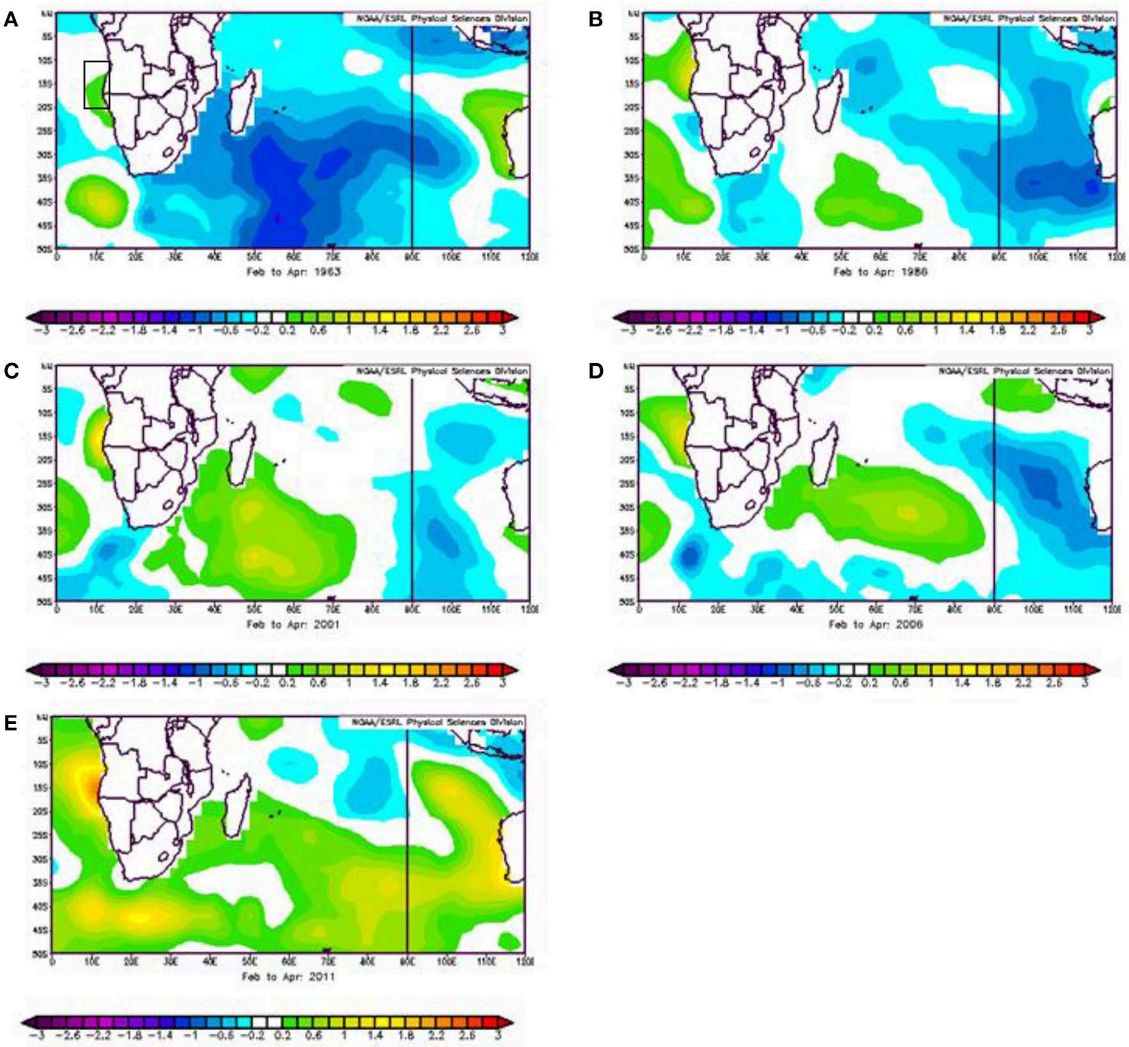

FIGURE 4 | Regional SST anomalies during the 5 strong events (A) 1963, (B) 1986, (C) 2001, (D) 2006, (E) 2011. Contour interval is 0.2°C. The ABA box used to define the Benguela Niño events is shown in **A**).

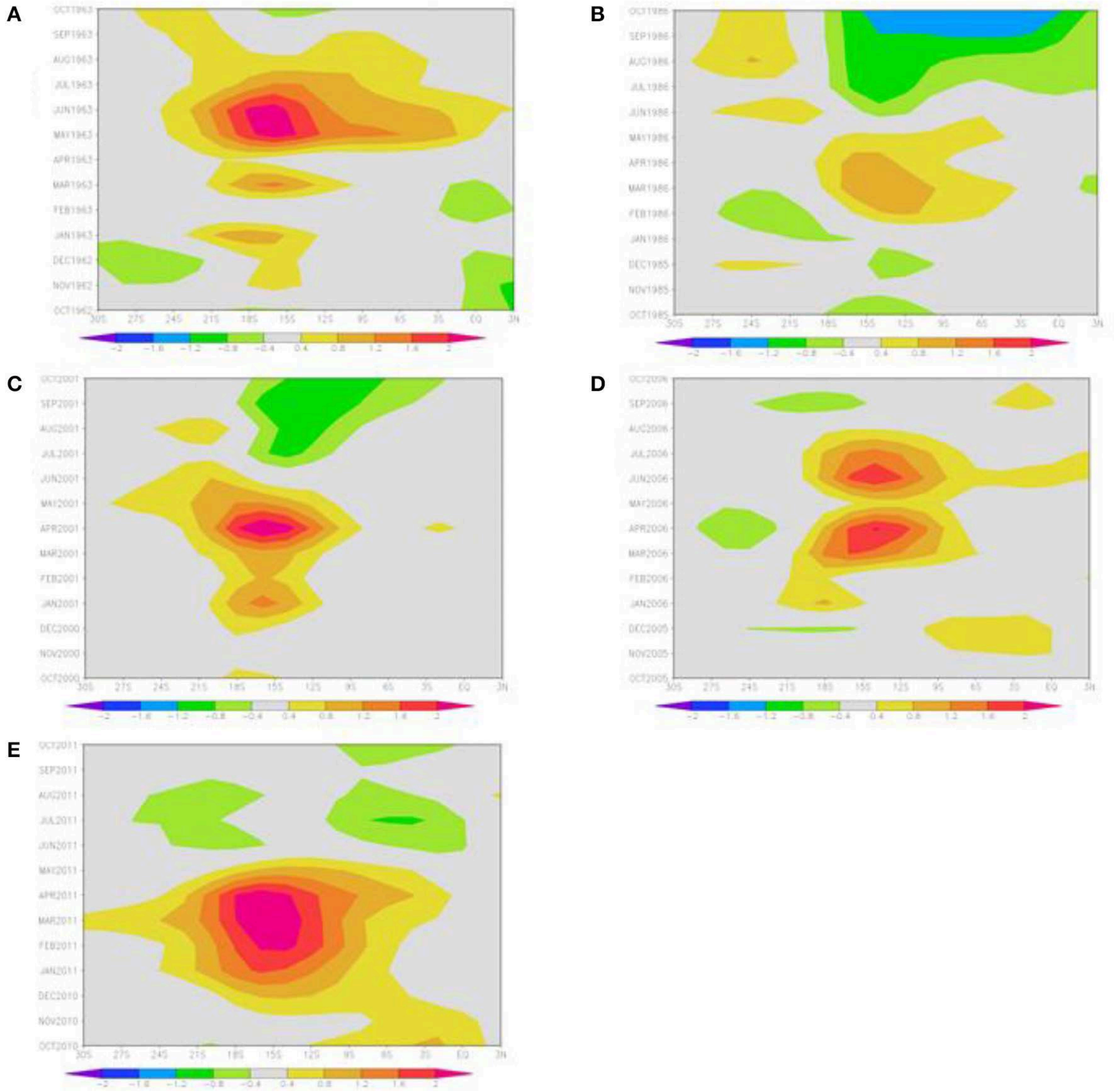

FIGURE 5 | Hovmoller plot of SST anomaly (°C) along 10°E from 30°S to 3°N for the five strong events (A) 1963, (B) 1986, (C) 2001, (D) 2006, (E) 2011 from October of the preceding year to October of the event year.

intensity during JFM, and which is in its positive phase when there are warm SST anomalies in the southwest and cool SST anomalies off Western Australia (Behera and Yamagata, 2001). In this phase, increased summer rainfall also typically occurs over southern Africa (Behera and Yamagata, 2001; Reason, 2001, 2002) due to increased low level moisture flux from the western Indian Ocean toward southern Africa. Using the subtropical dipole index defined as the difference in SST anomaly between a western box (55–65°E, 37–27°S) and an eastern box (90–100°E, 28–18°S), **Table 1** shows that 1986, 2001, 2006, and 2011 correspond to a positive dipole with only 1963 of the five being a negative dipole event. All these five events are either neutral with respect to El Niño or occurred during La Niña. **Table 1** also shows that five of the other six events not considered in detail here correspond to negative South Indian Ocean dipole SST anomalies, confirmed in plots of the regional SST anomalies for these cases (not shown), and unfavorable for good summer rains.

Moisture Flux and Circulation Anomalies

Figure 6 shows the 850 hPa moisture flux anomalies for FMA 1963, 1986, 2001, 2006, and 2011. All cases show areas of increased moisture flux convergence over parts of Angola and Namibia, favorable for increased rainfall. The areas of increased (decreased) moisture flux convergence partially correspond to those of enhanced (reduced) rainfall in **Figure 3**. Relative to **Figure 2**, each case also shows increased moisture flux from the western tropical Indian Ocean or northern Mozambique Channel, although the anomalies are relatively weak for 1986. The moisture flux anomalies over the tropical Indian Ocean appear

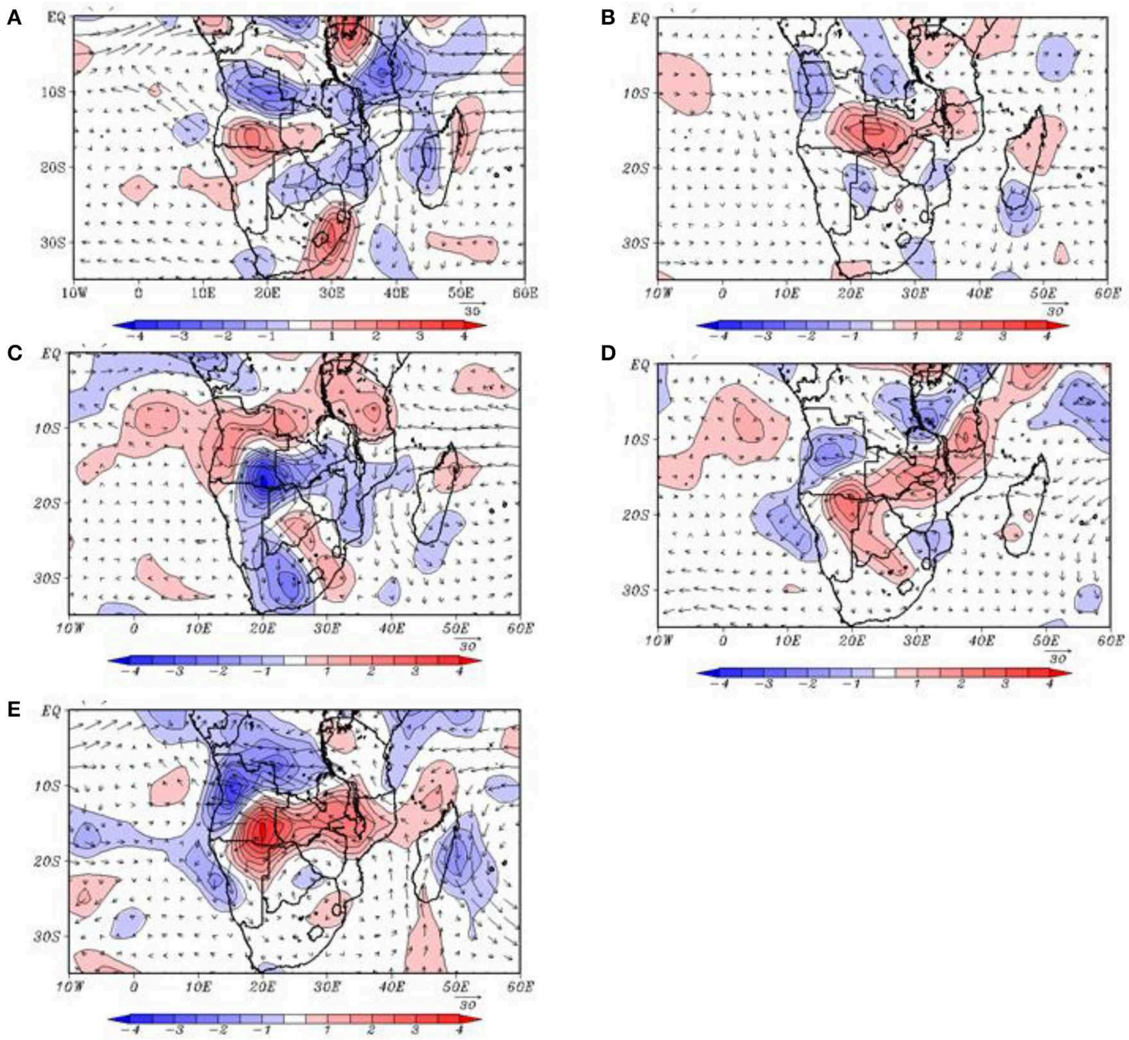

FIGURE 6 | FMA anomalies in moisture fluxes and divergence (contour interval 0.5 × 10^{-8} gkg^{-1} s^{-1}) at the 850 hPa level for (A) 1963, (B) 1986, (C) 2001, (D) 2006, and (E) 2011. Areas of relative convergence are shaded and a scale vector in gkg^{-1} ms^{-1} is shown.

strongest in 1963 and extend across tropical southern Africa to the northern Angolan coast. On reaching the East African coast, some of the moisture flux turns northwestward and some southwestward, thereby opposing the mean flow and leading to relative convergence over the eastern landmass. A cyclonic anomaly exists over the tropical South East Atlantic, feeding moisture back into the Congo basin where it converges over eastern Zambia and southern Tanzania with that coming from the tropical Indian Ocean.

In the case of 2001, some of the western Indian Ocean moisture flux turns southward across Mozambique and the southern part of the Channel with the rest converging over central southern Africa with a westerly flux from the tropical South East Atlantic. Anomalies in the southern Mozambique Channel and subtropical South West Indian Ocean are weak except for 1963 and 2001 which have northerly to northwesterly anomaly that opposes the mean flow and hence lead to relative convergence over Mozambique. By contrast, there are southerly to southeasterly anomalies in the southern Mozambique Channel in 2011, thereby augmenting the mean flow in places and leading to relative divergence over central and northern Mozambique and reduced rainfall there.

In addition to 2001, there is also a westerly flux from the tropical South East Atlantic in 1986 and 2006, although relatively weak in these two seasons. The situation in 2011 is more complex as easterly flux across the southern Congo and Angola then partially recirculates over northern Namibia and the coastal South East Atlantic Ocean and back toward central Namibia. In general however, the common important feature in each case is the enhanced flux toward the eastern landmass from the tropical western Indian Ocean/northern Mozambique Channel. This enhanced moisture flux is weakest in 1986, the event with the smallest spatial extent and magnitude of increased rainfall over southern Africa.

Low level moisture convergence is one factor needed for rainfall production, and **Figure 2** suggests that, on seasonal scales, the Angola low, the southern Mozambique Channel region, and the areas near Lakes Victoria and Tanganyika, are where large values occur. However, another factor needed for substantial rainfall, particularly deep convection and the development of thunderstorms, is strong uplift through the troposphere. On average, anticyclonic conditions typically exist at 700 hPa and up through the middle troposphere over much of South Africa, Namibia, Botswana and southern Angola during the summer. This mid-level anticyclone, known as the Botswana High, caps the shallow heat lows (including the Angola Low) that are present in the summer half of the year over the western regions of subtropical southern Africa. Thus, in order for deep convection and associated rainfall to occur, these mid-level anticyclonic conditions need to break down or be shifted away from the landmass.

Figure 7 shows anomalies in 500 hPa geopotential height with each case showing negative anomalies over most of subtropical southern Africa and hence a weakening in the mean anticyclonicity. This level was chosen as representative of mid-level tropospheric conditions in this region that receives most of its summer rainfall through deep convection as thunderstorms (either isolated or organized systems). The patterns that are most favorable for convective rainfall are ones where the negative anomalies over southern Angola/northern Namibia (the Angola low source region for the cloud bands) stretch southeastwards toward the South West Indian Ocean to allow a link up with a midlatitude frontal feature (needed for tropical-extratropical cloud band development) together with an anticyclonic feature near the Mozambique coast. The latter is important to assist in advecting more moisture from the western Indian Ocean toward the landmass. All cases show the NW-SE orientation of the cyclonic anomalies over subtropical southern Africa with 2001 and 2006 also showing a clear anticyclonic feature near Mozambique, suggesting that these two seasons might be expected to have the most widespread regions of increased rainfall, consistent with **Figure 3**. The cyclonic anomalies over southern Africa are particularly strong in 1963, helping to explain the relatively large and widespread rainfall anomalies that occurred in that summer despite the SST anomalies off Angola and the ABA index being relatively weak and the SST anomalies in the South West Indian Ocean and the SIOD index being negative (**Figure 4**, **Table 1**).

The favorable atmospheric conditions in **Figures 6–7** are further reinforced by the anomalies in omega (pressure tendency) at the 500 hPa level (**Figure 8**), indicating that there was relative uplift in the middle troposphere over most of the areas of increased rainfall in southern Africa implying favorable conditions for deep convection. Most of the areas of relative subsidence at this level correspond to ones of reduced rainfall in **Figure 3**. Both 1963 and 1986 show positive omega anomalies over Botswana, and parts of Namibia and South Africa consistent with mainly dry conditions there. These positive omega

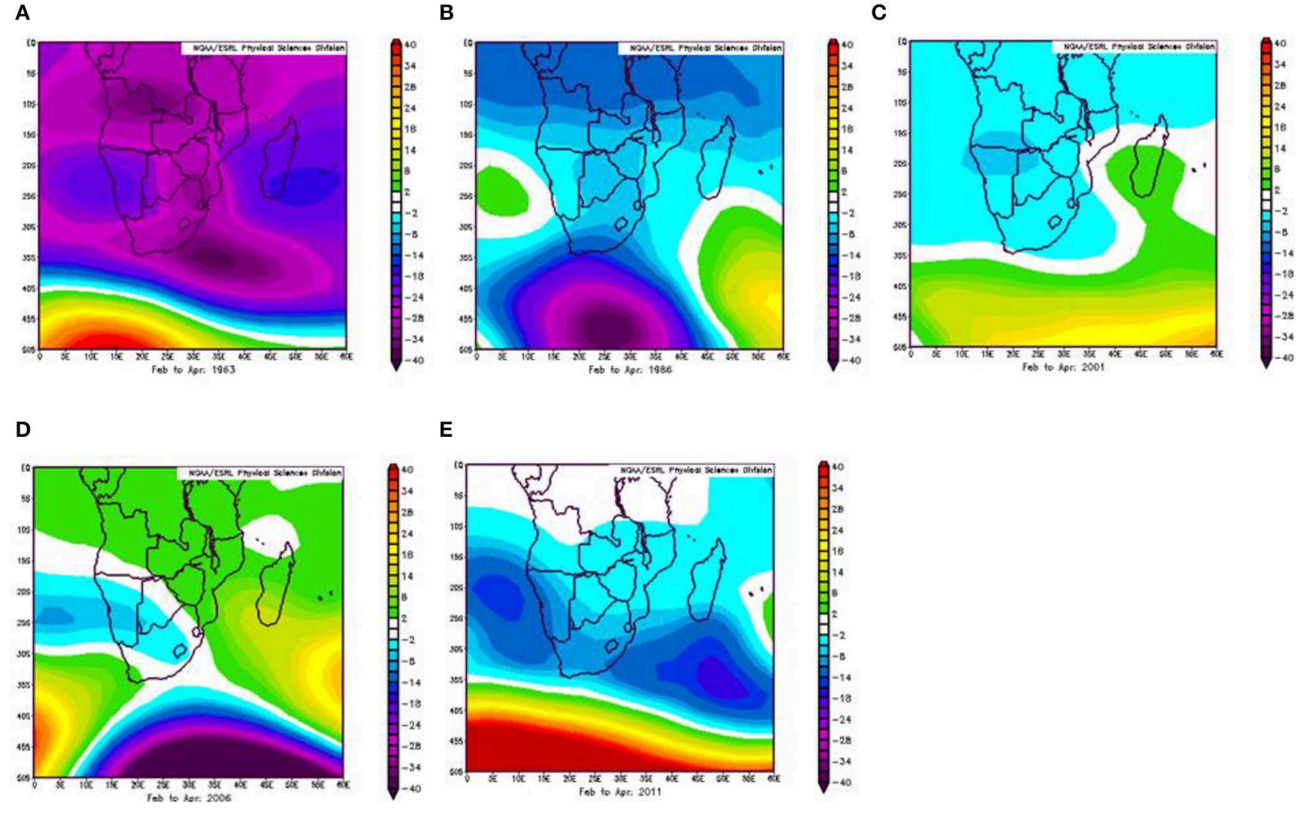

FIGURE 7 | FMA geopotential height anomalies at the 500 hPa level for (A) 1963, (B) 1986, (C) 2001, (D) 2006, and (E) 2011. Contour interval is 2 m.

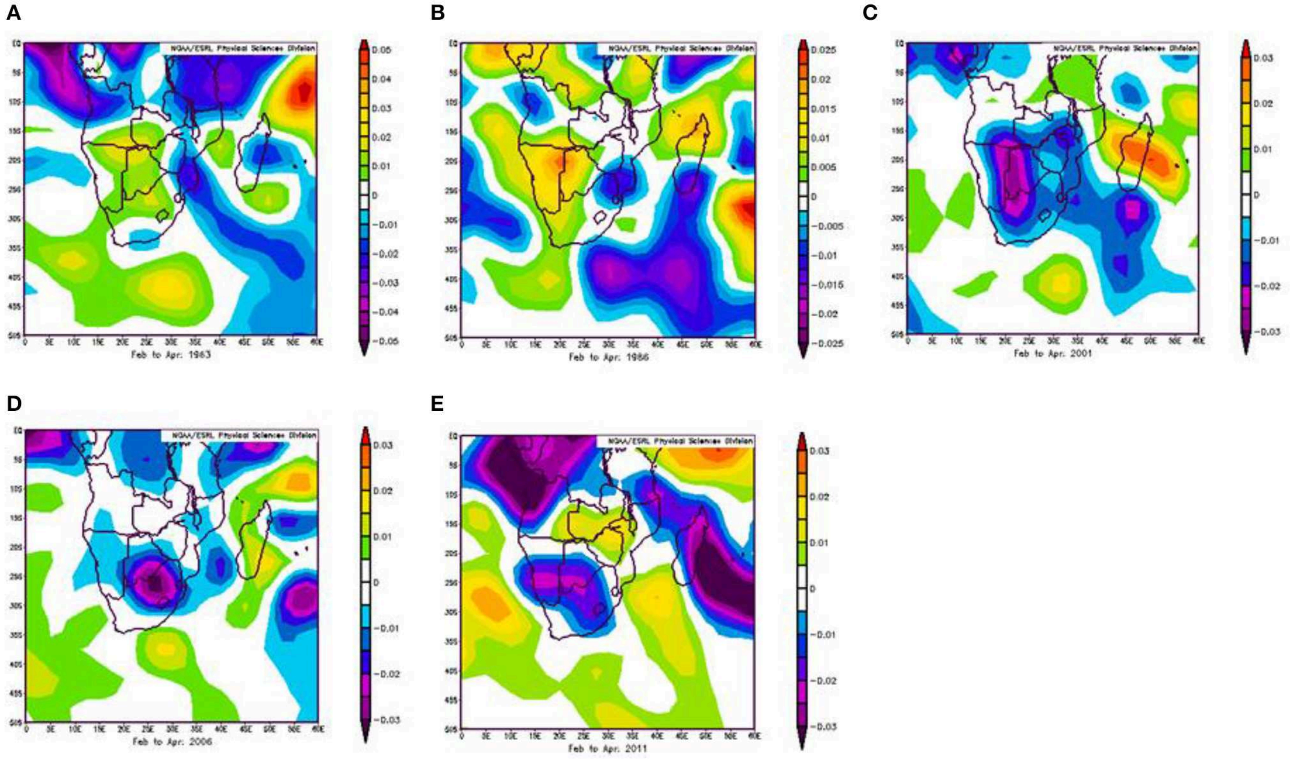

FIGURE 8 | FMA omega (pressure tendency) at the 500 hPa level for (A) 1963, (B) 1986, (C) 2001, (D) 2006, and (E) 2011. Contour interval is 0.005 Pas^{-1}.

anomalies are largest and most widespread in 1986, consistent with this season showing weaker positive rainfall anomalies than the other four.

The rainfall anomaly patterns in **Figure 3** for 1963 and 1986 are broadly consistent with those generated by the HadAM3 GCM when forced with an idealized SST anomaly in the tropical South East Atlantic Ocean superimposed upon observed global monthly mean SST forcing (Hansingo and Reason, 2009). The model produced the largest positive rainfall anomaly over the central and southern Angolan coast with weaker positive anomalies extending into northern Namibia and eastwards into the central landmass. When an idealization of the warm SST pole in the South West Indian Ocean is added to the forcing, as occurred in 2001, 2006, and 2011, the rainfall anomaly pattern quite closely resembles that in **Figure 3** for those years. The magnitudes of the rainfall anomalies in the model over certain inland areas are larger than those for the runs with just the Atlantic SST anomaly forcing. Conversely, when the warm SST anomaly in the South West Indian Ocean is replaced by a cool SST anomaly there, the model rainfall anomalies are reduced. These model results from Hansingo and Reason (2009) reinforce those indicated by the observational analyses that increased rainfall can be associated with the South East Atlantic warm events, with the areas of positive rainfall anomalies being more widespread and larger in magnitude when there are also positive SST anomalies in the subtropical South West Indian Ocean.

Summary

Since 1950, eleven strong warm SST events in austral summer have occurred in the tropical South East Atlantic off the Angolan and northern Namibian coasts. Each is accompanied by increases in coastal Angolan rainfall, with 10 cases also showing areas of wetter conditions somewhere in northern Namibia. Emphasis here is focussed on the five wettest events showing largest and most widespread positive rainfall anomalies over Africa south of 10°S; namely, 1963, 1986, 2001, 2006, 2011. While most of these five events occurred in the last decade, the timing of the total set of eleven events is mainly concentrated around the late fifties to mid-sixties, the mid-eighties, and then the most recent 15 years. The most recent event analyzed, 2011, is of particular interest as the devastating floods in Namibia and Angola displaced several hundred thousand people and the ephemeral Kuiseb River was able to flow as far as the Namibian coast near Walvis Bay for the first time since 1963.

Most of the summer rainfall in Africa, south of 10°S, is brought about by tropical extra-tropical cloud bands that link a tropical low somewhere over the land to a westerly disturbance passing south of South Africa. Each of the five wettest events showed increased low level moisture flux from the western Indian Ocean together with relative convergence of this moisture somewhere over Angola with the secondary moisture source coming from the tropical South East Atlantic Ocean. Areas of increased (decreased) southern African rainfall in each event only partially correspond to the areas of enhanced (reduced) low level moisture flux.

Another factor needed for deep convection and heavy rainfall to develop in the cloud bands is strong uplift through the troposphere. Associated with this is a need for the seasonally present mid-level anticyclone over southern Africa, the Botswana High, to break down or shift away from the landmass. Each of the five wettest events shows mid-level cyclonic anomalies, favorable for cloud band development, as well as strong areas of negative pressure tendency throughout the mid-troposphere to about the 500 hPa level, favorable for deep convection, and which correspond to the areas of increased rainfall in each case.

Four of the five wettest events also show a warm anomaly in the South West Indian Ocean known to be favorable for increased summer rainfall (Reason and Mulenga, 1999; Behera and Yamagata, 2001; Reason, 2001). Previous experiments (Hansingo and Reason, 2009) with the HadAM3 AGCM forced with idealizations of the observed tropical South East Atlantic and South West Indian Ocean SST anomalies confirm that there is increased rainfall over Angola and further inland in the model when forced with just the Atlantic SST anomalies superimposed on climatology. These positive rainfall anomalies are increased over interior areas as well as eastern South Africa and southern Mozambique when the South West Indian Ocean SST anomalies are added to the forcing.

Taken together, the observational and model analyses confirm the importance of both the tropical south east Atlantic and the western Indian Oceans as moisture sources for southern African summer rainfall during these warm SST events off the coast of Angola and northern Namibia. They also highlight the complexity of interannual rainfall variability over southern Africa which is sensitive not only to Atlantic and Indian Ocean SST anomalies but also to ENSO.

Acknowledgments

This work is based on the BSc (Hons) thesis of the second author. We thank NOAA CDC and KNMI Climate Explorer (http://climexp.knmi.nl) for data access and plotting tools.

References

Baines, P. G., and Folland, C. K. (2007). Evidence for a rapid global climate shift across the late 1960s. *J. Clim.* 20, 2721–2744. doi: 10.1175/JCLI4177.1

Behera, S. K., and Yamagata, T. (2001). Subtropical SST dipole events in the southern Indian Ocean. *Geophys. Res. Lett.* 28, 327–330. doi: 10.1029/2000GL011451

Chang, P., Fang, Y., Saravanan, R., Link, J., and Seidel, H. (2006). The cause of the fragile relationship between the Pacific El Niño and the Atlantic Niño. *Nature* 443, 324–328. doi: 10.1038/nature05053

Cook, C., Reason, C. J. C., and Hewitson, B. C. (2004). Wet and dry spells within particular wet and dry summers in the South African summer rainfall region. *Clim. Res.* 26, 17–31. doi: 10.3354/cr026017

D'Abreton, P., and Lindesay, J. (1993). Water vapour transport over southern Africa during wet and dry early and late summer months. *Int. J. Climatol.* 13, 151–170.

Fauchereau, N., Trzaska, S., Richard, Y., Roucou, P., and Camberlin, P. (2003). Sea surface temperature co-variability in the Southern Atlanitc and Indian Oceans and its connections with the atmospheric circulation in the southern Hemisphere. *Int. J. Climatol.* 23, 663–677. doi: 10.1002/joc.905

Florenchie, P., Lutjeharms, J. R. E., Reason, C. J. C., Masson, S., and Rouault, M. (2003). The source of Benguela Niños in the South Atlantic Ocean. *Geophys. Res. Lett.* 30, 1505. doi: 10.1029/2003GL017172

Florenchie, P., Reason, C. J. C., Lutjeharms, J. R. E., Rouault, M., Roy, C., and Masson, S. (2004). Evolution of interannual warm and cold events in the southeast Atlantic Ocean. *J. Clim.* 17, 2318–2334. doi: 10.1175/1520-0442(2004)017<2318:EOIWAC>2.0.CO;2

Hansingo, K., and Reason, C. J. C. (2009). Modelling the atmospheric response over southern Africa to SST forcing in the southeast tropical Atlantic and southwest subtropical Indian Oceans. *Int. J. Climatol.* 29, 1001–1012. doi: 10.1002/joc.1919

Harrison, M. S. J. (1984). A generalized classification of South African summer rain-bearing synoptic systems. *J. Climatol.* 4, 547–560. doi: 10.1002/joc.3370040510

Hart, N. C. G., Reason, C. J. C., and Fauchereau, N. (2010). Tropical-extratropical interactions over southern Africa: three cases of heavy summer season Rainfall. *Monthly Weather Rev.* 138, 2608–2623. doi: 10.1175/2010MWR3070.1

Hermes, J. C., and Reason, C. J. C. (2005). Ocean model diagnosis of interannual co-evolving SST variability in the South Indian and Atlantic Oceans. *J. Clim.* 18, 2864–2882. doi: 10.1175/JCLI3422.1

Hirst, A. C., and Hastenrath, S. (1983). Atmosphere–ocean mechanisms of climate anomalies in the Angola–tropical Atlantic sector. *J. Phys. Oceanogr.* 13, 1146–1157.

Kalnay, E., Kanamitsu, M., Kistler, R., Collins, W., Deaven, D., Gandin, L. et al. (1996). The NCEP/NCAR 40-Year Reanalysis Project. *Bull. Amer. Meteor. Soc.* 77, 437–471.

Manatsa, D., Reason, C. J. C., and Mukwada, G. (2012). On the decoupling of the IODZM from southern African rainfall variability. *Int. J. Climatol.* 32, 727–746. doi: 10.1002/joc.2306

Miller, A. J., Cayan, D. R., Barnett, T. P., Graham, N. E., and Oberhuber, J. M. (1994). The 1976-77 climate shift of the Pacific Ocean. *Oceanography* 7, 21–26. doi: 10.5670/oceanog.1994.11

Philander, S. G. H., and Pacanowski, R. C. (1986). A model of the seasonal cycle of the Tropical Atlantic. *J. Geophys. Res.* 91, 14192–14206.

Reason, C. J. C. (2001). Subtropical Indian Ocean SST dipole events and southern African rainfall. *Geophys. Res. Lett.* 28, 225–228. doi: 10.1029/2000GL012735

Reason, C. J. C. (2002). Sensitivity of the southern African circulation to dipole SST patterns in the South Indian Ocean. *Int. J. Climatol.* 22, 377–393. doi: 10.1002/joc.744

Reason, C. J. C., and Jagadheesha, D. (2005). Relationships between South Atlantic SST variability and atmospheric circulation over the South African region during austral winter. *J. Clim.* 18, 3339–3355. doi: 10.1175/JCLI3474.1

Reason, C. J. C., Landman, W., and Tennant, W. (2006). Seasonal to decadal prediction of southern African climate and its links with variability of the Atlantic Ocean. *Bull. Amer. Meteor. Soc.* 87, 941–955. doi: 10.1175/BAMS-87-7-941

Reason, C. J. C., and Mulenga, H. M. (1999). Relationships between South African rainfall and SST anomalies in the South West Indian Ocean. *Int. J. Climatol.* 19, 1651–1673.

Rouault, M., Florenchie, P., Fauchereau, N., and Reason, C. J. C. (2003). South east tropical Atlantic warm events and southern African rainfall. *Geophys. Res. Lett.* 30, 8009. doi: 10.1029/2002GL014840

Rouault, M., Illig, S., Bartholomae, C., Reason, C. J. C., and Bentamy, A. (2007). Propagation and origin of warm anomalies in the Angola Benguela upwelling system in 2001. *J. Mar. Syst.* 68, 477–488. doi: 10.1016/j.jmarsys.2006.11.010

Rouault, M., Servain, J., Reason, C. J. C., Bourles, B., Rouault, M. J., and Fauchereau, N. (2009). Extension of PIRATA in the tropical south-eastAtlantic:An initial one-year experiment. *Afr. J. Mar. Sci.* 31, 63–71. doi: 10.2989/AJMS.2009.31.1.5.776

Schneider, U., Fuchs, T., Meyer-Christoffer, A., and Rudolf, B. (2008). *Global Precipitation Analysis Products of the GPCC*. Global Precipitation Climatology Centre (GPCC), Deutscher Wetterdienst. Available online at: ftp://ftp-anon.dwd.de/pub/data/gpcc/PDF/GPCC_intro_products_2008.pdf.

Shannon, L. V., Boyd, A. J., Brundrit, G. B., and Taunton-Clark, J. (1986). On the existence of an El Niño-type phenomenon in the Benguela system. *J. Mar. Res.* 44, 495–520. doi: 10.1357/002224086788403105

Singleton, A. T., and Reason, C. J. C. (2007). A numerical model study of an intense cut-off low pressure system over South Africa. *Mon. Wea. Rev.* 135, 1128–1150. doi: 10.1175/MWR3311.1

Smith, T. M., and Reynolds, R. W. (2004). Improved Extended Reconstruction of SST (1854-1997). *J. Clim.* 17, 2466–2477. doi: 10.1175/1520-0442(2004)017<2466:IEROS>2.0.CO;2

Vigaud, N., Richard, Y., Rouault, M., and Fauchereau, N. (2007). Water vapour from the tropical Atlantic and summer rainfall in tropical southern Africa. *Clim. Dyn.* 28, 113–123. doi: 10.1007/s00382-006-0186-9

Vigaud, N., Richard, Y., Rouault, M., and Fauchereau, N. (2009). Moisture transport between the South Atlantic Ocean and southern Africa: relationships with summer rainfall and associated dynamics. *Clim. Dyn.* 32, 113–123. doi: 10.1007/s00382-008-0377-7

Conflict of Interest Statement: The authors declare that the research was conducted in the absence of any commercial or financial relationships that could be construed as a potential conflict of interest.

frontiers
in Earth Science

ORIGINAL RESEARCH
published: 23 June 2015
doi: 10.3389/feart.2015.00030

On the spatial coherence of rainfall over the Saloum delta (Senegal) from seasonal to decadal time scales

Malick Wade[1]*, *Juliette Mignot*[2,3,4], *Alban Lazar*[4], *Amadou T. Gaye*[1] and *Matthieu Carré*[5]

[1] *Laboratory of Physics of the Atmosphere and Ocean Simeon Fongang, Cheikh Anta Diop University, Dakar, Senegal,* [2] *Climate and Environmental Physics, Physics Institute, University of Bern, Bern, Switzerland,* [3] *Oeschger Centre for Climate Change Research, University of Bern, Bern, Switzerland,* [4] *LOCEAN Laboratory, IRD-UPMC-CNRS-MNHN, Sorbonne Universités (Univ. Paris VI), Paris, France,* [5] *Institut des Sciences de l'Evolution de Montpellier, Université de Montpellier, CNRS, IRD, Ecole pratique des hautes études, Montpellier, France*

A paleoreconstruction of the length and intensity of the rainy season over western Africa has been recently proposed, using analysis of fossil mollusk shells from the Saloum delta region, in western Senegal. In order to evaluate the significance of local long-term reconstructions of precipitations from paleoclimate proxies, and to better characterize the spatial homogeneity of rainfall distribution in northern Africa, we analyze here the spatial representativeness of rainfall in this region, from seasonal to decadal timescales. The spatial coherence of winter episodic rainfall events is relatively low and limited to surrounding countries. On the other hand, the summer rainfall, associated with the West African Monsoon, shows extended spatial coherence. At seasonal timescales, local rainfall over the Saloum is significantly correlated with rainfall in the whole western half of the Sahel. At interannual and longer timescales, the spatial coherence extends as far as the Red Sea, covering the full Sahel region. This spatial coherence is mainly associated to the zonal extension of the Inter Tropical Convergence Zone (ITCZ). Coherently, summer rainfalls appear to be driven by Sea Surface Temperature (SST) anomalies mainly in the Pacific, the Indian Ocean, the Mediterranean basin, and the North Pacific. A more detailed analysis shows that consistency of the spatial rainfall coherence is reduced during the onset season of the West African Monsoon.

Keywords: variability, rainfall, coherence, Saloum, Sahel

Edited by:
Belen Rodriguez-Fonseca,
Universidad Complutense de Madrid,
Spain

Reviewed by:
Eduardo Zorita,
Hemlholtz-Zentrum Geesthacht,
Germany
Daniel F. Nadeau,
Polytechnique Montreal, Canada

****Correspondence:***
Malick Wade,
Laboratory of Physics of the
Atmosphere and Ocean Simeon
Fongang, Cheikh Anta Diop University,
BP 5085 Dakar-Fann, Senegal
malick172@yahoo.fr

Specialty section:
This article was submitted to
Atmospheric Science,
a section of the journal
Frontiers in Earth Science

Received: *27 February 2015*
Accepted: *28 May 2015*
Published: *23 June 2015*

Citation:
Wade M, Mignot J, Lazar A, Gaye AT and Carré M (2015) On the spatial coherence of rainfall over the Saloum delta (Senegal) from seasonal to decadal time scales.
Front. Earth Sci. 3:30.
doi: 10.3389/feart.2015.00030

Introduction

The Sahel region in Western Africa is a semi-arid area located at the southern boundary of the Sahara desert and covered by grassland, shrubs, and small, thorny trees. The term is often applied to the whole region extending some 5000 km across Africa from the Atlantic coast to the Red Sea and from the Sahara to the humid savanna at roughly 10°N. The Sahel is also sometimes defined as the area in which the mean daily rainfall is between 0.5 and 1.5 mm, or in terms of annual mean, between 200 and 600 mm (**Figure 1**). In this study, as we focus on the western African monsoon, we define "Sahel" between the latitudes of 12 and 18°N and extending eastward up to 20°E (**Figure 1**). It includes much of the countries of Mauritania, Senegal, Mali, Niger, Chad Burkina Faso, and Nigeria. The climate variability over the Sahel region, which hosts about 70 millions of people, and which surface is equivalent to Europe, has been extensively documented during the past decades. Much attention is paid in particular to the monsoon season, which lasts from May to October

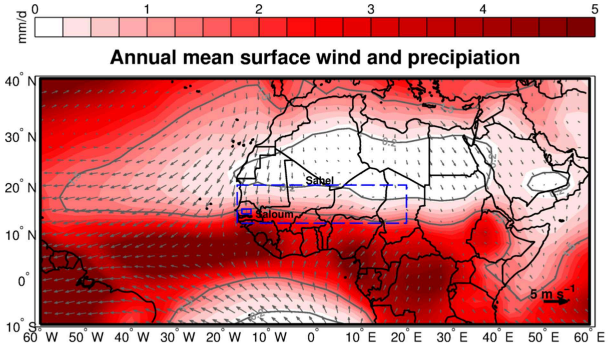

FIGURE 1 | Annual mean of precipitation (shaded, mm/d) and surface wind (vector, m/s). The blue rectangle shows the Sahel region defined in the text and the small blue rectangle indicates the location of Saloum River Delta. The 0.2 and 1.5 mm/d isohyets are highlighted in gray contours.

north of the equator because of its crucial impact on agriculture and public health. Many studies were in particular motivated by the dramatic shift that the West African Monsoon (WAM) has experienced from wetter conditions in the 1950s and 1960s to much drier ones from the 1970s to the 1990s (e.g., Hulme, 1992; Lamb and Peppler, 1992; Nicholson et al., 2000; Le Barbé et al., 2002; L'Hôte et al., 2002; Dai et al., 2004). This drying is one of the most significant droughts at the regional scale observed during the twentieth century at a global scale (e.g., African Monsoon and Multidisciplinary Analyses International Scientific Steering Committee, 2005). Substantial variations of precipitations also occur at much shorter time scales, from daily to intraseasonal, with equally important consequences for the local resources (e.g., Sultan et al., 2005; Berg et al., 2009; Marteau, 2011).

The sub-seasonal, or intra-seasonal, rainfall variability during the summer monsoon season results from complex interactions between processes with various time and space scales (e.g., Diedhiou et al., 1999; Janicot et al., 2011). Intermittent regional modes have been identified, which represent an envelope modulating the occurrences of mesoscale convective systems (Laing and Fritsch, 1993, 1997; Hodges and Thorncroft, 1997; Mathon and Laurent, 2001). They are controlled on the one hand by internal atmospheric dynamics; in particular the development of synoptic scale African Easterly Waves (AEW; Reed et al., 1977; Duvel, 1990; Thorncroft and Hoskins, 1994a,b; Diedhiou et al., 1999; Kiladis et al., 2006) or synoptic scale Kelvin waves (Mounier et al., 2007). Monsoon flux and convection are significantly modulated by these waves (e.g., Fink and Reiner, 2003; Dieng et al., 2014).

At the seasonal time scale, West African climate is very sensitive to the continental surface boundary conditions (Charney and Shukla, 1981). Zheng and Eltahir (1998) document the impact of the vegetation distribution on West Africa Monsoon (WAM) system. In particular, they detail the impact of deforestation along the Guinean coast on surface net radiation and the reduction of boundary layer entropy, leading to weaker convection over the Sahel.

Although land surface processes might play a role also at even lower frequency, oceanic forcing is the dominant driver of the interannual to decadal WAM variability (Zeng et al., 1999; Biasutti et al., 2008). The El Niño–Southern Oscillation (ENSO) phenomenon (Janicot et al., 2001), the Atlantic Niño (Giannini et al., 2003) and the Mediterranean Sea (Rowell, 2003) have been identified to have an important impact on the WAM system and possibly on its predictability (Ward, 1998) on interannual time scales. Palmer (1986) suggested early a major influence of ENSO on Sahel precipitation. The teleconnection mechanism between the Tropical Pacific ocean and West Africa during warm ENSO events (El Niño) was explained with more details by Rowell (2001): the interaction of atmospheric equatorial Kelvin wave from the tropical Pacific with an off-equator Rossby wave (response to the zonal SST gradient between the East Indian Ocean and West Pacific) increases the large-scale subsidence over Africa. This weakens convective activity and thereby reduces the monsoon flow over West Africa. Nevertheless, this relationship is likely modulated by decadal variations of mean annual SSTs (Janicot et al., 2001).

More generally, at interannual to decadal time scale, several studies, including the pioneering works by Lamb (1978a,b) and Hastenrath (1984, 1990), and more recent modeling studies (e.g., Rowell et al., 1995; Vizy and Cook, 2002; Losada et al., 2010; Mohino et al., 2011) highlighted the influence of Sea Surface Temperature (SST) anomalies on precipitation variability over the Sahel. There is yet a debate on the location of the most important anomalies: Hoerling et al. (2006) attribute the drying of the 1980s to the interhemispheric gradient in the Atlantic Ocean, whereas Giannini et al. (2003) and Bader and Latif (2003) emphasize the role of the Indian Ocean. Other model studies indicated a relationship between changes in land-use and precipitation (Charney, 1975; Paeth et al., 2005, 2009; Abiodun et al., 2008; Davin and de Noblet-Ducoudré, 2010). In any case, knowledge of the interannual to decadal variability in the monsoon circulation is still quite limited (Afiesimama et al., 2006; Maloney and Shaman, 2008). The simulations of the fifth Coupled Model Intercomparison Project (CMIP5) confirm results from previous generations of models attributing a substantial role of anthropogenic emissions in driving precipitation changes in the Sahel (Biasutti, 2013). They also suggest that in a warming world, the WAM season may be shifted toward the end of the year, as they report a drying spring and wetting fall. Biasutti and Sobel (2009), Patricola and Cook (2010) and Monerie et al. (2012, 2013) similarly found a robust lag of the monsoon onset in the western Sahel together with an increase of the precipitation at the end of the season in the central African Sahel in the CMIP3 and CMIP5 climate models ensembles.

Episodic winter rainfall events, known as ≪ heug ≫ or ≪ mango ≫ rain by the local population, also occur and affect mainly Cape Verde, Senegal and Mauritania between late October and March. These events are much less documented than summer precipitations, as they concern much more intermittent and weaker events. Nevertheless, they have had dramatic consequences in the past, causing floods and deaths among humans and cattle. A few studies based on observations (Seck, 1962; Gaye et al., 1994; Gaye and Fongang, 1997; Thorncroft and Flocas, 1997; De Félice, 1999; Knippertz and

Fink, 2008) and models (Meier and Knippertz, 2009) found that winter rainfalls are associated to an intrusion of high level cold air masses from extratropics.

In spite of all these studies, the variability of Sahelian rainfall is still poorly constrained, partly because of the limited timespan of the instrumental record. In this regard, paleoclimate reconstructions are often of great help to better constrain the variability of poorly observed systems (Nicholson, 1994). However, there is a massive disequilibrium between our knowledge of long-term climate variability in northern continents and in Western Africa. Regarding the last 1000 years, several reconstructions of the northern hemisphere climate trends were put together from thousands of records from diverse archives, now yielding a relatively coherent picture of the past thermal variations over this regions (e.g., Fernández-Donado et al., 2013). Yet, only one marine coring site off the Senegal River (Mulitza et al., 2008) is available to document environmental changes during the last millennium in western Sahel. Using geochemical records from the sediments of Lake Bosumtwi, Ghana, Shanahan et al. (2009) proposed a reconstruction of the natural variability of the African monsoon over the past three millennia. Their study confirmed that intervals of severe drought lasting for periods ranging from decades to centuries are characteristic of the monsoon and are linked to natural variations in Atlantic temperatures. In the Saloum region, located on the Senegalese Atlantic coast (**Figure 1**) and highly sensitive to changes in the evaporation-precipitation budget, an exceptional opportunity for paleo-monsoon reconstruction is offered by the presence of fossil shell middens that can be used as high resolution archives (Azzoug et al., 2012a). Mollusks indeed record in the geochemistry of their shells the surrounding environmental conditions. Combining high resolution isotopic records with tidal growth increments, Azzoug et al. (2012b) showed that the duration of the rainy and dry seasons can be quantitatively estimated in the Saloum Delta over the last ~2000 years. While their work opens stimulating perspectives for the investigation of the seasonality of the WAM in the past, the relationship between local and regional rainfall variability needs to be assessed before extending paleoclimate reconstructions in the Saloum to the WAM in general. Precipitation is indeed known to be a patchy feature with small spatial scale (e.g., Houze and Cheng, 1977; Leary and Houze, 1979; Nicholson, 1995; Chen et al., 1996; Rickenbach and Rutledge, 1998; Lebel et al., 2009).

Here, we propose to test the spatial representativeness of precipitations measured locally over the Saloum Delta for the whole Sahel region at seasonal to decadal time scales. There is a strong east-west uniformity of climate and vegetation conditions in the Sahel. This is well illustrated by the regular zonal organization of the mean annual isohyets (**Figure 1**). The spatial coherence of annual and decadal anomalies is also very strong on the first order. Using 110 selected stations regularly distributed in West Africa and covering the years 1933–1940, Moron (1994) defined three main coherent regions at the peak of the sahelian rainy season: a "continental" Sahel, a "western" Sahel and a "Guinean" region, confirming previous analysis by Janicot (1992) and Nicholson and Palao (1993). Fontaine and Janicot (1996) later simplified this classification as they found that the western and continental Sahel rainfall anomalies were of the same sign for the majority of stations they analyzed. More recently, east–west contrasts have also been noted at decadal timescales (Dieppois et al., 2013) as well as at longer timescales, related to the long-term trends in response to climatic forcing (e.g., Lebel et al., 2009; Monerie et al., 2012; Biasutti, 2013).

For our analysis, we consider successively seasonal, interannual, and decadal time scales of modern records of precipitation over the region and we test how representative of the regional monsoon variability these local precipitations are. We also investigate the link of these local precipitation events with large scale SSTs. Results are interpreted in the light of present understanding of the dynamics of the WAM and heug rainfalls.

Materials and Methods

Data

Our analysis is primarily based on the monthly Global Precipitation Climatology Project (GPCP) version 2.2 (Adler et al., 2003; Huffman et al., 2009), which, under the World Climate Research Program (WCRP) and the Global Energy and Water Exchanges project (GEWEX), provides a global coverage with satellite and gauge information at 2.5° resolution. More details about the dataset can be found at ftp://precip.gsfc.nasa.gov/pub/gpcp-v2.2/doc/V2.2_doc.pdf. We use the monthly data over the period [1979–2012].

In order to validate the robustness of our results, we use both the Tropical Rainfall Measuring Mission (TRMM) precipitations and records from two rain gauges located in the Saloum River Delta. In this study, TRMM precipitations version 3B42 (Huffman et al., 2007; Liu, 2015) are used, they contain output from the TRMM Algorithm 3B42 that are merged high quality (HQ)/infrared (IR) precipitation and root-mean-square (RMS) precipitation-error estimates. The output is given over 0.25×0.25 degree grid boxes daily. More details of the algorithm can be found here: http://trmm.gsfc.nasa.gov/3b42.html. We use the monthly data over the period [1998–2012]. Rain gauge data set was made available by the Regional Centre for the Improvement of Plant Adaptation to Drought (Centre Régional pour l'Amélioration de l'Adaptation à la Sécheresse (CERAAS), Salack et al., 2011). Two rain gauges located in the vicinity of the Saloum River Delta ([14.5°W-14°N and 15°W-14.2°N]) were averaged and monthly data are used over the period [1979–2010].

Previous results have shown that GPCP and TRMM precipitation datasets have similar distribution patterns over the Tropics in spite of some differences in amplitude and location (Rui and Yunfei, 2005). Results show in particular that GPCP tends to underestimate the monthly precipitation over the land region with sparse rain gauges in contrast to regions with a higher density of rain gauge stations. The absolute bias between the two data sets is however less than 10% while the rain rate is less than $10\,\mathrm{mm\,d^{-1}}$.

The large-scale circulation and dynamics in the atmosphere and ocean surface associated to the precipitation variability are also investigated. For this, we use wind, geopotential height and outgoing longwave radiation (hereafter OLR) data from the operational analysis of the National Centers for Environmental Prediction (http://www.esrl.noaa.gov/psd/data/) at 2.5 × 2.5° latitude–longitude horizontal resolution (Kalnay et al., 1996). Monthly OLR data are used over the period [1979–2012] to analyze rainfall events in terms of atmospheric convection. Indeed more convective activity implies higher and colder cloud tops, which emit less infrared radiation into space. Hence, negative OLR anomalies indicate enhanced moist convection. Several evidences have already shown that OLR is a powerful proxy for the WAM onset (e.g., Fontaine et al., 2008). Finally, we used the Hadley Centre Global Sea Ice and SST (HadISST) dataset version 1.1 (Rayner et al., 2003), which is a monthly dataset of 1° × 1° spatial resolution covering the period from 1870 to present.

Data Processing and Time Scale Filtering

In this study, we focus on the rainfall variability over the Saloum Delta and the Sahel regions respectively (**Figure 1**). The first region corresponds to the very small domain defined the 1° × 1° region [16°W-17°W; 14°N-15°N]. The second one is more regional, and corresponds to the average over the region [18W-20°E; 12°N-18°N]. Averages over these to regions define the Saloum rainfall index and the Sahel rainfall index respectively.

Unless stated otherwise, we focus on two seasons. First, winter is defined here by the months January-February-March (JFM). Precipitation over the Saloum delta and the Sahel region are much more sporadic during this season. Nevertheless, the so-called "heug" rainfalls may have important local consequences and may also appear in paleo-records. The summer is then defined here by the months July-August-September. This is the monsoon season, during which rainfalls are most intense. Given the suggested sensitivity of the onset and demise seasons to external forcing (Biasutti and Sobel, 2009; Patricola and Cook, 2010; Monerie et al., 2012, 2013; Biasutti, 2013), and the sensitivity of the Saloum paleoclimate proxy to the duration of the rainy season (Azzoug et al., 2012b), we will also pay special attention to the onset and demise season defined over the months June-July (JJ) and September-October (SO) respectively.

In practice, the seasons defined above are retrieved from the whole dataset, linearly detrended and band-pass filtered in order to distinguish seasonal, interannual and decadal time scales: the seasonal band is isolated by applying a high-pass filter to the monthly data from the corresponding season with a cutoff frequency of 3 months. This is not the canonical definition of the seasonal timescale found in the literature because we use monthly data. However, our results show that it carries information significantly different from the interannual timescale. The interannual variability is extracted by considering 3-month averages for JFM and July-August-September (JAS) and a high-pass filter with a cutoff frequency of 8 years is applied to filter out the decadal variability. We also use 2-month averages for the specific case of the onset JJ and demise SO of the WAM. Finally, a lowpass filter is applied with a cutoff frequency of 8 years in order to capture the decadal variability and filter out the interannual variability. Decadal variability is not analyzed for the winter season due to the very intermittent character of winter events, as shown below.

For each time scale, regression between the normalized Saloum rainfall index and other variables are calculated. These regressions are computed as the covariance between the normalized index and specific variables, and are thus given in units of the given variable. This tool was preferred to correlations as it gives an indication of the amount of signal associated to the process under investigation. Significance of the regressions is tested with a bootstrap procedure (Monte Carlo technique). This procedure consists in randomly re-sampling the rainfall index to re-compute the regression. This is done a large amount of times so as to define the noise level. We show results that are significant at the 95% level, after 500 permutations. Monte Carlo simulation methods are especially useful in studying systems with a large number of coupled degrees of freedom, such as fluids.

Validation of the Rainfall Indexes

We first show the time evolution of rainfall averaged over the Saloum region during the period 1979–2012 for GPCP, 1979–2010 for the rain gauge and 1998–2012 for TRMM data respectively and for all seasons defined by 3 months averages (**Figure 2**, Top panels). Since the amount of winter rainfall is much smaller than summer rainfall, we represent the seasons running from October to May (**Figures 2A,C**) and the ones running from April to November (**Figures 2B,D**) separately, using two different color scales. The ratio among the scales indicates that summer events are of the order of 20 times larger than the winter events. This ratio holds for all three data sets, GPCP, the rain gauge and TRMM. The panels highlight a strong variability for summer and winter. In winter, important rainfall events are detected in 1993–1994 and in 2001–2002 (up to 0.2 mm/day) while practically no rainfall was detected between December and March from 1982 to 1990. In summer, precipitations are typically of the order of 6–8 mm/day in JAS, with substantial interannual variations. The monsoon season was particularly intense in 2000, in 2003 and in 2009, and it was particularly weak in 1983, 1991, 2002, and 2006.

For both seasons, and from 1998 onward, this variability is consistent in all three data sets. In summer, we note a slight shift in the 1999–2000 maximum: TRMM records a slightly weaker maximum, occurring in 2000 rather than 1999. The rain gauge records in fact two maxima, one in 1998 and one in 2000. TRMM also presents lower values by roughly 1 mm/d for the 2003 maximum while the rain gauge values are stronger by 1 mm/d as compared to the GPCP data. Note that this comparison between TRMM and GPCP differs from the results of Rui and Yunfei (2005) who rather found that GPCP tends to underestimate land precipitations as compared to TRMM. This could be due to the fact that we use here updated version of the two datasets. The difference in extreme values between the rain gauge and the GPCP might simply be due to the fact that the GPCP data set is based on objective analysis of station data which might have led to a smoothing of extreme values. Note that the winter event in 2002–2003 is on the other hand rather stronger in the GPCP as compared to the rain gauge records.

Figure 2 (bottom panels) shows the seasonal anomaly of these rainfall time series. The climatology is defined over the

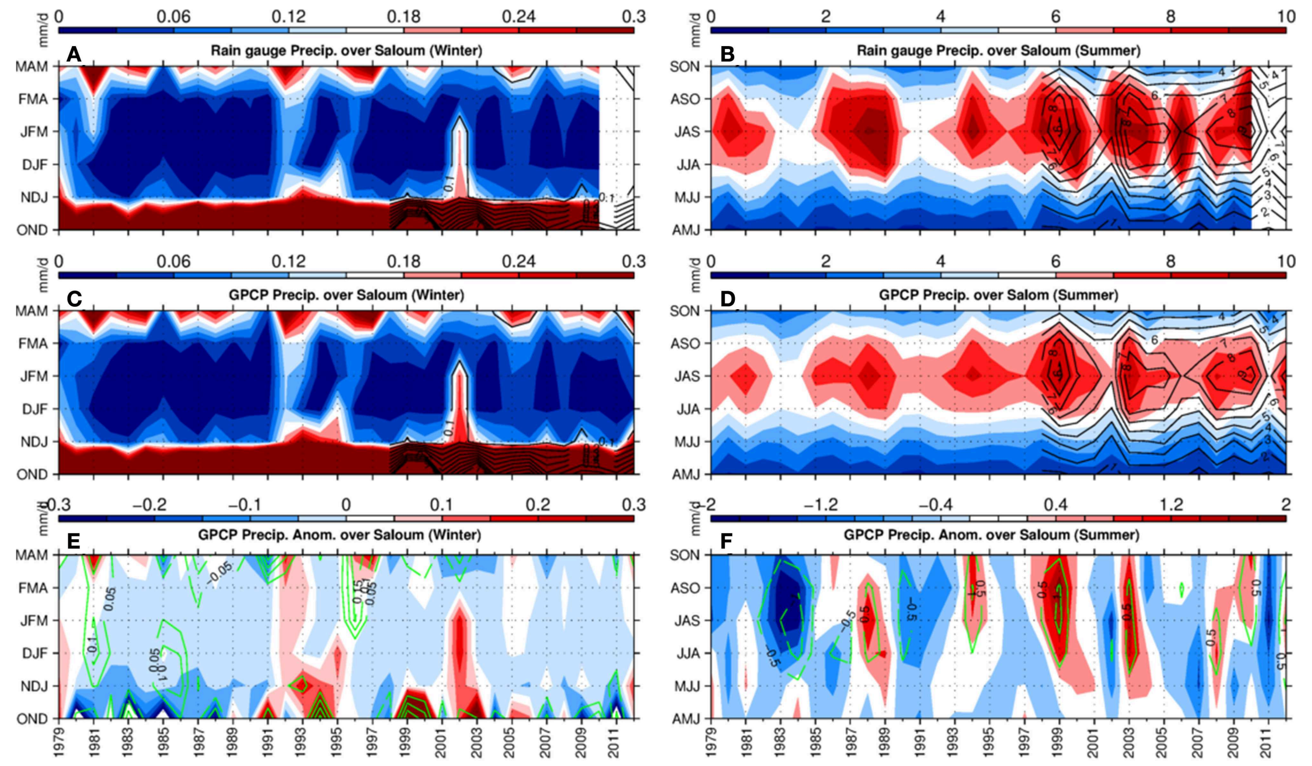

FIGURE 2 | Time evolution of the rainfall (shaded) in the Saloum region during winter for (A) the rain gauge and (C) for GPCP precipitation and during summer for (B) the rain gauge and (D) for GPCP precipitation. TRMM precipitations are shown in contours in all four panels. The vertical axis of the plot shows the different seasons of the year. Left Panels are centered over the winter season and right panels over the summer season, with adapted color scales. **(E,F)** Show GPCP precipitation anomalies, during winter and summer, respectively, calculated with respect to the seasonal cycle over the reference period 1979–2012. Anomalies averaged for the whole Sahel region computed over the same period with GPCP are superimposed in green contours.

period [1979–2012] for GPCC and [1998–2012] for TRMM. The coherence of both time series is confirmed. TRMM slightly underestimates the winter maximum of 2001–2002 as compared to GPCP. This might be due to the length of record used to calculate the climatological mean (1979–2012 for GPCP and 1998–2012 for TRMM). Regarding the summer season, the temporal shift of 1999–2000 is again detected. The negative anomalies rainfall observed in 2007 in GPCP product reach their maximum value in 2006 in TRMM product. Beyond these slight differences, both precipitation records are rather consistent, as also discussed by Rui and Yunfei (2005) and give similar results in the analysis that follows. Therefore, and because of its longer temporal coverage, we focus on the GPCP data set in the following. **Figure 2** (bottom panels) also shows that in general, the temporal sequence of rainfall anomalies over the Saloum region is not fully coherent with that of the whole Sahel region and especially during winter. Strong winter rainfall signal like in 2002 is clearly visible on the Saloum average but not in the Sahel region. On the other hand, winter rainfall events are detected in 1980, 1985, and 1995, but they are largely absent from the Saloum record. In summer (**Figure 2D**), the agreement is stronger, although some temporal shifts also exist. This pre-analysis thus indicates that rainfall events over the Saloum region and over the whole Sahel region are not equivalent. In the following, we investigate more precisely the spatial and temporal domains over which Saloum rainfall are representative, and the associated mechanisms.

Winter Rainfall Structure

We examine here the spatial pattern associated with winter rainfall events over the Saloum region. For this, regression maps of precipitation over the eastern tropical Atlantic and western African continent with the Saloum rainfall index are represented for time scales from seasonal to interannual (**Figure 3**). At seasonal time scales (**Figure 3**, top), winter rainfall events over the Saloum region are significantly correlated with rainfall events over the Senegal and the southwestern half of Mauritania. This pattern extends over the ocean toward the southwest until roughly 20°W and 7°N. Such northwest/southeast orientation for heug precipitation events is consistent with results from previous studies (Gaye and Fongang, 1997). In spite of small areas of significant regressions further east, the regression pattern generally does not extend over the whole Sahel region, as also found by Thorncroft and Flocas (1997), Gaye and Fongang (1997) and De Félice (1999).

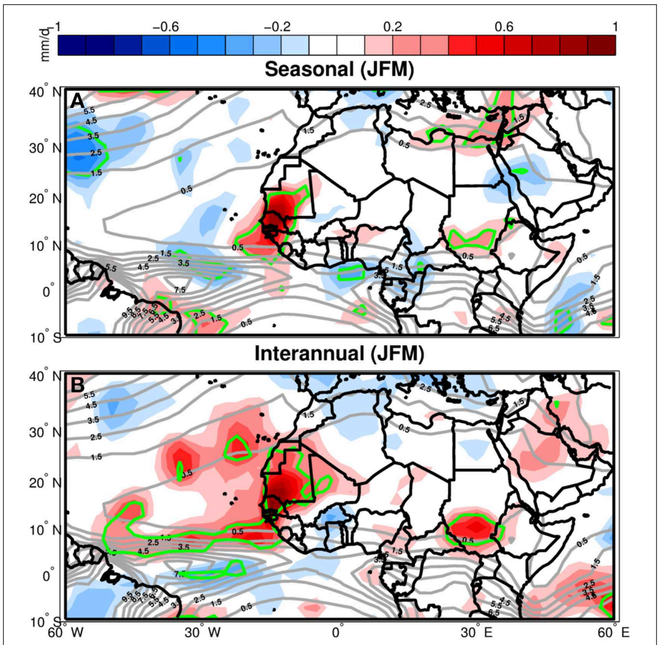

FIGURE 3 | Spatial regression (in mm/day) in winter (JFM) between Saloum rainfall and rainfall over the rest of the domain for (A) Seasonal, (B) Interannual time scale. Green contours delimit areas where the regression is significant at 95% level using a Monte Carlo simulation. Gray contours represent the mean (JFM) climatological rainfall (mm/d).

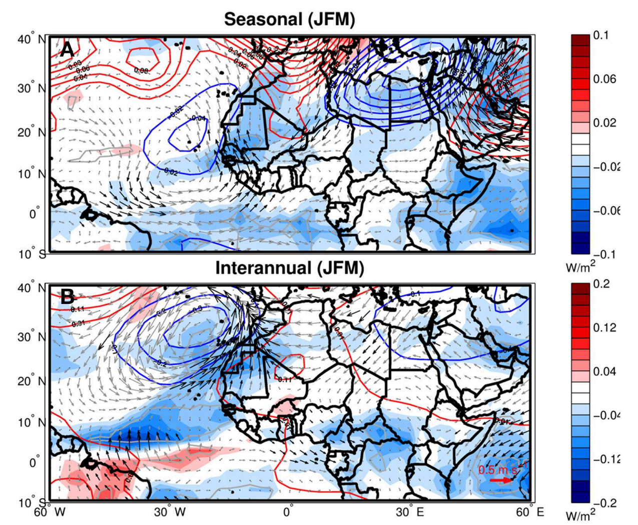

FIGURE 4 | Regression maps in winter (JFM) between Saloum rainfall index with OLR (shaded, W/m²), geopotential height at 400 hPa (red: positive and blue: negative contours, m) and 400 hPa winds (vectors, m/s) for: (A) Seasonal; (B) Interannual time scale. Gray contours delimit areas where the OLR is significant at the 95% level using a Monte Carlo simulation.

At interannual time scales, Saloum winter rainfall is also significantly correlated with adjacent areas in Senegal and the southwest Mauritania, but additionally, the pattern extends slightly eastward along the border between Mali and Mauritania as compared to higher frequencies. Interestingly, over the ocean, significant positive regressions are also found along about 10°N far to the west, and reach values of about 0.5 near Africa, right at the northern edge of the seasonal mean rainfall associated to the Inter Tropical Convergence Zone (ITCZ). This may indicate that interannual variability of heug events is associated with anomalous northward position of the eastern marine ITCZ. Yet, given that correlations over the oceanic extension amount 0.5 (not shown), this phenomenon could account for only about 25% of the winter Saloum winter rainfall variance.

In order to gain understanding on the dynamical origin of these winter rainfalls, we calculate the regression of the Saloum rainfall index with the OLR, the surface wind and the geopotential height at 400 mb (**Figure 4**). At seasonal timescales, it is found that, land OLR regressions values are always negative with maxima around the Saloum region. As expected, it indicates that local precipitation is associated with cloud cover increase and enhanced atmospheric moisture. Furthermore, anomalous upper level geopotential height shows an anomalous low over the adjacent ocean, associated with a quasi-stationary disturbance of the mean distribution of the geopotential in the mid-latitudes. Over the Sahara, the southward extension of high pressures from the extratropics confirms the role of intrusions of air masses from the North in setting the winter rainfalls over the western Sahel region, as noted already by Seck (1962). At low-level, moist southerlies enter the area. This situation favors the creation of unstable air mass and convective dynamics (Knippertz and Martin, 2005). At interannual timescales, anomalous OLR is mostly significant over the oceanic band. It is enhanced on the northern edge of the mean ITCZ and reduced on the southern edge, thereby confirming a northward shift of the eastern marine ITCZ. Locally, as for seasonal timescale, an upper level cyclonic disturbance is located to the west of the african continent while a poleward transport of tropical moisture is found at low-levels. Note that because of our use of monthly mean values, the anomalous geopotential structures found both at seasonal and interannual timescales are not significant at the 95% level. Nevertheless, the dynamical elements are consistent with previous comprehensive studies of Knippertz and Martin (2005), Meier and Knippertz (2009) and Knippertz and Fink (2008), primarily based on single case-studies. To our knowledge, this is the first time that these mechanisms are described at lower frequencies.

Monsoon Rainfall Structure

Sumer Rainfall

We examine now the regression between Saloum rainfall index and rainfalls over the tropical Atlantic and adjacent african land during the season of the WAM. At seasonal time scales (**Figure 5**), regressions are positive, greater than 0.5 mm/d and statistically significant up to Niger and Chad. This homogeneous regression over the Sahel region is similar to the results of Janicot et al. (2011, their **Figure 5** at lag 0) computed from a Sahel index. Note however that this latter study uses daily data and thus includes shorter time scales than the one displayed here.

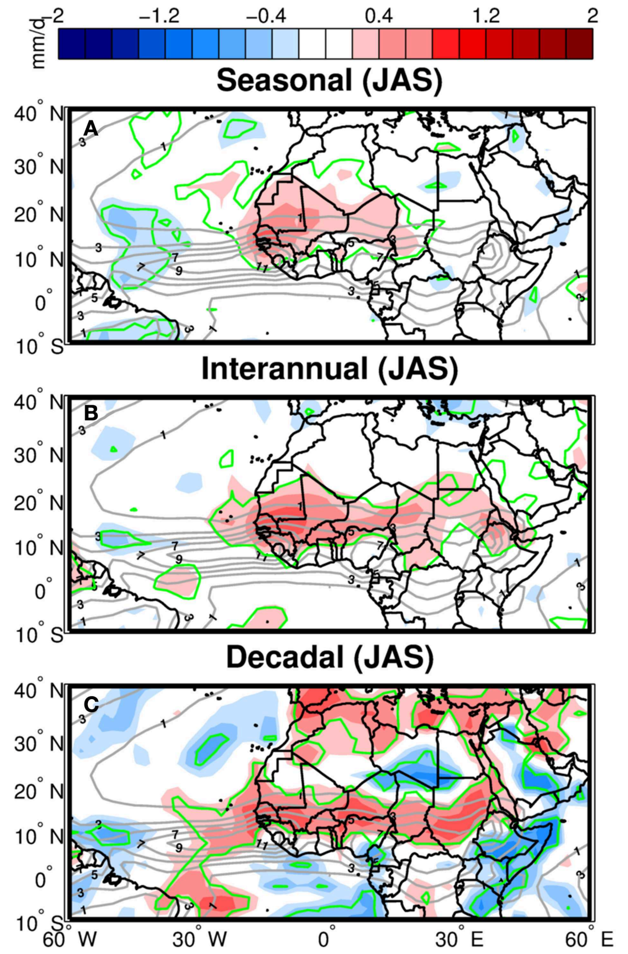

FIGURE 5 | Spatial regression (in mm/day) in summer (JAS) between rainfall in the Saloum region and over the rest of the domain for (A) Seasonal, (B) Interannual, and (C) Decadal timescale. Green contours delimit areas where the regression is significant at 95% level using a Monte Carlo simulation. Gray contours represent the mean climatological (JAS) rainfall (mm/d).

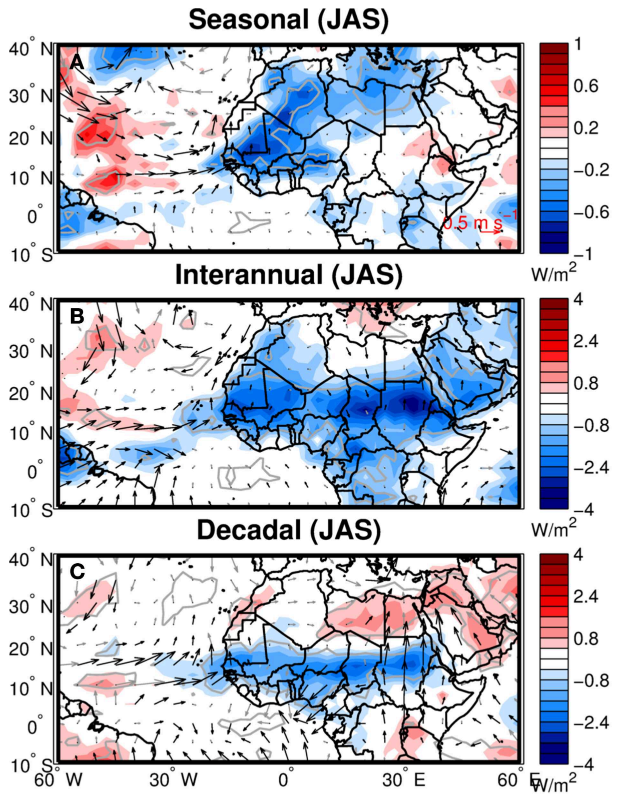

FIGURE 6 | Regression maps in summer (JAS) between Saloum rainfall and OLR (shaded, W/m^2) and surface winds (vectors, m/s) for: (A) Seasonal, (B) Interannual, and (C) Decadal time scale. Gray contours delimit areas where the regression is significant at the 95% significance level using a Monte Carlo simulation.

At interannual time scale, the significant regression pattern extends zonally eastward over the whole Sahel region up to eastern Africa, as well as westward over the Atlantic ocean. This is associated with the signature of the WAM at this time scale. Similar results are found for the decadal time scale, with more extended significant regressions over the adjacent ocean, until 40°W roughly and over the Mediterranean basin. At the sahelian latitude, a striking signal is observed above the tip of eastern Africa, where regressions are strongly negative. Decadal rainfall variability in Sahelian West Africa seems thus more out of phase with east-Africa than with the Gulf of Guinea area.

These results indicate that precipitation variability measured over the Saloum Delta are largely representative of the variability found over West Africa at seasonal timescales, and of the whole Sahel region at interannual and decadal scales. At all frequencies, the anomalous tropical precipitations are located at the northern edge of the mean ITCZ. This is confirmed on **Figure 6** that displays regression of OLR and surface winds on the summer Saloum rainfall index. At seasonal time scale, OLR exhibits a negative anomaly around Senegal, South of Mauritania and West of Mali (**Figure 6A**), suggesting deep atmospheric convection. This pattern is associated with a convergence of surface winds. This and the limited scale of the anomalous OLR pattern, indicate clearly that the seasonal rainfall anomalies are due to meso-scale convective systems. At interannual and decadal timescales, the convective signal extends further east over the Sahel region. Regressions are significant until as far as 15°E, from about 10 to 20°N roughly. Significant regressions are observed over the ocean, consistently with the precipitation structures described in **Figure 5**. It is interesting to note a clear reduction in the intensity and extension of the negative OLR pattern from interannual to decadal scales which was not expected from the rainfall regression patterns. These findings show that at these time scales, rainfalls in the region are spatially coherent and are associated to large-scale atmospheric convection (ITCZ).

Onset and Demise of the Rainfall Season

In this section, we focus on the months leading in and out of the rainy season. Biasutti and Sobel (2009), Monerie et al. (2012) and Biasutti (2013) have indeed noticed a drying trend of the rainy season over the past decades, consistently with observations, in the CMIP3 models and the CMIP5 models, but also a delay in the rainy season in the future, with negative trends in the onset months (June–July, hereafter JJ) in particular over the western Sahel and positive trends in the demise months (September–October, hereafter SO) in the central Sahel (Biasutti, 2013). Although the topic has received some attention over the last years, including works on the predictability of the onset and demise dates (e.g., Laux et al., 2008) and association with atmospheric dynamics (Sultan and Janicot, 2003), these two seasons are less studied than the fully developed monsoon period.

Figure 7 shows the spatial coherence of Saloum rainfall during the onset and demise season at seasonal to decadal timescales. In June-July, Saloum precipitations are significantly correlated with regions locally confined over western Africa (Senegal and eastern Mali) and adjacent ocean. A few areas in the Central Sahel also show significant regressions. These patterns strongly resemble those obtained for winter rainfall variability (**Figure 3**), indicating a possible connection between winter rainfall season and the onset season. Although still significant over the western Africa, spatial regressions at decadal timescales on the onset season are not representative of any larger scale signal. No significant regression is found over the adjacent ocean. Regarding the end of the rainy season however, strong longitudinal and meridional coherence of rainfall over the whole Sahel region is obvious in **Figure 7** at seasonal to decadal timescales. During this period, the WAM is in its southward displacement stage but still located in the Sahel, and zonal coherence of rainfall in the Sahel is therefore expected. These structures are similar to those obtained by Biasutti (2013) regarding the future trends of the onset and demise seasons: the onset of the WAM is more associated to local processes, while, when established, the monsoon events seem to enter its demise stage with an extended spatial coherency, which is observed at all timescales.

Oceanic Forcings of the WAM

Many studies have shown that the WAM over the Sahel region is associated with phenomena in neighboring regions, in particular the Mediterranean basin and the Tropical band over the Atlantic Ocean, but also the Pacific Ocean the Indian sub-continent and the African land. These teleconnections are found to be active from intraseasonal to multidecadal timescales (e.g., Lamb and Peppler, 1992; Janicot et al., 1998; Ward, 1998; Giannini et al., 2003; Losada et al., 2010). More specifically, several studies have focused on SST-driven variability of Sahel rainfall (e.g., Hoerling et al., 2006; Hagos and Cook, 2008; Caminade and Terray, 2009; Mohino et al., 2010; Rodríguez-Fonseca et al., 2011). Many significant links have been found, especially at seasonal to decadal timescales, and it has also been shown that, these teleconnections might evolve with time: for example, the sign of the regression

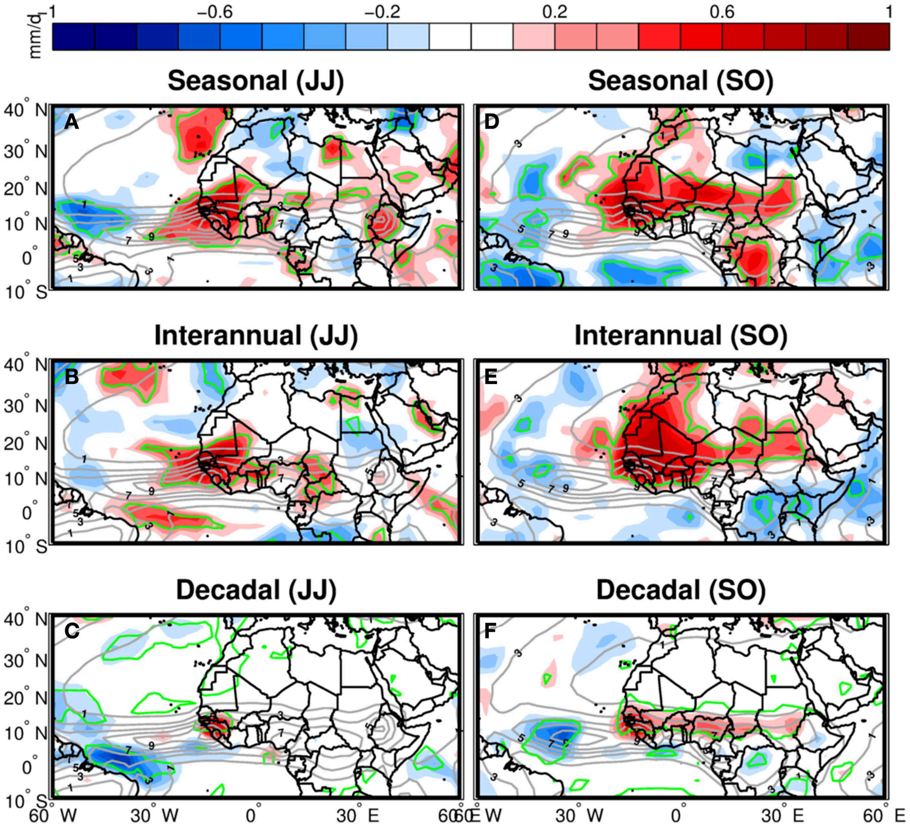

FIGURE 7 | As for Figure 5 but for June–July (JJ, A–C) and September–October (SO, D–F).

between SST anomalies in the equatorial Atlantic and in the Pacific has changed after the 1970s (Rodríguez-Fonseca et al., 2009).

In order to deepen our analysis of the relationship between the Saloum and the Sahel summer rainfalls, and to further gain confidence in the spatial coherency of summer precipitation patterns over Saloum with the WAM, we now investigate SST anomalies associated with precipitation anomalies over the Saloum region.

We propose an overview of similarities and differences between the SST patterns driving rainfalls locally and regionally respectively. Note nevertheless that distinguishing precisely among the different modes of variability is a complex topic that requires specific analysis (e.g., Mohino et al., 2010) and is beyond the scope of our study. We concentrate on the WAM season since no link between SST variability and the heug rainfall has been found (Seck, 1962; Meier and Knippertz, 2009). **Figure 8** shows lagged-regression maps between the JAS Saloum rainfall index and global SSTs during the same season.

The SST regression maps associated to summer precipitation over the Saloum at seasonal time scale are patchy for negative lags. Significant anomalously warm SST anomalies are found in all tropical basins during the months preceding the precipitation signal but correlation values are rather weak (not shown). This structure is largely consistent with SST regressions over the Sahel index (not shown), although the tropical Pacific signal is stronger here. At lag zero however, a signal similar to the intraseasonal projection of the summer North Atlantic Oscillation (NAO, Keeley et al., 2009; Bladé et al., 2012) appears in the north Atlantic and is significant off North America, suggesting that seasonal variability over west Africa (see **Figure 5**) is linked to that of the northern Atlantic basin.

At interannual time scale, the SST structure leading anomalous summer precipitation over the Saloum shows more spatial coherency: significant anomalously warm SSTs are found mainly over the tropical southern Atlantic and the subtropical North Atlantic basin with an extension over the Mediterranean basin. Interestingly, no significant anomalies are found in the northern tropics, at the latitude of the Saloum. These structures are again very consistent with those obtained from the Sahel index except that signals in the Atlantic are much stronger and slightly shifted to the west in the Saloum case. Warm anomalies are also found in the western equatorial Pacific and they extend poleward above up to 30° of latitude. Areas of negative regressions are found in the eastern equatorial Pacific indicating that at this time scale, El Niño (La Niña) events are typically associated with reduced (enhanced) WAM seasons a couple of months later. These anomalies are again very consistent with regressions using the Sahel rainfall index, but the areas of statistical significance are smaller here. The dominant influence of the tropical Pacific on the variability of the WAM at interannual timescales as indeed been shown in many studies (e.g., Giannini et al., 2003; Mohino et al., 2010; among others).

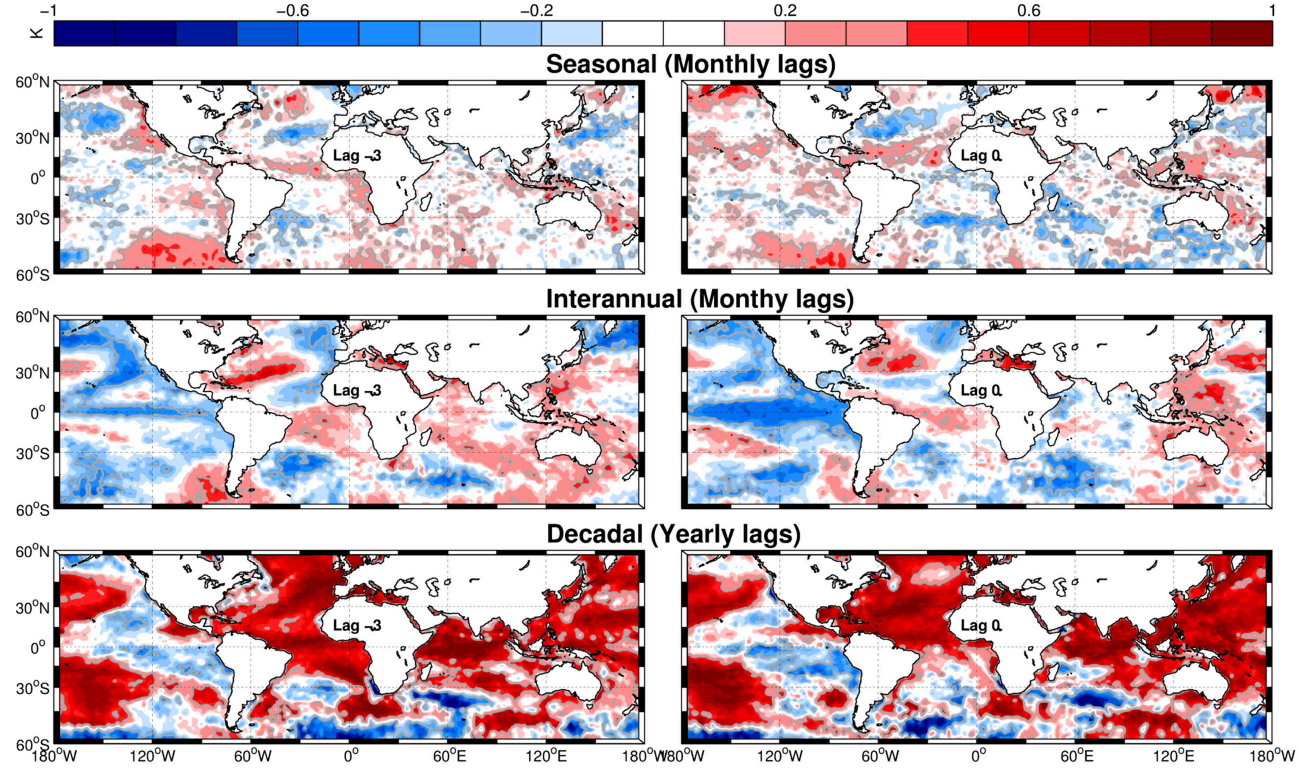

FIGURE 8 | Lagged regression maps at different time scales of Saloum rainfall index and SST during summer (JAS). Units of the color scale are K. Contours show area where regressions are statistically significant at the 95% level using a Monte Carlo simulation.

Here, we confirm a similar mechanism driving the rainy period locally over the Saloum Delta. In phase with the Saloum precipitation, significant SSTs anomalies are primarily found in the western Pacific, the northern tropical and the equatorial Atlantic. Lamb (1978a) and Vizy and Cook (2002) show a dipole pattern of precipitations in the Sahel and the Gulf of Guinea in which enhanced precipitations are associated with negative SST anomalies in the Equatorial Atlantic. It has recently been shown that, the sign of SST anomalies in the equatorial Atlantic associated to enhanced precipitation in the Sahel depends on the time period of analysis which opened the question about the non stationarity of the link between SST and precipitation (e.g., Rodríguez-Fonseca et al., 2011).

At decadal timescales, finally, precipitations over the Saloum regions are associated with warm oceanic anomalies over the tropical and subtropical Atlantic basin, the Indian Ocean and the Mediterranean basin. These findings confirm previous results regarding the influence of the Atlantic Multidecadal Oscillation (AMO, e.g., Folland et al., 1986; Rowell et al., 1995; Knight et al., 2006; Zhang and Delworth, 2006; Ting et al., 2009), the Interdecadal Pacific Oscillation (IPO, e.g., Mohino et al., 2010) and the Indian Decadal Variability (IDV, e.g., Bader and Latif, 2003; Giannini et al., 2003; Lu and Delworth, 2005; Mohino et al., 2010).

Conclusions

Azzoug et al. (2012b) recently opened promising perspectives with a new technique to quantitatively reconstruct the monsoon variability as well as the duration of the rainy and dry seasons in the Saloum Delta over the past millennia. Their methods are aimed at assessing the natural variability of the WAM over long periods. However, such generalization may deserve some care since precipitations are known to have patchy features with small spatial scale (Houze and Cheng, 1977; Leary and Houze, 1979; Nicholson, 1995; Chen et al., 1996; Rickenbach and Rutledge, 1998; Lebel et al., 2009). In this study, we show how the local Saloum rainfall is coherent with the regional Sahel rainfall at seasonal to decadal time scales. Results show that at seasonal time scale, the winter Saloum rainfalls known as “heug” or “mango” rainfalls, are not coherent over the whole Sahel region. It is representative of a limited area over western Africa, including Senegal, southern Mauritania and western Mali, and the oceanic regions adjacent to Senegal and Guinea. A slight increase of this domain is found at interannual time scale, in particular over the ocean where the signal seems to reveal a northward shift of the ITCZ. At all time scales, precipitations in winter are associated with an upper level anomalous cyclonic circulation to the west of the precipitative area and low level winds from the tropics potentially transporting moisture, and favoring convection. This is consistent with previous studies, which rather focus of specific case-studies.

During summer, Saloum rainfalls are more intense, and more coherent at the regional scale. At seasonal time scales, statistically significant regressions are found over the whole western half of sahelian Africa, including Niger. This finding is similar to the results of Janicot et al. (2011) computed from a Sahel index. At interannual time scale, significant regressions encompass the whole sahelian band, and even extend westward over the ocean. Regressions increase at decadal time scale over the Sahel region. These results suggest a good consistency between Saloum and Sahel precipitation events during the monsoon season and tend to support the regional significance of local paleoclimate reconstructions in the Saloum.

Furthermore, in order to further deepen our understanding of the connection of the Saloum rainy season and the WAM, we have diagnosed the links between SST anomalies and Saloum rainfalls during the WAM season by computing lagged-regression maps between the JAS Saloum rainfall index and global SSTs during the same season. At seasonal time scale, significant warm SST anomalies in the vicinity of the Saloum Delta are detected during the months preceding the precipitation signal, suggesting that local SSTs can play a role. Very weak SST signal can be seen over the equatorial Atlantic leading the seasonal Saloum rainfall variability. A horsehoe-like SST pattern in the North Atlantic in phase with the rainy season may be indicative of an influence of the NAO. These structures are largely consistent with SST regression over the Sahel index (not shown). At interannual time scale, precipitations over the Saloum region are typically associated with ENSO events in the tropical Pacific and warm anomalies over the equatorial and North tropical basins. At decadal time scale, AMO, IPV and possibly global warming are potential drivers of the Saloum rainfall variability, consistently with previous studies dedicated to the WAM.

On the other hand, analysis for the months of JJ and SO showed different behaviors for the onset and demise of the monsoon season. In June-July, precipitations in the Saloum region are significantly correlated with closely surroundings regions (Senegal and eastern Mali) but are not representative of the whole Sahel region. Nearly similar patterns were obtained during winter, indicating a possible connection between winter rainfall season and the onset season. Interestingly, as opposed to findings for other seasons, the spatial extent of the significant regression region tends to decrease at lower frequencies, suggesting that the decadal scale modulation of the early-WAM precipitation over the Saloum delta are local events. Regarding the termination of the rainy season, on the other hand, strong coherence is found over the whole Sahel region at seasonal to decadal time scales, consistently with results found for the fully developed WAM season.

Our study provides a framework for a more robust and accurate interpretation of recent paleoclimate proxies proposing a reconstruction of the monsoon seasonality in western Sahel. Our results show that proxy reconstructions of the monsoon season and its termination can generally be extrapolated to the Sahelian band. Furthermore, as indicated in the introduction, another proxy reconstruction of African rainfall has been proposed by Shanahan et al. (2009) from a sediment core taken in the lake Bosumtwi, Ghana. This location is further east and south than the Saloum Delta, and rainfalls are thus subject to different dynamics. Extension of the present study to this location may also be needed for a more accurate interpretation of this record. We emphasize that the spatial scale is also a crucial issue for applications such as crop yields or water resources. More generally, our study turns to the question of regionalization of the WAM region and downscaling (Paeth et al., 2011). Further work is, indeed, needed in order to better understand the regional coherence of the different phases of the WAM over the whole domain.

Acknowledgments

This research was supported by the AWA program (Approche écosystémique de la gestion des pêches et de l'environnement marin dans les eaux ouest-africaines) and by CNRS-INSU LEFE program through the Saloum project (P.I. M.C.).

References

Abiodun, B. J., Pal, J. S., Afiesimama, E. A., Gutowski, W. J., and Adedoyin, A. (2008). Simulation of west African monsoon using RegCM3 Part II: impacts of deforestation and desertification. *Theor. Appl. Climatol.* 93, 245–261. doi: 10.1007/s00704-007-0333-1

Adler, R. F., Huffman, G. J., Chang, A., Ferraro, R., Xie, P., Janowiak, J., et al. (2003). The Version-2 Global Precipitation Climatology Project (GPCP) monthly precipitation analysis (1979–Present). *J. Hydrometeorol.* 4, 1147–1167.

Afiesimama, E. A., Pal, J. S., Abiodun, B. J., Gutowski, W. J., and Adedoyin, A. (2006). Simulation of West African monsoon using the RegCM3. Part I: model validation and interannual variability. *Theor. Appl. Cimatol.* 86, 23–37. doi: 10.1007/s00704-005-0202-8

African Monsoon and Multidisciplinary Analyses International Scientific Steering Committee, (AMMA ISSC). (2005). *The International Science Plan for AMMA*.

Azzoug, M., Carré, M., Chase, B. M., Deme, A., deMorais, L. T., Lazar, A., et al. (2012a). Positive Precipitation-Evaporation budget from AD 460 to 1090 in the Saloum Delta (Senegal), indicated by mollusk oxygen isotopes. *Glob. Planet. Change* 98–99, 54–62. doi: 10.1016/j.gloplacha.2012.08.003

Azzoug, M., Carré, M., and Schauer, A. J. (2012b). Reconstructing the duration of the West African Monsoon season from growth patterns and isotopic signals of shells of *Anadara senilis* (Saloum Delta, Senegal). *Palaeogeogr. Palaeoclimatol. Palaeoecol.* 346–347, 145–152. doi: 10.1016/j.palaeo.2012.06.001

Bader, J., and Latif, M. (2003). The impact of decadal-scale Indian Ocean sea surface temperature anomalies on Sahelian rainfall and the North Atlantic Oscillation. *Geophys. Res. Lett.* 30, 2169. doi: 10.1029/2003gl018426

Berg, A., Quirion, P., and Sultan, B. (2009). Can weather index drought insurance benefit to least developed countries' farmers? a case study on burkina faso. *Weather Clim. Soc.* 1, 71–84. doi: 10.1175/2009WCAS1008.1

Biasutti, M. (2013). Forced Sahel rainfall trends in the CMIP5 archive. *J. Geophys. Res.* 118, 1613–1623. doi: 10.1002/jgrd.50206

Biasutti, M., Held, I., Sobel, A., and Giannini, A. (2008). SST forcings and Sahel rainfall variability in simulations of the twentieth and twenty-first centuries. *J. Clim.* 21, 3471–3486. doi: 10.1175/2007JCLI1896.1

Biasutti, M., and Sobel, A. (2009). Delayed seasonal cycle and African monsoon in a warmer climate. *Geophys. Res. Lett.* 36, 707. doi: 10.1029/2009GL041303

Bladé, I., Liebmann, B., Fortuny, D., and van Oldenborgh, G. J. (2012). Observed and simulated impacts of the summer NAO in Europe: implications for projected drying in the Mediterranean region. *Clim. Dyn.* 39, 709–727. doi: 10.1007/s00382-011-1195-x

Caminade, C., and Terray, L. (2009). Twentieth century Sahel rainfall variability as simulated by the ARPEGE AGCM, and future changes. *Clim. Dyn.* 35, 75–94. doi: 10.1007/s00382-009-0545

Charney, J. G. (1975). Dynamics of deserts and drought in the Sahel. *Q. J. R. Meteorol. Soc.* 101, 193–202. doi: 10.1002/qj.49710142802

Charney, J. G., and Shukla, J. (1981). "Predictability of monsoons," in *Monsoon Dynamics*, eds J. Lighthill and R. P. Pearce (New York, NY: Cam Definition and predictability of an OLR-based West African monsoon onset bridge University Press), 99–109.

Chen, S. S., Houze, R. A. Jr., and Mapes, B. E. (1996). Multiscale variability of deep convection in relation to large-scale circulation in TOGA COARE. *J. Atmos. Sci.* 53, 1380–1409.

Dai, A., Trenberth, K. E., and Qian, T. (2004). A global data set of Palmer Drought Severity Index for 1870-2002: relationship with soil moisture and effects of surface warming. *J. Hydrometeorology* 5, 1117–1130.

Davin, E. L., and de Noblet-Ducoudré, N. (2010). Climatic impact of global-scale deforestation: radiative versus non-radiative processes. *J. Clim.* 23, 97–112. doi: 10.1175/2009JCLI3102.1

De Félice, P. (1999). *La Pluie au Sahel. Ecologie et Agronomie Appliquée, l'Harmattan.* Paris.

Diedhiou, A., Janicot, S., Viltard, A., de Felice, P., and Laurent, H. (1999). Easterly wave regimes and associated convection over West Africa and tropical Atlantic: results from NCEP/NCAR and ECMWF reanalysis. *Clim. Dyn.* 15, 795–822. doi: 10.1007/s003820050316

Dieng, A. L., Eymard, L., Sall, S. M., Lazar, A., and Leduc-Leballeur, M. (2014). Analysis of strengthening and dissipating Mesoscale Convective Systems propagating off the West African coast. *Mon. Weather Rev.* 142, 4600–4623. doi: 10.1175/MWR-D-13-00388.1

Dieppois, B., Diedhiou, A., Durand, A., Fournier, M., Massei, N., Sebag, D., et al. (2013). Quasi-decadal signals of Sahel rainfall and West African monsoon since the mid-twentieth century. *J Geophys. Res. Atmos.* 118, 12587–12599. doi: 10.1002/2013JD019681

Duvel, J. P. (1990). Convection over tropical Africa and the Atlantic ocean during northern summer. Part, I. I. Modulation by easterly waves. *Mon. Weather Rev.* 118, 1855–1868.

Fernández-Donado, L. González-Rouco, J. F., Raible, C. C., Ammann, C. M., Barriopedro, D., García-Bustamante, E., et al. (2013). Large-scale temperature response to external forcing in simulations and reconstructions of the last millennium. *Clim. Past* 9, 393–421. doi: 10.5194/cp-9-393-2013

Fink, A. H., and Reiner, A. (2003). Spatiotemporal variability of the relation between African easterly waves and West African squall lines in 1998 and 1999. *J. Geophys. Res.* 108, ACL 5-1–5-17. doi: 10.1029/2002JD002816

Folland, C. K., Palmer, T. N., and Parker, D. E. (1986). Sahel rainfall and worldwide sea temperatures, 1901–85. *Nature* 320, 602–607. doi: 10.1038/320602a0

Fontaine, B., and Janicot, S. (1996). Sea surface temperature fields associated with West African rainfall anomaly types. *J. Clim.* 9, 2935–2940.

Fontaine, B., Louvet, S., and Roucou, P. (2008). Definition and predictability of an OLR-based West African monsoon onset. *Int. J. Climatol.* 28, 1787–1798. doi: 10.1002/joc.1674

Gaye, A. T., and Fongang, S. (1997). "Some aspects of interactions between tropical region and temperate zones in northern hemisphere winter season," in *Proceedings 22nd Conference on Hurrican and Tropical Meteorology,* (Colorado), 232–233.

Gaye, A. T., Fongang, S., Garba, A., and Badiane, D. (1994). Study of Heug rainfall in Senegal using conventional data and meteosat imagery. *Veille Climatique Satellitaire* 49, 61–71.

Giannini, A., Saravannan, R., and Chang, P. (2003). Oceanic forcing of Sahel rainfall on interannual to interdecadal time scales, *Science* 302, 1027–1030. doi: 10.1126/science.1089357

Hagos, S., and Cook, K. (2008). Ocean warming and late-twentieth-century Sahel drought and recovery. *J. Clim.* 21, 3797–3814. doi: 10.1175/2008JCLI 2055.1

Hastenrath, S. (1984). Interannual variability and annual cycle. Mechanism of circulation and climate in the tropical Atlantic sector. *Mon. Weather Rev.* 112, 1097–1107.

Hastenrath, S. (1990). Decadal-scale changes of the circulation in the tropical Atlantic sector associated with Sahel drought. *Int. J. Climatol.* 10, 459–472. doi: 10.1002/joc.3370100504

Hodges, K. I., and Thorncroft, C. D. (1997). Distribution and statistics of African mesoscale convective weather systems based on ISCCP METEOSAT imagery. *Mon. Weather Rev.* 121, 2821-2837.

Hoerling, M., Hurrell, J., Eischeid, J., and Phillips, A. (2006). Detection and attribution of 20th century northern and southern African rainfall change. *J. Clim.* 19, 3989–4008. doi: 10.1175/JCLI3842.1

Houze, R. A. Jr., and Cheng, C.-P. (1977). Radar characteristics of tropical convection observed during GATE: mean properties and trends over the summer season. *Mon. Weather Rev*. 105, 964–980.

Huffman, G. J., Adler, R. F., Bolvin, D. T., and Gu, G. (2009). Improving the global precipitation record: GPCP version 2.1. *Geophys. Res. Lett*. 36, L17808. doi: 10.1029/2009gl040000

Huffman, G. J., Bolvin, D. T., Nelkin, E. J., Wolff, D. B., Adler, R. F., Gu, G., et al. (2007). TheTRMM Multisatellite Precipitation Analysis (TMPA): Quasi-global, multiyear, combined-sensor precipitation estimates at fine scales. *J. Hydrometeorol*. 8, 38–55. doi: 10.1175/JHM560.1

Hulme, M. (1992). Rainfall changes in Africa: 1931–1960 to 1961–1990. *Int. J. Climatol.* 12, 685–699.

Janicot, S. (1992). Spatiotemporal variability of West African rainfall. Part I: regionalizations and typings. *J. Clim.* 5, 489–511.

Janicot, S., Caniaux, G., Chauvin, F., de Coetlogon, G., Fontaine, B., Hall, N., et al. (2011). Intraseasonal variability of the West African monsoon. *Atmos. Sci. Lett.* 12, 58–66. doi: 10.1002/asl.280

Janicot, S., Harzallah, A., Fontaine, B., and Moron, V. (1998). West African monsoon dynamics and eastern equatorial Atlantic and Pacific SST anomalies (1970–1988). *J. Clim*. 11, 1874–1882. doi: 10.1175/1520-0442-11.8.1874

Janicot, S., Trzaska, S., and Poccard, I. (2001). Summer Sahel-ENSO teleconnection and decadal time scale SST variations. *Clim. Dyn*. 18, 303–320. doi: 10.1007/s003820100172

Kalnay, E., Kanamitsu, M., Kistler, R., Collins, W., Deaven, D., Gandin, L., et al. (1996). The NCEP/NCAR 40-Year Reanalysis Project. *Bull. Am. Meteorol. Soc.* 77, 437–471.

Keeley, S. P. E., Sutton, R. T., and Shaffrey, L. C. (2009). Does the North Atlantic Oscillation show unusual persistence on intraseasonal timescales? *Geophys. Res. Lett*. 36, L22706. doi: 10.1029/2009GL040367

Kiladis, G. N., Thorncroft, C. D., and Hall, N. M. (2006). Three dimensional structure and dynamics of African easterly waves. Part, I. Observations. *J. Atmos. Sci.* 63, 2212–2230.

Knight, J. R., Folland, C. K., and Scaife, A. A. (2006). Climate impacts of the Atlantic multidecadal oscillation. *Geophys. Res. Lett.* 33, L17706. doi: 10.1029/2006GL026242

Knippertz, P., and Fink, A. H. (2008). Dry-season precipitation in tropical West Africa and its relation to forcing from the extratropics. *Mon. Weather Rev*. 136, 3579–3596. doi: 10.1175/2008MWR2295.1

Knippertz, P., and Martin, J. E. (2005). Tropical plumes and extreme precipitation in subtropical and tropical West Africa. *Q. J. R. Meteorol. Soc*. 131, 2337–2365. doi: 10.1256/qj.04.148

Laing, A. G., and Fritsch, J. M. (1993). Mesoscale convective complexes in Africa. *Mon. Weather Rev*. 121, 2254-2263.

Laing, A. G., and Fritsch, J. M. (1997). The global population of mesoscale convective complexes. *Q. J. R. Meteorol. Soc.* 123, 389–405. doi: 10.1002/qj.49712353807

Lamb, P. J. (1978a). Case studies of tropical Atlantic surface circulation patterns during recent sub-Saharan weather anomalies, 1967 and 1968. *Mon. Weather Rev*. 106, 482–491.

Lamb, P. J. (1978b). Large-scale tropical Atlantic surface circulation patterns associated with sub-Saharan weather anomalies. *Tellus* 30, 240–251. doi: 10.1111/j.2153-3490.1978.tb00839.x

Lamb, P. J., and Peppler, R. A. (1992). Further case studies of tropical Atlantic surface circulation patterns associated with sub-Saharan drought. *J. Clim.* 5, 476–488.

Laux, P., Kunstmann, H., and Bárdossy, A. (2008). Predicting the regional onset of the rainy season in west africa. *Int. J. Climatol.* 20, 329–342. doi: 10.1002/joc.1542

Leary, C. A., and Houze, R. A. Jr. (1979). The structure and evolution of convection in a tropical cloud cluster. *J. Atmos. Sci.* 36, 437–457.

Le Barbé, L., Lebel, T., and Tapsoba, D. (2002). Rainfall Variability in West Africa during the years 1950-90. *J. Clim.* 15, 187–202. doi: 10.1175/1520-0442(2002)015<0187:RVIWAD>2.0.CO;2

Lebel, T., Cappelaere, C., Galle, S., Hanan, N., Kergoat, L., Levis, S., et al. (2009). AMMA-CATCH studies in the Sahelian region of West-Africa: an overview. *J. Hydrol.* 375, 3–13. doi: 10.1016/j.jhydrol.2009.03.020

L'Hôte, Y., Mahé, G., Somé, B., and Triboulet, J. P. (2002). Analysis of a Sahelian annual rainfall index from 1896 to 2000; the drought continues. *Hydrol. Sci. J.-J. Des. Sci. Hydrol.* 47, 563–572.

Liu, Z. (2015). Comparison of precipitation estimates between Version 7 3-hourly TRMM Multi-Satellite Precipitation Analysis (TMPA) near-real-time and research products. *Atmos. Res.* 153, 119–133. doi: 10.1016/j.atmosres.2014.07.032

Losada, T., Rodriguez-Fonseca, B., Polo, I., Janicot, S., Gervois, S., Chauvin, F., et al. (2010). Tropical response to the Atlantic equatorial mode: AGCM multimodel approach. *Clim. Dyn.* 35, 45–52. doi: 10.1007/s00382-009-0624-6

Lu, J., and Delworth, R. (2005). Oceanic forcing of the late 20th century Sahel drought. *Geophys. Res. Lett.* 32, L22706. doi: 10.1029/2005GL023316

Maloney, E. D., and Shaman, J. (2008). Intraseasonal Variability of the West African Monsoon and Atlantic ITCZ. *J. Clim.* 21, 2898–2918. doi: 10.1175/2007JCLI1999.1

Marteau, R. (2011). *Coherence Spatiale et Previsibilite Potentielle des Descripteurs Intra-Saisonniers de la Saison des Pluies en Afrique Soudano-Sahelienne: Application ala Culture du mil dans la Region de Niamey*. Ph.D. thesis, University of Bourgogne.

Mathon, V., and Laurent, H. (2001). Lifecycle of Sahelian mesocale convective cloud systems. *Q. J. R. Meteorol. Soc.* 127, 377–406. doi: 10.1002/qj.49712757208

Meier, F., and Knippertz, P. (2009). Dynamics and predictability of a heavy dry season precipitation event over West Africa: sensitiviy studies with a global model. *Mon. Weather Rev*. 137, 189–206. doi: 10.1175/2008MWR2622.1

Mohino, E., Janicot, S., and Bader, J. (2010). Sahel rainfall and decadal to multi-decadal sea surface temperature variability. *Clim. Dyn.* 37, 419–440. doi: 10.1009/s00382-010-0867-2

Mohino, E., Rodríguez-Fonseca, B., Losada, T., Gervois, S., Janicot, S., Bader, J., et al. (2011). SST-forced signals on West African rainfall from AGCM simulations—Part I: changes in the interannual modes and model intercomparison. *Clim. Dyn*. 37, 1707–1725. doi: 10.1007/s00382-011-1093-2

Monerie, P.-A., Fontaine, B., and Roucou, P. (2012). Expected future changes in the African monsoon between 2030 and 2070 using some CMIP3 and CMIP5 models under a medium-low RCP scenario. *J. Geophys. Res*. 117:D16111. doi: 10.1029/2012JD017510

Monerie, P.-A., Roucou, P., and Fontaine, B. (2013). Mid-century effects of Climate Change on African monsoon dynamics using A1B emission scenario. *Int. J. Climatol.* 33, 881–896. doi: 10.1002/joc.3476

Moron, V. (1994). Guinean and Sahelian rainfall anomaly indices at annual and monthly time scales (1933-1990). *Int. J. Climatol.* 14, 325–341. doi: 10.1002/joc.3370140306

Mounier, F., Kiladis, G. N., and Janicot, S. (2007). Analysis of the dominant mode of convectively coupled Kelvin waves in the West African monsoon. *J. Clim.* 20, 1487–1503. doi: 10.1175/JCLI4059.1

Mulitza, S., Prange, M., Stuut, J. B., Zabel, M., Dobeneck, T. V., Itambi, A. C., et al. (2008). Sahel mega-droughts triggered by glacial slowdowns of Atlantic meridional overturning, Paleoceanography. *Paleoceanography* 23, PA4206. doi: 10.1029/2008PA001637

Nicholson, S. E. (1994). Century-scale series of standardized annual departures of African rainfall, in Trends (93): compendium of Data on Global Change. *Carbon*, 952–962.

Nicholson, S. E. (1995). "Environmental change within the historical period," in *The Physical Geography of Africa,* eds A. S. Goudie, W. M. Adams, and A. Orme (Oxford: Oxford University Press), 60–75.

Nicholson, S. E., and Palao, I. M. (1993). A re-evaluation of rainfall variability in the Sahel, Part, I. Characteristics of rainfall fluctuations. *Int. J. Climatol.* 13, 371–389. doi: 10.1002/joc.3370130403

Nicholson, S. E., Some, B., and Kone, B. (2000). An analysis of recent rainfall conditions in West Africa, including the rainy seasons of the 1997 El Niño and the 1998 La Niña years. *J. Clim.* 13, 2628–2640.

Paeth, H., Born, K., Girmes, R., Podzun, R., and Jacob, D. (2009). Regional climate change in tropical and northern Africa due to green house forcing and land use changes. *J. Clim.* 22, 114–132. doi: 10.1175/2008JCLI2390.1

Paeth, H., Born, K., Podzun, R., and Jacob, D. (2005). Regional dynamical downscaling over West Africa: model evaluation and comparison of wet and dry years. *Meteorol Z* 14, 349–367. doi: 10.1127/0941-2948/2005/0038

Paeth, H., Hall, N. M. J., Gaertner, M. A., Alonso, M. D., Moumouni, S., Polcher, J., et al. (2011). Progress in regional downscaling of West African precipitation. *Atmos Sci. Lett.* 12, 75–85. doi: 10.1002/asl.306

Palmer, T. N. (1986). Influence of the Atlantic, Pacific and Indian Oceans on Sahel rainfall. *Nature* 322, 251–253. doi: 10.1038/322251a0

Patricola, C. M., and Cook, K. H. (2010). Northern African Climate at the end of the 21st Century: integrated application of regional and global climate models. *Clim Dyn.* 35, 193–212. doi: 10.1007/s00382-009-0623-7

Rayner, N. A., Parker, D. E., Horton, E. B., Folland, C. K., Alexander, L. V., Rowell, D. P., et al. (2003). Global analyses of sea surface temperature, sea ice, and night marine air temperature since the late nineteenth century. *J. Geophys. Res. Atmos.* 108, 4407. doi: 10.1029/2002JD002670

Reed, R. J., Norquist, D. C., and Recker, E. E. (1977). The structure and properties of African wave disturbances as observed during Phase III of GATE. *Mon. Weather Rev*. 105, 334–342.

Rickenbach, T. M., and Rutledge, S. A. (1998). Convection in TOGA COARE: horizontal scale, morphology, and rainfall production. *J. Atmos. Sci*. 55, 2715–2729.

Rodriguez-Fonseca, B., Janicot, S., Mohino, E., Losada, T., Bader, J., Caminade, C., et al. (2011). Interannual and decadal SST forced responses of the West African monsoon. *Atmos. Sci. Lett*. 12, 67–74. doi: 10.1002/asl.308

Rodríguez-Fonseca, B., Polo, I., García-Serrano, J., Losada, T., Mohino, E., Mechoso, C., et al. (2009). Are Atlantic Niños enhancing Pacific ENSO events in recent decades? *Geophys. Res. Lett*. 36, L20705. doi: 10.1029/2009GL040048

Rowell, D. P. (2001). Teleconnections between the tropical Pacific and the Sahel. *Q. J. R. Meteorol. Soc*. 127, 1683–1706. doi: 10.1002/qj.49712757512

Rowell, D. P. (2003). The impact of Mediterranean SSTs on the Sahelian rainfall season. *J. Clim.* 16, 849–862. doi: 10.1175/1520-0442(2003)016<0849:tiomso>2.0.co;2

Rowell, D. P., Folland, C. K., Maskel, K., Owen, J. A., and Ward, M. N. (1995). Variability of the summer rainfall over tropical North Africa (1906–92): Observations and modeling. *Q. J. R. Meteorol. Soc*. 121, 669–704.

Rui, L., and Yunfei, F. (2005). Tropical precipitation estimated by GPCP and TRMM PR observations. *Adv. Atmos. Sci.* 22, 852–864. doi: 10.1007/BF02918685

Salack, S., Muller, B., and Gaye, A. T. (2011). Rain-based factors of high agricultural impacts over Senegal. Part, I. Integration of local to sub-regional trends and variability. *Theor. Appl. Clim.* 10, 1–22. doi: 10.1007/s00704-011-0414-z

Seck, A. (1962). Le Heug ou pluies de saison sèche au Sénégal. *Ann. Geogr*. 385, 225–246. doi: 10.3406/geo.1962.16196

Shanahan, T. M., Overpeck, J. T., Anchukaitis, K. J., Beck, J. W., Cole, J. E., Dettman, D. L., et al. (2009). Atlantic forcing of persistent drought in West Africa. *Science* 324, 377–380. doi: 10.1126/science.1166352

Sultan, B., Baron, C., Dingkuhn, M., and Janicot, S. (2005). Agricultural impacts of large-scale variability of the West African monsoon. *Agric. For. Meteorol.* 128, 93–110. doi: 10.1016/j.agrformet.2004.08.005

Sultan, B., and Janicot, S. (2003). The West African monsoon dynamics. Part II: the "preonset" and "onset" of the summer monsoon. *J. Clim.* 16, 3389–3406. doi: 10.1175/1520-0442(2003)016<3389:TWAMDP>2.0.CO;2

Thorncroft, C. D., and Flocas, H. A. (1997). A case study of Saharan cyclogenesis. *Mon. Weather Rev.* 125, 1147–1165.

Thorncroft, C. D., and Hoskins, B. J. (1994a). An idealized study of African easterly waves. Part, I. A linear view. *Q. J. R. Meteorol. Soc.* 120, 953–982. doi: 10.1002/qj.49712051809

Thorncroft, C. D., and Hoskins, B. J. (1994b). An idealized study of African easterly waves. Part, I. I. A nonlinear view. *Q. J. R. Meteorol. Soc.* 120, 983–1015. doi: 10.1002/qj.49712051810

Ting, M., Kushnir, Y., Seager, R., and Li, C. (2009). Forced and internal twentieth century SST trends in the North Atlantic. *Clim. J.* 22, 1469–1481. doi: 10.1175/2008JCLI2561.1

Vizy, E. K., and Cook, K. H. (2002). Development and application of a mesoscale climate model for the tropics: influence of sea surface température anomalies on the West African monsoon. *J. Res. Atmos.* 107, 22. doi: 10.1029/2001jd000686

Ward, M. N. (1998). Diagnosis and short-lead time prediction of summer rainfall in tropical North Africa at interannual and multidecadal time scales. *J. Clim.* 11, 3167–3191.

Zeng, N., Neelin, J. D., Lau, K. M., and Tucker, C. J. (1999). Enhancement of interdecadal climate variability in the Sahel by vegetation interaction. *Science* 286, 1537–1540. doi: 10.1126/science.286.5444.1537

Zhang, R., and Delworth, T. L. (2006). Impact of Atlantic multidecadal oscillations on India/Sahel rainfall and Atlantic hurricanes. *Geophys. Res. Lett.* 33. doi: 10.1029/2006gl026267

Zheng, X., and Eltahir, E. A. B. (1998). The Role of Vegetation in the Dynamics of West African Monsoons. *J. Clim.* 11, 2078–2096. doi: 10.1175/1520-0442-11.8.2078

Conflict of Interest Statement: The authors declare that the research was conducted in the absence of any commercial or financial relationships that could be construed as a potential conflict of interest.

frontiers in
EARTH SCIENCE

ORIGINAL RESEARCH ARTICLE
published: 03 April 2014
doi: 10.3389/feart.2014.00003

The record precipitation and flood event in Iberia in December 1876: description and synoptic analysis

Ricardo M. Trigo[1]*, Filipa Varino[1], Alexandre M. Ramos[1], Maria A. Valente[1], José L. Zêzere[2], José M. Vaquero[3], Célia M. Gouveia[1] and Ana Russo[1]

[1] Instituto Dom Luiz (IDL), Faculdade de Ciências, Universidade de Lisboa, Lisboa, Portugal
[2] CEG, Instituto de Geografia e Ordenamento do Território, Universidade de Lisboa, Lisboa, Portugal
[3] Departamente de Física, Universidad de Extremadura, Mérida, Spain

Edited by:
Anita Drumond, University of Vigo, Spain

Reviewed by:
Sergio M. Vicente-Serrano, Spanish National Research Council, Spain
Eduardo Zorita, Hemlholtz-Zentrum Geesthacht, Germany

***Correspondence:**
Ricardo M. Trigo, Instituto Dom Luiz (IDL), Faculdade de Ciências, Universidade de Lisboa, Campo Grande, Ed C8, Piso 3, 1749-016 Lisboa, Portugal
e-mail: rmtrigo@fc.ul.pt

The first week of December 1876 was marked by extreme weather conditions that affected the south-western sector of the Iberian Peninsula (IP), leading to an all-time record flow in two large international rivers. As a direct consequence, several Portuguese and Spanish towns and villages located in the banks of both rivers suffered serious flood damage on 7 December 1876. These unusual floods were amplified by the preceding particularly autumn wet months, with October 1876 presenting extremely high precipitation anomalies for all western Iberia stations. Two recently digitized stations in Portugal (Lisbon and Evora), present a peak value on 5 December 1876. Furthermore, the values of precipitation registered between 28 November and 7 December were so remarkable that, the episode of 1876 still corresponds to the maximum average daily precipitation values for temporal scales between 2 and 10 days. Using several different data sources, such as historical newspapers of that time, meteorological data recently digitized from several stations in Portugal and Spain and the recently available 20th Century Reanalysis, we provide a detailed analysis on the socio-economic impacts, precipitation values and the atmospheric circulation conditions associated with this event. The atmospheric circulation during these months was assessed at the monthly, daily and sub-daily scales. All months considered present an intense negative NAO index value, with November 1876 corresponding to the lowest NAO value on record since 1865. We have also computed a multivariable analysis of surface and upper air fields in order to provide some enlightening into the evolution of the synoptic conditions in the week prior to the floods. These events resulted from the continuous pouring of precipitation registered between 28 November and 7 December, due to the consecutive passage of Atlantic low-pressure systems fuelled by the presence of an atmospheric-river tropical moisture flow over central Atlantic Ocean.

Keywords: floods, extremes precipitation, natural hazard, NAO, atlantic storms, atmospheric river

INTRODUCTION

Flooding events are one of most costly and wide reaching natural hazards which, although triggered by characteristic meteorological factors, can also be amplified by human intervention such as vegetation clearing and/or urban development (Smith and Ward, 1998).

The most common causes of floods are climate related, most notably heavy or continuous precipitation and snow melting. Human impacts on river catchments also influence flood behavior, where changes in land use have a direct impact on the magnitude and behavior of floods (Nott, 2006). Over the western sector of Iberia two main types of rain floods can be distinguished: (a) flash floods, usually affecting small hydrographical basins or urban areas, which are caused by very intense convective precipitation such as the case of Madeira in 2010 (Fragoso et al., 2012) and (b) floods in the major rivers that are caused by continuous intense large-scale precipitation (e.g., Lavers et al., 2011).

Changes in precipitation extremes in the Iberian Peninsula (IP) (Gallego et al., 2011; Santo et al., 2014a) are of particular concern since they can be responsible for flash floods (e.g., Ferraris et al., 2002), hydrological droughts (e.g., García-Herrera et al., 2007; Sousa et al., 2011) and landslides (e.g., Zêzere et al., 2008). The IP climate is affected by a relatively small number of large-scale modes of atmospheric circulation variability (e.g., Trigo et al., 2008). Of these patterns the North Atlantic Oscillation (NAO) is the main mode of low-frequency variability in the North Atlantic European sector to explain precipitation variability in western Iberia Peninsula (e.g., Hurrell, 1995; Jones et al., 1997; Rodríguez-Puebla et al., 1998; Trigo et al., 2004; Lorenzo-Lacruz et al., 2011). According to those results, positive (negative) values of NAO indices are related to below (above) average total precipitation over western Iberia Peninsula.

On the other hand, the variability of the dominant storm-tracks in the Northern Hemisphere affects also the surface climate, particularly the precipitation regimes (Trigo, 2006).

Extra-tropical cyclones correspond to one of the most prominent features of the mid-latitude climate and represent a major mechanism for poleward transport of heat and moisture (Peixoto and Oort, 1992) and are often associated with extreme weather conditions like precipitation and/or wind extremes (e.g., Raible, 2007; Liberato et al., 2011). In the IP, the hydrological cycle regime is sensitive to the timing and the position of the winter storms that are predominantly conditioned by the NAO phase (Ulbrich et al., 1999; Trigo et al., 2004).

Historical floods in major river basins of western IP, particularly the Tagus basin have been extensively analyzed (e.g., Benito et al., 2003a,b, 2004, 2005; Ortega and Garzón, 2004). These works have evaluated the temporal distribution of flood occurrence and magnitude within the context of climatic variability in Iberia during the last millennium. Some of these works show the existence of a link between historical floods and the NAO index for the basins of Guadalquivir (Benito et al., 2005) and Guadiana (Ortega and Garzón, 2004). Interestingly the impact of solar activity was also identified for some flood periods (Benito et al., 2004; Vaquero, 2004).

Unusual values of precipitation occurred in early December 1876 leading to large scale flood events in several major river basins in the central and southern sectors of the IP. Recently digitized data from several stations has helped to assess how exceptional this period was. According to records, on 5 December 1876, precipitation reached the highest value ever registered in Lisbon (110 mm in 24 h) since the daily measurements started in 1863, being only exceeded in 2008 (Fragoso et al., 2010). Thus, it still corresponds to the second highest value of daily precipitation ever observed in this city since the start of regular measurements. Similarly, the historical city of Evora registered 90 mm of precipitation on 7 December, a value that was only surpassed on 1944 and is also until today the second highest value ever. However, we will provide evidence that this was not a single event but more likely the culmination of consecutive rainfall episodes that struck central and southern sectors of the IP in the weeks since the preceding October of 1876. As a consequence, river banks of several rivers, including two large international Iberian rivers (Tagus, Guadiana) and the Spanish Guadalquivir suffered widespread floods that caused losses of human life and significant socio-economic impacts.

Atmospheric rivers (ARs) have received special attention in the last decade as they are often associated with extreme precipitation events (Ralph et al., 2006; Lavers et al., 2011). ARs are the water vapor core section of the broader warm conveyor belt, occurring over the oceans along the warm sector of extra-tropical cyclones (Bao et al., 2006). These water vapor bands are typically only a few 100 km across and are located in the lower troposphere, but can stretch over thousands of kilometers across the ocean and their water transportation rate can be at times as intense as that of major terrestrial rivers (Newell et al., 1992). The existence of ARs has been linked to previous heavy precipitation events and floods in Norway (Stohl et al., 2008), United Kingdom (Lavers et al., 2011), California (Dettinger, 2011) and also in Portugal (Liberato et al., 2013).

The aim of this work is to evaluate the impacts of December 1876 floods, with an important focus on the characterization of the short and long-term evolution of the atmospheric conditions responsible for such an extreme event. To achieve these goals, the following objectives must be addressed:

(1) To determine the spatial distribution of precipitation anomalies in the IP and the atmospheric conditions in the months prior to the early December 1876 event.
(2) To evaluate objectively, for the recently digitized stations of Lisbon and Evora, how exceptional was this precipitation event, at various temporal scales.
(3) To evaluate the role played by the atmospheric circulation, namely the NAO and ARs at the monthly-seasonal and daily-weekly scales respectively.

DATASETS AND METHODOLOGY

HISTORICAL SOURCES

The historical source data used were extracted from a comprehensive dataset of flooding and landslide events that occurred in Portugal since 1865 (Quaresma, 2009) and aggregated within the scope of DISASTER project (Zêzere et al., 2014). The DISASTER project allowed to construct a database on hydrogeomorphologic disasters in Portugal. This database was collected through the analysis of all available daily Portuguese newspapers since 1870, mainly from "Diario de Noticias" and "Século." This database provides detailed information on each individual hydro-meteorological event that took place from the late 19th century till the beginning of the 21th century including their specific location, event type (flood or landslide), involved rescue entities, date of the event and date of the publication. Furthermore, it also provides a large amount of additional contextual information for each event and affected town/region, such as the main socio-economic costs, human losses, people injured, disappeared, evacuated, and dislodged.

Additionally, the Spanish newspapers "La Ilustración Española y Americana," "El Magisterio Extremeño," and "La Crónica," were also analyzed for the days following the 1876 floods to improve the knowledge of the impacts of this event in Spain.

THE 20th CENTURY REANALYSIS

The new 20th Century Reanalysis version 2 (Compo et al., 2011) from the National Oceanic and Atmospheric Administration/Earth System Research Laboratory Physical Sciences Division (NOAA/ERSL PSD) was used. This dataset is suitable for this type of analysis because it is currently the only dataset that can provide a continuous 3-D description of many meteorological fields since 1871, i.e., a much longer period than the standard NCEP/NCAR (since 1948) or ECMWF (since 1958) Reanalysis datasets. Here the ensemble mean fields on a 2 by 2° global latitude-longitude grid were used.

Several fields were extracted related to both surface and troposphere levels: 3-h and daily precipitation rate, 6-h and daily sea level pressure and convective available potential energy (CAPE). In addition, for the upper levels (850, 500, and 250 hPa), the 6-h fields of geopotential height, air temperature, both wind components and specific moisture were also extracted.

Table 1 | Available precipitation station data from Portugal and Spain.

	Stations		Period	Registered from
Portugal	Lisbon	A	1863–1940	0 a.m.–24 p.m.
		A	1941–2010	9 a.m.–9 a.m.
		B	1876 (OND)	9 a.m.–9 a.m.
	Evora	A	1873–1887	9 a.m.–9 a.m.
		A	1906–2006	9 a.m.–9 a.m.
		B	1876 (OND)	9 a.m.–9.a.m.
	Porto	A	1906–2006	9 a.m.–9 a.m.
		B	1876 (OND)	9 a.m.–9 a.m.
	Guarda	B	1876 (OND)	9 a.m.–9 a.m.
	Coimbra	B	1876 (OND)	9 a.m.–9 a.m.
	Badajoz		1876 (OND)	9 a.m.–9 a.m.
Spain	Madrid		1876 (OND)	9 a.m.–9 a.m.
	Burgos		1876 (OND)	9 a.m.–9 a.m.
	Huesca		1876 (OND)	9 a.m.–9 a.m.
	Barcelona		1876 (OND)	9 a.m.–9 a.m.

"A" represents long-term data while "B" represents data for 1876 alone. With the exception of Lisbon all stations recorded the 24 h accumulated rainfall from 9 a.m from the previous day until 9 a.m of the corresponding day.

STATION DATA

Precipitation data from different sources were used in this work and a summary is provided in **Table 1** including the name, period and hour of observation. Two long term daily precipitation stations for Portugal (Lisbon and Evora) were digitized recently by the Geophysical Institute Infante Dom Luiz. Data from the Lisbon station was registered from 0 a.m. to 24 p.m. between 1863 and 1940 and from 9 a.m to 9 a.m of the following day from 1941 until 2010. The second precipitation extended series, corresponds to the stations of Evora with daily data recorded from 1873 to 1887 and 1906 to 2006 which were recorded between 9 a.m. and 9 a.m. These long-term time series have been digitized within the framework of the FP7 project ERA-CLIIM (Stickler et al., 2014). In a recent work by one of us the longest time series available for Portugal was evaluated comprehensively (Kutiel and Trigo, 2014). The series of monthly means of the Lisbon daily precipitation was examined in detail for temporal homogeneity using the software package RHTestsV3 (Wang and Feng, 2010) and no significant change-points were found. The choice of the test was based on its robustness and also based on one of the authors experience with it in recent applications to Portuguese temperature (Santo et al., 2014a) and precipitation (Santo et al., 2014b) series.

Moreover, we used additionally monthly precipitation data from three important locations in Portugal (Porto, Guarda and Coimbra) and five Spanish stations. For these stations, the extracted data corresponds to the period of the event: October–December 1876. In summary, the location of the 10 available stations (shown in **Figure 1**), is distributed as follows, five in mainland Portugal (Porto, Guarda, Coimbra, Evora, Lisbon) and five in Spain (Badajoz, Madrid, Burgos, Huesca, Barcelona). For all stations considered here, the climatological reference period used corresponds to the 1971–2000 normal.

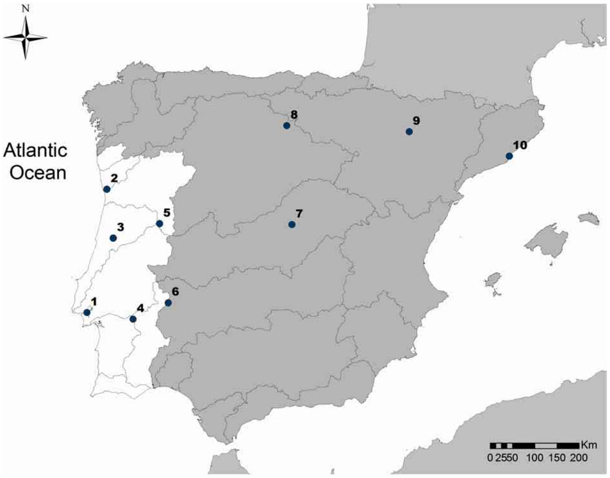

FIGURE 1 | Location of the available stations. 1- Lisbon, 2- Porto, 3- Coimbra, 4- Évora, 5- Guarda, 6- Badajoz, 7- Madrid, 8- Burgos, 9- Huesca, and 10- Barcelona.

NAO DATA

NAO data was accessed through the National Centre of Atmospheric Research (NCAR), Climate and Global Dynamics Division. Extracted data corresponds to the normalized difference of sea level pressures between Lisbon (Portugal) and Stykkisholmur/Reykjavik (Iceland) (Hurrell, 1995). Here we used the monthly mean NAO index from 1865 to 2012.

HISTORICAL DESCRIPTION OF THE RECORD BREAKING PRECIPITATION AND FLOODS EPISODES IN DECEMBER 1876

During the autumn and winter of 1876, the central and southern sectors of the IP were affected by consecutive rainy episodes during several weeks. In particular, the last week of November and the first week of December were characterized by the occurrence of precipitation every day with exceptionally high aggregated values.

As a consequence, river flows of several major rivers, including two large international Iberian rivers (Tagus and Guadiana) and the Spanish Guadalquivir mounted to impressive values on 7 of December leading to widespread floods throughout its embankments that caused scores of human casualties and widespread socio-economic impacts. In fact, a large number of villages and towns located on the shores of these rivers experienced major floods. The geographical location of some of these impacts can be seen in **Figure 2** where one can see that the most affected places are located in the Guadiana basin (SW of Iberia).

At this late stages of the 19th century both Iberian countries (Portugal and Spain) had developed regional and national wide newspapers that were keen to describe (and illustrate) the most important impacts of this episode. Among other publications, we have looked in detail into the following regularly published newspapers in Portugal (Diário de Noticias and Gazeta do Algarve) and in Spain (La Crónica, El Magisterio Extremeño and La Ilustración Española). According to the "Diário de Noticias" (14 December 1876), in Mértola (#4 in **Figure 2**) the Guadiana river had raised 25 meters—a fish was found inside a desk drawer, alive. In this town from the original 64 buildings on the left bank of the Guadiana river (the most sparsely populated part) only 3 left standing. Thus, almost 95% of the buildings were razed. Other Portuguese newspaper "Gazeta do Algarve" (13 December 1876) published: "For 3 days the Guadiana has an amazing current. . . Pomarão has disappeared (#3 in **Figure 2**). All houses were dragged, and we cannot recognize the place where they use to be anymore." The nearby towns of Alcoutim (right bank, Portugal, #2 in **Figure 2**) and Sanlucar del Guadiana (left bank, Spain) almost disappeared and only the houses in the highest places remained. The town of Vila Real de St António, located at the mouth of river Guadiana (#1 in **Figure 2**) was devastated and there were at least 11 deaths.

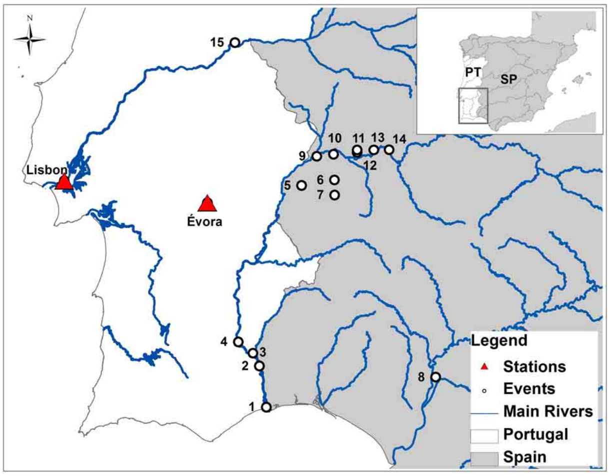

FIGURE 2 | Location of some of the most affected places by the flood of 1876 mentioned by several newspapers. 1- Vila Real de St António, 2- Alcoutim, 3- Pomerão, 4-Mértola, 5-Olivenza, 6-La Albuera, 7- Almendral, 8- Seville, 9- Badajoz, 10- Talavera la Real, 11- Puebla de la Calzada, 12- Montijo, 13- Gévora, 14- Mérida, 15- Vila Velha de Rodão.

In Spain, the damage caused by this flood event was also impressive. The consequences were particularly severe around Badajoz, a Spanish city located right on the border with Portugal (#9 in **Figure 2**). Some of the most important infrastructures of the city of Badajoz were destroyed (**Figure 3**) including communication routes by road and rail and telegraph lines. Moreover, the most important infrastructure in the city, the great Palmas bridge over the Guadiana river, collapsed after losing seven arches (**Figures 3A–C**). This bridge was a strategic point on the route Lisbon-Madrid and had never collapsed before, since it had been re-erected in 1612 (González Rodríguez, 1995). As a consequence of this event the city of Badajoz was isolated, almost surrounded by water, for 4 days. The communication route by rail was recovered only on 13 December, 1 week after the flood. The newspapers indicate widespread damage to homes and business, with a large number of houses presenting partial or total collapse, and in the aftermath hundreds of families become homeless.

Other cities located close to Badajoz in the Guadiana basin were equally affected (**Figure 2**), such as Mérida (where the

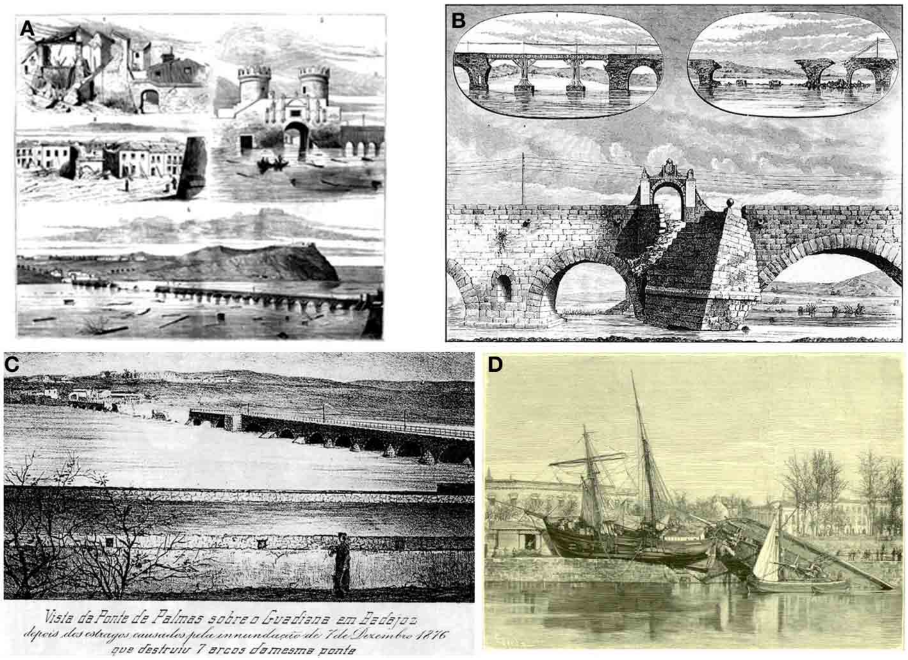

FIGURE 3 | Some engravings on the floods of December 1876. (A) four scenes from the city of Badajoz flooded by the waters of the Guadiana, including a picture of the importantly damaged Bridge of Palmas; **(B)** damages in the great Roman Bridge in the city of Mérida caused by the rising of Guadiana river; **(C)** an anonymous Portuguese engraving showing the seven lost arches in the Bridge of Palmas in Badajoz; and **(D)** shipwreck of a Swedish boat in Seville caused by the rising of Guadalquivir river. Engravings **(A,B,D)** were published in the newspaper "La Ilustración Española y Americana."

bridge on the Guadiana river was also damaged, #14 in **Figure 2**), Olivenza, La Albuera, Gévora, Almendral, Talavera la Real, Puebla de la Calzada, Montijo (#5,6,13,7,10,11,12 in **Figure 2**), and other minor villages. See, for example, the chronicles appeared in the local newspapers "La Crónica" (December 1876) and "El Magisterio Extremeño" (15 December 1876). In Seville, in the basin of the Guadalquivir river (#8 in **Figure 2**), a Swedish and an English ship were dragged into the city as a consequence of the intense river flow (**Figure 3D**).

According to Benito et al. (2003a), who have used the record from Vila Velha do Ródão gauge station the 1876 episode corresponds to the largest flood with an estimated discharge of 15,850 $m^3 s^{-1}$. The authors were analysing flooding in the Tagus river basin over the last millennium and the case of Alcantara, about 100 km upstream from Vila Velha de Rodão. The seven documented floods are referred to the Alcantara Roman bridge (built in AD 103,) and the largest flood during the last 200 years were also recorded in 1876 for which model peak discharge estimates of 14,800 $m^3 s^{-1}$ (Benito et al., 2003a). Additionally, palaeoflood hydrology of the Tagus River (Central Spain) was reconstructed from slackwater deposits and palaeostage indicators (Benito et al., 2003b) indicating that in Alcantara, the largest floods of the last 200 years were recorded in AD 1876, 1941, 1947, and 1856 in which the exact water stages documented floods mentioned before.

According to Loureiro (2009), the flood of 1876 was referenced as the biggest one ever recorded in Tagus when entering into Portuguese territory (in Vila Velha do Rodão, #15 in **Figure 2**). Besides measuring the river elevations in a cross section at this station, the Portuguese Hydrological Services had introduced in 1852 a hydrometer flay (measuring the river flow speed), thus allowing to put the outstanding flood of 1876 into a longer perspective. The flow rate was computed by Loureiro (2009) using the velocity-height curve equation also depicted in **Figure 4**. It should be noted that the curve calibration was restricted to the century prior to the introduction of major dams in river Tagus in the 1950s and 1960s, that have altered the river flow regime, smoothing large peak values (Trigo et al., 2004). Taking into account that the river height at Vila Velha do Rodão had been monitored (for river surface elevation) since the beginning of the 19th century, we are confident that the early December 1876 floods correspond to the absolute maximum since around 1800 and surpassing the other major floods that occurred in 1823, 1855, 1912, and 1941.

ASSESSING THE OBSERVED PRECIPITATION

THE EXCEPTIONAL WEEKLY PRECIPITATION AT LISBON AND EVORA

Looking at long-term daily series evaluated (Lisbon and Evora) it becomes evident that both stations present an extreme value on the 5 December 1876, but preceded by significant amounts of rainfall in, at least, the previous week. Therefore, with the aim of understanding the extent in time and the magnitude of this multi-daily event, we have computed the daily average for the accumulated precipitation values (from 1 to 10 days) for the entire time series and rank all values, with the top 10 events being represented in **Figure 5A** (Lisbon) and **Figure 5B** (Evora). This figure presents the 10 highest values of daily average accumulated precipitation (X axis) relative to events with successively more days (lengthier) as obtained by adding either; 1, 2, 3, or more (up to 10) days (Y axis). The colors allow a simple identification of the years in which the event occurred while the daily average of the accumulated precipitation for each time period is represented by the bar high (Z axis). Several conclusions can be inferred from this graphic, namely that:

(a) The 1876 episode (dark blue) was so intense (in magnitude but also in temporal span) that this episode dominates the upper ranks of rainiest events at longer time scales, hence the blue triangular shape of records that extends between 2 and 10 days.

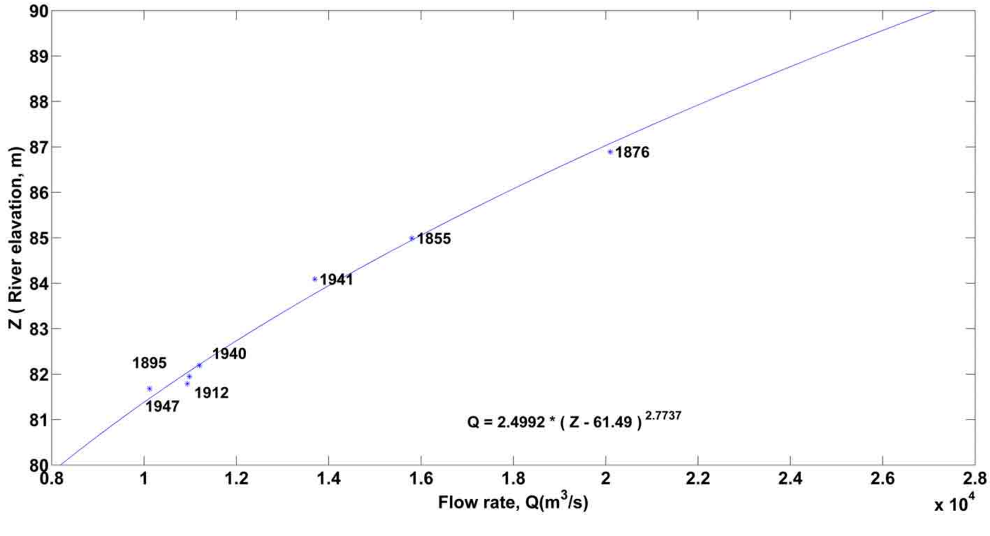

FIGURE 4 | Relation between river elevation (y-axis) and flow rate (x-axis) according to Loureiro (2009).

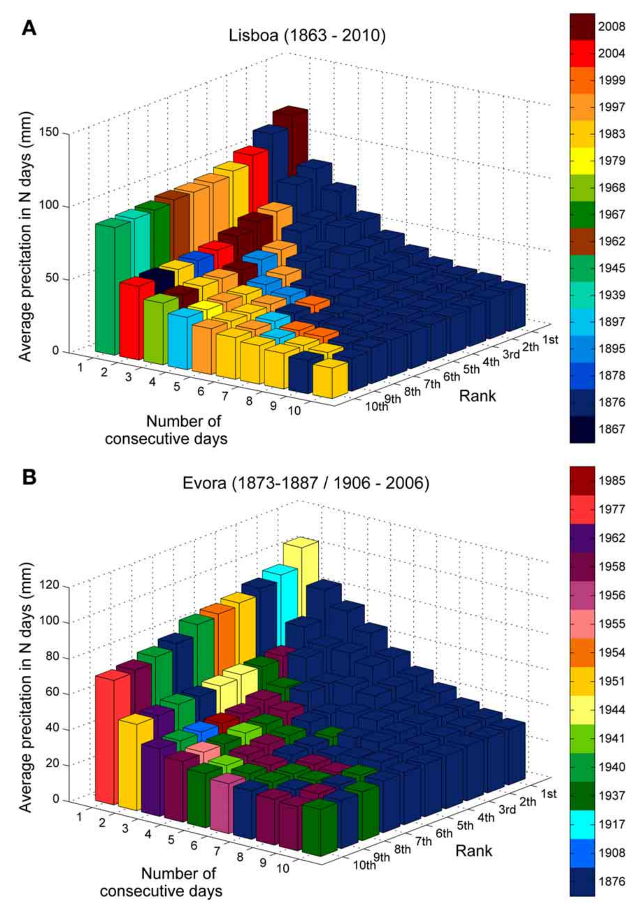

FIGURE 5 | The 10 highest values (rank) of accumulated precipitation from 1 to 10 consecutive days in (A) Lisbon for the period 1863–2010 and (B) Evora for the period 1873–1887, 1906–2006 respectively. The color bar scale represents the year with an extreme event that is included in the graphic. The vertical axis represents the average precipitation amount in 24 h.

(b) In Evora, two of the top 10 rainiest 1-day events (dark blue) were registered only 2 days apart during the December 1876 episode. Therefore, it is quite natural the overall dominance of record precipitation in upper ranks of rainiest events between 2 and 10 days.

(c) With the exception of 1876, the rainiest events in Lisbon at the daily scale have been observed in the last 30 years (1983, 1997, 2004, and 2008). In fact, the recent episode in February 2008 (dark red) corresponds to the absolute maximum daily value (Fragoso et al., 2010). On the contrary, in Evora, the rainiest events at the daily scale have occurred until the mid-20th century (1876, 1917, 1944, and 1951). This different time line in extreme rainy events is consistent with previous works that have shown an increase in extreme rainy episodes in Lisbon and a decrease in Evora and central IP during the last decades (Gallego et al., 2011; Kutiel and Trigo, 2014).

In order to summarize these results, **Table 2** shows the highest daily average precipitation in Lisbon and Evora (from 1 to 10 days) and the corresponding time interval. Again, it is possible to confirm that the record for 1 day precipitation belongs to 18 February 2008 (Lisbon) and 4 October 1944 (Evora), while looking at 2 and more days, the 1876 event is always the rainiest episode and the time interval persistently matches between 28 November and 7 December 1876. The longest period in which 1876 holds the highest value of accumulated precipitation corresponds to 14 days.

THE WET AUTUMN OF 1876

The early days of December 1876 were characterized by high values of precipitation in Lisbon and other Portuguese stations. However, the extreme flood events that struck large rivers such as Tagus and Guadiana would not have materialize if they depended only on the concentrated daily-to-weekly scale precipitation described in the previous section. In fact, the unusual precipitation observed in early December was preceded by intense rainfall throughout most of autumn. This is clearly depicted in **Figure 6** that shows the daily cumulative precipitation for both stations between 1 September and 10 December. Accordingly, during October and November the cumulative precipitation was close to the 95th percentile. However, the extreme rainy period in the first week of December prompted this rainfall index into absolute record values in both stations on 10 December 1876. Thus, it never rained so much in Lisbon and Evora during the first 100 days of the hydrological year (that starts at the beginning of September) as in that year of 1876.

We have computed the ratio of monthly precipitation for the months of October, November and December of 1876 in comparison with a 30-years normal period (1971–2000) and results are presented in **Figure 7**. In November and December most available stations in IP recorded more than twice the average climatological value. It is immediately striking the concentration of stations with high ratios within Portugal, particularly in December where almost all the stations registered 2–4 times more than the long-term average. We should stress the two most extreme case studies, namely; (1) Evora station that registered more than four times the average precipitation in December and (2) and Lisbon also in December that received more than three times the average precipitation. This implies that the last 3 months of 1876 registered considerable more precipitation than the average in western Iberia, even before the record 2–10 day precipitation observed in early December. We are confident that the pouring of almost continuous precipitation throughout these months contributed undoubtedly to soak the upper layers of soil and, thus, amplifying the intensity of floods on the days 6–8 December.

ASSESSING THE ATMOSPHERIC CIRCULATION

THE INFLUENCE OF THE NAO

Until recently, the unavailability of long-term reanalyses datasets excluded the possibility to study the atmospheric circulation associated with this event at different temporal and spatial scales, particularly in relation to mid and upper troposphere variables. The feasibility of such an approach has been made possible through the use of the 20CR (Compo et al., 2011) currently starting in 1871, i.e., sufficient to describe in detail the outstanding prolonged event of late 1876. Here, we will focus

Table 2 | Values and time period for higher precipitation value from 1 to 10 days.

Days of accumulated precipitation	Lisbon		Évora	
	Date of the highest value	Daily precipitation average (mm/day)	Date of the highest value	Daily precipitation average (mm/day)
1	18/02/2008	118.4	4/10/1944	104.0
2	5/12/1876–6/12/1876	85.1	6/12/1876–7/12/1876	83.5
3	4/12/1876–6/12/1876	72.5	5/12/1876–8/12/1876	59.4
4	3/12/1876–6/12/1876	56.4	4/12/1876–7/12/1876	65.7
5	3/12/1876–7/12/1876	46.5	3/12/1876–7/12/1876	55.2
6	2/12/1876–7/12/1876	39.8	3/12/1876–8/12/1876	47.9
7	2/12/1876–8/12/1876	35.0	3/12/1876–9/12/1876	41.2
8	29/11/1876–6/12/1876	31.8	30/11/1876–7/12/1876	36.6
9	28/11/1876–6/12/1876	30.7	30/11/1876–8/12/1876	33.8
10	28/11/1876–7/12/1876	28.3	29/11/1876–8/12/1876	31.4

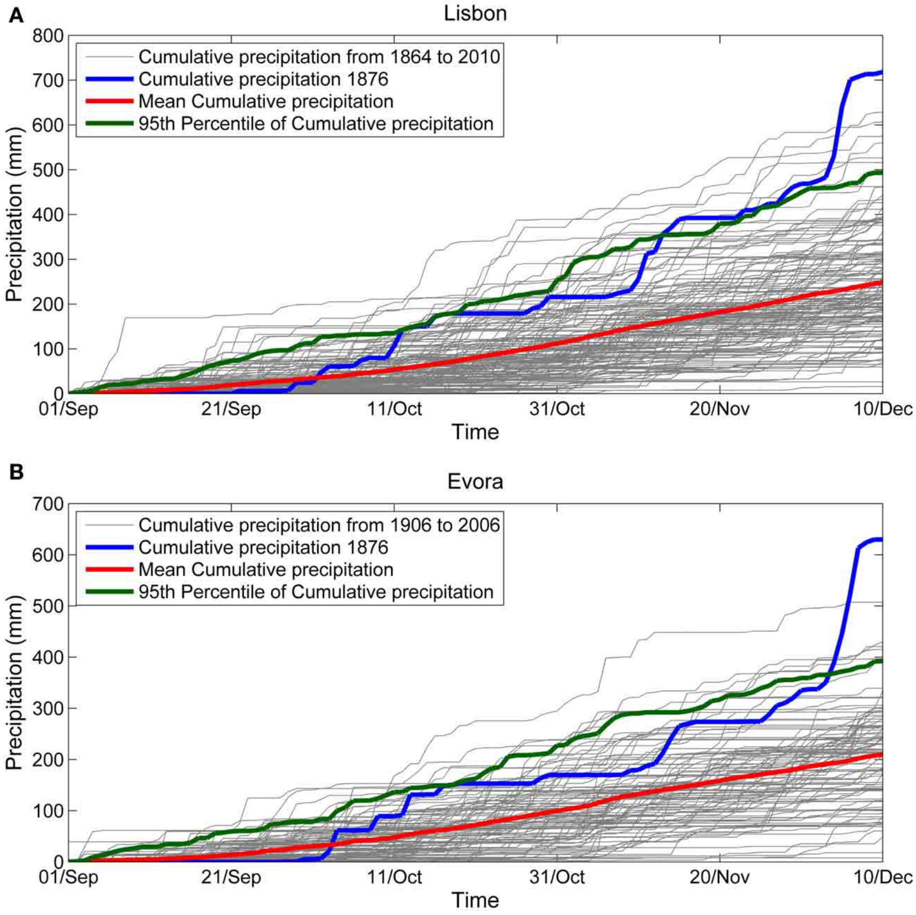

FIGURE 6 | Cumulative precipitation from the 1st of Setember to the 10th of December using sation data. Each year of cumulative precipitation for **(A)** Lisbon (1864–2010) and **(B)** Evora (1906–2006) is represented in gray. Mean and 95th percentile of precipitation is represented in red and green respectively and acumulated preciptiation in the year of 1876 is represented by the blue line.

on the large-scale atmospheric circulation patterns over the North-Atlantic and Europe at the monthly scale, based on the monthly mean and anomaly pressure fields. **Figure 8** provides the anomalous pressure field for the November (**Figure 8A**) and December (**Figure 8B**) months. For November, an intense pressure dipole appears over the Atlantic with a negative anomaly over Azores and a positive center located close to Iceland, i.e., a striking negative NAO configuration (Hurrell, 1995). The

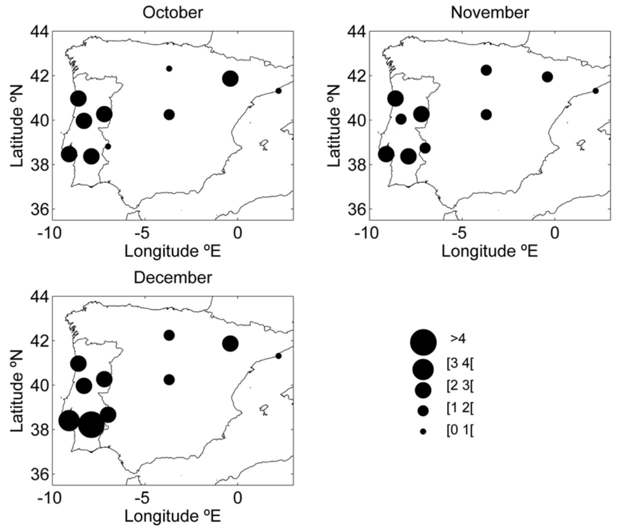

FIGURE 7 | Precipitation ratio in October, November and December 1876 when compared to the 1971–2000 average in several stations (Porto, Guarda, Coimbra, Lisbon, Evora, Badajoz, Madrid, Burgos, and Huesca). The climatological data for Spanish stations was obtained from Aemet (Agencia Estatal de Meteorología), and for Portuguese stations from IPMA (Portuguese Sea and Atmosphere Institute).

following month of December 1876 is also characterized by a similar North-South SLP dipole although with the negative and positive centers shifted toward the northeast. It is possible to state that all the 3 considered months (Oct/Nov/Dec) present an overall large-scale pattern that resemblance the NAO mode to a large extent, presenting strong negative NAO index values of −1.9, −4.4, and −2.1 respectively. It is important to stress that the NAO index registered in November 1876 corresponds to the absolute minimum record for the month of November between 1865 and 2012 (**Figure 9**). It is now well accepted that negative NAO index winter months are overwhelmingly associated with wetter-than-usual months over Iberia (e.g., Hurrell, 1995; Trigo et al., 2004), consequence of a southward shift of the main storm tracks in the Atlantic (Trigo et al., 2004; Trigo, 2006). In this regard the low NAO values registered between October and December of 1876 are bound to be reflected in the Iberian precipitation as previously described in **Figure 7**. These results are in good agreement with the ones obtained by Salgueiro et al. (2013) that used a new methodology to access the influence of NAO on flood magnitude of Tagus River since mid-19th century. They showed that the largest floods prior to construction of largest Tagus river dams (return period equal and over 25-years) occurred when a negative NAO dominated over a period of 10 days, starting at least 25 days prior to the peak.

Nevertheless, in order to reinforce the message we used the 2°× 2° precipitation fields form the 20CR reanalysis data to compute the monthly precipitation anomaly for the entire Iberia (**Figure 10**). The rationale for assessing the precipitation impact with the 20CR dataset is the possibility to provide a continuous representation of Iberia, unlike the sparse representation with the few available stations, additionally it also allows a visualization of sub-daily dynamics (every 6 h) that can be useful for some purposes. Despite the uncertainties of reanalysis values, a positive monthly anomaly over 200 mm appeared south and west of Iberia during November and above 250 mm in most western Iberia in December.

SYNOPTIC ANALYSIS LEADING TO THE DECEMBER 1876 EVENT

Besides the analysis at the monthly scale presented above, the 20CR reanalyses allows a more in depth study of the atmospheric conditions associated to the severe weather event at the 1–10 days scale in early December 1876. With the aim of promoting the visualization of complementary explanatory meteorological fields we have obtained sequences of 6-h (or daily at fixed hours) synoptic charts for several days during the peak precipitation period in early December (e.g., daily accumulated precipitation and daily mean sea level pressure evolution in **Figure 11**). Additionally, we have also computed hourly panels for surface and upper air fields that are capable of providing some additional light into the overall evolution of the synoptic conditions (e.g., 12 U.T.C example in **Figure 12**). Among these meteorological fields, we have paired precipitation rate and mean sea level pressure (SLP) (**Figure 12A**); precipitation rate and CAPE (**Figure 12B**); air temperature at 850 hPa and geopotential height at 500 hPa (**Figure 12C**); upper troposphere wind speed intensity and divergence at 250 hPa (**Figure 12D**). To complement these we provide also additional fields also at 12 UTC, namely; lower troposphere wind speed vectors and specific moisture content at 900 hPa (**Figure 13**) and wind speed intensity and divergence at 900 hPa on **Figure 13**). In order to avoid an excess usage of images, we will restrict the analysis to the most important panels for each case.

The evolution of daily accumulated precipitation values and associated daily mean sea level pressure contours from 2 until 7 of December 1876 are shown on **Figure 11**. A closer look at these fields reveals a persistent large region of significant precipitation lingering almost continuously over south-western Iberia. Moreover, from a dynamic perspective, it is also visible that these high values of precipitation are related to successive frontal systems that kept crossing the Atlantic Ocean, with a predominant SW to NE direction, while other low pressure system centers (albeit more intense) travel at higher latitudes, than what is usual at this time of the year (Trigo, 2006). A similar analysis was performed between 28 November and 2 December (figure not shown).

It is possible to state that during these 10 days western and southern Iberia were often under the influence of these consecutive low pressure systems between Azores, Madeira and western IP, characterized by strong winds and precipitation, particularly between 2 and 7 December. According to the 20 CR fields (and consistent with the observed data in Lisbon and Evora) the southern Portuguese territory registered precipitation throughout the entire analyzed period. Furthermore, based on these datasets it is possible to realize that the heaviest precipitation occurred in two main phases:

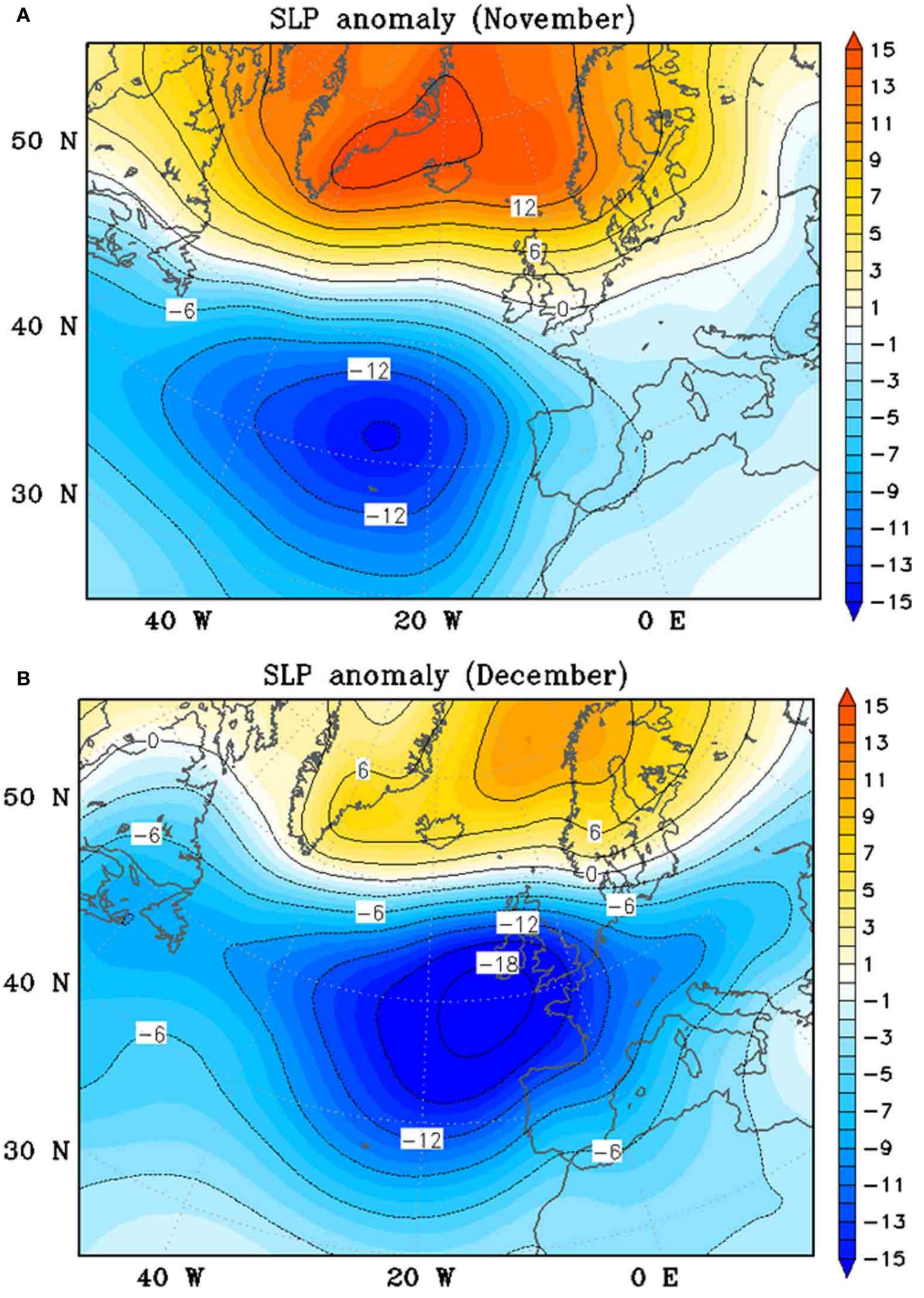

FIGURE 8 | November (A) and December (B) 1876 sea level pressure anomaly in hPa when compared with the average period 1901–2000.

(1) The first pulse corresponds to the movement of the low pressure system crossing the Atlantic Ocean between the 28 and 30 November, increasing considerably the amount of precipitation rate over the coastal western IP, that had remained on that sector for more than 48 h until it finally dissipated on the night of 30 November. The movement of the geopotential height field at 500 hPa (not shown) exhibits a cut-off low over the ocean moving northeast while the low pressure system moved in the same direction at surface (Nieto et al., 2005);

(2) The second pulse, started on 2 December, with a new air frontal system mass, that had developed over the Atlantic ocean and reached the western IP (**Figure 11**). In this occasion, the pulse is more enduring and remains over Portugal

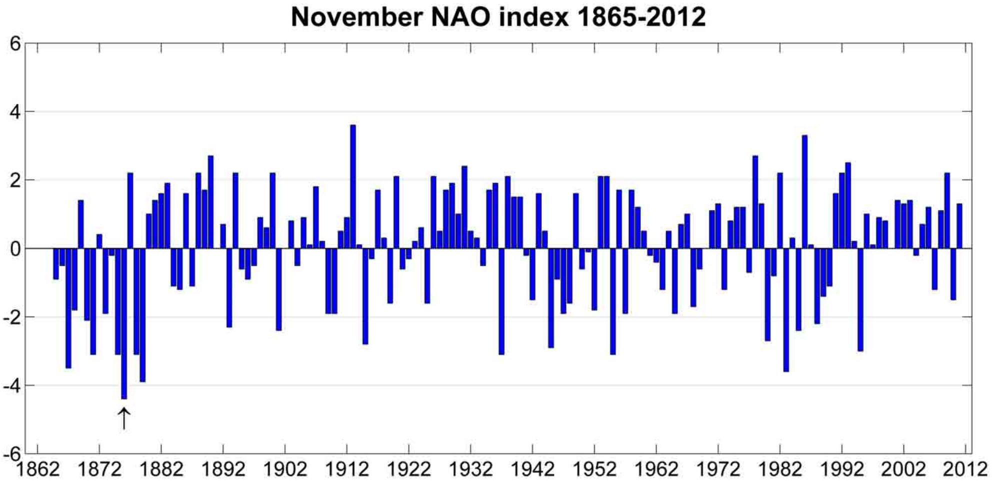

FIGURE 9 | November NAO index from 1865 to 2012.

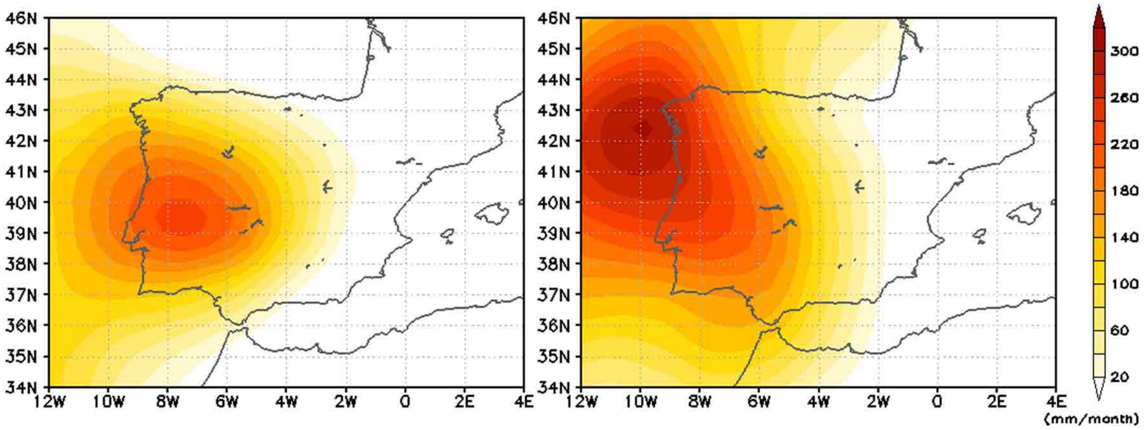

FIGURE 10 | Monthly precipitation anomaly from the 20CR for November (left) and December (right) 1876 (climatological normal for the period 1901–2000).

> almost uninterruptedly until 7 December. For this second phase the main center of the associated depression kept an almost stationary location west of the British Islands, but allowing the associated successive frontal systems and squall instability lines to reach Iberia.

A more in depth analysis of the synoptic conditions for the 5 December 1876 (the day with the highest amount of precipitation in the entire event) can be seen in **Figures 11**, **12**. In **Figure 12C** it is possible to observe the geopotential height at 500 hPa and air temperature at 850 hPa, being dominated by the presence in altitude of a low pressure center and the clear fingerprint of the warm mass intrusion just west of the IP. One of the factors that contributed for the maintenance of this low pressure system for so long at roughly the same location was most probably the presence of the southward displaced jet stream at 250 hPa (**Figure 12D**). For the period spanning between 2 and 7 December, the westerly winds remained at an average latitude of 42°N, lower than usual (Trigo, 2006), inducing strong divergence in altitude at the end of the jet (over western Iberia) as shown on **Figure 12D** (solid lines). This upper level divergence was accompanied by intense convergence at the surface (**Figure 13**, dotted lines), responsible for the intensification of the lower pressure system.

In addition, and looking in more detail into the dynamic fields of specific moisture during those days (2–5 December—**Figure 13**) one can identify a distant source of moisture. Throughout this period there is a long and narrow band of moisture at 900 hPa being transported from sub-tropical latitudes, over the Atlantic Ocean, toward extratropical latitudes, by southwestern winds at 900 hPa above 20 m/s strengthen the atmospheric flow toward Iberia. This combination of wind and specific moisture characteristics concentrated in such a narrow band suggests the presence of an AR (Ralph et al., 2004; Ralph and Dettinger, 2011). The identification of AR in the Atlantic region has actually been mentioned in some studies as the trigger factor of some floods in Europe, namely in Britain (Lavers et al.,

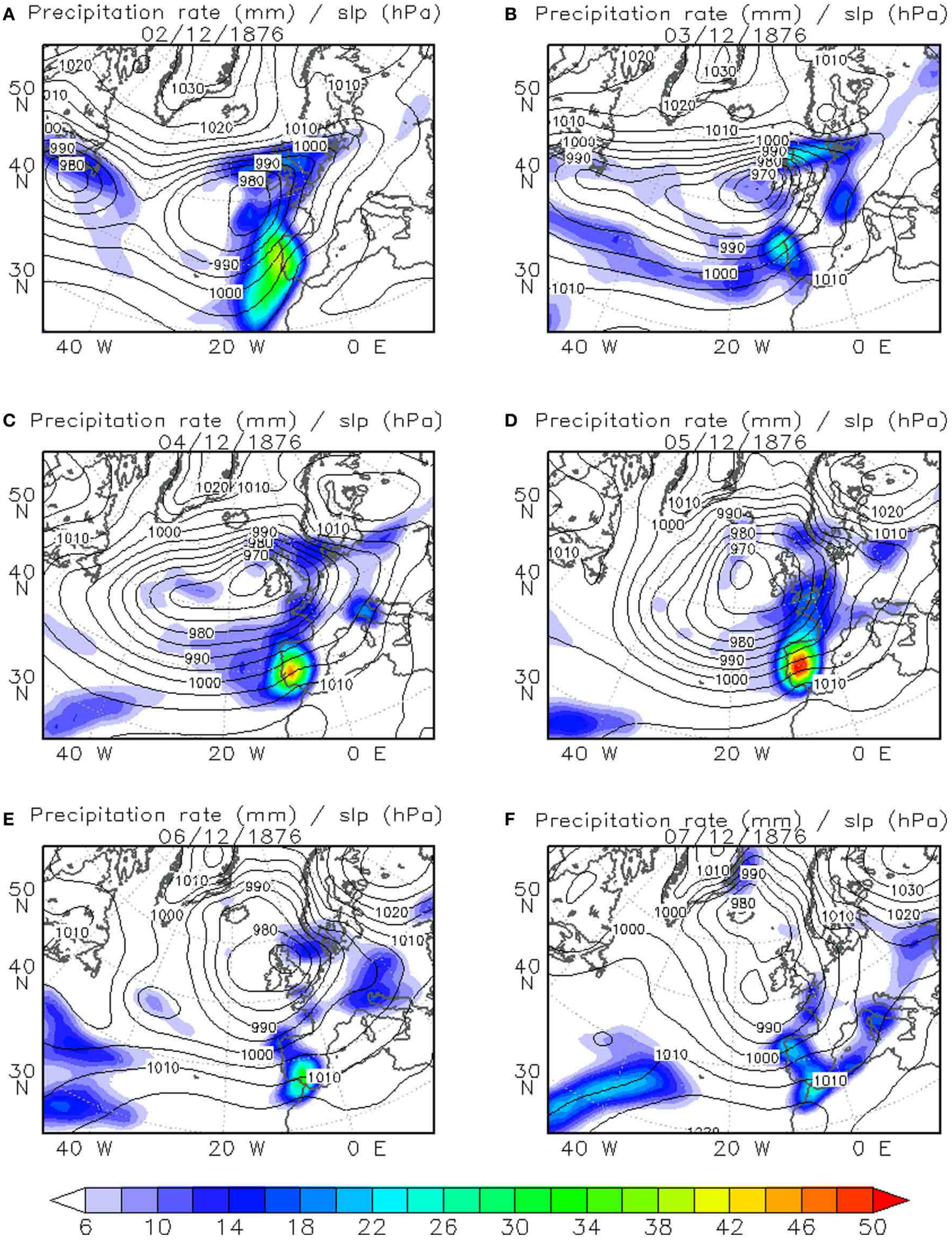

FIGURE 11 | Daily mean precipitation intensity colors (mm) and daily mean sea level pressure, contours (hPa), for: (A) 02/12/1876; (B) 03/12/1876; (C) 04/12/1876; (D) 05/12/1876; (E) 06/12/1876; (F) 07/12/1876.

2011), Norway (Stohl et al., 2008), as well as in Portugal (Liberato et al., 2013). The criterion to the identification of AR involve the presence of, a long (>2000 km) and narrow (<500 km) band of moisture in the lowest atmospheric levels from the tropics with high integrated water vapor (above 2 cm) which is equivalent to 5 g/kg of specific moisture but also wind speed above 12.5 ms^{-1} (Lavers et al., 2011). These characteristics are all present not only between 2 and 5 December (**Figure 13**) but also during some of

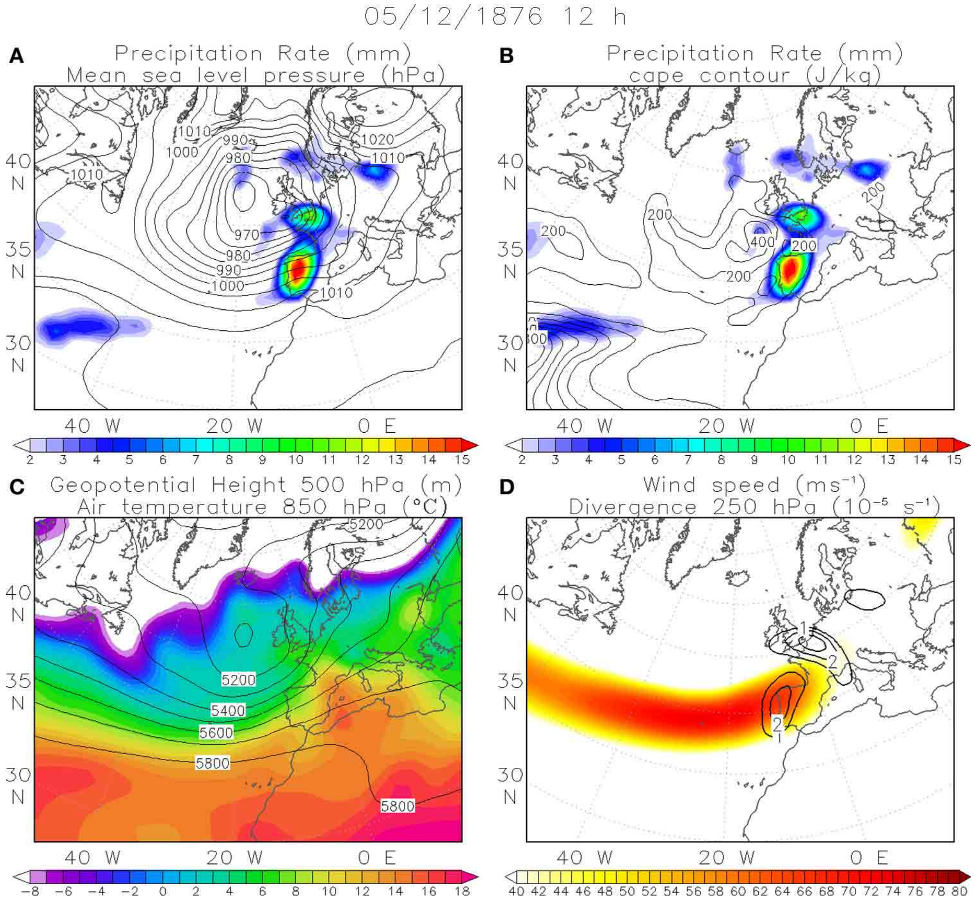

FIGURE 12 | Weather conditions on the 5 December 1876 at 12 a.m. (A) precipitation rate (colors, mm) and mean sea level pressure contours (hPa); **(B)** precipitation rate (colors, mm) and CAPE contours (J kg^{-1}); **(C)** geopotential height at 500 hPa (m, contours) and air temperature (°C, colors) 850 hPa, **(D)** wind speed intensity (colors, ms^{-1}) and divergence (solid) and convergence (dotted) contours at 250 hPa.

the previous days. The presence of this AR is responsible for an additional content of moisture availability reaching the western IP in the days prior to the floods.

Favorable large-scale conditions for vertical movements (uplift mechanism which induced deep convection activity) in addition with the presence of the AR (high specific humidity) contributed to enhanced the precipitation for more than a week. The combined effect of these physical mechanisms allows putting in context the extraordinary amounts of precipitation registered in both Lisbon and Evora during those days. In Lisbon it was registered 238.8 mm from 2 December until 7 December (i.e., 60% of the monthly total for this December) and in Evora the total amount reached 275.8 mm (68% of monthly total). In both cases the precipitation felt during that week was more than 2.5 times the long-term December average. The rainiest day in Lisbon was 5 December 1876 having registered from 0 a.m. to 24 p.m., 110 mm, the second highest value in Lisbon series since 1863 and surpassed recently in 2008 (Fragoso et al., 2010).

CONCLUDING REMARKS

The December of the year 1876 was characterized by exceptionally high aggregated values of precipitation in Southern Portugal and Spain culminating on the extreme flow levels reached on the 7 December in several rivers, including two large international Iberian rivers (Tagus and Guadiana) as well as the Spanish river Guadalquivir. I the case of Guadiana and Tagus rivers it is possible to state that these floods correspond to the largest events since the early 19th century (surpassing the other major floods that took place in 1823 and 1855). This extremeness is quantified objectively for Tagus that had already a river speed gauge working since 1852 attributing the value of 20,000 cubic meters per second for the 7 December's flow rate. Moreover, the extraordinary magnitude of the Guadiana floods can be assessed by the destruction of large sections of the bridge crossing the river in Badajoz, and the destruction of the rail link to Madrid. Despite the widespread floods throughout the embankments of these rivers, natural disasters were not evaluated as seriously as today and we were not able to obtain conclusive figures for the scores of human casualties and dislodge people neither the total economic losses.

The two long term precipitation time series available (Lisbon and Evora) were analyzed to put the December 1876 event into a longer temporal context. For Lisbon, the 1876 episode was so intense (in magnitude but also in temporal span) that it dominates the upper ranks of rainiest events at longer time scales

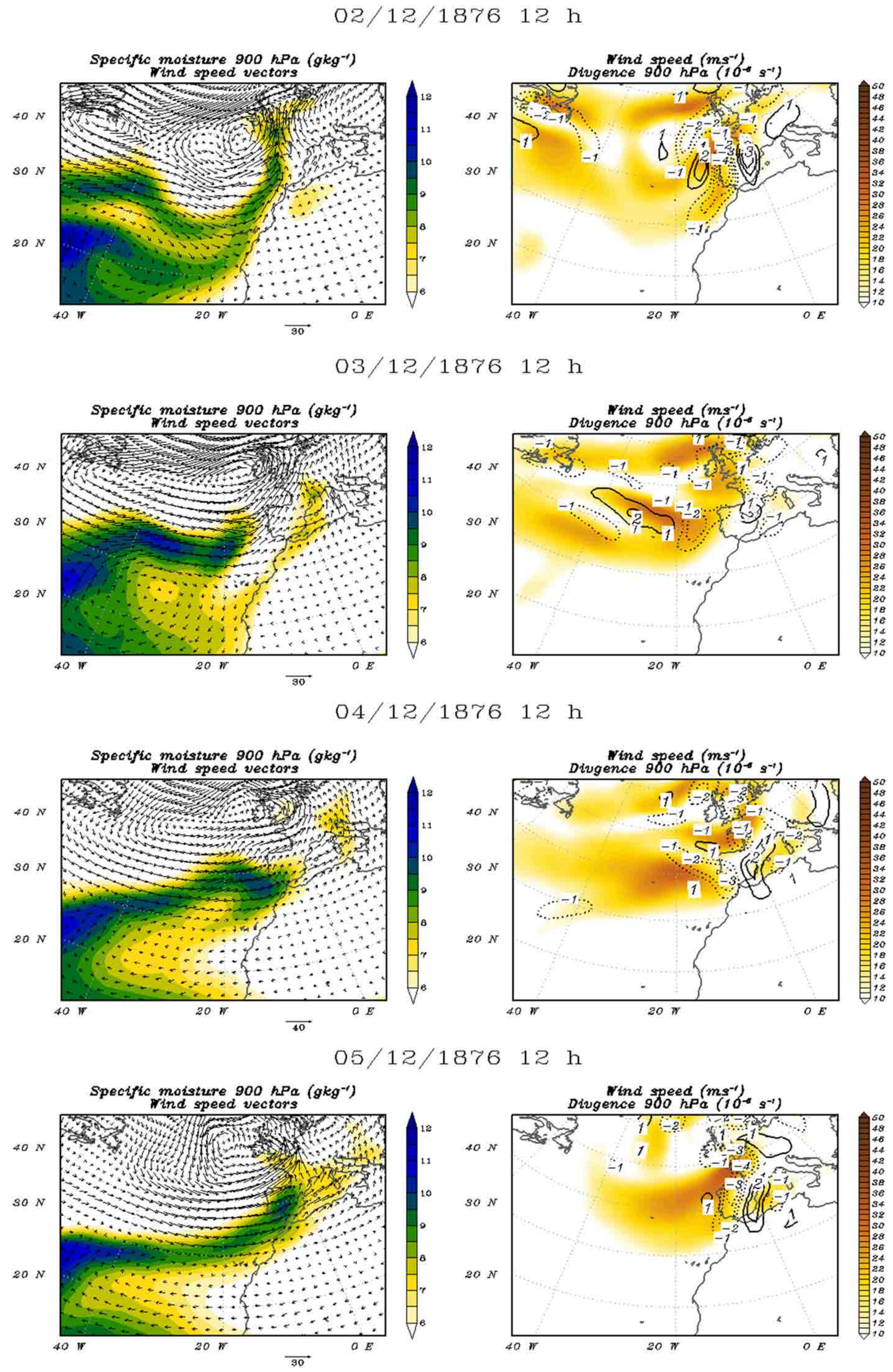

FIGURE 13 | Wind speed and direction (arrows) and specific moisture (gkg^{-1}) color contours at 900 hPa **(left panels)**, wind speed intensity (colors, ms^{-1}) and divergence (solid) and convergence (dotted) contours at 900 hPa **(right panels)** for selected days.

showing accumulated precipitation records that extends between 2 and 10 days. In Evora two of the top 10 rainiest 1-day events were registered only 2 days apart during the December 1876 episode resulting again on the pre-eminence of record precipitation in upper ranks of rainiest events between 2 and 10 days.

Looking at the daily cumulative precipitation for both stations between 1 September and 10 December we were able to assess the evolution throughout autumn months of the precipitation affecting southern Iberia. Accordingly, during October and November the cumulative precipitation was close to the 95th percentile.

Therefore, the extreme rainy period in early December implied new absolute record values in both stations.

The large-scale circulation affecting the North-Atlantic area favored the occurrence of such anomalous rainfall periods in southern Iberia In particular the low NAO values registered between October and December of 1876 (−1.9, −4.4, and −2.1 respectively) are associated with the Iberian precipitation since it is well known that negative NAO index in winter months are associated with wetter-than-usual months over Iberia (e.g., Hurrell, 1995; Trigo et al., 2004).

As mention before, the period of most intense precipitation occurred between 28 November and 7 December. Several frontal systems stroke the IP almost continually during those days with a particular intense period of precipitations on the 3–5 December that culminated on the 7th of December flood events. To evaluate the role of the atmospheric circulation at a daily basis, several meteorological fields were analyzed during this first week of December 1876. During this period, two different meteorological situation affected the IP at the synoptical scale: (a) between the 28 and 30 November, the movement of the low pressure system crossing the Atlantic Ocean associated with a cut-off low increasing considerably the amount of precipitation rate over the coastal western IP, and (b) started on 2 December, an extra-tropical cyclone near the British Island become almost stationary, during the following days where its frontal system mass remains over Portugal almost uninterruptedly until 7 December. We have also shown that the intense precipitation observed in the 2nd period was associated to a combination of wind and specific moisture characteristics at 900 hPa (concentrated in a quite narrow strip) clearly suggesting the presence of an AR.

ACKNOWLEDGMENTS

This work was supported by the Portuguese Foundation for Science and Technology (FCT) through project Klimhist (PTDC/AACCLI/119078/2010). Ricardo Trigo and Maria Antonia Valente were supported by ERA-CLIM (European Union, FP7, Grant Agreement Nr. 265229). Alexandre M. Ramos was supported by the Portuguese Foundation for Science and Technology (FCT) through grant FCT—DFRH—SFRH/BPD/84328/2012. The event data impacts information and newspapers was provided by Ivânia Quaresma.

REFERENCES

Bao, J.-W., Michelson, S. A., Neiman, P. J., Ralph, F. M., and Wilczak, J. M. (2006). Interpretation of enhanced integrated water vapor bands associated with extratropical cyclones: their formation and connection to tropical moisture. *Mon. Weather Rev.* 134, 1063–1080. doi: 10.1175/MWR3123.1

Benito, G., Barriendos, M., Llasat, C., Machado, M., and Thorndycraft, V. R. (2005). "Impactos sobre los riesgos naturales de origen climático," in *Evaluación preliminar de los impactos en España por efecto del Cambio Climático*, ed J. M. Moreno (Coordinador) (Madrid: Ministerio de Medioambiente), 527–548.

Benito, G., Díez-Herrero, A., and Fernandez de Villalta, M. (2003a). Magnitude and frequency of flooding in the Tagus Basin (Central Spain) over the last millennium. *Clim. Change* 58, 171–192. doi: 10.1023/A:1023417102053

Benito, G., Díez-Herrero, A., and Fernández de Villalta, M. (2004). Flood response to NAO and Solar Activity in the Tagus Basin (Cental Spain) over the last millennium. *Clim. Change* 66, 27–28. doi: 10.1023/B:CLIM.0000043334.30365.e0

Benito, G., Sopeña, A., Sánchez-Moya, Y., Machado, M. J., and Pérez-González, A. (2003b). Palaeoflood record of the Tagus River (Central Spain) during the Late Pleistocene and Holocene. *Quaternary Sci. Rev.* 22, 1737–1756. doi: 10.1016/S0277-3791(03)00133-1

Compo, G. P., Whitaker, J. S., Sardeshmukh, P. D., Matsui, N., Allan, R. J., Yin, X., et al. (2011). The twentieth century reanalysis project. *Q. J. R. Meteorol. Soc.* 137, 1–28. doi: 10.1002/qj.776

Dettinger, M. (2011). Climate change, atmospheric rivers, and floods in california - a multimodel analysis of storm frequency and magnitude changes1. *J. Am. Water Resour. Assoc.* 47, 514–523. doi: 10.1111/j.1752-1688.2011.00546.x

Ferraris, L., Rudari, R., and Siccardi, F. (2002). The uncertainty in the prediction of flash floods in the northern Mediterranean environment. *J. Hydrometeorol.* 3, 714–727. doi: 10.1175/1525-7541(2002)003%3C0714:TUITPO%3E2.0.CO;2

Fragoso, M., Trigo, R. M., Pinto, J. G., Lopes, S., Lopes, A., Ulbrich, S., et al. (2012). The 20 February 2010 Madeira flash-floods: synoptic analysis and extreme rainfall assessment. *Nat. Hazards Earth Syst. Sci.* 12, 715–730. doi: 10.5194/nhess-12-715-2012

Fragoso, M., Trigo, R. M., Zêzere, J. L., and Valente, M. A. (2010). The exceptional rainfall event in Lisbon on 18 February 2008. *Weather* 65, 31–35. doi: 10.1002/wea.513

Gallego, M. C., Trigo, R. M., Vaquero, J. M., Brunet, M., García, J. A., Sigró, J., et al. (2011). Trends in frequency indices of daily precipitation over the Iberian Peninsula during the last century. *J. Geophys. Res.* 116, 1–18. doi: 10.1029/2010JD014255

García-Herrera, R., Hernández, E., Barriopedro, D., Paredes, D., Trigo, R. M., Trigo, I. F., et al. (2007). The outstanding 2004/05 drought in the iberian peninsula: associated atmospheric circulation. *J. Hydrometeorol.* 8, 483–498. doi: 10.1175/JHM578.1

González Rodríguez, A. (1995). *La puerta de Palmas y el puente viejo (1460–1994): Badajoz cara al Guadiana.* Badajoz: Caja Rural.

Hurrell, J. W. (1995). Decadal trends in the North Atlantic Oscillation: regional temperatures and precipitation. *Science* 269:676. doi: 10.1126/science.269.5224.676

Jones, P., Jonsson, T., and Wheeler, D. (1997). Extension to the North Atlantic Oscillation using early instrumental pressure observations from Gibraltar and south−west Iceland. *Int. J. Climatol.* 17, 1433–1450. doi: 10.1002/(SICI)1097-0088(19971115)17:13<1433::AID-JOC203>3.0.CO;2-P

Kutiel, H., and Trigo, R. M. (2014). The rainfall regime in Lisbon in the last 150 years. *Theor. Appl. Climatol.* doi: 10.1007/s00704-013-1066-y

Lavers, D. A., Allan, R. P., Wood, E. F., Villarini, G., Brayshaw, D. J., and Wade, A. J. (2011). Winter floods in Britain are connected to atmospheric rivers. *Geophys. Res. Lett.* 38:L23803. doi: 10.1029/2011GL049783

Liberato, M., Pinto, J., Trigo, I., and Trigo, R. (2011). Klaus–an exceptional winter storm over northern Iberia and southern France. *Weather* 66, 330–334. doi: 10.1002/wea.755

Liberato, M. L. R., Pinto, J. G., Trigo, R. M., Ludwig, P., Ordóñez, P., Yuen, D., et al. (2013). Explosive development of winter storm Xynthia over the subtropical North Atlantic Ocean. *Nat. Hazards Earth Syst. Sci.* 13, 2239–2251. doi: 10.5194/nhess-13-2239-2013

Lorenzo-Lacruz, J., Vicente-Serrano, S. M., López-Moreno, J. I., González-Hidalgo, J. C., and Morán-Tejeda, E. (2011). The response of Iberian rivers to the North Atlantic Oscillation. *Hydrol. Earth Syst. Sci.* 15, 2581–2597. doi: 10.5194/hess-15-2581-2011

Loureiro, J. M. (2009). *Rio Tejo: as grandes cheias: 1800–2007, 1st Edn*. Tágides, Lisboa: ARH do Tejo I.P.

Newell, R. E., N. E. Newell, Y. Zhu, and C. Scott. (1992). Tropospheric rivers? A pilot study. *Geophys. Res. Lett.* 19, 2401–2404. doi: 10.1029/92GL02916

Nieto, R., Gimeno, L., de la Torre, L., Ribera, P., Gallego, D., García-Herrera, R., et al. (2005). Climatological features of cutoff low systems in the northern hemisphere. *J. Clim.* 18, 3085–3103. doi: 10.1175/JCLI3386.1

Nott, J. (2006). *Extreme Events: A Physical Reconstruction and Risk Assessment*. Cambridge: Cambridge University Press. doi: 10.1017/CBO9780511606625

Ortega, J. A., and Garzón, G. (2004). "Influencia de la oscilación del Atlántico norte en las inundaciones del Río Guadiana," in *Riesgos naturales y antrópicos en Geomorfología*, eds G. Benito and A. Díez Herrero (Madrid: CSIC), 117–126.

Peixoto, J. P., and Oort, A. H. (1992). *Physics of Climate.* New York, NY: American Institute of Physics, 412–433.

Quaresma, I. (2009). *Inventariação e Análise de Eventos Hidro-Geomorfológicos com Carácter Danoso em Portugal Continental*. M.S. thesis, Faculty of Letters, University of Lisbon, 100.

Raible, C. C. (2007). On the relation between extremes of midlatitude cyclones and the atmospheric circulation using ERA40. *Geophys. Res. Lett.* 34:L07703. doi: 10.1029/2006GL029084

Ralph, F. M., and Dettinger, M. D. (2011). Storms, floods, and the science of atmospheric rivers. *Eos Trans. Am. Geophys. Union* 92, 265. doi: 10.1029/2011EO320001

Ralph, F. M., Neiman, P. J., Wick, G. A., Gutman, S. I., Dettinger, M. D., Cayan, D. R., et al. (2006). Flooding on California's Russian River: role of atmospheric rivers. *Geophys. Res. Lett.* 33:L13801. doi: 10.1029/2006GL026689

Ralph, F., Neiman, P., and Wick, G. (2004). Satellite and CALJET aircraft observations of atmospheric rivers over the eastern North Pacific Ocean during the winter of 1997/98. *Mon. Weather Rev.* 132, 1721–1745. doi: 10.1175/1520-0493(2004)132%3C1721:SACAOO%3E2.0.CO;2

Rodríguez-Puebla, C., Encinas, A. H., Nieto, S., and Garmendia, J. (1998). Spatial and temporal patterns of annual precipitation variability over the Iberian Peninsula. *Int. J. Climatol.* 18, 299–316.

Salgueiro, A. R., Machado, M. J., Barriendos, M., Pereira, H. G., and Benito, G. (2013). Flood magnitudes in the Tagus River (Iberian Peninsula) and its stochastic relationship with daily North Atlantic Oscillation since mid-19th Century. *J. Hydrol.* 502, 191–201 doi: 10.1016/j.jhydrol.2013.08.008

Santo, F. E., de Lima M. I. P., Ramos, A., and Trigo, R. M. (2014b). Trends in seasonal surface air temperature in mainland Portugal, since 1941. *Int. J. Climatol.* doi: 10.1002/joc.3803

Santo, F. E., Ramos, A. M., Lima, M. I. P., and Trigo, R. M. (2014a). Seasonal changes in daily precipitation extremes in mainland Portugal from 1941 to 2007. *Reg. Environ. Chang.* doi: 10.1007/s10113-013-0515-6

Smith, K., and Ward, R. (1998). *Floods: Physical Processes and Human Impacts.* Chichester: John Wiley and Sons.

Sousa, P. M., Trigo, R. M., Aizpurua, P., Nieto, R., Gimeno, L., and Garcia-Herrera, R. (2011). Trends and extremes of drought indices throughout the 20th century in the Mediterranean. *Nat. Hazards Earth Syst. Sci.* 11, 33–51. doi: 10.5194/nhess-11-33-2011

Stickler, A., Bronnimann, S., Valente, M. A., Bethke, J., Sterin, A., Jourdain, S., et al. (2014). ERA-CLIM: historical surface and upper-air data for future reanalyses. *Am. Met. Soc.* doi: 10.1175/BAMS-D-13-00147.1

Stohl, A., Forster, C., and Sodemann, H. (2008). Remote sources of water vapor forming precipitation on the Norwegian west coast at 60°N–a tale of hurricanes and an atmospheric river. *J. Geophys. Res.* 113:D05102. doi: 10.1029/2007JD009006

Trigo, I. F. (2006). Climatology and interannual variability of storm-tracks in the Euro-Atlantic sector: a comparison between ERA-40 and NCEP/NCAR reanalyses. *Clim. Dyn.* 26, 127–143. doi: 10.1007/s00382-005-0065-9

Trigo, R. M., Pozo-Vázquez, D., Osborn, T. J., Castro-Díez, Y., Gámiz-Fortis, S., and Esteban-Parra, M. J. (2004). North Atlantic oscillation influence on precipitation, river flow and water resources in the Iberian Peninsula. *Int. J. Climatol.* 24, 925–944. doi: 10.1002/joc.1048

Trigo, R. M., Valente, M. A., Trigo, I. F., Miranda, P. M. A., Ramos, A. M., Paredes, D., et al. (2008). The impact of North Atlantic wind and cyclone trends on European precipitation and significant wave height in the Atlantic. *Ann. N.Y. Acad. Sci.* 1146, 212–34. doi: 10.1196/annals.1446.014

Ulbrich, U., Christoph, M., Pinto, J. G., and Corte-Real, J. (1999). Dependence of winter precipitation over Portugal on NAO and baroclinic wave activity. *Int. J. Climatol.* 390, 379–390.

Vaquero, J. M. (2004). Solar Signal in the number of floods recorded for the Tagus River Basin over the Last Millenium. *Clim. Change* 66, 27–28. doi: 10.1023/B:CLIM.0000043146.37662.de

Wang, X. L., and Feng, Y. (2010). *RHtestsV3 User Manual*. Toronto, ON: Climate Research Division, Science and Technology Branch, Environment Canada.

Zêzere, J. L., Pereira, S., Tavares, A. O., Bateira, C., Trigo, R. M., Quaresma, I., et al. (2014). DISASTER: a GIS database on hydro-geomorphologic disasters in Portugal. *Nat. Hazards*. doi: 10.1007/s11069-013-1018-y

Zêzere, J. L., Trigo, R. M., Fragoso, M., Oliveira, S. C., and Garcia, R. A. C. (2008). Rainfall-triggered landslides in the Lisbon region over 2006 and relationships with the North Atlantic Oscillation. *Nat. Hazards Earth Syst. Sci.* 8, 483–499. doi: 10.5194/nhess-8-483-2008

Conflict of Interest Statement: The authors declare that the research was conducted in the absence of any commercial or financial relationships that could be construed as a potential conflict of interest.

Received: 03 February 2014; accepted: 16 March 2014; published online: 03 April 2014.
Citation: Trigo RM, Varino F, Ramos AM, Valente MA, Zêzere JL, Vaquero JM, Gouveia CM and Russo A (2014) The record precipitation and flood event in Iberia in December 1876: description and synoptic analysis. Front. Earth Sci. 2:3. doi: 10.3389/feart.2014.00003
This article was submitted to Atmospheric Science, a section of the journal Frontiers in Earth Science.

ADVANTAGES OF PUBLISHING IN FRONTIERS

FAST PUBLICATION

Average 90 days
from submission
to publication

COLLABORATIVE PEER-REVIEW

Designed to be rigorous –
yet also collaborative, fair and
constructive

RESEARCH NETWORK

Our network
increases readership
for your article

OPEN ACCESS

Articles are free to read,
for greatest visibility

TRANSPARENT

Editors and reviewers
acknowledged by name
on published articles

GLOBAL SPREAD

Six million monthly
page views worldwide

COPYRIGHT TO AUTHORS

No limit to
article distribution
and re-use

IMPACT METRICS

Advanced metrics
track your
article's impact

SUPPORT

By our Swiss-based
editorial team

frontiers

EPFL Innovation Park · Building I · 1015 Lausanne · Switzerland
T +41 21 510 17 00 · info@frontiersin.org · frontiersin.org